THE UNIVERSITY *of* EDINBURGH

Carbon burning in stars: An experimental study of the $^{12}C(^{12}C, p)^{23}Na$ reaction towards astrophysical energies

Elia Lizeth Morales Gallegos

Doctor of Philosophy
The University of Edinburgh
August 2017

Abstract

Fusion reactions between ^{12}C nuclei are among the most important in stellar evolution since they determine the destiny of massive stars ($>$ 8 $M_{\odot}$). At thermonuclear energies (E_{cm}=1.5 $\pm$ 0.3 MeV), the ^{12}C+^{12}C reactions mainly proceed through ^{20}Ne + α and ^{23}Na + p channels. Since these energies are much lower than the height of the Coulomb barrier (E_{cm}= 6.1 MeV), the direct measurements of the ^{12}C+^{12}C reactions are very challenging because of the extremely small cross sections involved and the high beam-induced background originating from impurities in the targets. In addition, the ^{12}C+^{12}C reaction forms ^{24}Mg at relatively high excitation energies (above the ^{12}C 13.93 MeV thresholds) where molecular configurations are possible. Theoretical models fail to reproduce such structures and as a result, the extrapolation of high-energy cross section data towards the energy of astrophysical interest remain uncertain by 2-3 orders of magnitude. Further experimental efforts to measure at the lowest accessible energies are therefore in need. However, additionally to the extremely low cross sections and the resonant structure, the measurements at stellar energies of the ^{12}C+^{12}C reactions are troublesome due to natural hydrogen and deuterium contamination in the carbon targets. These target contaminants hamper the measurement of the ^{12}C+^{12}C process in all exit channels given that the ^{12}C +^{1,2} H reactions cross sections are considerably higher than that of the reaction of interest. In consequence, the use of ultra-low H content graphite targets and a study of the target behaviour under beam bombardment are necessary. This work focused on the experimental measurements of the ^{12}C(^{12}C, p)^{23}Na and ^{12}C(^{12}C, α)^{20}Ne reactions using charge particle detection. Although both channels were measured, only the proton channel was analysed and discussed in this thesis due to time constrains.

The experiment was performed at the 3 MV pelletron tandem accelerator of the CIRCE (Centre for Isotopic Research on the Cultural and Environmental heritage) laboratory in Caserta, Italy. The experimental approach involved the development of optical calculations for optimal beam transportation (using the software COSY), the use of a fourΔE-Erest detectors system (a variable pressure CF_4 ionization chamber used as the ΔE detector and a 300 mm^2 Si detector used as the Erest) called GASTLY (GAs Silicon Two-Layer sYstem) and a study of the deuterium (hydrogen does not contribute to the beam-induced background at the detection angles and beam energies used here) contamination in graphite targets.

The GASTLY detectors were placed at backward angles (121, 143 and 156° respect to the beam axis) and the ^{12}C+^{12}C reactions were investigated using carbon beams of E_{cm}= 4.30 - 2.52 MeV with intensities of the order of μA. Highly Ordered Pyrolytic Graphite (HOPG) and highly pure (99.8%) natural graphite targets were used for the deuterium contamination study. A thermocamera was used to constantly monitor the target temperature during beam bombardment, allowing the investigation of target's deuterium content as a function of target temperature. Results showed a decrease in target's deuterium content of 53 - 80% in the target's temperature range of 200 - 1200°C, depending on the type of target and detection angle. Furthermore, it was found that surrounding the scattering chamber with a nitrogen atmosphere while measuring low counting rate reactions (such as ^{12}C+^{12}C at low energies), the HOPG target's deuterium content decreases to about half its original value for a target temperature in the range between 800 - 1100°C. For the ^{12}C+^{12}C reactions measurements, the HOPG target was used, maintaining high target temperatures.
The p_{0-6} proton groups of the $^{12}C(^{12}C, p)^{23}Na$ reaction were analysed and their yields, cross sections and astrophysical S-factors were obtained and are presented in this thesis. A comparison with previous data available in the literature is also presented, together with an indication for possible improvements in future investigations.

Lay Summary

Stellar evolution can be described as a sequence of gravitational contraction epochs followed by "burning" stages where nuclear reactions take place. In the third burning phase, $^{12}C+^{12}C$ reactions are among the most important mechanisms since they determine the final fate of massive stars: whether they will explode as supernovae or die as white dwarfs. Experimentally, the measurement of these reactions at astrophysical energies is very challenging due to their extremely small cross sections, heavy resonant structure and the inevitable presence of natural hydrogen and deuterium contaminants in the carbon targets. Over the years, several groups have measured the $^{12}C+^{12}C$ reactions at low energies. However, to date, no measurement has been possible at energies below $E_{cm} = 2.14$ MeV. In addition, measurements at $E_{cm} < 3.0$ MeV present large uncertainties due to the targets H contamination. In this work, the measurement of the $^{12}C+^{12}C$ reactions over a wide energy range was performed using the CIRCE accelerator in Caserta, Italy. We used the ΔE-Erest particle identification technique to unequivocally identify protons and α particles, avoiding the need to rely on kinematic calculations to disentangle between the two. Since the purity of the carbon targets is crucial to measure the $^{12}C+^{12}C$ reactions, a study of the targets deuterium content as a function of target temperature was also performed. The $^{12}C(^{12}C,p)^{23}Na$ reaction cross section and $\tilde{S}$-factors were extracted using a thick target yield approach. We confirmed most of the resonances in the $^{12}C+^{12}C$ reactions $\tilde{S}$-factors reported in the literature and observed new possible resonances. To our knowledge, our data have the smallest energy step measured so far which might be the reason of the observation of new narrow resonances. However, a more in-depth analysis based on theoretical modelling should be attempted.

Declaration

I declare that this thesis was composed by myself, that the work contained herein is my own except where explicitly stated otherwise in the text, and that this work has not been submitted for any other degree or professional qualification except as specified.

Parts of this work have been published in:

- L. Morales-Gallegos *et al.*, ^{12}C+^{12}C reactions at astrophysical energies: Tests of targets behaviour under beam bombardment - AIP Conference Proceedings 1595, 254 (2014).
- L. Morales-Gallegos *et al.*, Tests of carbon targets for ^{12}C+^{12}C reactions at astrophysical energies - Journal of Physics 578, 012002 (2015).

Others will be submitted for publication as follows:

- L. Morales-Gallegos *et al.*, Reduction of deuterium contamination in carbon targets for ^{12}C+^{12}C reaction studies of astrophysical interest - European Physical Journal A (in preparation)
- M. Romoli, L. Morales-Gallegos *et al.*, Development of a two-stage detection array for low energy light charged-particles in nuclear astrophysics applications - European Physical Journal A (in preparation).
- L. Morales-Gallegos *et al.*, Cross section measurements of the ^{12}C(^{12}C,p) ^{23}Na reaction towards astrophysical energies - Physical Review C (in preparation).
- L. Morales-Gallegos *et al.*, Cross section measurements of the ^{12}C(^{12}C,α) ^{20}Ne reaction towards astrophysical energies - Physical Review C (in preparation).

(Elia Lizeth Morales Gallegos, August 2017)

Acknowledgements

First of all, I would like to thank my supervisors, Marialuisa Aliotta and Lucio Gialanella who supported me through thick and thin. Thank you both for all your academic and personal advice.
I thank the whole ERNA collaboration and all the friends and colleagues at the CIRCE laboratory. In particular Antonino Di Leva for his tremendous support throughout all this work, Mauro Romoli for all his work and time spent in the development of GASTLY, Raffaele Buompane for all his experimental advice, Leandro Gasques for his huge contribution throughout the late stages of the experiment, Giuseppe Porzio for his work with the accelerator and automation of instrumentation, Antonio Palmieri for all the technical work, Mario De Cesare, Jeremias Duarte, David Rapagnani and Gianluca Imbriani for their invaluable contributions throughout all the experiment. Also, Antonio D'Onofrio, Filippo Terrasi, Isabella, Brunella, Luisa, Mauro, Fabio, Carmina, Simona (apologies if I have unintentionally forgotten someone) for all the support, friendship and encouragement. I cannot imagine a better team than you. Thanks also to Tom Davinson for all the advice throughout the experiment, to Daniel Shrümann for all the knowledge he shared with me and to Carlo Bruno for the huge help and support during the data taking and analysis. I would also like to acknowledge the financial support of CoNaCyT, the University of Campania, the INFN-Naples, the INNOVA company and the Royal Society.

Finally, I would like to extend my gratitude to my immediate and extended family, in particular to my parents who have always been my strength and to Guido for being my happiness and future. We did it!!

Science knows no country,
because knowledge belongs to humanity,
and is the torch which illuminates the world.
-Louis Pasteur

Thanks to all for the wonderful journey!

Contents

List of Figures

List of Tables

Chapter 1

Astrophysical introduction

The current state of the Universe is the result of the evolution of primordial matter, mainly composed of hydrogen and helium [1]. The clusterization of primordial matter was led by gravitational forces, consenting the creation of galaxies and stars [2–4]. The evolution of these newly formed stars allows the formation of new and heavier elements (stellar nucleosynthesis) and it is determined by gravitational contraction epochs and nuclear reactions grouped in "burning stages". These burning stages consist in the ignition of hydrogen, helium, carbon, oxygen, neon and silicon producing all the elements in the periodic table up to iron. The reactions that take place at the interior of a star, and thus the evolutionary stages experienced by it, are determined by the mass of the star and the temperature and composition of its core. Figure 1.1 shows the energy emitted by a star experiencing all available burning stages as a function of the temperature of its core.
In the following sections, the general aspects of stellar evolution are described.

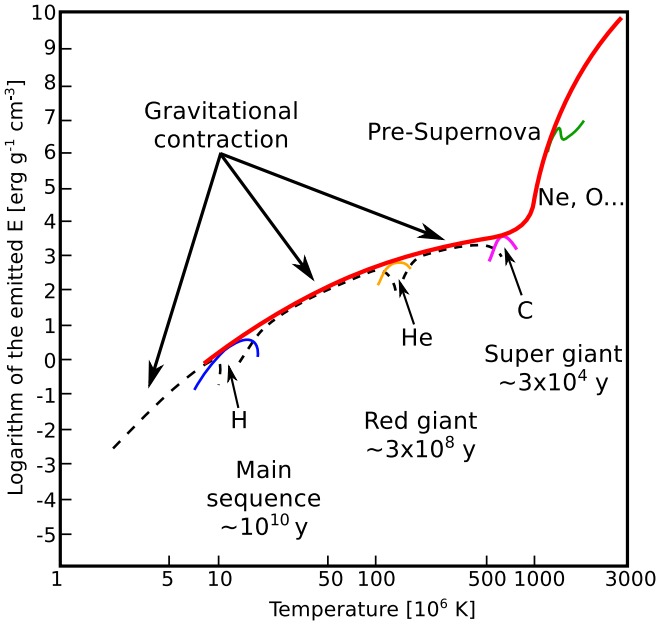

Figure 1.1: Approximate total energy emitted by a star experiencing all the evolutionary stages as a function of its core temperature. The approximate duration of each burning phase is also shown. Figure adapted from [5].

1.1 Principles of stellar evolution

The early universe ($\sim 10^{13}$ s after the Big Bang) can be described as a gas of particles (at a temperature of $\sim 10^{12}$ K) composed mainly by neutrinos, antineutrinos, electrons, positrons, photons and traces of protons and neutrons in a state of equilibrium thanks to the creation and annihilation of particles. When the temperature of this gas dropped to about 10^{11} K, the density of the universe was so low ($\rho = 3.8$ x 10^9 g/cm^3) that neutrinos and antineutrinos ceased interacting with the other particles and photons causing an instability due to the lack of the creation-annihilation process. Moreover, when the temperature of the universe reached 10^9 K, most of the photons did not have enough energy to create electron-positron pairs, which disrupted the original equilibrium [6]. When a large mass of this gas is compressed to a small volume, its gravitational force becomes sufficiently great to provoke a gravitational collapse. Protons and neutrons start to interact in the formation of nuclei, and when the temperature of the gas drops to ∼5000 K, it is mainly composed of hydrogen and helium with traces of heavier elements (commonly referred to as "metals") [7]. Since the acceleration of gravity at the edge of a gaseous cloud is inversely proportional to the square of the cloud's radius, the collapse will gain rapidity as the cloud becomes smaller. After this instability begins, the cloud may be nearly in the condition of free fall for a short period of time. The directed motion of the free fall is then converted into thermal energy and, as a consequence, the temperature of the gas starts to increase. When the acceleration of the fall becomes small (determined by the onset of ionization and the consequent rise of opacity[1]), half of the gravitational energy must have been converted into internal thermal energy, according to the Virial Theorem [9]:

$$\mathrm{K} = -\frac{1}{2}\,\Sigma\,\mathrm{F_{ij}}(\mathrm{r_i} - \mathrm{r_j}) = \frac{1}{2}\,\Sigma\,\frac{\mathrm{G m_i m_j}}{\mathrm{r_{ij}}}, \tag{1.1}$$

where K is the total kinetic energy of the assembly of particles. F, r and m refer to the force, position and mass of a pair of points (i and j) in the gaseous cloud, respectively. Each term in the sum equals the negative of the potential energy due to the interaction of i and j. Thus, when summed over all particle pairs, the kinetic energy becomes half of the total potential energy Ω of the star:

$$\mathrm{K} = -\frac{\Omega}{2} \tag{1.2}$$

[1]The opacity is defined as the capacity of a star to absorb radiation and it determines the rate at which energy is lost as radiation from the surface, and hence the rate of release of gravitational energy [8].

The increasing temperature, along with the increasing density of the star, causes a rapid increase in pressure that decelerates the collapse to a quasi-static state. As the collapse slows down, the virial theorem becomes the prevailing principle governing the subsequent evolution of the star. Half of each gravitational energy increment in the star is converted to kinetic energy and the other half is used in the production of radiation. Although some of this radiation escapes, a considerable amount is employed in the ionization of the constituent matter [9]. Since about 90% of the matter in a new star is hydrogen (being helium the vast majority of the remaining percentage), the inner temperature cannot exceed 10^4 K until hydrogen has been ionized. When hydrogen and helium in the core of the star are ionized, hydrostatic equilibrium is achieved [10]. However, this equilibrium cannot be accomplished if the surface of the star is not hot enough given that the internal thermal energy would escape (via radiation or convection) provoking, eventually, the collapse of the core due to gravitation. Since stars contracting towards the main sequence[2] (see figure 1.2) require high surface temperatures and large radii, their luminosity is very large.

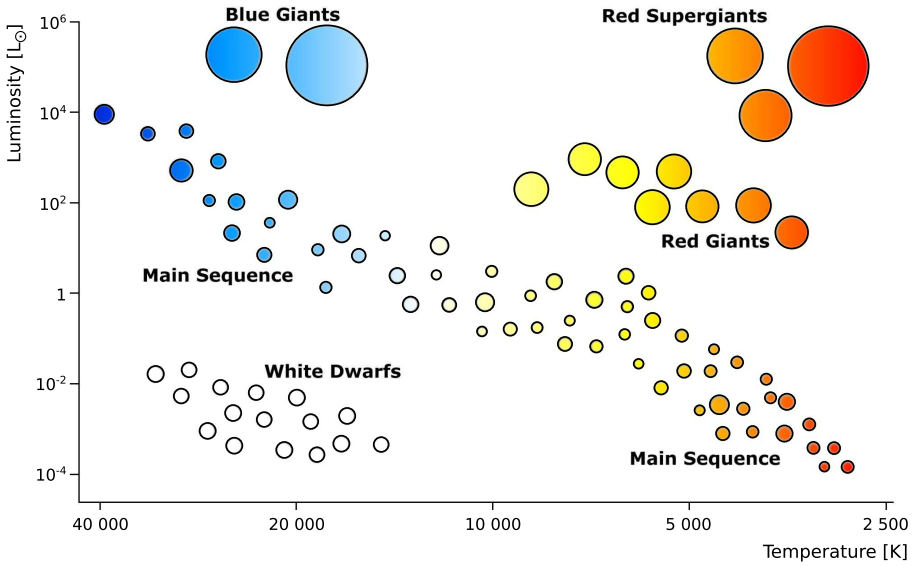

Figure 1.2: Hertzsprung-Russell diagram (H-R). This diagram shows the stellar classification of stars and arrange them according to their luminosity as a function of their surface temperature (increasing to the left).

[2]The main sequence is the region in the Hertzprung-Russell diagram where the stars convert H into He. Typically, stars spend 90% of their lives on the main sequence. Most of the known stars are located in this region [6].

The early contractions of a star are fast and very luminous. As the star approaches the main sequence in the H-R diagram, its evolution becomes slow. After a few million years in a fully convective state, the radiative core of the star moves outward (and the convection zone shrinks) until the star achieves its final main sequence size. During this process, the central temperature of the star increases until it becomes sufficient to produce thermonuclear reactions [6]. It should be noted that stellar structure and evolution depend on the initial mass and (to a lesser extent) chemical composition of the star. In order to trigger thermonuclear fusion reactions, the initial mass of the star should be $M \geq 0.013\ M_{\odot}$ [11].

1.2 Hydrogen burning

The initial abundances of the majority of the stars are dominated by hydrogen (∼90%) and helium (∼10%). The most important reactions are the ones capable to convert hydrogen into helium (at typical temperatures of 10^7 K and typical densities of 10 g/cm^3 [6]). The two major ways to achieve this are the so called proton-proton chains and the CNO cycle, described as follows.

p-p chains. The first step of a proton-proton reaction p+p $\rightarrow$ ^{2}He does not produce stable nuclei via electromagnetic or strong interaction [6]. Therefore, it only contributes to a statistical equilibrium between ^{2}He and two protons (as depicted in figure 1.3). On the other hand, Hans Bethe [12] demonstrated that the weak interaction gives rise to the $p + p \rightarrow d + e^+ + \nu$ reaction (Q = 1.44 MeV).
This reaction then proceeds to the so called p-p chains summarized in figure 1.4. In this figure, only three main possible paths called PPI, PPII and PPIII are shown.
The main effect of the p-p chains is that of converting four protons into one ^{4}He nucleus though two β decays and the emission of neutrinos. The overall energy liberated is about 26.7 MeV per reaction sequence [6].

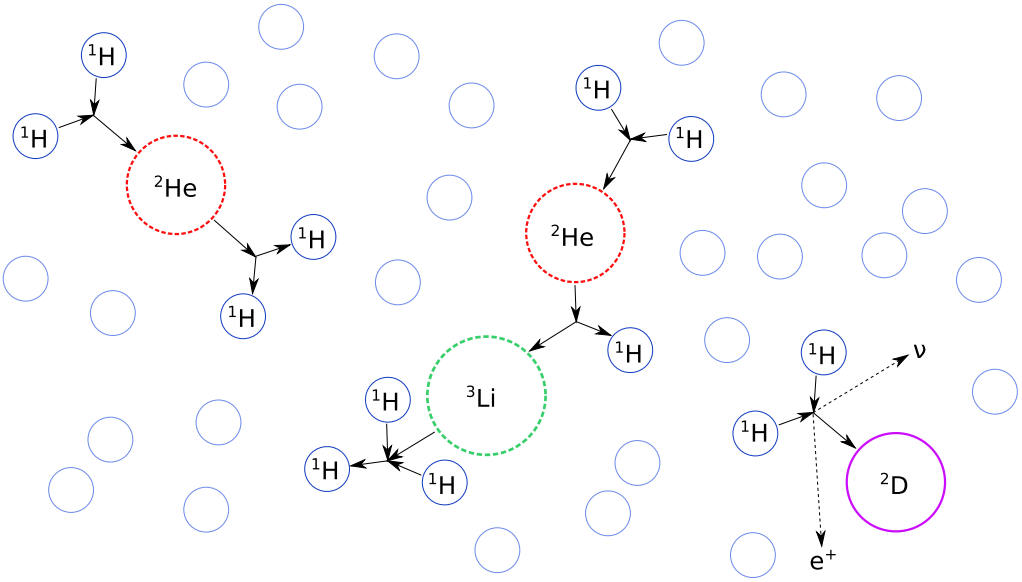

Figure 1.3: Schematic representation of a p-p reaction in the interior of a star. The nuclear and electromagnetic forces do not contribute to the fusion of hydrogen into helium (they lead to unstable elements). The weak force however, synthesizes the deuterium. Figure adapted from [6].

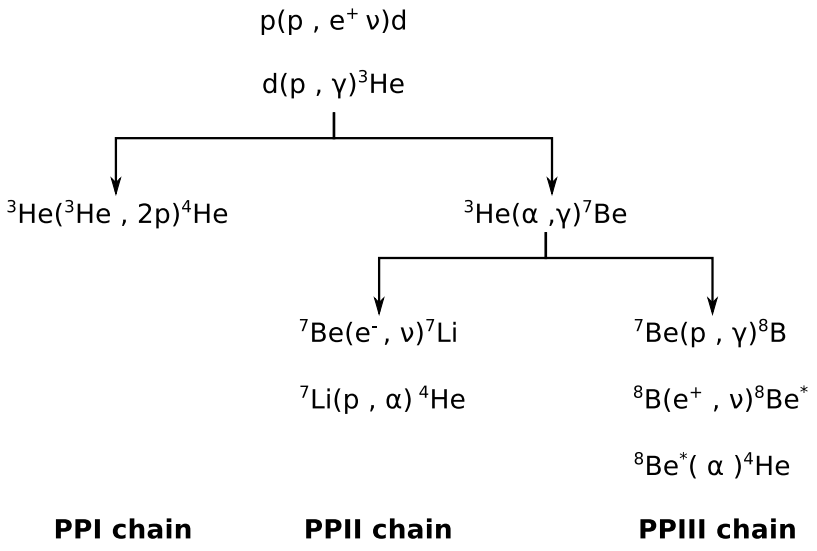

Figure 1.4: Three of the main p-p reaction chains for the conversion of hydrogen into helium. Figure adapted from [6].

CNO cycle. If a star is formed of pure hydrogen, the only possible way to proceed evolving will be through the p-p chains. However, as mentioned before, most stars have traces of heavier elements [9]. This leads to the necessity of considering other reactions as possible sources of energy. The favoured reactions will be those with the smallest Coulomb barrier and highest abundances. Other than helium, the lightest elements that fulfil these conditions are carbon and nitrogen. The mechanism of this burning process was originally suggested by Bethe and von Weizsäcker [12, 13]. They showed that a series of reactions (called the CN cycle) use carbon and nitrogen nuclei only as a catalyst for the conversion of hydrogen into helium, thus consuming only hydrogen. This cycle is schematically shown in figure 1.5. As an example, if one takes a ^{12}C nucleus as a starting point, hydrogen is converted into helium though the following sequence of reactions:

$$^{12}\mathrm{C}(\mathrm{p},\gamma)^{13}\mathrm{N}(\mathrm{e}^{+},\nu)^{13}\mathrm{C}(\mathrm{p},\gamma)^{14}\mathrm{N}(\mathrm{p},\gamma)^{15}\mathrm{O}(\mathrm{e}^{+},\nu)^{15}\mathrm{N}(\mathrm{p},\alpha)^{12}\mathrm{C}$$

were the net result of the cycle would be $4\mathrm{p} \rightarrow {}^{4}\mathrm{He} + 2\mathrm{e}^{+} + 2\nu$ (Q = 26.73 MeV) [6].

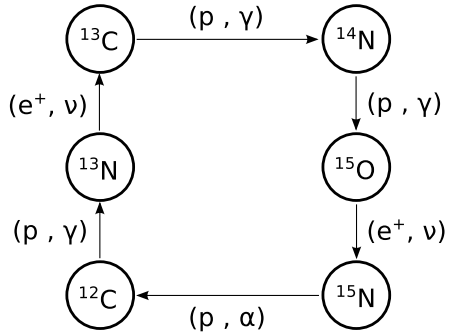

Figure 1.5: The CN cycle. Carbon and nitrogen nuclei serve only as catalyst for the conversion of hydrogen into helium. Figure adapted from [6].

It was later realised that oxygen also plays a role in the CN cycle producing ^{14}N. Subsequently, other cycles involving carbon, nitrogen and oxygen were discovered and the CN cycle was then updated to the CNO cycle showed in figure 1.6, where four cycles can be appreciated.

It should be noted that for a star to undergo hydrogen burning through the p-p chain or the CNO cycle, its initial mass should be at least 0.1 $M_{\odot}$ or 0.15 $M_{\odot}$, respectively. The stellar temperature necessary for each hydrogen burning path is also different, as can be seen in figure 1.7.

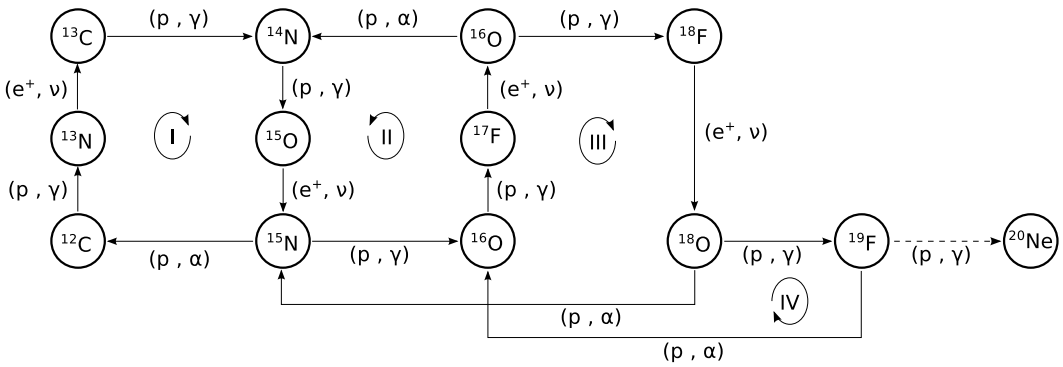

Figure 1.6: The CNO cycles involved in the conversion of hydrogen into helium. Catalytic material could be lost via the ^{19}F(p,γ)^{20}Ne reaction. Figure adapted from [6].

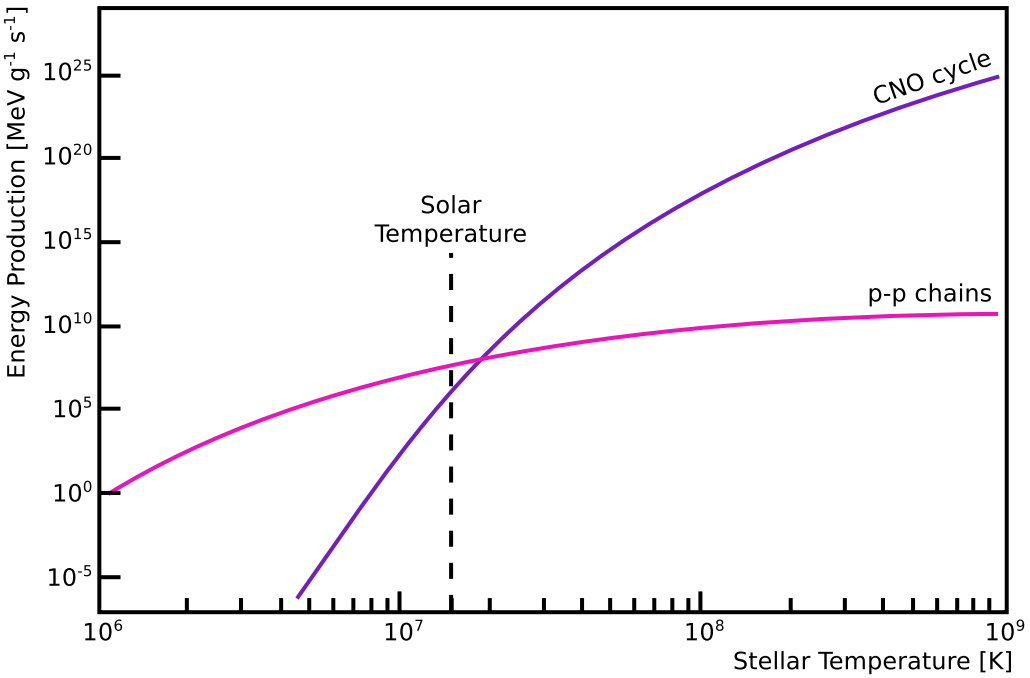

Figure 1.7: Energy production rate of the p-p chains and the CNO cycle as a function of temperature. Figure adapted from [6].

1.3 Helium burning

After hydrogen burning the core of the evolving star now consists mainly of ^{4}He. Since hydrogen is now exhausted, the star is left with no energy to support its gravitational force, hence a new contraction begins, which increases the internal temperature ($\sim 10^8$ K with typical densities of 10^2g/cm^3) and the shell of the star expands and cools down (entering the Red Giants zone in the H-R diagram). As a consequence, if the star has a mass > 0.5 M$_\odot$ the helium burning phase starts. Nuclear reactions among helium nuclei form ^{12}C in what is known as the triple α-process depicted in figure 1.8. In the first step of this process, two α particles combine to form ^{8}Be in its ground state. Although this nucleus is unstable (Q = -92.1 keV) against decay into two α particles, its lifetime is longer than the transit time of two α particles with kinetic energies corresponding to Q, resulting in a small equilibrium concentration: α+$\alpha \rightleftharpoons {}^8$Be [6]. In the second step of the triple α-process the ^{8}Be nuclei capture an additional α particle, giving rise to the ^{8}Be$(\alpha,\gamma)^{12}$C reaction.

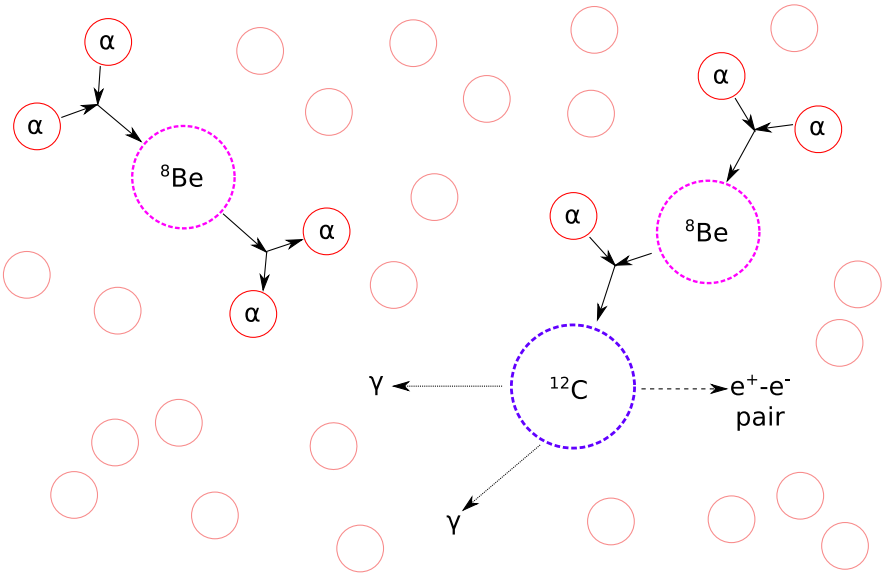

Figure 1.8: Schematic representation of the triple α-process. In the fist step of this process, a small abundance of ^{8}Be is built up to equilibrium with its α particle decay products. In the second step, the ^{8}Be nuclei capture an additional α particle forming ^{12}C through the ^{8}Be$(\alpha,\gamma)^{12}$C reaction. Figure adapted from [6].

Another key reaction of helium burning is also ^{12}C$(\alpha,\gamma)^{16}$O, which together with the star convective mechanisms, determines the abundance of carbon and oxygen in the universe [14].

1.4 Carbon burning

It is worth remarking that the mass of the star plays an important role in its evolution. Not only it determines the manner in which carbon is burned, but its lifetime [4,15,16]. Low-mass stars ($< M_{UP}$[3]) does not initiate carbon burning since their central temperature is not high enough to release energy by thermonuclear reactions. Consequently, the core of these stars begins to contract, increasing its density and radiating away its thermal energy. Following the virial theorem (as discussed previously), the temperature in the core of the star rises during the contraction. This contraction continues until the next burning phase begins at an adequate rate or until electron degeneracy provides enough pressure to halt the contraction (white dwarfs) [9]. However, there is a mass limit necessary to prevent gravitational collapse. This limit is called the Chandrasekhar limit and it is equal to 1.4 $M_\odot$ [6]. More massive stars cannot be solely support by electron degeneracy pressure, therefore, they collapse and form neutron stars or black holes.
In the carbon burning stage, the core of the star consists mainly of ^{12}C and ^{16}O. Of all the possible fusion reactions involving these nuclei, the ^{12}C+^{12}C process has the smallest Coulomb barrier and therefore, it initiates the carbon burning phase. Consequently, the formation of neon, sodium and magnesium is achieved through a set of reactions called carbon burning [6,11]:

$$^{12}\text{C}+^{12}\text{C} \rightarrow ^{20}\text{Ne} + \alpha \text{ (Q = 4.62 MeV)}$$
$$^{12}\text{C}+^{12}\text{C} \rightarrow ^{23}\text{Na} + \text{p} \text{ (Q = 2.24 MeV)}$$
$$^{12}\text{C}+^{12}\text{C} \rightarrow ^{23}\text{Mg} + \text{n} \text{ (Q = -2.62 MeV)}$$

If electron degeneracy pressure becomes dominant prior to the onset of carbon burning, the star becomes a CO white dwarf [18]. If a star has a mass $> M_{UP}$, its core remains in a non-degenerate state and carbon begins to burn at temperatures of about 5 x 10^8 K and densities $\sim$ 3 x 10^6 g/cm^3 [6]. M_{UP} represents the stellar mass that separates these two paths of evolution and it is determined by the ^{12}C+^{12}C reaction rate.
In the carbon burning phase, neutrino losses in the core (due to electron annihilation, plasma neutrino decay or photoneutrino processes [9]) are the dominant energy-loss mechanism, which causes the massive stars cores to evolve so rapidly that their envelope and appearance (red supergiants) do not have time to change significantly before the rest of the nuclear fuel has been consumed.

[3] M_{UP} is defined as the minimum initial mass a star has to posses in order to experience a carbon burning phase [17].

1.5 Advanced burning stages

When all the carbon fuel has been exhausted, the core of the star is mainly composed by neon, sodium and magnesium [6]. If the star has a mass >11 $M_{\odot}$, its carbon-exhausted core experiences a rise in temperature (1.7 x 10^9K) and density (4 x 10^6 g/cm^3) until photons begin to photodisintegrate (break down into α particles) ^{20}Ne due to its weak bound with α particles [4]. At the end of the relatively brief (of the order of a few years) neon burning phase, the core of the star consists primarily of ^{16}O and ^{24}Mg. The core temperature and density rise again (2.3 x 10^9 K and 10^7 g/cm^3, respectively) until oxygen starts to react with itself synthesizing silicon and sulphur mainly (oxygen burning phase). Argon and calcium are also produced along with small amounts of chlorine, potassium and other nuclei up to scandium. Silicon burning follows the oxygen phase, where temperature and density of the core rise once more (4.1 x 10^9 K and 3 x 10^7 g/cm^3). Before the temperature of the core reaches a temperature higher than 3.5 x 10^9 K (required to provide enough penetration of the Coulomb barrier), the ^{28}Si+^{28}Si reaction does not occur. Instead, the photodisintegration of silicon take place. From this stage on in the evolution of a star, the photodisintegration is the dominant process. Since the time scale of each successive process becomes increasingly shorter, the burning stages might merge immediately into the next [6].
At the end of the silicon burning stage, the α particles produced by photodisintegration of heavy elements are captured by the remaining silicon and other nuclei such as argon, calcium and sulphur, resulting in the formation of iron and nickel (pre-supernova star). These elements do not participate in any reactions (since they are the most tightly bound of all nuclei) thus, they do not prevent gravitational collapse. This heavy stellar core is now surrounded by many distinct layers consisting primary of a specific element: silicon, oxygen, neon, carbon, helium and hydrogen. When the silicon is exhausted there are no other reactions capable to counterbalance the gravitational collapse. This collapse is eventually halted when the density in the core of the pre-supernova star reaches 2.7 x 10^{14} g/cm^3 (nuclear matter density). Since nuclear matter is nearly incompressible, the core of the star (with typical temperatures of 34.8 x 10^9 K) "bounces" destroying the star in a phenomenon known as a supernova. A supernova takes place in the form of an explosion expelling much or all of the material of the star at velocities ranging from 1,000 to 20,000 km/s, driving a shock wave that sweeps up an expanding shell of gas and dust called a supernova remnant [19].

In summary, the evolution of stars consist of burning stages that can be experienced depending on the initial mass of the star. The evolution of a sufficiently massive star ends in a spectacular explosion called supernova. In table 1.1, a summary of all the evolutionary stages experienced by a 20 $M_{\odot}$ star, the products of each stage, core temperature and timescale are given.

Table 1.1: Evolutionary stages of a 20 $M_{\odot}$ star. Products of each burning stage, typical core temperature and timescale are shown.

Burning stage	Products	Temperature [K]	Timescale [yr]
Hydrogen burning	He	1-4 x 10^7	10^7
Helium burning	C, O	1-2 x 10^8	10^6
Carbon burning	Ne, Na, Mg	5 x 10^8	300
Neon burning	Mg, Si	1.7 x 10^9	< 1
Oxygen burning	Si, S	2.3 x 10^9	< 1
Silicon burning	Ti to Zn	4.1 x 10^9	2 days

From this description of the burning phases in stars follows that the heavy-ion reactions such as $^{12}C+^{12}C$, $^{12}C+^{16}O$, $^{12}C+^{20}Ne$ and $^{16}O+^{16}O$ play an important role in the behaviour of highly developed starts [6]. The present work focused on the study of the $^{12}C+^{12}C$ reactions that are crucial for the understanding of the explosion of massive stars and determine whether supernova remnants would become white dwarfs, black holes or neutron stars. Moreover, the $^{12}C+^{12}C$ reactions cross section is decisive in the determination of the limiting mass M_{UP} that dictates if a star would experience evolutionary stages beyond carbon burning. A more detail description on the importance of the $^{12}C+^{12}C$ reactions is given in chapter 3.
In the following chapter, a general description of the formalism needed to describe the nuclear reactions mechanism in stars is provided. A discussion on the experimental procedures is also presented.

Chapter 2

Thermonuclear reactions in stars

The process of stellar nucleosynthesis and the energy generation mechanism can be reproduced by nuclear reactions calculations for stellar density and temperature conditions distinctive of a particular stellar scenario [4].
In this chapter, a brief description of the theoretical formalism linked to the modelling of stellar reaction rates is given. The experimental approach used to extract the astrophysical relevant quantities is also discussed in the following sections.

2.1 Nuclear physics overview

The simplest nuclear reaction can be written as x+A $\rightarrow$ y+B or (as usually expressed) A(x,y)B, where x and A represent the projectile and target of the reaction (entrance channel) while y and B denote the emerging nuclei (exit channel). If the masses of particles in the entrance and exit channels are M_i, energy conservation leads to the definition of the nuclear reaction Q-value: $Q = (M_x + M_A - My - M_B)c^2$ [6, 11]. The sign of the Q-value indicates if the reaction produces energy (positive) or if the reaction requires energy in order to trigger the process (negative).
A complicated, yet crucial, quantity in stars, is the probability of a given nuclear reaction to take place. This probability is governed by the effective area of the system projectile-target, known as the cross section σ (typically given in units of barn = 1 x 10^{-24} cm^2). The cross section can be parametrized as [11]:

$$\sigma(E) = \frac{1}{E}\exp(-2\pi\eta)\ S(E), \tag{2.1}$$

where S(E) is the so called S-factor, that contains all nuclear effects [20] and includes the effects of the centrifugal barrier on the penetrability of particles with orbital angular momentum $l > 0$ [21]. The term $e^{-2\pi\eta}$ is known as the Gamow factor and it is proportional to the probability of penetrating through the Coulomb barrier of particles with zero angular momentum [22].

The quantity η is the Sommerfeld parameter and is given by:

$$\eta \ = \ \frac{\mathrm{Z_1 \ Z_2 \ e^2}}{\hbar v}, \tag{2.2}$$

where $\mathrm{Z_i}$ and v are the atomic numbers and velocity of the interacting nuclei, e is the elementary charge and $\hbar$ is the reduced Plank constant. In numerical units, the Sommerfeld parameter translates into:

$$\eta(\mathrm{E}) = 0.1575 \ \mathrm{Z_1 Z_2} \left(\frac{\mu}{\mathrm{E}}\right)^{\frac{1}{2}}, \tag{2.3}$$

where μ represents the reduced mass of the system in amu[1] and E is the interaction centre of mass energy in MeV [1].
Since the cross section is energy-dependent, it also depends on the relative velocity v between projectile and target nucleus [6]: $\sigma = \sigma(v)$. Considering a stellar gas with $\mathrm{N_{x,A}}$ particles per $\mathrm{cm^3}$ and relative velocities v, the nuclear reactions rate r (in reactions per $\mathrm{cm^3}$ per s) is given by:

$$\mathrm{r} = \mathrm{N_x N_A} v\sigma(v) \tag{2.4}$$

In a stellar environment, the nuclei interact in a range of velocities v-v+dv. Considering this range of velocities, equation 2.4 becomes the reaction rate per particle pair and it is given by:

$$\mathrm{r} = \mathrm{N_x N_A} \int_0^\infty \mathrm{P}(v) v\sigma(v)\mathrm{d}v \ \equiv \mathrm{N_x N_A} \ < \sigma v > \tag{2.5}$$

In most cases, the stellar plasma is in a non-degenerate state and the nuclei move in a non-relativistic fashion, allowing us to approximate the stellar plasma by an ideal gas [23] (considering the stellar scenario as a fully ionised plasma and the particles as point-like and non-interacting). Accordingly, the velocities of nuclei can be described by a Maxwell Boltzmann distribution. The probability of a nuclear reaction to occur depends on the relative velocities of the interacting nuclei, which is Maxwellian if the separate nuclei can be described by Maxwell Boltzmann distributions. In such cases, the probability that the relative velocity has a value between v and $v + \mathrm{d}v$ is given by:

$$\mathrm{P}(v)\mathrm{d}v = \left(\frac{\mu}{2\pi \mathrm{kT}}\right)^{\frac{3}{2}} \mathrm{e}^{-\mu \mathrm{v}^2/(2\mathrm{kT})} 4\pi v^2 \mathrm{d}v, \tag{2.6}$$

[1]The atomic mass unit (amu) is defined as 1/12 of the mass of a neutral atom of ^{12}C.

where k is the Boltzmann constant (k = 8.62 x 10^{-11} MeV/K) and T is the temperature (in K) of the astrophysical scenario in which a given reaction takes place.

Since E = $\mu v^2/2$, the above distribution can be written as an energy distribution:

$$\mathrm{P(E)dE} = \left(\frac{2}{\sqrt{\pi}(\mathrm{kT})^{\frac{3}{2}}}\right)\sqrt{\mathrm{E}}\ \mathrm{e}^{-\mathrm{E/kT}}\ \mathrm{dE} \tag{2.7}$$

Given that equation 2.7 has a maximum when E = kT/2, it becomes [6]:

$$< \sigma\nu >= \left(\frac{8}{\pi\mu}\right)^{\frac{1}{2}} \frac{1}{(\mathrm{kT})^{\frac{3}{2}}} \int_0^\infty \mathrm{E}\ \sigma(\mathrm{E})\ \mathrm{e}^{-\mathrm{E/kT}}\ \mathrm{dE} \tag{2.8}$$

Translating to the astrophysical S-factor:

$$< \sigma \mathrm{v} >= \left(\frac{8}{\pi\mu}\right)^{\frac{1}{2}} \frac{1}{(\mathrm{kT})^{\frac{3}{2}}} \int_0^\infty \mathrm{S(E)}\ \exp\left(-\frac{\mathrm{E}}{\mathrm{kT}} - 2\pi\eta(\mathrm{E})\right)\ \mathrm{dE}, \tag{2.9}$$

In stars, resonant and non-resonant mechanisms can take place and they both contribute to the total reaction rate of a given process. In the following sections, both mechanisms are discussed.

2.1.1 Non-resonant reactions

For non resonant reactions, the astrophysical S-factor S(E) varies smoothly with energy, the energy dependence in equation 2.9 is mainly dominated by the exponential term. The first part of the exponential -E/kT, which measures the number of particles available in the energy tail of the Maxwell-Boltzmann distribution, vanishes at high energies. The second exponent -$2\pi\eta$(E), which is proportional to the penetration through the Coulomb barrier, becomes very small at low energies. The product of both terms leads to a peak $\mathrm{E_0}$ of the integrand and it is known as the Gamow peak. Equation 2.9 has a maximum when:

$$\mathrm{E_0}\ =\ 0.122\mu^{\frac{1}{3}}(\mathrm{Z_1Z_2\ T_9})^{\frac{2}{3}}\ \mathrm{keV}, \tag{2.10}$$

where T_9 is the temperature of the stellar plasma in units of 10^9 K [21].

E_0 represents the effective mean energy for thermonuclear fusion reactions at a given temperature T [6].
Since equation 2.9 is a sharply peaked exponential function, it can be approximated by a Gaussian function. This way, the FWHM (Full Width at Half Maximum) value can be obtained [11]:

$$\Delta E_0 \;=\; 0.2368\ (Z_1{}^2\ Z_2{}^2\ \mu)^{\frac{1}{6}}\ T_9{}^{\frac{5}{6}} \tag{2.11}$$

Equations 2.10 and 2.11 define a range of energies where a given reaction will take place in stellar scenarios. This range is known as the Gamow window and it is given by [1]:

$$E_0\ \pm\ \Delta E_0/2 \tag{2.12}$$

The concept of Gamow peak is thought for non-resonant reactions, however, it is not applicable to resonant reactions since the contributions of resonances to $<\sigma\nu>$ have to be considered. Nevertheless, equation (2.12) is still useful given that it shows which resonances are, a priori, the most important [6].

2.1.2 Resonant reactions

In non-resonant reactions, the cross sections vary smoothly with energy and equations 2.10 - 2.12 are applicable. On the contrary, in resonant reactions, the cross sections vary heavily in the proximity of a particular energy E_R.
For resonant reactions, the cross section $\sigma(E)$ for an isolated (there are no overlapping resonances in the vicinity) resonance, is given by the Breit-Wigner formula:

$$\sigma_{BW}(E) = \pi\lambda\!\!\!^{-2}\frac{2J+1}{(2J_1+1)(2J_2+1)}(1+\delta_{1,2})\frac{\Gamma_a\Gamma_b}{(E-E_R)^2+(\Gamma/2)^2} \tag{2.13}$$

where J is the angular momentum of the excited state in the compound nucleus, J_1 and J_2 are the spins of the projectile and target nucleus, respectively, and Γ_i are the (energy dependent) partial and total widths of the decay channels. The term $1+\delta_{1,2}$ has to be included to avoid double counting identical particles in the entrance channel.
In order for a resonant state to be formed, angular momentum and parity conservation laws must be satisfied: $\vec{J} = \vec{j}_1+\vec{j}_2+\vec{l}$ [6] where $(-1)^1\pi(j_1)\pi(j_2) =$

$\pi(\mathrm{J})$, where $\pi(\mathrm{j})_\mathrm{i}$ are the parities of the reacting particles and $\pi(\mathrm{J})$ the parity of the resonant state [24, 25].

Given the energy dependence of the cross section defined in equation (2.13), the stellar reaction rate (eq. 2.9) can be written as:

$$< \sigma\nu >= \left(\frac{8}{\pi\mu}\right)^{\frac{1}{2}} \frac{1}{(\mathrm{kT})^{\frac{3}{2}}} \int_0^\infty \sigma_{\mathrm{BW}}(\mathrm{E})\mathrm{E} \exp\left(-\frac{\mathrm{E}}{\mathrm{kT}}\right) \mathrm{dE}, \tag{2.14}$$

If we define $\omega = (1 + \delta_{12})(2\mathrm{J} + 1)/[(2\mathrm{J}_1 + 1)(2\mathrm{J}_2 + 1)]$, the reaction rate equation translates into:

$$< \sigma\nu >= \frac{\sqrt{2\pi}\hbar^2}{(\mu\mathrm{kT})^{3/2}}\omega \int_0^\infty \frac{\Gamma_\mathrm{a}\Gamma_\mathrm{b}}{\mathrm{E} - (\mathrm{E_R})^2 + \Gamma^2/4} \exp\left(-\frac{\mathrm{E}}{\mathrm{kT}}\right) \mathrm{dE}, \tag{2.15}$$

For a narrow resonance ($\Gamma \ll \mathrm{E_R}$), the latter equation becomes:

$$< \sigma\nu >= \frac{\sqrt{2\pi}\hbar^2}{(\mu\mathrm{kT})^{3/2}} 2\omega \frac{\Gamma_\mathrm{a}\Gamma_\mathrm{b}}{\Gamma} \exp\left(-\frac{\mathrm{E}}{\mathrm{kT}}\right) \int_0^\infty \frac{\Gamma/2}{(\mathrm{E_R} - \mathrm{E}) + \Gamma^2/4} \mathrm{dE}, \tag{2.16}$$

Taking equation 2.15 at E=$\mathrm{E_R}$ and $\gamma \equiv \Gamma_\mathrm{a}\Gamma_\mathrm{b}/\Gamma$, the reaction rate is now:

$$< \sigma\nu >= \frac{\sqrt{2\pi}}{(\mu\mathrm{kT})}^{3/2} \hbar^2 \exp\left(-\frac{\mathrm{E}}{\mathrm{kT}}\right) \omega\gamma, \tag{2.17}$$

where the $\omega\gamma$ term is known as the resonance strength, and it is explicitly written as:

$$\omega\gamma = (1 + \delta_{12}) \frac{2\mathrm{J} + 1}{(2\mathrm{J}_1 + 1)(2\mathrm{J}_2 + 1)} \frac{\Gamma_\mathrm{a}\Gamma_\mathrm{b}}{\Gamma} \tag{2.18}$$

For broad resonances, the energy dependence of the resonance partial and total widths are important and should be considered. This transforms equation 2.13 into [6]:

$$\sigma_{\mathrm{BW}}(\mathrm{E}) = \sigma_{\mathrm{BW}}(\mathrm{E_R}) \frac{\mathrm{E_R}}{\mathrm{E}} \frac{\Gamma_\mathrm{a}(\mathrm{E})}{\Gamma_\mathrm{a}(\mathrm{E_R})} \frac{\Gamma_\mathrm{b}(\mathrm{E})}{\Gamma_\mathrm{b}(\mathrm{E_R})} \frac{(\frac{1}{2}\Gamma(\mathrm{E_R}))^2}{(\mathrm{E} - \mathrm{E_R})^2 + (\frac{1}{2}\Gamma(\mathrm{E}))^2}, \tag{2.19}$$

where $\sigma(E_R)$ is the cross section evaluated at the resonant energy (E=E_R).

In order to obtain the total rate of a given reaction, all processes (resonant and non-resonant) contributing to the reaction mechanism should be considered [11]:

$$< \sigma v >_{total} = \Sigma < \sigma v >_{NR} + \Sigma < \sigma v >_{BR} + < \sigma v >_{nonR} + < \sigma v >_{C} \quad (2.20)$$

where NR, BR, nonR and C correspond to the narrow resonances, broad resonances, non resonant and constant processes, respectively.

2.2 Experimental extraction of astrophysical quantities

In the laboratory, rather than directly measuring cross section of a nuclear reaction, one measures quantities related to it. Here, we present the approach that will be used for the present study.
The number of events detected in an experiment are transformed into Yields, which are calculated according to beam energy and intensity, type of target and detector efficiency. Once the yields are calculated, the cross sections and, eventually, the astrophysical S-factors can be obtained.
In this work, a thick target approach was used. Differentiating two thick target yields at consecutive energies (as long as the energy step is not greater than any possible resonance width) one can obtain the "thin target yield" that can be later used in the calculation of the cross sections and S-factors. A detailed description of this approach can be found in the following sections.

2.2.1 Reaction yields and cross sections

Once the number of events N of a given reaction is obtained, we can derive the yield Y of the reaction using [11]:

$$Y = \frac{\text{total number of reactions}}{\text{total number of incident beam particles}} = \frac{N_R}{N_b} \quad (2.21)$$

The total number of reactions is defined as $N_R = N/B\eta W$, where N is the number of events detected, B is the probability of emission per reaction (branching ratio), η is the efficiency of the detector used and W is the angular correlation. If the reaction under study proceeds to only one final state or

if the yield is calculated for a specific transition B=1. Considering that $N_b = Q/q\ e$, the reaction yield is given by:

$$Y = \frac{N\ q\ e}{\eta\ Q\ W\ B}, \tag{2.22}$$

where q and e correspond to the charge state of the beam and the electronic charge (e = 1.602 x 10^{-19} C), respectively and Q is the total charge (in coulombs) collected during the beam irradiation.

Once the reaction yields are obtained experimentally, one can calculate the cross sections σ. If we define the number of particles per unit volume as n and the target thickness as Δx (Δx must be thin enough so the particles do not overlap), the reaction yield can be written as:

$$Y = \sigma\ n\ \Delta x \tag{2.23}$$

In order to calculate the number of particles per unit volume, we make use of the stopping cross section, defined as:

$$\epsilon = \frac{1}{n}\frac{dE}{dx}, \tag{2.24}$$

where dE/dx is known as the stopping power.

Therefore, the final equation of the reaction yield for a thin target would be:

$$Y = \sigma\frac{\Delta x}{\epsilon} \tag{2.25}$$

If the target is thick so that the particles start to overlap, the cross section should be integrated over all the target thickness:

$$Y(E) = \int \sigma(E) n\ dx = \int_{E-\Delta E}^{E} \frac{\sigma(E)}{\epsilon(E)} dE, \tag{2.26}$$

where E is the incident beam energy and ΔE corresponds to the energy lost in the target (the target thickness in energy units).

If the target is infinitely thick (the beam completely stops in the target) the limits of the integral of equation 2.26 go from 0 to E. Therefore, if we differentiate our infinitely thick target yield (equation 2.22) Y^{∞} over a small

enough energy step Δ (smaller than the width of any possible reaction resonances present in the measured energy rage), we can calculate the reaction cross section:

$$\sigma(\mathrm{E}) = \frac{\epsilon\ [\mathrm{Y}^{\infty}(\mathrm{E}) - \mathrm{Y}^{\infty}(\mathrm{E}-\Delta)]}{\mathrm{W}\ \Delta} = \frac{\epsilon\ \mathrm{Y}_{\mathrm{diff}}}{\mathrm{W}\ \Delta}, \tag{2.27}$$

If the angular distribution of the reaction under study is isotropic W = 1. Since equation 2.27 is defined over a range of energies, the cross section cannot be assigned to any of the end points (E or E-Δ). Hence, a point in between should be defined: the median energy $\mathrm{E}_{\mathrm{med}}$. This energy is the point where the area under the cross section curve is divided equally between E and E-Δ [6]. Given that at low energies, the σ behaviour is roughly an exponential drop-off (due to the Coulomb barrier penetrability), the thick target yield will, on average, be of the form:

$$\mathrm{Y}^{\infty}(\mathrm{E}) = \mathrm{Y}^{\infty}(\mathrm{E}-\Delta)\exp[\mathrm{A}(\mathrm{E}-\Delta)] \tag{2.28}$$

Solving for A and approximating the increase between E and E-Δ as linear, $\mathrm{E}_{\mathrm{med}}$ can be expressed as [26]:

$$\mathrm{E}_{\mathrm{med}} = (\mathrm{E}-\Delta) + \Delta\left(\frac{\ln[\frac{1}{2} + \mathrm{Y}^{\infty}(\mathrm{E})/2\mathrm{Y}^{\infty}(\mathrm{E}-\Delta)]}{\ln[\mathrm{Y}^{\infty}(\mathrm{E})/\mathrm{Y}^{\infty}(\mathrm{E}-\Delta)]}\right) \tag{2.29}$$

Using this median energy the cross section σ_{med} can be calculated. However, this definition is only valid when the cross section between two consecutive energies is approximately constant. Instead, when the energy step increases, the determination of the cross section can change considerably. In order to deconvolute the cross section, we make use of the so called effective energy $\mathrm{E}_{\mathrm{eff}}$, defined as (see [27] for the full derivation):

$$\mathrm{E}_{\mathrm{eff}} = \mathrm{E}_0 - \frac{1}{2}\Delta + \frac{[1 + \mathrm{R}_2^2\Delta^2/12]^{1/2} - 1}{\mathrm{R}_2}, \tag{2.30}$$

where E_0 is the central energy between the two points used in the calculation of $\mathrm{Y}_{\mathrm{diff}}$ and R_2 is the second derivative of σ, in this case calculated using $\mathrm{E}_{\mathrm{med}}$, thus:

$$\mathrm{R}_2 \equiv \left(\frac{\mathrm{d}^2\sigma_{\mathrm{med}}}{\mathrm{dE}^2}\right)\Big/\left(\frac{\mathrm{d}\sigma_{\mathrm{med}}}{\mathrm{dE}}\right) \tag{2.31}$$

With the calculation of $\mathrm{E}_{\mathrm{eff}}$, the correct cross section can now be calculated using again equation 2.27.

2.2.2 Astrophysical S-factors

From the calculation of the cross section, it is possible to obtain the astrophysical S-factor values simply by using equation 2.1.
However, for measurements involving heavy nuclei reactions the data are better presented in terms of the modified S-factor $\tilde{S}(E)$ given that the conventional S-factor does not include the penetrability approximations of heavy ions. The $\tilde{S}$ is related to the astrophysical S-factor by [6]:

$$\tilde{S}(E) = E\ \sigma(E)\ \exp(2\pi\eta + gE), \tag{2.32}$$

where g is a constant related to the nuclear separation and it is given by [28]:

$$g = 0.122\ \Big(\frac{\mu\ R^3}{Z_1\ Z_2}\Big)^{1/2}, \tag{2.33}$$

where R is the square-well radius in fermis.

Using these relations, the cross sections and S-factors of a particular nuclear reaction can be extracted from the experimentally available information.

The following chapter presents a review of the current status of knowledge on the $^{12}C+^{12}C$ reaction, its astrophysical impact and the main experimental challenges involved in its laboratory investigation.

Chapter 3

^{12}C+^{12}C reactions in stars

^{12}C+^{12}C reactions take place in stars at typical densities of 2-5 x 10^6 g/cm^3 [29, 30] and at a typical temperature of 5 x 10^8 K. This corresponds to an energy range[1] of $E_0 = 1.5 \pm 0.3$ MeV [31]. At these energies, ^{12}C+^{12}C reactions proceed through the ^{20}Ne+α and ^{23}Na+p channels, known as the α and p channels, respectively. As can be seen in figure 3.1, at stellar energies, the neutron channel (^{23}Mg+n) of the ^{12}C+^{12}C process is closed. Even though at higher energies, the neutron channel opens, its rate is about two orders of magnitude lower than that of the proton and alpha channels [32], reducing the relevant study of the ^{12}C+^{12}C reactions to the α and p channels.

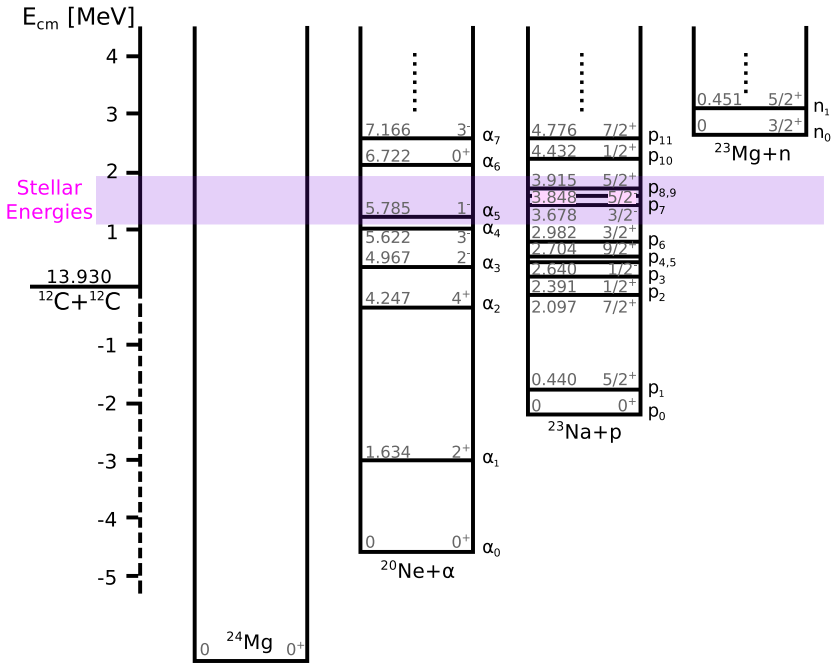

Figure 3.1: Energy level diagram relevant to the exit channels of the ^{12}C+^{12}C reactions. The highlighted region represents the stellar energy region at which the ^{12}C+^{12}C reactions take place. Only the alpha and proton channels are opened at those energies.

[1]All the energies reported in this chapter are in the centre of mass system, unless stated otherwise.

3.1 Astrophysical impact

As discussed in chapter 1, the evolution of stars depends critically on their initial mass. The quantity M_{UP} dictates if a star becomes a white dwarf (if its mass is $< M_{UP}$) or if it will experience carbon burning (if its mass is $> M_{UP}$). This decisive quantity is determined by the $^{12}C+^{12}C$ reactions. The value of M_{UP} was proposed for the first time by Becker and Iben [17] who provided a relation between M_{UP}, the metallicity of the star (the fraction of stellar mass composed by elements heavier than He) and its initial He content. They found a value of $M_{UP} = 9\ M_{\odot}$ for a star with nearly solar composition. However, later studies (see [18] and references therein) led to a revised value of $M_{UP} = 7.8\ M_{\odot}$ for stars with solar composition. There are many uncertainties affecting the determination of M_{UP} and the $^{12}C+^{12}C$ reactions cross section is among the most important ones [18].
Knowing the $^{12}C+^{12}C$ reactions cross sections is crucial to determine M_{UP}, a quantity relevant for several astrophysical issues such as [18,33,34]: the chemical enrichment of the interstellar matter due to different type of supernova explosions; the ratio between core-collapse supernovae and thermonuclear supernovae; the luminosity function of certain stars; the ratio between different types of white dwarfs, etc. Furthermore, a variation of the $^{12}C+^{12}C$ reactions cross section could change the final properties of a massive star right before its supernova explosion and alter its behaviour [33, 34]. The knowledge of the total rate of the $^{12}C+^{12}C$ reactions is also decisive for 25 $M_{\odot}$ stars at solar metallicity considering that a factor of 10 change in this rate would affect the convection zone structure and nucleosynthesis of these stars [35]. In addition, knowing the $^{12}C+^{12}C$ fusion reaction cross section, is essential to model X-ray bursts systems [36, 37] and explosions on the surface of neutron stars [38].
Unfortunately, the Gamow window for the $^{12}C+^{12}C$ reactions is much lower than the height of the Coulomb barrier (6.3 MeV), making the cross sections very small ($\ll 10^{-9}$ b) and extremely difficult to measure in the laboratory [1, 39].

3.2 Previous experiments

Considerable efforts to measure the $^{12}C+^{12}C$ reactions at low energies have been made over the past four decades. Several groups have used charged particles detection [28, 40–42], gamma ray spectroscopy [39, 43–50] and a combination of both techniques [51] to measure the α and p channels of the $^{12}C+^{12}C$ reactions.

Different types of targets have been used, from self-supporting natural carbon foils (8-50 μg/cm^2) [28, 40, 43, 45, 46, 49–51] and high-purity graphites [41], to thick (1 mm) natural graphites [39, 44, 47, 48] and thick high-purity graphites [42]. Regardless of the type and thickness of the targets, hydrogen and deuterium contamination have always been a problem when pushing the ^{12}C+^{12}C reactions measurements to energies below E = 3.9 MeV.
For example, Patterson *et al.* [28], using forward detection angles, could not observed the proton channel of the ^{12}C+^{12}C reactions at energies lower than E= 3.23 MeV on account of a strong recoil of protons produced by the hydrogen contamination in the target. A similar problem was faced by Mazarakis and Stephens [40] and Barron-Palos *et al.* [39]. Both groups found strong peaks in their spectra also due to hydrogen contamination in their targets even though they used different techniques and different type of targets. Sample spectra obtained by Mazarakis and Stephens at E = 3.92 MeV and Barron-Palos *et al.* at E = 3.00 MeV are shown in figures 3.2 and 3.3, respectively. It can be seen from these figures that hydrogen and deuterium contamination in the targets limits the measurements of the ^{12}C+^{12}C reactions, regardless of the detection technique used.

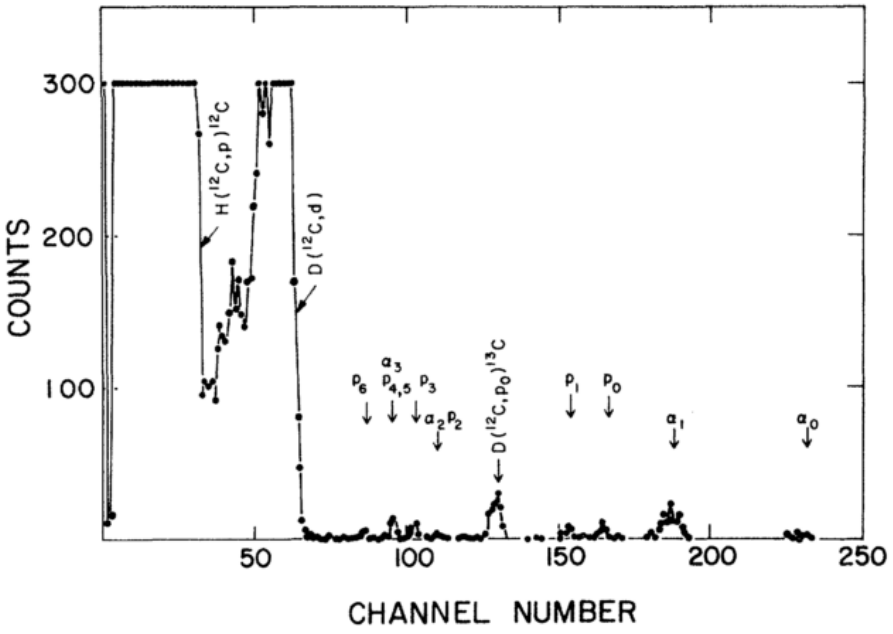

Figure 3.2: Sample spectrum for the ^{12}C+^{12}C reactions (α and p channels) taken using charge particle detection at an angle of 20^o and E = 3.92 MeV [40]. Reactions with the target contaminants (at low channels) can be seen hindering the ^{12}C+^{12}C reaction products at low energies.

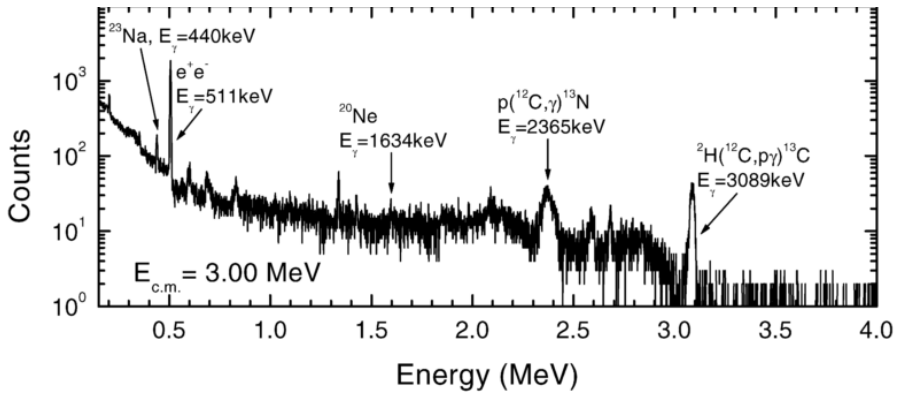

Figure 3.3: Sample gamma-ray spectrum at E = 3.0 MeV for the ^{12}C+^{12}C reactions [39]. Notice that the two prominent peaks at E = 3.1 MeV and E = 2.4 MeV correspond to hydrogen contamination in the target. When going to lower energies, the yield from the ^{12}C+^{12}C reactions decreases exponentially and the reaction signal is masked by these contaminants.

Thus, in more recent experiments, great attention was paid in choosing high purity targets. This was the case of Spillane *et al.* [44] who used a 99.8% purity graphite target, which allowed the measurement of the ^{12}C+^{12}C reactions down to E = 2.10 MeV. However, given that the target still contained a small quantity of hydrogen, the measured cross sections present very large error bars as can be seen in figure 3.4, which shows the modified S-factor $\tilde{S}$(E) of the ^{12}C(^{12}C, p)^{23}Na and ^{12}C(^{12}C, α)^{20}Ne reactions measured by various groups. Due to the large uncertainties, doubt about the estimate of the lowest energies cross sections has also been experienced in the past few years [21, 50].
Spillane *et al.* also found a resonance at E = 2.14 MeV but it has not been confirmed. Since this energy is near the astrophysically relevant energies, a resonance within the Gamow window has been theorised. In the past few years, various calculations had been made in order to understand the impact of a resonance in the ^{12}C+^{12}C reaction at stellar energies [18,33,52]. According to these calculations, the existence of said resonance would reduce the value of M_{UP} from 7-8 $M_\odot$ to 4-5 $M_\odot$, making the carbon burning in stars more efficient and thus, producing less compact pre-supernova structures. Also, the remnants of these supernovae would be smaller than the standard models predictions. Finally, the existence of such a resonance could increase by 25-30% (depending on its strength) the central density of white dwarfs (compared to standard models). The limiting mass between a neutron star and a black hole would be also affected [18].

Another issue of the $^{12}C+^{12}C$ reactions cross section can be noticed in figure 3.4 where different data sets (for both exit channels) agree in some energy regions whilst in others, there is a difference of orders of magnitude in the $\tilde{S}$-factor. These discrepancies have not yet been understood, which suggests the need of further experimentation.

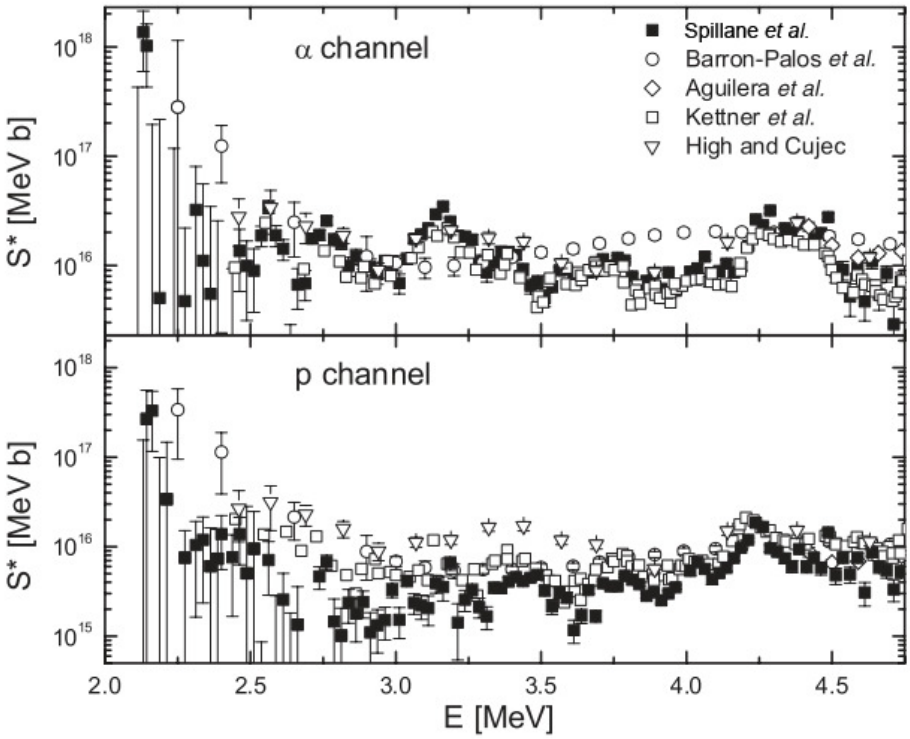

Figure 3.4: $\tilde{S}$-factor of the $^{12}C+^{12}C$ reactions obtained by five different groups using gamma-ray spectroscopy. The discrepancy between data sets in certain energy regions is not yet understood. Low energy data is governed by large uncertainties due to the H contamination in the targets. Figure taken from [44].

In addition to experimental discrepancies, different theoretical models also show considerable discrepancies between each other as shown in figure 3.5 and they do not reproduce the resonant-like structures that the $^{12}C+^{12}C$ reactions cross section presents [53–57]. These structures complicate the extrapolation from high energy data [15, 35, 36, 44, 45]. In the figure 3.5, three theoretical models are presented along with three experimental data sets. The shown models correspond to empirical extrapolations made by Fowler and Jiang (this second using a hindrance effect associated with the incompressibility of nuclear matter [58]) and calculations with the barrier penetration model made by Gasques (see [57] and references therein).

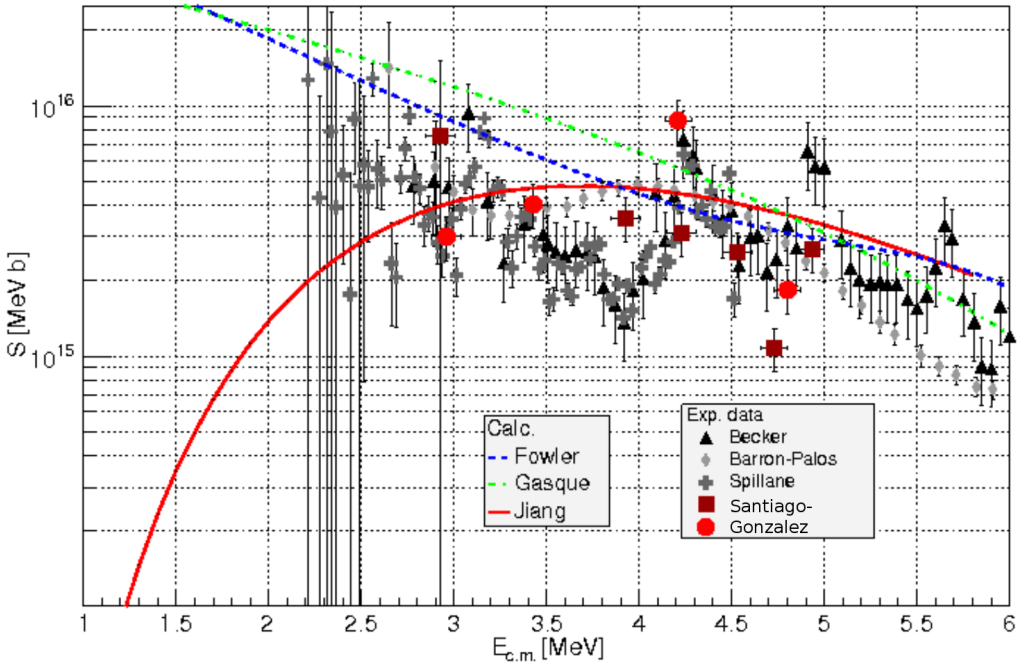

Figure 3.5: S-factor of the $^{12}C+^{12}C$ reactions obtained by three different groups using charged particle detection (Becker [41]), gamma-ray spectroscopy (Barron-Palos [39]) and a combination of both techniques (Santiago-Gonzalez [51]). Three different theoretical models are displayed showing discrepancies of orders of magnitude in the energy region of astrophysical interest (E < 3.0 MeV). Figure taken from [51].

None of the proposed models reproduced the experimental trends and large discrepancies persist at the lowest energies. These resonances have been qualitatively explained as vibrational or rotational molecular configurations, however, they are still not well understood [21, 59].

In summary, a new measurement of the $^{12}C+^{12}C$ reactions is extremely important because of three main reasons: 1) there are still several discrepancies between different data sets; 2) Spillane *et al.* [44] found a large resonance at the lowest measured energy which, if confirmed, it would affect a large number of stellar rates with profound astrophysical implications; and 3) the theoretical models do not agree with each other and they fail to reproduce the resonant nature of this fusion reaction, making the extrapolation of available data to stellar energies very uncertain.

3.3 Aim of this work

For the reasons discussed, a measurement of the $^{12}C+^{12}C$ reactions at the lowest energies possible is needed and, to this end, a considerable effort to reduce hydrogen and deuterium contaminants in the carbon targets should also be attempted.
The aim of this work was to measure experimentally the $^{12}C+^{12}C$ reactions using charge particle detection and the thick target approach discussed in chapter 2.2 for the extraction of cross sections and modified astrophysical S-factors over a wide energy region. An additional study on target contamination was also performed in order to understand the target behaviour under beam bombardment.
The work presented here, represents a first step towards measurements at astrophysical energies which will hopefully give some light on the existence of resonances within the Gamow window.
Due to time constrains, only the proton channel of the $^{12}C+^{12}C$ reactions is presented here. In the following chapters, the experimental configuration used in this work and the obtained results are presented and discussed in detail.

Chapter 4

Experimental set-up

As mentioned in previous chapters, the aim of this work was to measure the ^{12}C(^{12}C,p)^{23}Na and ^{12}C(^{12}C,α)^{20}Ne reactions using charge particle detection. However, only the proton channel is presented in this thesis.
The experiment was performed using the 3 MV pelletron tandem accelerator of the CIRCE (Centre for Isotopic Research on the Cultural and Environmental heritage) laboratory, Department of Mathematics and Physics of the University of Campania L. Vanvitelli-INNOVA in Caserta, Italy. In collaboration with the Italian National Institute of Nuclear Physics (INFN) and supported in part by the Royal Society.
Since this project started at the beginning of my Ph.D., all the elements necessary to measure the ^{12}C+^{12}C reactions had to be designed, bought and built from scratch. Therefore, initial work focused on: the development of optical calculations for optimal beam transportation; preliminary tests in a small scattering chamber; the development of a telescope detector array called GASTLY (GAs Silicon Two-Layer sYstem); and the use of a large scattering chamber able to house the full set-up.
In the following sections, a detailed description of the laboratory, beamline development, scattering chambers, detectors and experimental configuration used for the ^{12}C+^{12}C reactions measurements is presented.

4.1 CIRCE accelerator

The accelerator at the CIRCE laboratory is a 3 MV pelletron tandem and its layout is shown in figure 4.1. Since the CIRCE accelerator was originally designed to perform Accelerator Mass Spectrometry (AMS) measurements [60], the beam transport system includes a series of magnetic and electrostatic filters to achieve a sufficient mass resolution and a low level of impurities [26]. The system main components are: an ion source (S1), three electrostatic analysers (ESA), two analysing magnets (BM) a switching magnet and five available beamlines, one (20°) devoted to the ^{12}C+^{12}C reactions measurements. A detailed description of these elements can be found in the following section.

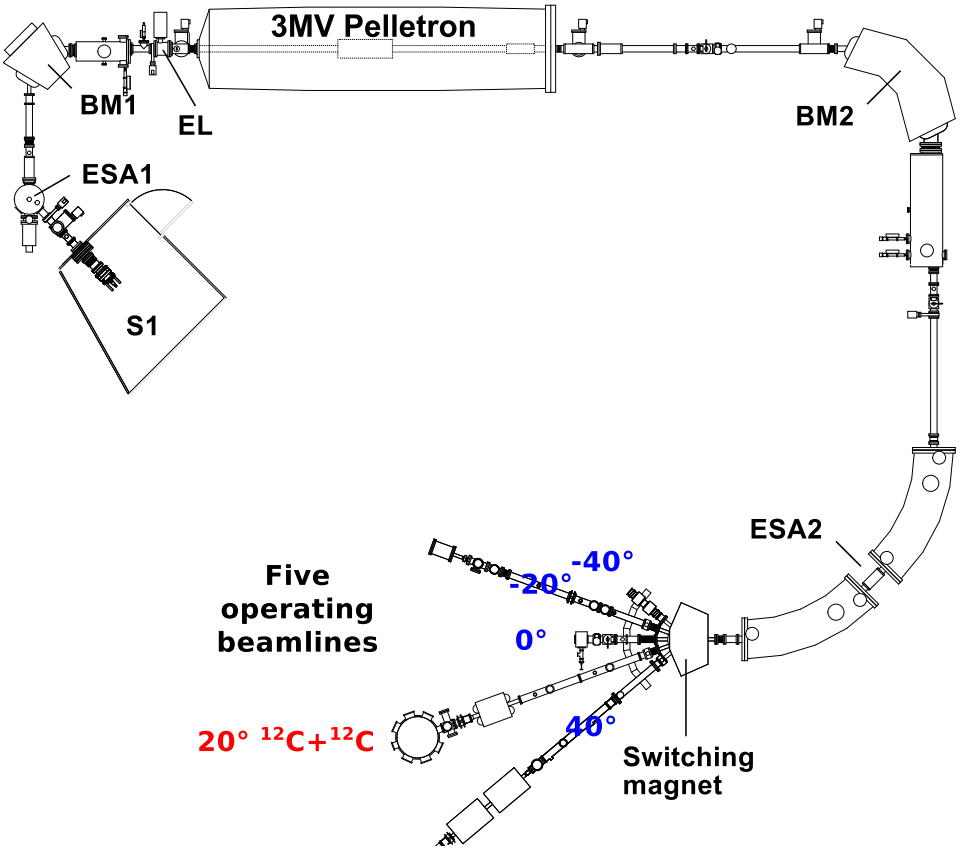

Figure 4.1: Layout of the CIRCE accelerator complex consisting in: ion source (S1), electrostatic analysers (ESA) for beam purity, analysing magnets (BM) for mass selection, an Einzel lens (EL) for beam focusing, the 3 MV Pelletron tank, the switching magnet for beamline choice and the five experimental beamlines available. Some components not relevant to the present experiment are not shown here.

4.1.1 Ion production, acceleration and transport

Experimental measurements of cross sections at energies lower than the Coulomb barrier (as is the case of the ^{12}C+^{12}C reactions) require high ion beam currents of the order of μA [6]. The CIRCE accelerator Cs sputter ion source is capable of producing a ^{12}C beam (using a 2 mm diameter Al cathode filled with commercial graphite) of up to 17 pμA on target. In this source (see figure 4.2), a Cs oven at about 130ºC produces Cs vapour that is transported into an enclosed area between a cool cathode and a heated ionizer (a tungsten filament). Since the ionization energy of Cs (3.89 eV) is lower than the work function of tungsten (4.55 eV), the most outer electron

of Cs transfers to the ionizer easily (ionization efficiency ∼100% at a surface temperature > 1000°C) [61]. The ionized Cs atoms are accelerated and focused towards the cathode containing the desired beam species (e.g. graphite for a carbon beam), which are sputtered out of the cathode, extracted and pre-accelerated to form the beam. It should be noted that the ions produced by this Cs source are negative, a necessary condition due to the orientation of the high voltage and stripping gas configuration of the accelerator (discussed below) [62].

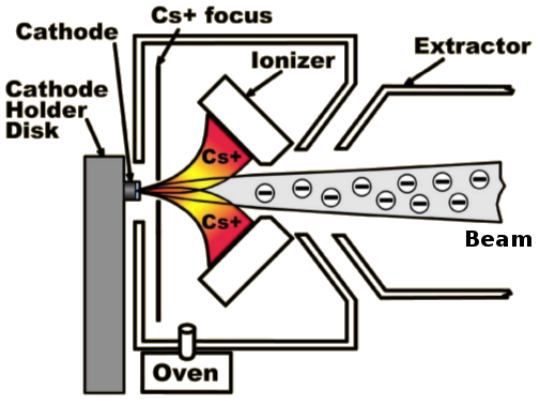

Figure 4.2: Sketch of the CIRCE sputter ion source. The oven, Cs, ionizer, cathode and extractor can be seen forming the beam (see text for further details).

A spherical electrostatic analyser (ESA1) follows the ion source and cuts the energy tail of the beam with a bending angle of ± 45°. After the ESA1, a 90° double focusing analysing magnet (BM1) is encountered by the beam, allowing a high resolution mass analysis for all stable isotopes [60]. Exiting the BM1, the beam is focused by an Einzel lens (EL) to the accelerating terminals. Since this is a tandem accelerator, the ions are brought to high energies in two stages. In the first stage, the negative ions are accelerated to the positive terminal (maximum tension ∼3 MV). An argon gas stripper removes the electrons of the negative ions, resulting in positive ions (of all possible charge states) that are accelerated again once they exit the terminal. Two chains formed by metal "pellets" (hence the name "Pelletron") are used to charge the high voltage terminal. Long term stability is achieved using Generating Volt Meter (GVM) feedback on the charging system high voltage supply. An analysing magnet (BM2) placed after the accelerator tank is used to bend only the isotope of interest. Eventually, the beam encounters two 45° electrostatic analysers (ESA2) that suppress any type of contamination the beam could carry [60]. At this stage, the isotope and impurity-free beam

(in mass m per charge state q) is ready to be channelled to one of the five available beam lines through the switching magnet. Several tests performed by Terrasi *et al.* [60] concluded that the resolutions of the accelerator are $\frac{M}{\Delta M}$= 725 for mass and $\frac{E}{\Delta E}$ = 700 for energy.

4.2 Beamline development

Given that at the beginning of this project the beamline for the $^{12}C+^{12}C$ reactions measurements did not exist, a series of elements necessary for this investigation were developed. In order to design the beamline, I performed optical calculations to achieve an optimal beam transport to the graphite target. The elements of the 20° beamline considered for the optical calculations are shown in figure 4.3: a quadrupole lens for beam focusing, a cross pipe connector for the installation of a "cold finger" liquid nitrogen dewar acting as cold trap and a scattering chamber designed by the INFN (Naples) mechanical design service and built by the STREAS company.

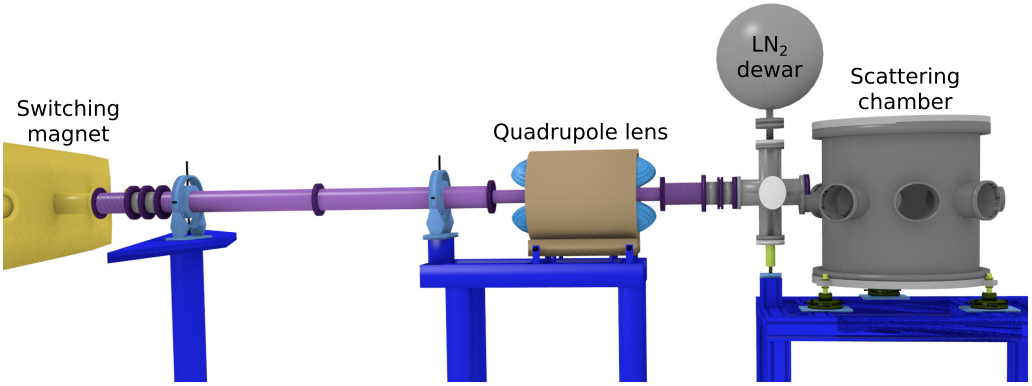

Figure 4.3: 3D rendering of the $^{12}C+^{12}C$ reactions measurements beamline showing its main components: switching magnet, quadrupole lens, liquid nitrogen dewar's cross pipe connector and scattering chamber (see text for details).

The optical calculations were done using the COSY INFINITY [63] software and taking into account the elements placed after the accelerator tank, the quadrupole lens and scattering chamber dimensions and the available space in the laboratory. Optical calculations allowed optimizing the position for the scattering chamber and the quadrupole lens (considering its maximum magnetic fields B_{max} = 4500 gauss) in order to have minimum dispersion of the beam at the target position. The calculations simulate the trajectories of the beam particles as they pass through the beamline right after exiting

the accelerator tube. Figure 4.4 shows the final results viewed from the horizontal (left) and vertical (right) planes, where the waist of the beam (the location where the beam is the smallest, thus best focused) is positioned on the surface of the target. The beam exits the accelerator tank (left to right) reaching the analysing magnet (BM2), which focuses the beam into the electrostatic analyser (ESA2) to eventually reach the switching magnet. The beam then enters the quadrupole lens that focuses it again to reach the target at the centre of the scattering chamber. In these results, a beam energy ($q = 3^+$) of $E_{lab} = 8.0$ MeV (intermediate beam energy used in the $^{12}C+^{12}C$ reactions measurements, see chapter 6) was simulated and the quadrupole lens magnetic fields were set to $B_{horiz} = 2180$ gauss and $B_{vert} = 2480$ gauss (about half of the maximum values). These results are achieved by positioning the quadrupole lens at 270 cm from the accelerator's switching magnet and the target (the centre of the scattering chamber) at 90 cm from the quadrupole lens.

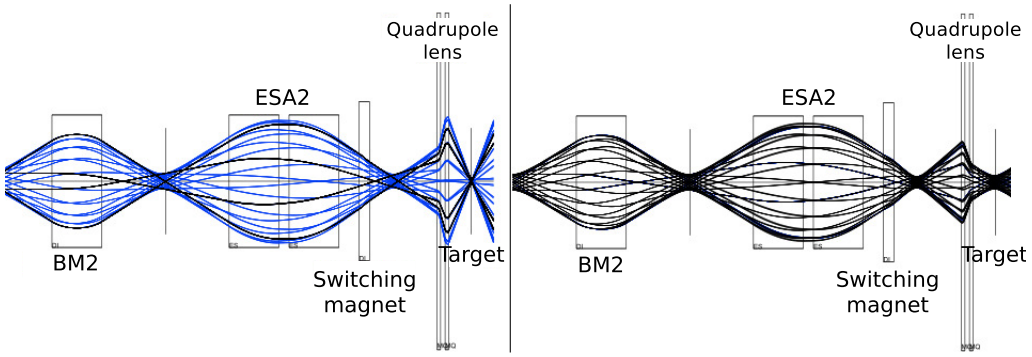

Figure 4.4: Beam trajectories through the different elements along the beamline (after exiting the accelerator tank), as calculated with COSY. The quadrupole lens is positioned at 270 cm from the switching magnet and the target at 90 cm from the lens. Horizontal (left) and vertical (right) planes passing through the beam axis are shown.

Once the optimum positions were calculated, I designed all supports and levellers (as shown in figure 4.3) to then order the components from STREAS (beamline pipes), NEC (beamline pipe supports and levellers), Bosch (scattering chamber support) and a local blacksmith (quadrupole lens support).

4.3 Small scattering chamber

While preparing the 20° beamline of the accelerator complex, an available small scattering chamber was positioned at the -40° beamline. This small chamber (sketched in figure 4.5) was used to perform preliminary tests on targets, which aimed at developing the methodology used later in the final set-up and at monitoring target's behaviour under beam bombardment as well as residual gas in the chamber.

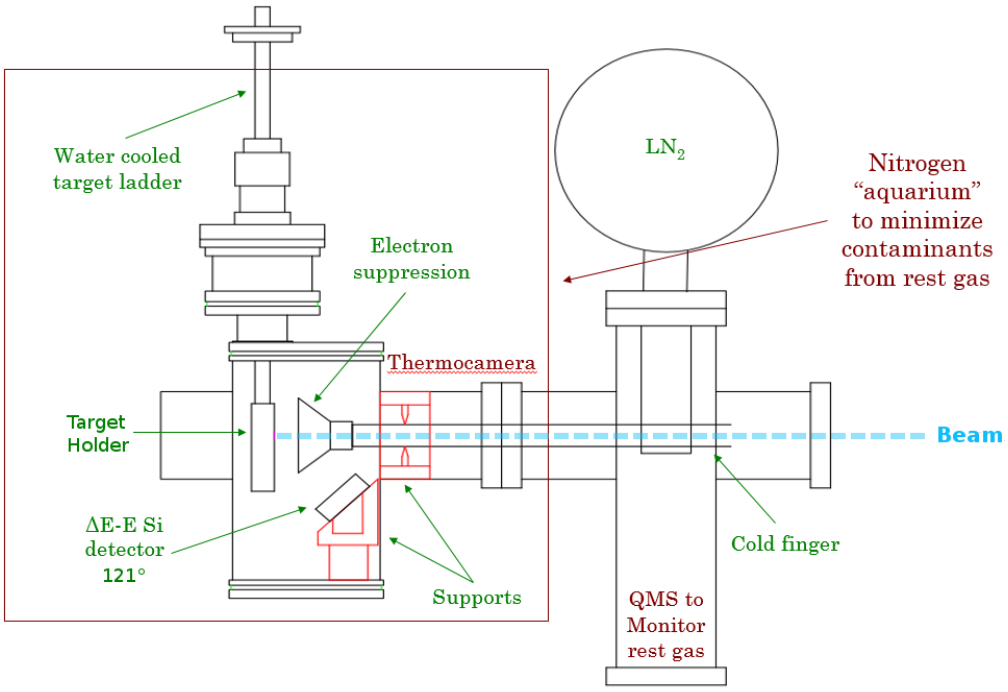

Figure 4.5: Sketch of the small chamber set up housing a Si telescope detector, a target holder and a cold finger with umbrella for electron suppression purposes. Outside the chamber a thermocamera and QMS were placed to monitor the temperature of the target and the composition of the residual gas, respectively. The chamber was later surrounded by a N_2 atmosphere, referred to as the "aquarium" (see text for further details).

The small chamber housed a water-cooled target ladder able to accommodate two targets and two collimators (3 and 6 mm in diameter) for beam focusing and a Si telescope detector. The detector consisted in a thin (50 μm) ΔE Si detector (17 mm of diameter) and a thick (300 μm) Erest Si detector (300 mm^2 of active area). This ΔE-Erest detector was placed at 121° (imposed by geometrical constraints) with respect to the beam axis. A

2 μm (nominal thickness) aluminium foil was placed in front of the detector to protect it from scattered particles. A cold finger (maintained at liquid nitrogen temperature) extended to the target to minimise carbon deposition on target. This pipe ends in a wired "umbrella" biased with a potential of -300 V, for secondary electron suppression purposes to correctly measure the beam current on target. The chamber was latterly enclosed in a nitrogen atmosphere (hereafter the "aquarium") as part of the target contamination study discussed in chapter 5.
A calibrated FLIR SC325 thermocamera was also tested with the small chamber. This camera has a reading accuracy of $\pm$ 2% [64] and was later used to constantly monitor the target temperature during beam bombardment (see chapter 5). Since the thermocamera uses infra-red technology, a viewport with a 3 mm thick Ge window was used. This window, contrary to a normal glass window, is transparent to the wavelengths to which the thermocamera is sensitive (7.5 μm - 13 μm). Additionally, in the interest of monitoring the residual gas inside the chamber, a quadrupole mass spectrometer (QMS, Pfeiffer Prisma 200 [65]) was also tested. A description of the tests performed with the thermocamera and QMS is given in chapter 5.2.

4.4 GASTLY scattering chamber

After building the 20º beamline at CIRCE, the previously mentioned large scattering chamber (ϕ = 60 cm, h = 70 cm) was installed, along with the thermocamera, QMS and the nitrogen "aquarium". A 3D rendering of the downstream part of the 20º beamline can be seen in figure 4.6

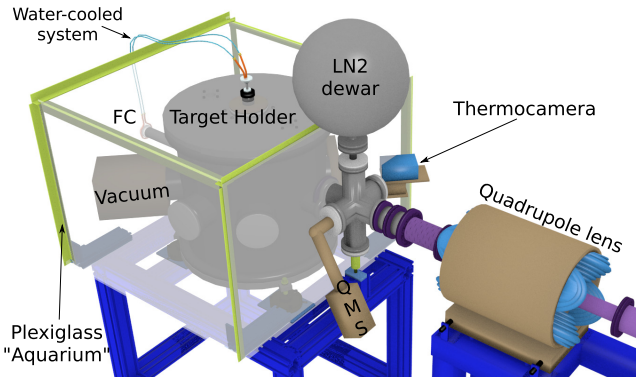

Figure 4.6: 3D rendering of the downstream part of the 20º beamline. The scattering chamber can be seen surrounded by a plexiglass structure flushed with N_2 at atmospheric pressure. The thermocamera and QMS previously tested were also installed.

This chamber housed a detection system called GASTLY (see section 4.5 for a detailed description) and the water-cooled copper target ladder tested with the small chamber. A 3D printed sphere with conductive paint surrounded the target and was kept at -300 V for electron suppression purposes (section 4.3). The sphere had 25 x 25 mm^2 ports to allow for passage of the beam and the detection of particles. A cold finger kept at LN_2 temperature, extended to a distance of about 5 cm from the target (due to geometrical constraints, this distance could not be made shorter) to minimise carbon deposition (see figure 4.7).

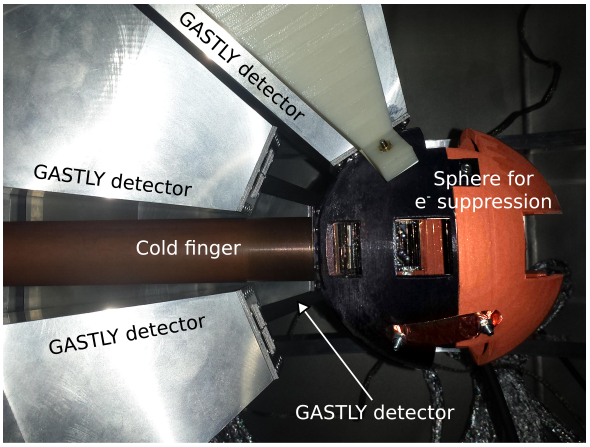

Figure 4.7: Picture of the inside of the scattering chamber for the $^{12}C+^{12}C$ reactions measurements. Four GASTLY detectors can be seen, along with the electron suppression sphere and the cold finger.

One of the seven ports of the GASTLY scattering chamber was devoted to the installation of the thermocamera. A thermal image of the target under beam bombardment is shown in figure 4.8, where the target ladder can be appreciated along with the electron suppression sphere and the beam spot on the target (E_{lab} = 8.0 MeV $^{12}C^{3+}$).
The QMS for residual gas composition monitoring (previously tested in the small chamber), was installed on another port of the scattering chamber. Figure 4.9 shows a top view sketch of the chamber and all the external elements used for the $^{12}C+^{12}C$ measurements. For beam focusing purposes, the port opposite to the beam entrance was equipped with a Faraday cup (FC). The chamber's vacuum pumping system consisted of an ABM roughing pump (model VDE0530) and a Pfeiffer Asslar turbo pump (model TMH 521). The use of this vacuum system along with an identical turbo pump placed upstream the quadrupole lens, permitted to achieve typical vacuum values inside the scattering chamber of 10^{-6} mbar (with beam on target).

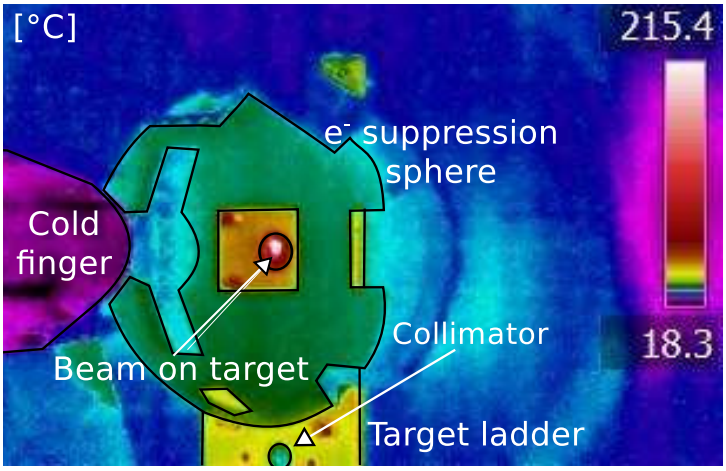

Figure 4.8: Colour coded image of the beam bombarded target with an E_{lab} = 8.0 MeV $^{12}C^{3+}$ beam. The cold finger, the front side of the electron suppression sphere and the target ladder can be seen together with the beam impinging on the target. Contour lines have been added for clarity.

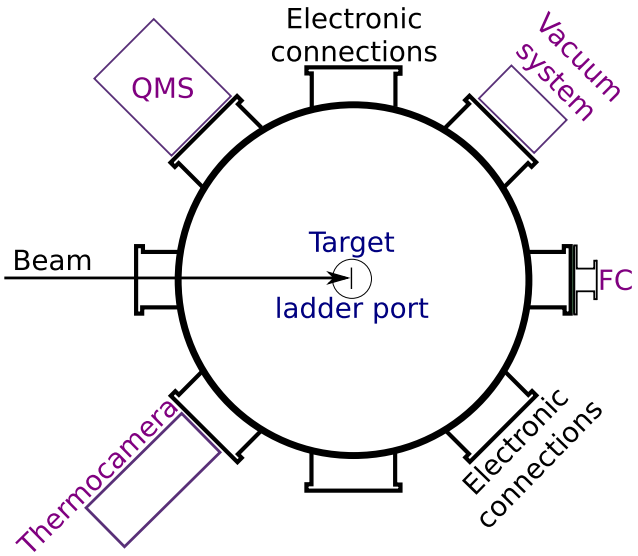

Figure 4.9: Top view sketch of the scattering chamber showing the external elements used for the ^{12}C+^{12}C reactions measurements. The beam direction, thermocamera, QMS and Faraday cup (FC) for beam focusing are shown. The chamber vacuum system and the ports used for the connection of the detectors electronics are also marked. The target ladder is positioned from the top of the scattering chamber.

4.5 GASTLY detection system

A two-stage detection array called GASTLY (GAs Silicon Two-Layer sYstem) was specifically designed to detect low energy charged-particles to fulfil the requirements for the $^{12}C+^{12}C$ reactions cross sections measurements. Each GASTLY module consists of an ionization chamber (IC) and a silicon strip detector (SSD), housed in an aluminium pyramidal frame, which provide the ΔE-Erest stages for standard particle identification (see section 4.5.1). Figure 4.10 shows a schematic 3D view of the full GASTLY array (eight detectors). In the $^{12}C+^{12}C$ reactions experiment, only four detectors called A, B, C and D were used. The original positions of the detectors were calculated with the target surface in the exact centre of the chamber [66]. However, the target ladder used in this experiment shifted the target position 2 mm upstream due to the need of adding a 1 mm plate to hold a thick (1 mm) target. This shift translated into slightly different detection angles compared to the nominal geometrical ones. Table 4.1 shows the detector positions, angular ranges and distances to the target recalculated for the $^{12}C+^{12}C$ reactions experiment conditions. Hereafter, the detector positions will be called 121º, 143º, 156ºUP and 156ºDOWN, for simplicity.

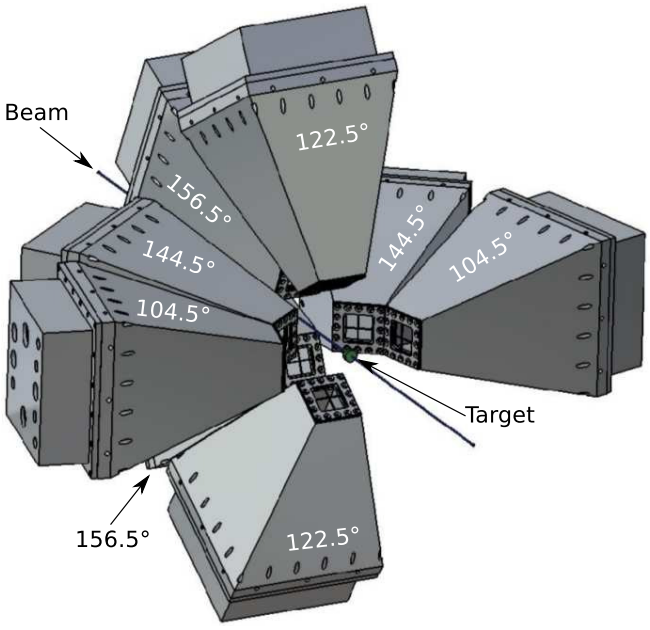

angles

Figure 4.10: 3D rendering of the full GASTLY array. Eight GASTLY modules are positioned around the target in the backward hemisphere, with respect to the beam direction.

Table 4.1: Central positions θ_0 of the four GASTLY detectors used in the $^{12}C+^{12}C$ reactions experiment. Uncertainties were calculated considering the 2 mm shift from the nominal values. Angular coverage $\Delta\theta$, vertical plane angles ϕ_0 and distance between target and detector entrance window d_{TE} are also provided (see section 4.5.1 for details).

θ_0 [deg.]	$\Delta\theta$ [deg.]	ϕ_0 [deg]	d_{TE} [mm]
120.7 ± 0.9	18 ± 0.5	90 ± 0.05	53.0 ± 1
143.2 ± 0.6	18 ± 0.5	0 ± 0.05	53.0 ± 1
155.9 ± 0.3	13 ± 0.3	90 ± 0.05	82.2 ± 1
155.9 ± 0.3	13 ± 0.3	270 ± 0.05	82.2 ± 1

The choice of these positions was based on geometrical constraints: the need to leave free the thermocamera port view and the partial shadow the target holder presented at smaller horizontal angles (due to the previously mentioned target shift). Figure 4.11 shows a side view (vertical plane) of the chamber where three of the four detectors can be seen as well as the electron suppression sphere, the beam direction and the cold finger. A top view (horizontal plane) of the chamber is presented in figure 4.12, which shows the 143° detector position. As shown in table 4.1, the detectors at 156° are located farther away from the target than the other two detectors. This difference in distance translates into a difference in angular detection ranges and geometrical efficiencies (see section 4.7 for details).

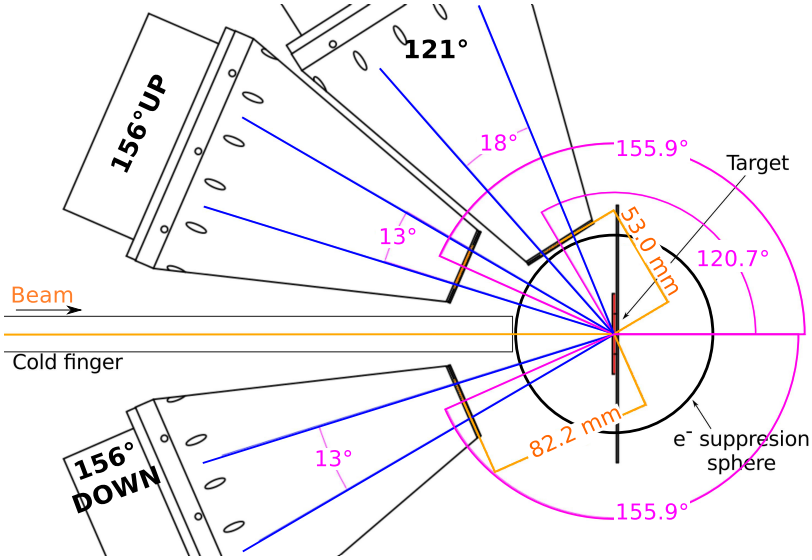

Figure 4.11: Vertical plane of the scattering chamber showing three GASTLY detectors, the position of the target, their distance to the target, the electron suppression sphere, the cold finger and the direction of the beam.

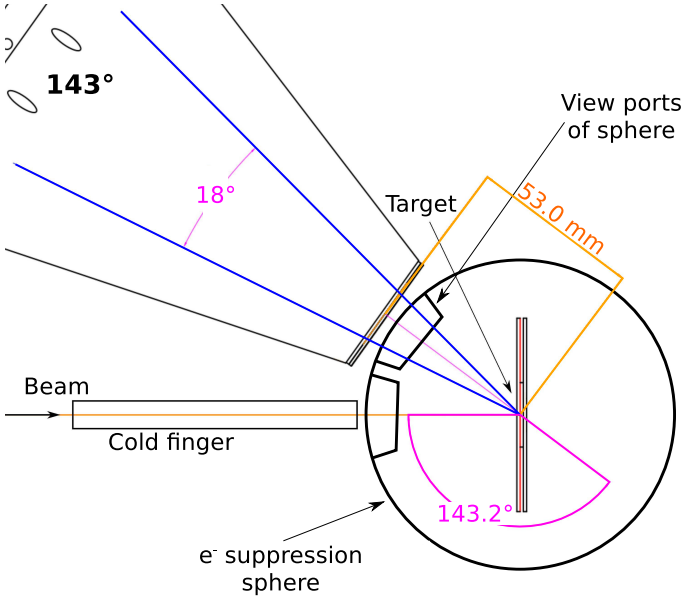

Figure 4.12: Horizontal plane of the scattering chamber showing the GASTLY detector located at 143º. The position of the target, the target-detector distance, the electron suppression sphere, the cold finger and the direction of the beam are also shown.

Since the $^{12}C+^{12}C$ reactions measurements lasted several months and the electronic modules were used in other experiments, the positions of the GASTLY detectors changed between the two main data taking campaigns. Incidentally, this event allowed us to test the reproducibility of the results of the $^{12}C+^{12}C$ reactions measurements over a common energy region (see chapter 6). This change in position, obliged us to differentiate between configurations (called Old and New). Table 4.2 summarizes the positions of the A, B, C and D GASTLY detectors used in the two campaigns.

Table 4.2: Positions of the GASTLY detectors used in both Old and New configurations.

Detector	**Old config.**	**New config.**
A	143°	156°DOWN
B	121°	156°UP
C	156°UP	121°
D	156°DOWN	143°

4.5.1 Detectors description

As mention previously, each GASTLY module consists of an ionization chamber (IC) and a silicon strip detector (SSD), housed in an aluminium pyramidal frame. A detailed description of each detector is given in the following sections.

Ionization chamber

The ionization chamber consists of a fibreglass (FR-4) frame shaped as a truncated pyramid with square section surrounded with a PVC housing. Its key components are a cathode (entrance window), a Frisch grid, an anode, several guard rings, and a suitable gas (CF_4 for the $^{12}C+^{12}C$ reactions experiment) maintained at an appropriate pressure (depending on application). A schematic view of an individual GASTLY detector is shown in figure 4.13.

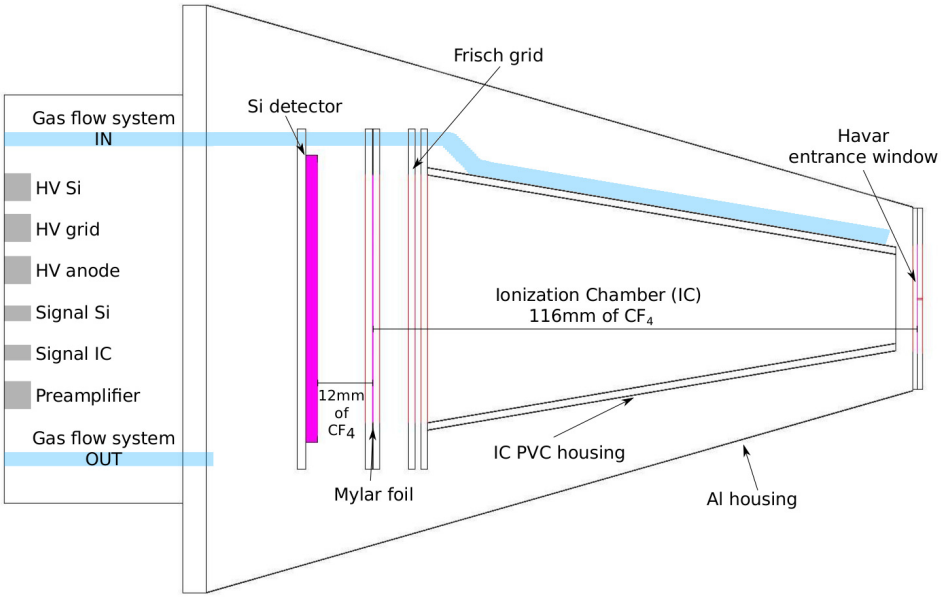

Figure 4.13: Sketch of a GASTLY detector. Each detector consists of a Havar entrance window, a 116 mm long IC filled with CF_4 (variable pressure), a Frisch grid, a Mylar foil used as anode and a Si detector. The detector electronics and gas flow system are housed inside an aluminium pyramid.

For the $^{12}C+^{12}C$ reaction measurements, the entrance window was a 23 x 23 mm^2 Havar foil (with a measured thickness of 2.6 $\pm$ 0.2 μm, see Appendix C for further details) grounded to the main pyramidal structure. The window is supported by a cross frame (98% transparency) so as to minimise the

probability for foil breakage and deformation due to the pressure gradient. The entrance window acts as a cathode to the IC and can be easily replaced to meet the requirements of specific applications (e.g. to sustain higher gas pressures in the IC or to minimise energy losses). For the ^{12}C+^{12}C experiment the anode was an aluminized Mylar foil (50 μg/cm^2 of Al) of measured thickness of 1.6 $\pm$ 0.2 μm (see Appendix C). These thicknesses were chosen to keep the detection energy threshold as low as possible. Figures 4.14 and 4.15 show the kinematic curves of the ^{12}C(^{12}C,α_0)^{20}Ne and ^{12}C(^{12}C,p$_{0,6}$)^{23}Na reactions, respectively, calculated for a beam energy of E$_{lab}$ = 6 MeV and 35 mbar of CF_4 in the IC. The thickness of the havar foil was chosen to allow the α particles to be detected by the ΔE detector however maintaining a robust foil to prevent breakage due to high pressures in the IC. On the other hand, the thickness of the mylar foil was chosen thin enough to minimise energy loss of low energy protons.

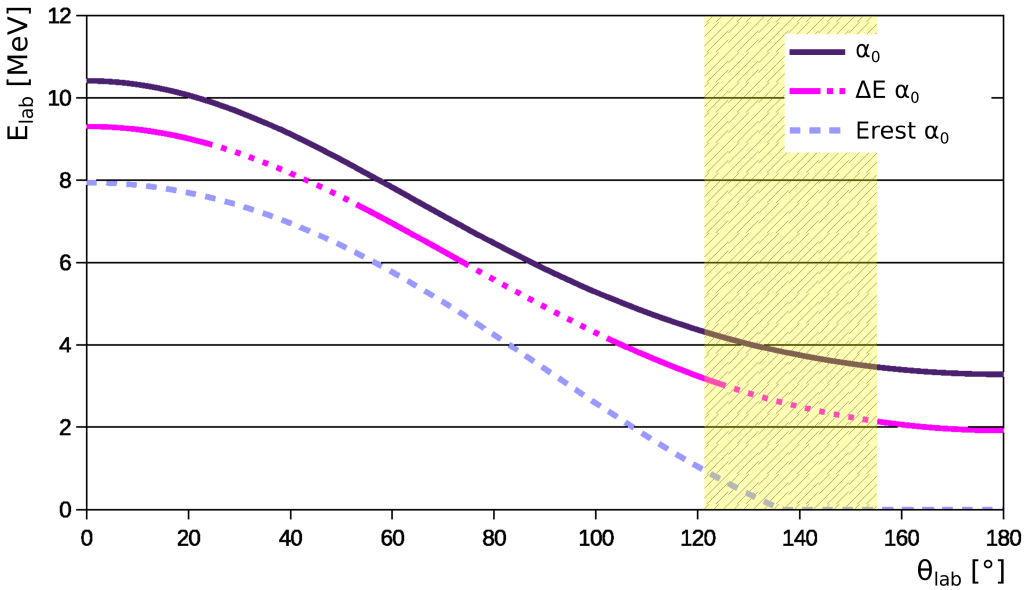

Figure 4.14: Kinematic curves of the ^{12}C(^{12}C,α_0)^{20}Ne reaction obtained with a beam energy of E$_{lab}$ = 6 MeV in 35 mbar of CF_4 in the IC. The original energies (continuous line) and the energies deposited in the ΔE (continuous+dotted line) and Erest (dashed line) detectors (following energy loss calculations) by the α_0 group are shown. The shaded area represents the full angular coverage of the GASTLY detectors.

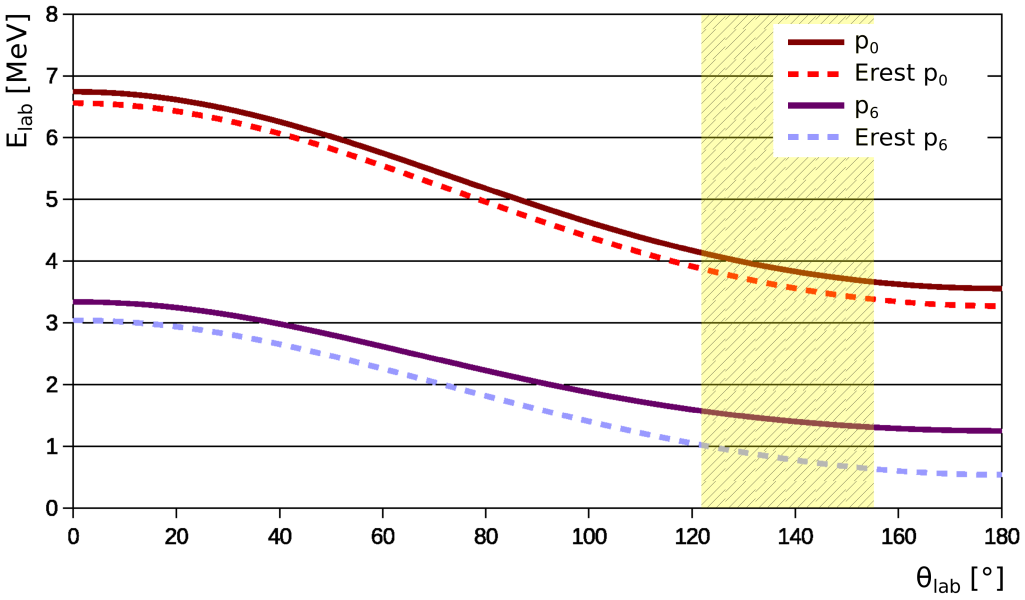

Figure 4.15: Kinematic curves of the $^{12}C(^{12}C,p_{0,6})^{23}Na$ reaction obtained with a beam energy of $E_{lab} = 6$ MeV in 35 mbar of CF_4 in the IC. The original energies (continuous lines) and the energies deposited in the Erest (dashed lines) detector (following energy loss calculations) by the p_0 and p_6 proton groups are shown. The shaded area represents the full angular coverage of the GASTLY detectors.

The active region of the IC, defined as the distance between the entrance window and the anode, is 116 mm long. The Frisch grid consists of a mesh of gold-coated tungsten wires (20 μm diameter) arranged perpendicularly to one another at 3 mm pitch in both directions ($\sim$ 99% transparency). The grid is placed upstream of the anode at a distance of 9.5 mm and is kept at a positive voltage lower than that used for the anode. The bias applied to the Frisch grid reduces to zero (ground) the cathode through a resistive partition of guard rings connected in series by means of 3.3 MΩ resistors, as shown in figure 4.16. Each guard ring consists of a gold-coated copper strip (3 mm width, 4 mm pitch) printed on the inner face of each side of the fibreglass pyramid. Special care was taken to avoid any deformation of the electric field inside the IC active region, by minimising discontinuities arising from the soldering of metallic parts (guard rings and Frisch grid wires).
As previously mentioned, the IC was operated with CF_4 gas for the $^{12}C+^{12}C$ reaction experiment. This gas was chosen for its high electron drift velocity, its high ionization power and its absence of H, that could alter the charged particle measurements of the $^{12}C+^{12}C$ reactions (see chapter 3). The gas enters the IC active region from the inlet connector at the back of the housing

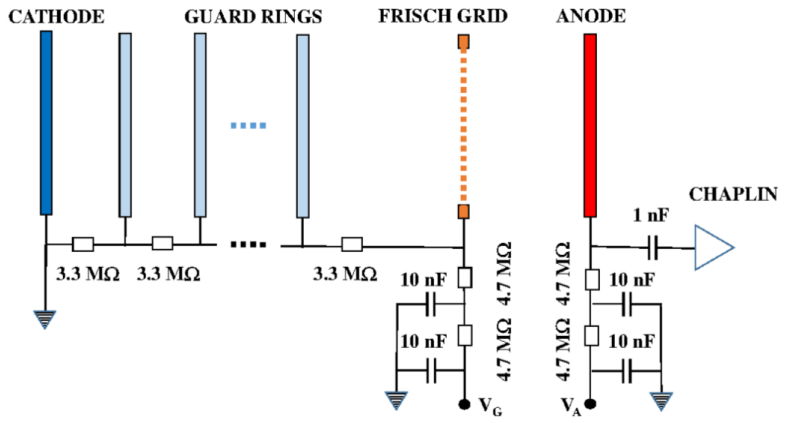

Figure 4.16: Scheme of the bias and filtering circuit for the GASTLY ionization chamber. The bias is applied to the Frisch grid through a resistive partition of guard rings connected in series.

and into a hole near the entrance window, through a Rilsan [67] pipe (external and internal diameters of 4 and 2 mm, respectively) inside the housing, and it flows to the outlet connector also placed at the back of the aluminium structure (see figure 4.13).
The gas filling systems of all detectors are connected in parallel to a unique entrance from a MKS module (model PR4000B) and a single exit to a pressure gauge (MKS baratron 626). An pressure controller (MKS 250E) regulates the pressure inside the ionization chambers and maintains it constant within ±0.25 mbar. The pressure is also measured at the exit pipe of the gas flow system using a Pfeiffer Asslar (model D-35614) compact full range gauge in order to guarantee an approximately uniform pressure throughout the ionization chamber volume. The aluminium housing is sealed for in-vacuum operations and acts as gas container (volume of about 1.5 litres). Being electrically grounded, it also shields the IC electrodes and the inner readout electronics from the environmental electromagnetic noise.

Silicon strip detectors

The second stage of each GASTLY module consists of a 58 x 58 mm^2 silicon strip detector (SSD, Canberra PF-16CT-58*58-300EB/D4) with a nominal thickness of 300 ± 15 μm [68]. Its front face is segmented into 16 strips (3.5 x 58.0 mm^2 each) separated by about 0.1 mm of passivated inter-strip region, while the back ohmic face is unsegmented. The detector's dead layers, according to its data-sheet, are less than 50 nm on the front side and less than 1500 nm on the rear side [66]. Although the Erest detectors are segmented,

they were used as a single Si detector in the present experiment due to a lack of sufficient electronic modules.
The opening size of the pyramid was chosen to maximise the solid angle covered by the silicon detector placed immediately behind the ionization chamber (at 12 mm from the anode). Because of geometrical constraints, some detector positions subtended a smaller solid angle than the others; this aspect is discussed further in section 4.7.

4.5.2 Detector electronics

In order to minimize electronic and environmental noise, that would affect the detection of low energy particles, the GASTLY readout electronics are mounted on printed circuit boards arranged in a stack behind the silicon detector and inside the aluminium housing. The electronics consists of two hybrid low-noise charge home-made preamplifiers called CHAPLIN (CHArge Preamplifier Low-noise Infn Naples), one for the SSD signal and another for the IC signal. These preamplifiers have been widely used with different experimental devices, showing excellent performance [69, 70]. The CHAPLIN output signals are fed into a shaping SPectroscopy AMplifier (SPAM), designed to match the CHAPLIN low-impedance output. The main features of the CHAPLIN and SPAM modules are summarised in tables 4.3 and 4.4, respectively [66].

Table 4.3: Specifications of the home-made preamplifiers CHAPLIN of the GASTLY detectors.

Input capacitance:	30 pF
Rise time @ Csource = 2 pF:	22 ns
Falltime @ Csource = 2 pF:	3.3 μs
Sensitivity:	30 mV/MeV in Si eq. (measured)
Noise @ C source = 0 pF:	300 e rms
Feedback resistance:	10 MΩ
Open loop gain:	10^4 V/V
Power dissipation:	180 mW
Max energy converted:	200 MeV (+ve output signal)
	270 MeV (-ve output signal)
Output signal polarity:	Inverted
Power supply:	+12 V, -12 V

Table 4.4: Specifications of the home-made spectroscopy amplifiers SPAM of the GASTLY detectors.

Input:	16 ch. (50 Ω or 1 kΩ) (Coax. cable)
Output:	16 ch. (max gain 1000x) (ECL conn.)
10x-Output:	16 ch. (max gain 10000x) (ECL conn.)
Fast-Output:	16 ch. (ECL conn.)
Output standard:	differential or single ended
Fine gain:	12-bit DAC (via software)
Coarse gain:	3-bit DAC (via software)
Shaping time:	0.5, 1.0, 2.0 and 4.0 μs (via software)
P-Z cancell.:	12-bit DAC full scale (via software)
Output polarity:	positive or negative (via software)
Fast-Output polarity:	positive or negative (via software)
Fast-Output gain:	1x or 5x (via software)
Base-line restor.:	automatic
Power dissipation:	48W

Following several tests at the University of Naples the anode and grid of all ionization chambers are biased to given voltages depending on the IC pressure (see table 4.5). The signals of all GASTLY detectors are then processed by a series of electronic components as sketched in figure 4.17. The signals from the CHAPLIN pre-amplifiers enter the SPAM amplifier where, in order to generate the trigger, they divide into fast and amplified (10x) outputs. The Si detector signals pass through the fast output of the SPAM to then enter a constant fraction (CF, EG & G-ESN CF8000) discriminator. For the smaller and slower IC signals the amplified signal of the SPAM was used along with a single channel analyser module (SCA Ortec model 850) in spite of the greater time jitter (compared to a CF). Both SSD and IC signals arrive to a logic module (EG & G-ESN LF4000) that generates an OR signal which is used as the trigger of the acquisition system (ADC FAIR System [71]). This type of trigger guarantees the collection of all events (above an energy threshold) regardless of the pressure in the ionization chamber (i.e. an event is collected even if the IC pressure is so high that the particle does not reach the SSD or if the particle is so energetic that it does not interact with the gas in the ionization chamber).

Table 4.5: Bias applied to the grid and anode of the GASTLY IC according to the gas pressure within the IC. The last column shows the unchanged bias of the silicon detector.

IC Pressure [mbar]	**Grid [V]**	**Anode [V]**	**SSD [V]**
35	68	78	40
50	98	112	40
70	137	157	40
100	196	224	40
150	293	336	40
200	391	448	40

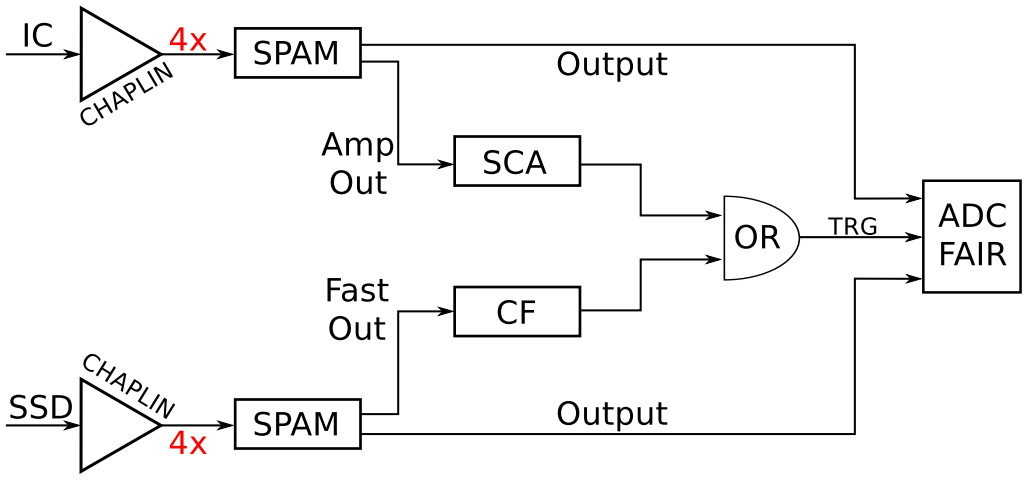

Figure 4.17: Sketch of the electronic chain used to process the GASTLY detectors signals. The IC and SSD signals used to trigger the ADC are shown (see text for further details).

4.6 Detectors Calibrations

In order to get accurate spectra the detectors used in this experiment had to be well calibrated. Since the protons emitted by the $^{12}C(^{12}C,p)^{23}Na$ reaction have enough energy to reach the silicon detectors, the ionization chamber acts only as dead layer. Thus, a calibration of the silicon detectors using proton beams was performed.
In the following sections, the silicon detectors proton calibration is presented. For completeness, the calibration of ionization chambers and silicon detectors for α particle identification is described in appendix B given that they are needed for the analysis of the $^{12}C+^{12}C$ reactions α channel.

4.6.1 SSD proton calibration

For the proton calibration of the silicon detectors, elastic scattering of protons in gold targets was exploited. Five proton beams at different energies were used: E_{lab}= 1, 2, 3, 4 and 4.9 MeV. The energies correspond to the widest proton beam energy range allowed by the accelerator.
An internal calibration for the Old configuration data was needed because during the first measurements campaign, some electronic modules had to be replaced.
In the following sections, both proton and internal calibrations for the New and Old configurations, respectively are presented.

New configuration

Using proton beams and a thin gold target, the calibration of the GASTLY detectors in the New configuration was done with an empty IC and after removing the foils (havar and mylar) to avoid energy loss uncertainties. A typical spectrum of protons from the elastic Au+p reaction can be seen in figure 4.18. Since the gold target is not thin enough to produce a Gaussian shaped peak in the detectors spectra, a step function was used in order to fit the spectrum. In this way, the deflection point of the fit marks the channel to be associated to the kinematic proton energy (calculated for the detectors central angles using CatKin [72]) of the Au+p reaction at each beam energy.

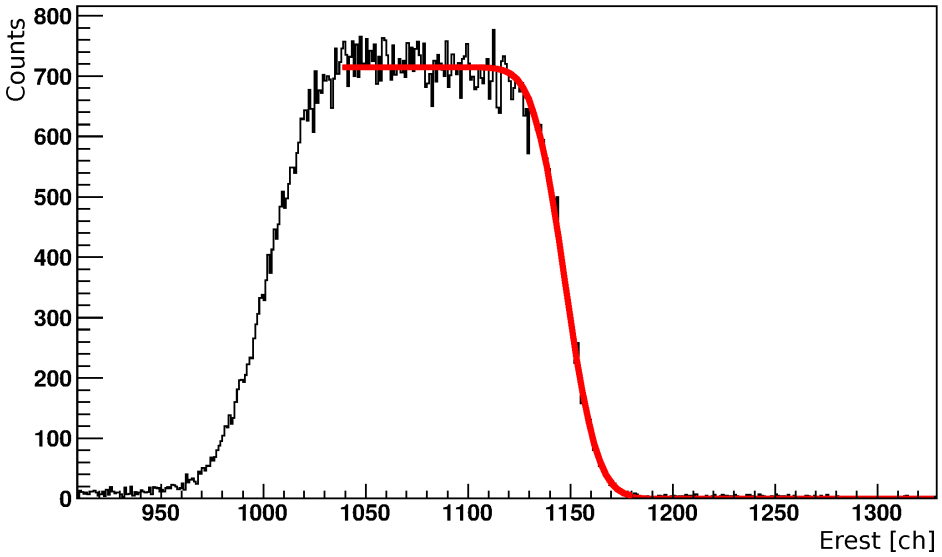

Figure 4.18: Typical Au+p scattering spectrum used for proton calibration of the GASTLY Si detectors in the New configuration. The deflection point of a step function fit (bold line) provides the channel to be associated to the kinematic proton energy of the Au+p reaction at each beam energy). This spectrum was taken using a E_{lab} = 2 MeV proton beam and the detector at the 156°UP position.

The obtained calibration functions (see figure 4.19) are:

- 156°UP: f(x) [MeV] = 0.001716 x[ch] - 0.007198
- 156°DOWN: f(x) [MeV] = 0.001594 x[ch] - 0.019995
- 143°: f(x) [MeV] = 0.001578 x[ch] - 0.000266
- 121°: f(x) [MeV] = 0.001536 x[ch] - 0.008710

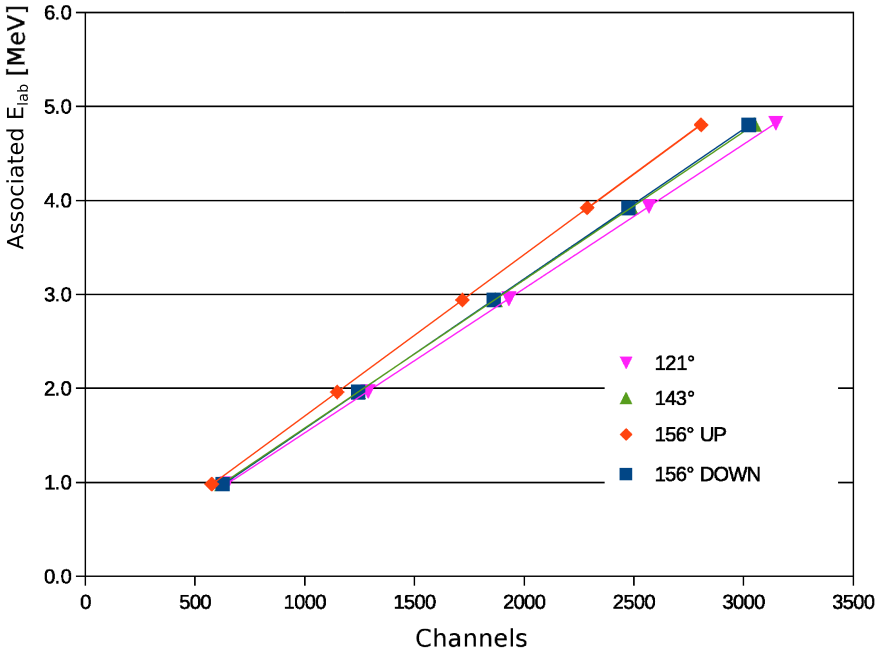

Figure 4.19: Proton calibration functions for the silicon detectors in the New configuration. This calibration was made using a proton beam with energies E_{lab}= 1.0 - 4.9 MeV impinging onto a 1 μm gold foil.

Old configuration

Even though a similar calibration with proton beams was done for the Old configuration data, an unexpected problem with some electronic modules in the first campaign of measurements obliged us to perform an internal calibration of the Erest spectra. In order to internally calibrate the silicon detectors using the $^{12}C+^{12}C$ spectra, kinematic calculations were performed (see appendix A). Figure 4.20 shows a typical proton silicon spectrum were the p_0 and p_1 peaks are clearly identifiable. The central position of these peaks (in channels) in the silicon spectra at several energies (E_{lab} = 6.25 - 8.60 MeV) was taken. Each position was associated with its corresponding Erest energy calculated. The calibration functions (see figure 4.21) are:

- 156°UP: f(x) [MeV] = 0.001529 x[ch] + 0.103619
- 156°DOWN: f(x) [MeV] = 0.001595 x[ch] + 0.178365
- 143°: f(x) [MeV] = 0.001602 x[ch] + 0.048382
- 121°: f(x) [MeV] = 0.001812 x[ch] - 0.164696

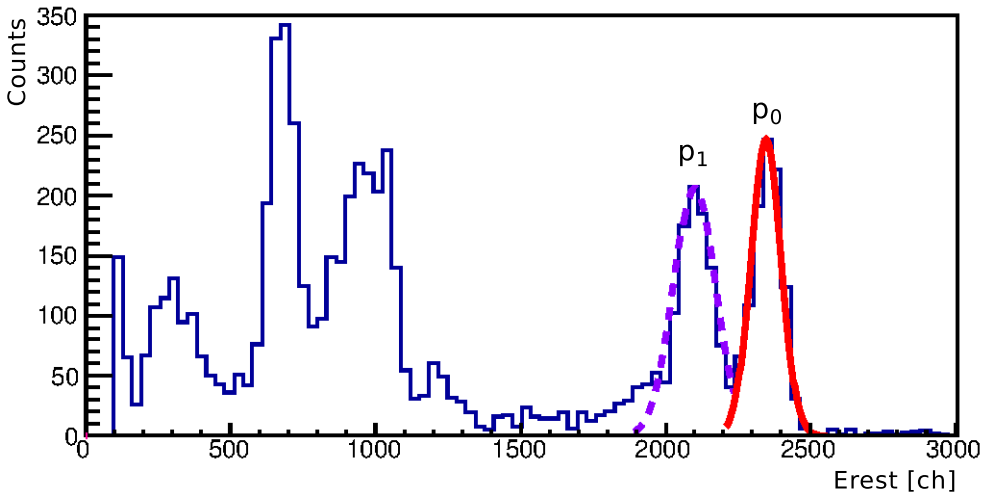

Figure 4.20: Typical proton silicon spectrum used for the detectors internal calibration. Gaussian functions were used to obtain the central peak positions of p_0 and p_1 peaks to associate to calculated Erest energies. This spectrum was obtained with the 156°UP detector at E_{lab} = 7.10 MeV.

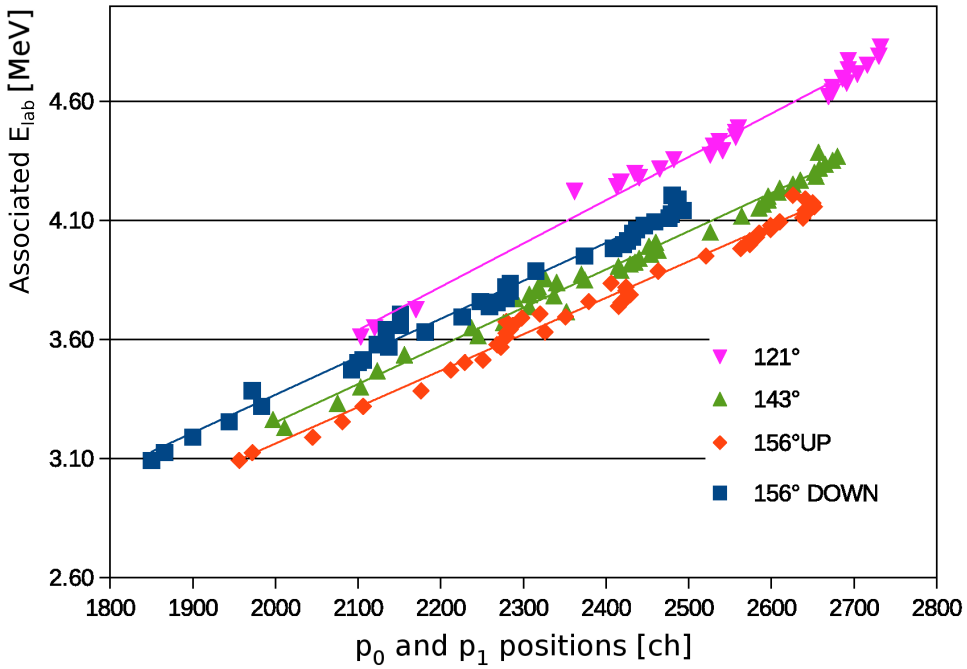

Figure 4.21: Si detectors internal calibration functions for the detection of protons in the Old configuration. This calibration was made taking the position of the p_0 and p_1 peaks of the $^{12}C+^{12}C$ spectra at several beam energies (E_{lab} = 6.25 - 8.60 MeV).

4.7 Detector efficiencies

An important parameter to know before the calculation of any measured cross section is the detector efficiency η. In this case, the GASTLY detectors geometrical efficiency (or solid angle) was measured[1] using a calibrated alpha source (3 mm diameter) placed at the target position. This source contains two isotopes: ^{241}Am (E = 5.486 MeV) and ^{239}Pu (E = 5.157 MeV). Knowing the number of detected particles N_d (taken from the detectors spectra), the runtime R_t and the alpha source activity at the time of the measurement A_α, the efficiency η can be calculated using the following equation:

$$\eta = \frac{N_d}{A_\alpha R_t}, \tag{4.1}$$

where A_α is given by:

$$A_\alpha = A_0 \exp\left[\frac{-\ln(2)}{t_{1/2}}\ t\right], \tag{4.2}$$

A_0 is the total activity of the source in 2π, $t_{1/2}$ is the half life of the source and t is the time elapsed between the date the source was produced (25/03/10) and the date the measurements were performed.
In order to calculate the solid angles subtended by the Si detectors ($\eta = \Omega/4\pi$), the gas in the ionization chambers was removed. The efficiency measurements of the ionization chambers were also performed and, for completeness, they are included in this thesis in appendix B.
Table 4.6 shows the values and results of the solid angle calculations, considering A_0 = 4076.5 Bq and $t_{1/2}$ = 8800150 days since the source is $\sim$ 98% plutonium.
It can be seen from table 4.6 that the efficiency of the detectors placed at 156° is much lower than that of the detectors at 121° and 143°. Two features contribute to this difference: 1) the difference in detector-target distance and 2) a shadowing caused by the inner pyramid, as shown in figure 4.22.

[1] Given that the η measured here depends purely on the detectors geometry, we do not need to distinguish between Old and New configurations.

Table 4.6: Values for the Si detectors efficiency measurements. The second and third columns correspond to the calculation of the alpha source activity at the moment the measurements were performed, the next two columns are the runtime and number of events of each run. The resultant efficiency and the derived solid angle are shown in the last two columns. The uncertainties in the solid angle were calculated propagating the statistical error of N_d.

Detector	**t [days]**	$\mathbf{A_\alpha}$ **[Bq]**	$\mathbf{R_t}$ **[s]**	$\mathbf{N_d}$	η_{Si}	Ω **[msr]**
121°	2084	4075.831	567	14479	0.0063	**79** ± 0.7
143°	2081	4075.832	439	11399	0.0064	**80** ± 0.7
156°UP	2086	4075.830	567	7703	0.0033	**41** ± 0.5
156°DOWN	2087	4075.830	648	8539	0.0032	**40** ± 0.4

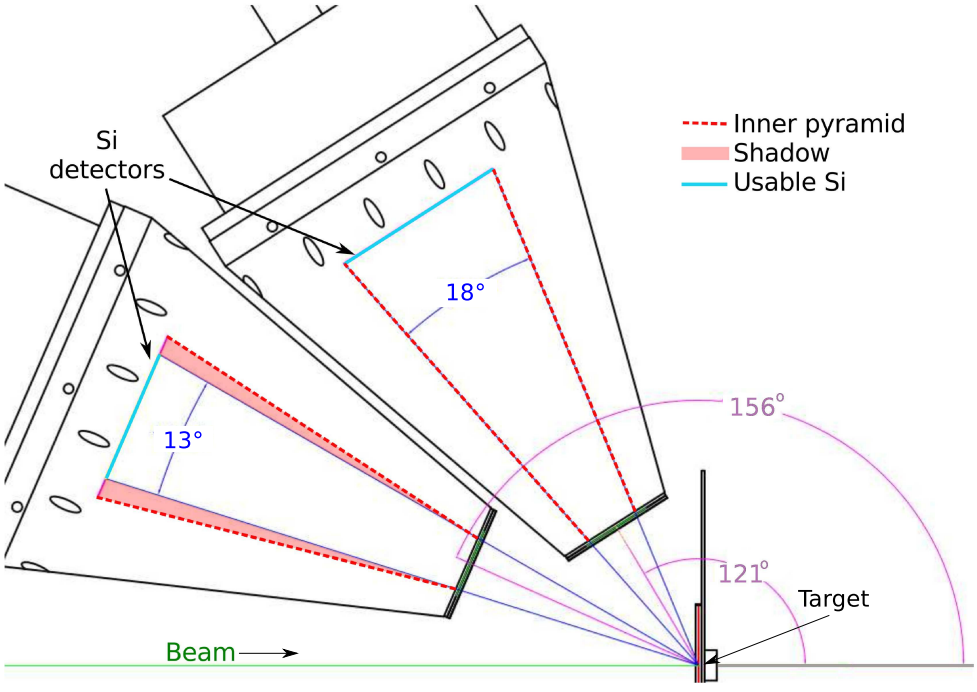

Figure 4.22: Sketch of detector's geometry for the two detectors at 156 and 121°. As shown, the entrance of the inner pyramid (dashed lines) causes a "shadow" in the Si detector at 156° due to its larger distance from the target.

Chapter 5

Carbon target behaviour under beam bombardment: reduction in deuterium contamination

As discussed in chapter 3, additionally to the extremely low cross sections and the resonant structure, the measurements at stellar energies of the $^{12}C+^{12}C$ reactions are troublesome due to natural hydrogen and deuterium contamination in the carbon targets [73]. These target contaminants hamper the measurement of the $^{12}C(^{12}C,p)^{23}Na$ reaction[1] given that the $^{12}C+^{1,2}H$ reactions cross sections are considerably higher than that of the reaction of interest. For this reason, a great effort has to be devoted to the production of targets with ultra-low $^{1,2}H$ content.

The natural content of H in carbon targets is inevitable since it is easy for light elements to be fixed between graphite layers. Thus, a single crystal graphite with a certain thickness would be ideal to avoid this problem. However, such type of crystal is impossible to obtain [74]. An alternative to single crystal graphites is the Highly Ordered Pyrolitic Graphite (HOPG), which has an extremely high degree of orientation of small graphite crystals along one direction [74, 75], and the highest 3-dimensional ordering degree [76]. These properties prevent, at least theoretically, the light elements from entering and being fixed between layers, thus reducing the hydrogen and deuterium contamination to the surface of the target. However, experiments with atomic hydrogen inside graphites have been scarce due to the complexity that detecting this impurity represents [77, 78].

Some groups have tried to reduce the H contamination in graphite targets by heating the targets up with different methods: either using resistive heating to rise the temperature of $9 - 88$ $\mu g/cm^2$ carbon foils (placed on a tantalum backing) to 1800°C [43] or heating thick (1mm) graphite targets at 400°C [39] and 700°C [44] through intense beam energy deposition. In all cases, an improvement in the target purity was observed but never quantified.

As part of this thesis work, we have attempted to quantify the beam induced background reduction in thick (1 mm) HOPG and Natural Graphite (NG,

[1]The α channel of the $^{12}C+^{12}C$ reaction is not affected by H contaminants in the targets at low energies: $p(^{12}C,\alpha)^{9}B$ (Q = -1.34); $d(^{12}C,\alpha)^{10}B$ (Q = -7.55).

99.8% purity) targets as a function of target temperature for the first time. In the following sections, a detailed description of this investigation is presented.

5.1 Beam-induced background: general considerations

For the $^{12}C+^{12}C$ reactions measurements, eight different sources of beam-induced background are in principle possible. Four can be identified as direct processes: $p(^{12}C,p)^{12}C$, $d(^{12}C,d)^{12}C$, $p(^{12}C,d)^{11}C$ and $d(^{12}C,p)^{13}C$. Since the elastic scattering reactions do not produce any protons at backward angles (as used in this work) and the $p(^{12}C,d)^{11}C$ reaction (Q= -16.497 MeV) remains closed at all energies investigated here, only $d(^{12}C,p)^{13}C$ (Q = 2.722 MeV) is relevant for this study. The four other processes can be identified as "two-step" as they are initiated by either hydrogen or deuterium contamination in the target scattered at forward angles by the beam. Their interaction with a further ^{12}C nucleus in the target could then give rise to "secondary" protons or deuterons (as depicted in figure 5.1) through either: $^{12}C(p,p)^{12}C$, $^{12}C(d,d)^{12}C$, $^{12}C(p,d)^{11}C$ or $^{12}C(d,p)^{13}C$. For the experimental conditions of the present study (see chapter 4), protons and deuterons from secondary elastic scattering are either stopped in the ΔE detector or emerge from it with very little energy and thus remain well outside the region of interest of the $^{12}C(^{12}C,p)^{23}Na$ reaction. Once again, the $^{12}C(p,d)^{11}C$ reaction remains a closed channel. Consequently, only secondary protons from the $^{12}C(d,p)^{13}C$ reaction are of concern as a source of beam-induced background. One might expect that the proton yield from this secondary process would form a continuum in the ΔE-Erest matrix because the initial step, *i.e.* the Rutherford scattering of the carbon beam on ^{2}H impurities, forms a continuum of scattered deuterium energies [42]. However, the $^{12}C(d,p)^{13}C$ reaction cross section is dominated by a resonance at E_d= 1.2 MeV [79], thus the probability for the secondary fusion reaction (intrinsically low) is only appreciable for scattered deuteron energies near the resonant value. As a result, the position of these secondary protons in the ΔE-Erest matrix (or in the individual spectra) remains essentially unchanged regardless of the ^{12}C beam energy. Eventually, for $^{12}C+^{12}C$ reactions measurements at $E_{lab} < 2$ MeV[2], the energy of scattered deuterons becomes insufficient to excite the resonance and the secondary proton yield decreases drastically [42].

[2]All the energies mentioned here and in the following chapters, will be given in the laboratory frame (and noted as E from now on), unless explicitly stated otherwise.

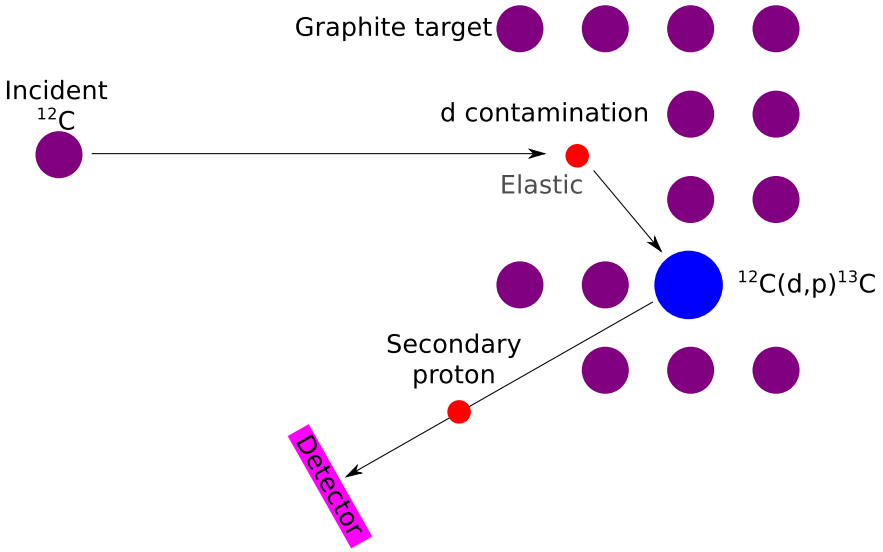

Figure 5.1: Sketch of the production of secondary protons due to deuterium contamination inside a carbon target. An incident ^{12}C nucleus impinges on a deuterium contaminant inside the target which then interacts with a ^{12}C nucleus in the target, producing a "secondary" proton.

In summary, for the experimental conditions used in this investigation (backward angles and low energies), only deuterium impurities in the target give rise to background protons, through either the direct or the "two-step" reactions $\mathrm{d}(^{12}\mathrm{C},\mathrm{p})^{13}\mathrm{C}$ and $^{12}\mathrm{C}(\mathrm{d},\mathrm{p})^{13}\mathrm{C}$, respectively. Hereafter, we refer to protons from the direct process as primary and from the "two-step" process as secondary protons.
To study the deuterium content in HOPG and NG targets, we produced E = 8.0 MeV $^{12}\mathrm{C}^{3+}$ beams with intensities of 10 - 50 μA . The choice of beam energy was dictated by a compromise between high statistics and sufficient separation between proton peaks (at large angles) from the ^{12}C fusion reactions and protons from beam-induced background on deuterium contaminants in the targets. During the beam bombardment of the targets, the QMS (chapter 4.3) was utilized to monitor the residual gas composition of the scattering chamber with the aim to asses its influence (if any) on the deuterium content of the targets. Additionally, the thermocamera was used to record the temperature of the targets at all times in order to investigate any possible relation between the target deuterium contamination and target temperature, as detailed in the following sections.

5.2 Initial tests in the small scattering chamber

During the installation of the $^{12}C+^{12}C$ beamline, the small chamber (chapter 4.3) was used to investigate the deuterium content in both HOPG and NG targets. Using a E = 8.0 MeV ^{12}C beam and a $\Delta E - E_{total}$ ($E_{total} = \Delta E + Erest$) matrix, the energy region of the $^{12}C+^{2}H$ secondary protons was identified (see figure 5.2). This type of matrix was used in an attempt to separate the secondary proton region from the $^{12}C(^{12}C,p_2)$ reaction group. However, the counting rate of these secondary protons is so low that a deuterium contamination study was impossible.
Given that using a ΔE detector increases the uncertainties due to energy loss calculations, we decided to use the Erest spectra to minimise said uncertainties. As can be seen in figure 5.3, proton groups from the $^{12}C+^{12}C$ reaction could be identified in the Erest spectra. However, the low counting rate of the secondary protons from the $^{12}C+^{2}H$ reaction did not allow us to identify a peak. Similarly, the low statistics along with the energy position of the p_7 peak (at 121°), made the identification of the $^{12}C+^{2}H$ primary proton peak impossible as well.
Even though the data taken with the small chamber proved inconclusive to a measurement of the deuterium content in the targets, these tests allowed us to evaluate other components of the set-up (QMS, nitrogen "aquarium" and thermocamera) later used for the measurements in the larger scattering chamber with the GASTLY array.

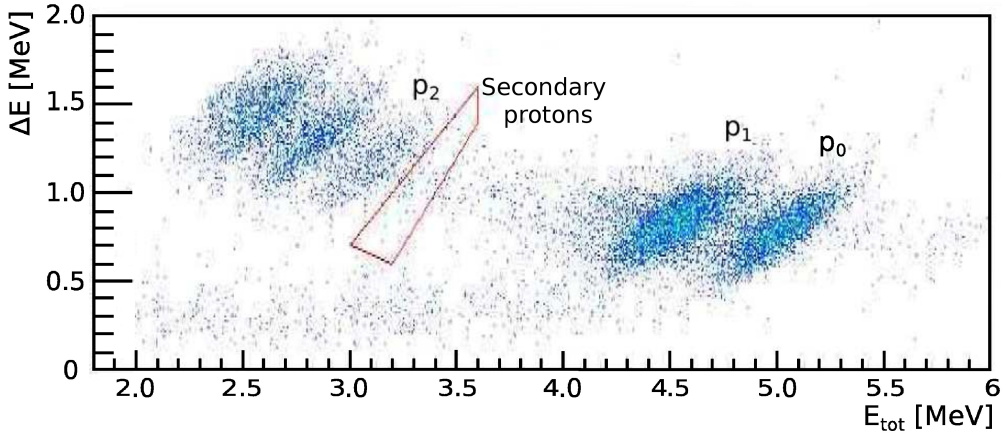

Figure 5.2: Typical $\Delta E - E_{total}$ matrix taken with the Si telescope using an E= 8.0 MeV $^{12}C^{3+}$ beam. The region of the expected secondary protons is marked.

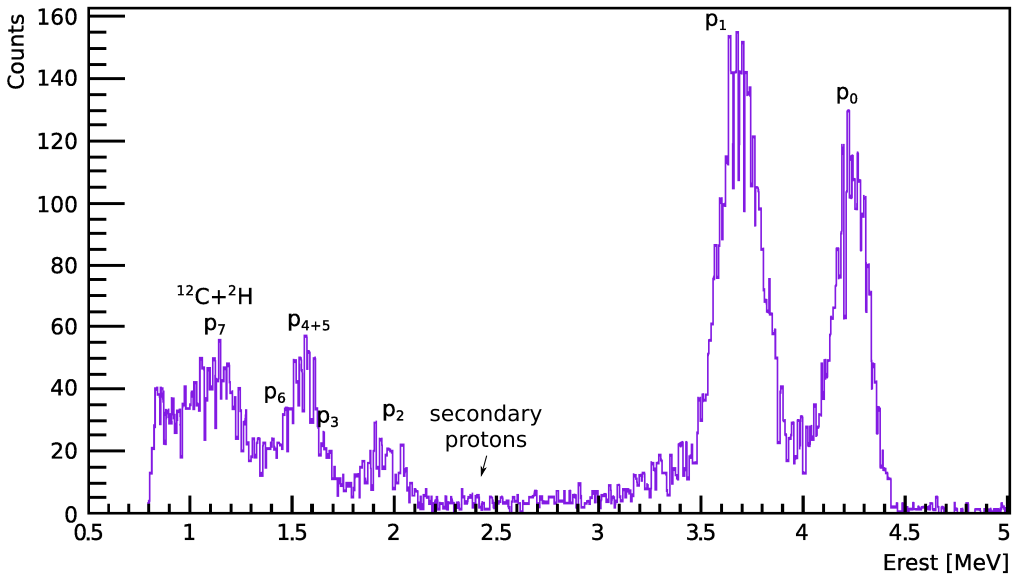

Figure 5.3: Typical Erest spectrum from the Si telescope using an E= 8.0 MeV $^{12}C^{3+}$ beam. It is clear that the ^{2}H content of the target cannot be quantified using this spectrum due to poor statistics (secondary protons) and overlap between primary protons and contributions from the $^{12}C(^{12}C,p_7)^{23}Na^*$ reaction (see text for further details).

Residual gas in the chamber

To control the residual gas of the chamber and, in particular, reduce the hydrogen fraction, the chamber was enclosed within a nitrogen environment ("aquarium") at atmospheric pressure so as to avoid leak of light mass elements into the chamber. The residual gas composition was monitored using the QMS (chapter 4.3) with and without enclosing the chamber in the "aquarium". As can be seen in figure 5.4, the H isotopes were reduced by nearly 50% with the use of the "aquarium".
This test was then repeated with the GASTLY scattering chamber and consistent results were obtained (section 5.3.1).

Temperature attenuation

Extensive testing showed that the thermocamera measurements change with the Ge window at high temperatures (chapter 4.3). These changes were well calibrated (calibration certificate No. SED04024 by FLIR) and taken into account during the analysis. The attenuation obtained with the thermocamera

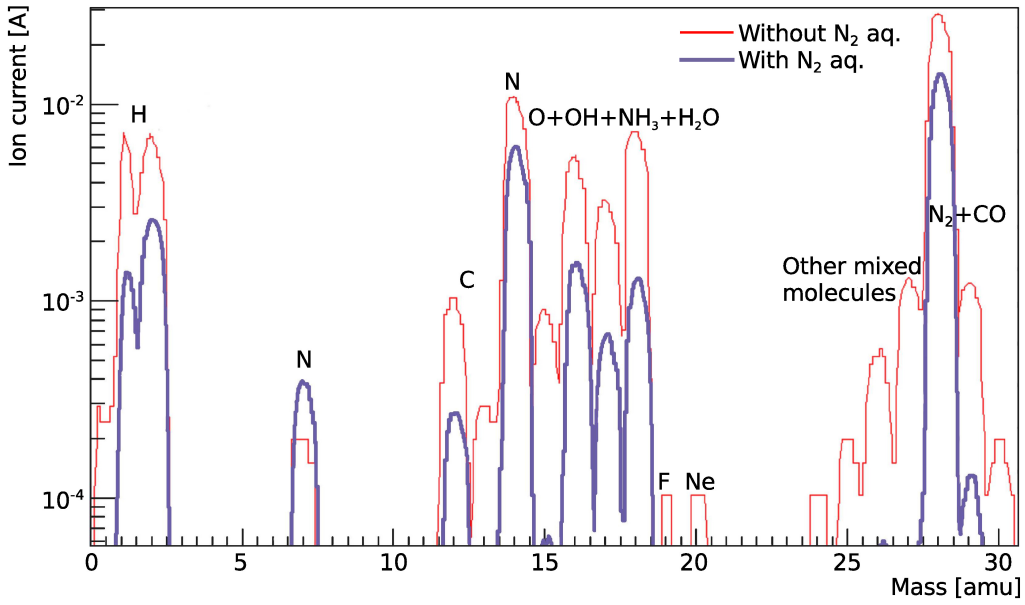

Figure 5.4: Pressure-normalized spectra from residual gas composition in the chamber with (bold line) and without (thin line) nitrogen "aquarium". A clear reduction of H and other elements can be seen after installing the "aquarium" as well as an expected increase of nitrogen.

looking through the Ge window can be seen in figure 5.5, where the measurements performed by FLIR are shown. Using a black body the temperature with and without Ge window was measured. From these data, I obtained an attenuation function by plotting the temperature measured by the thermocamera using the Ge window as a function of the temperature measured without the Ge window (called "real temperature"), as shown in figure 5.6. The obtained attenuation function is the following:

$$\text{f(x)[°C]} = 1.108643 \text{ x } -2.118453,$$

where x is the measured temperature in °C through the Ge window.

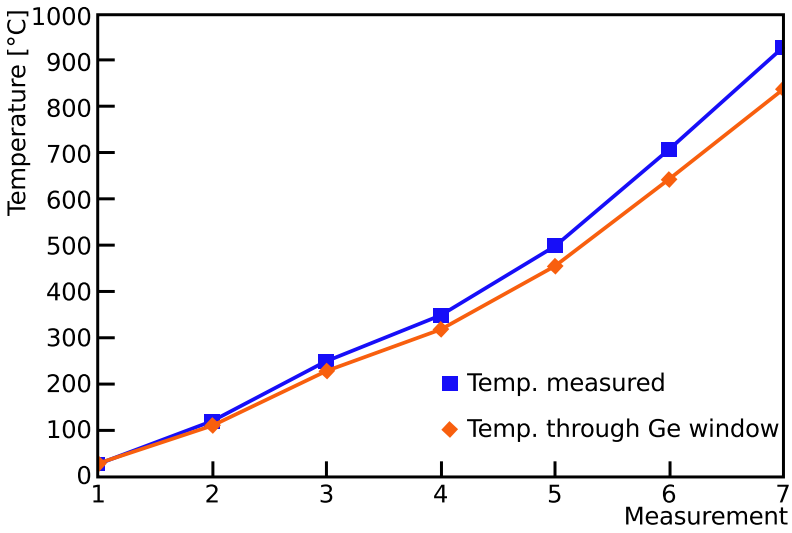

Figure 5.5: Attenuation of temperature due to the Ge window. Measured temperatures by the thermocamera with (diamonds) and without (squares) the Ge window are shown.

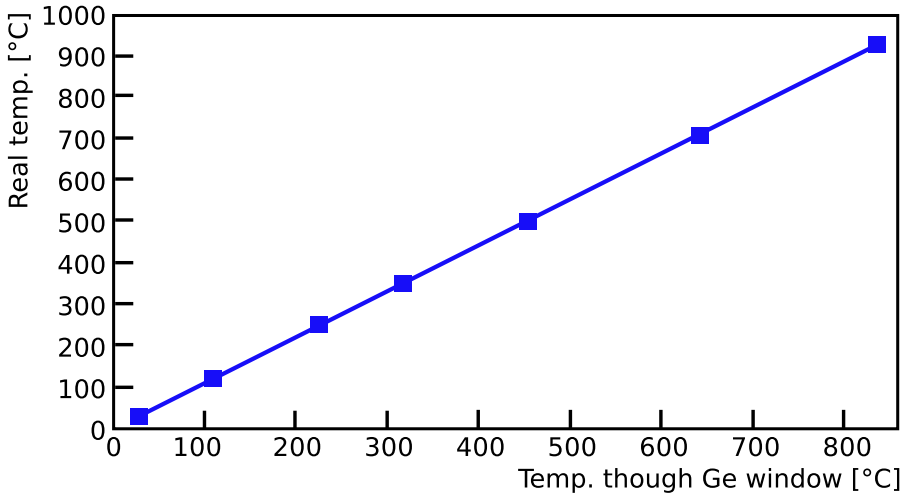

Figure 5.6: Real temperature as a function of measured temperature through the Ge window (results obtained using the data shown in figure 5.5).

5.3 Deuterium reduction investigation

Once the installation of the 20º beamline was completed, the deuterium contamination study was repeated using the GASTLY detectors in the Old configuration (see table 4.1). $^{12}C^{+3}$ beams of E = 8.0 MeV were used along with the thermocamera for target temperature measurements and the QMS to monitor the residual gas composition of the chamber. The pressure in the ionization chambers was set to 35, 50 and 70 mbar. As can be seen in figure 5.7, the expected proton energies of the p_0 and p_7 groups are high enough to reach the silicon detectors. Since the SSD resolution (∼1%) is superior compared to the IC (∼4%) [66], it was decided to use only the Erest spectra rather than the E_{total} spectra for the analysis of the proton channel, in order to have a clearer identification of the proton groups and minimize uncertainties associated with energy loss calculations. However, a ΔE-Erest matrix was used to build the proton Erest spectra so as to discriminate all α particles effectively (see chapter 6 for details).

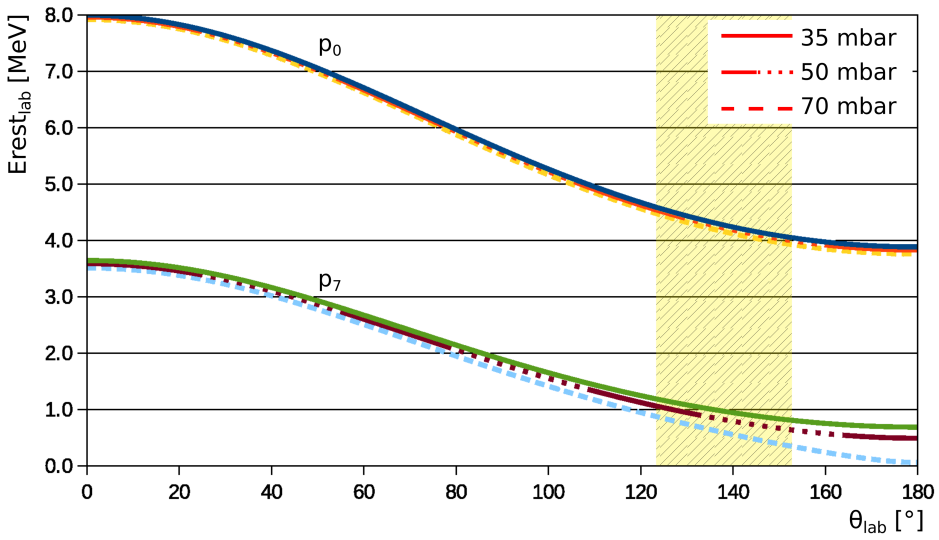

Figure 5.7: Kinematic Erest curves of the $^{12}C(^{12}C,p_{0,7})^{23}Na$ reaction at a beam energy E_{lab} = 8.0 MeV and different pressures in the IC. The shaded area represents the angular coverage of the GASTLY detectors.

Since the initial tests in the small chamber demonstrated that the identification of the $^{12}C+^{2}H$ secondary protons is inaccessible due to extremely small counting rates, we focused on the primary protons peak. Both HOPG and NG targets were analysed and the composition of the residual gas was studied with and without the N_2 "aquarium". All Erest spectra were properly

background subtracted (see chapter 6.1) and each run was divided in time intervals according to target temperature behaviour during the run (section 5.3.2). The contribution of the $^{12}C(^{12}C,p_7)$ peak to the $^{12}C+^{2}H$ reaction peak was also taken into account, given their partial kinematic overlap. Finally, target deuterium content plots as a function of target temperature were produced. This procedure is explained in detail in the following sections.

5.3.1 Influence of the residual gas on the purity of the target

The QMS measurements performed in the small chamber demonstrated a reduction in the H isotopes present in the residual gas of the chamber of nearly 50% when surrounding the scattering chamber by a nitrogen atmosphere ("aquarium"). Thus, a plexiglass structure was also built around the GASTLY scattering chamber (figure 4.6). A QMS spectrum with and without the use of the "aquarium" is shown in figure 5.8. It can be seen that, given the dimensions of the chamber, the nitrogen atmosphere does not make an immediate difference in the rest gas composition, but it takes about 15 minutes before it produces noticeable effects. Subsequently, the same $\sim$50% decrease in hydrogen isotopes noticed in the small chamber test could be also observed. Following this result, it was decided to study the deuterium content of the HOPG and NG targets in four different scenarios: 1) HOPG target without the "aquarium", 2) HOPG target with the "aquarium", 3) NG target without the "aquarium" and 4) NG target with the "aquarium". Unfortunately, the data taken with the NG target without the "aquarium" could not be analysed due to poor statistics and further runs were not possible because of time constraints.

5.3.2 Temperature as a criterion to select data sets

The runs used to analyse the deuterium content of the targets were chosen considering the temperature behaviour of the target during the beam bombardment: increasing, decreasing or staying constant over time. The variation of target temperature was done by changing the beam intensities (using collimating slits located upstream the accelerator's ESA2) and opening or closing the water-cooling system of the target ladder.
Four runs with different temperature behaviours were chosen as summarized in table 5.1, where the scenario, temperature behaviour over time and range of the measured temperatures are shown.

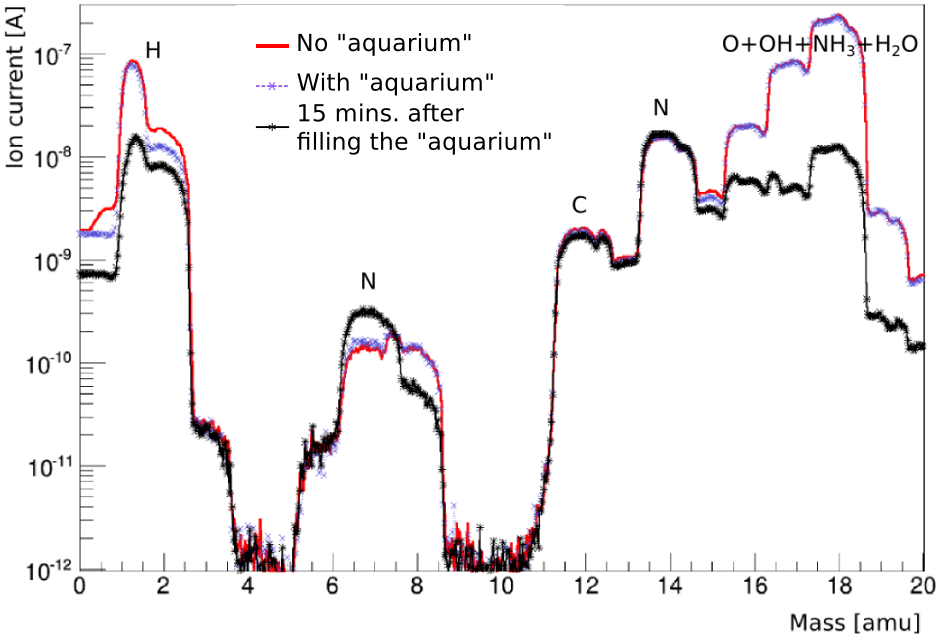

Figure 5.8: Residual gas spectrum in the GASTLY chamber. Even if not immediately, the N_2 "aquarium" changes the rest gas composition inside the chamber. QMS spectra are shown when the "aquarium" was not filled (continuous line), right after filling it (x-dotted line), and 15 minutes after filling (star-continuous line).

Table 5.1: Runs chosen to analyse the deuterium content of the targets.

Scenario	**Temp. behaviour**	**Temp. rage**	**Name**
HOPG target no "aquarium"	Continuously decreasing over time	(1100 - 200)°C	**HOPG no aq.**
HOPG target with "aquarium"	Constant	900°C	**HOPG aq. 1**
	Constant	1000°C	**HOPG aq. 2**
NG target with "aquarium"	Continuously increasing over time	(400 - 800)°C	**NG aq.**

To understand if there is a relation between the target temperature and its deuterium contamination, the runs were divided in time intervals according to the target temperature behaviour. The size of each interval was chosen so as to guarantee a maximum change in temperature of no more than 150°C. Intervals where the temperature changes were drastic (normally due to an abrupt absence of the beam for a short period of time) were discarded. An example of these divisions can be seen in figure 5.9 which shows the time intervals for the HOPG no aq. run. Different time intervals were chosen in this run (300 and 150 s); the intervals in white correspond to the discarded data (because of abrupt temperature changes) while the shaded intervals were the ones used in the analysis.

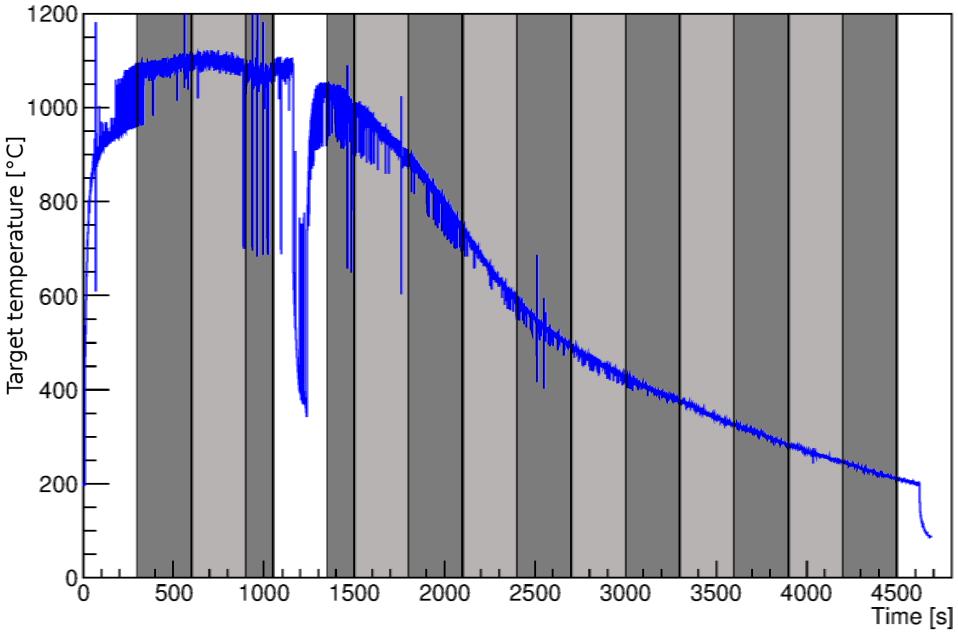

Figure 5.9: Target temperature profile over time for a run taken with an HOPG target and no "aquarium" at a beam energy E = 8.0 MeV. The excluded time intervals are shown in white, while the grey tones correspond to intervals used in the analysis.

5.3.3 The p_7 contribution

All spectra analysed for the targets deuterium content study are shown in figures 5.10 - 5.12 where all the proton groups peaks are identified and their kinematic broadening is shown in bands of different tones[3]. Note that the proton groups of the $^{12}C+^{12}C$ reactions are well separated, and thus can be easily identified in both 156° detectors spectra due to their small angular range (13°, see chapter 4.1). On the other hand, the detectors at 121° and 143° cover a larger angular range (19°) and thus the separation between different proton peaks becomes less clear.
A difference should be noted in the proton spectra of both detectors at 156° at low energies (figure 5.12). The reason for this difference is that the threshold of the 156°DOWN detector was set higher than it should have been, thus cutting out some low energy protons.
We can also observe that the protons from the $^{12}C+^{12}C$ p_7 group, contribute to the $^{12}C+^{2}H$ primary protons peak. Also, given the larger angular detection range of the 121° and 143° detectors, the $^{12}C+^{2}H$ peak has not only the contribution of the p_7 peak, but also the p_6 group. It is important to take these contributions into account given that they can alter the results of the targets deuterium content study.

[3]The detector resolution is not included in the size of the bands.

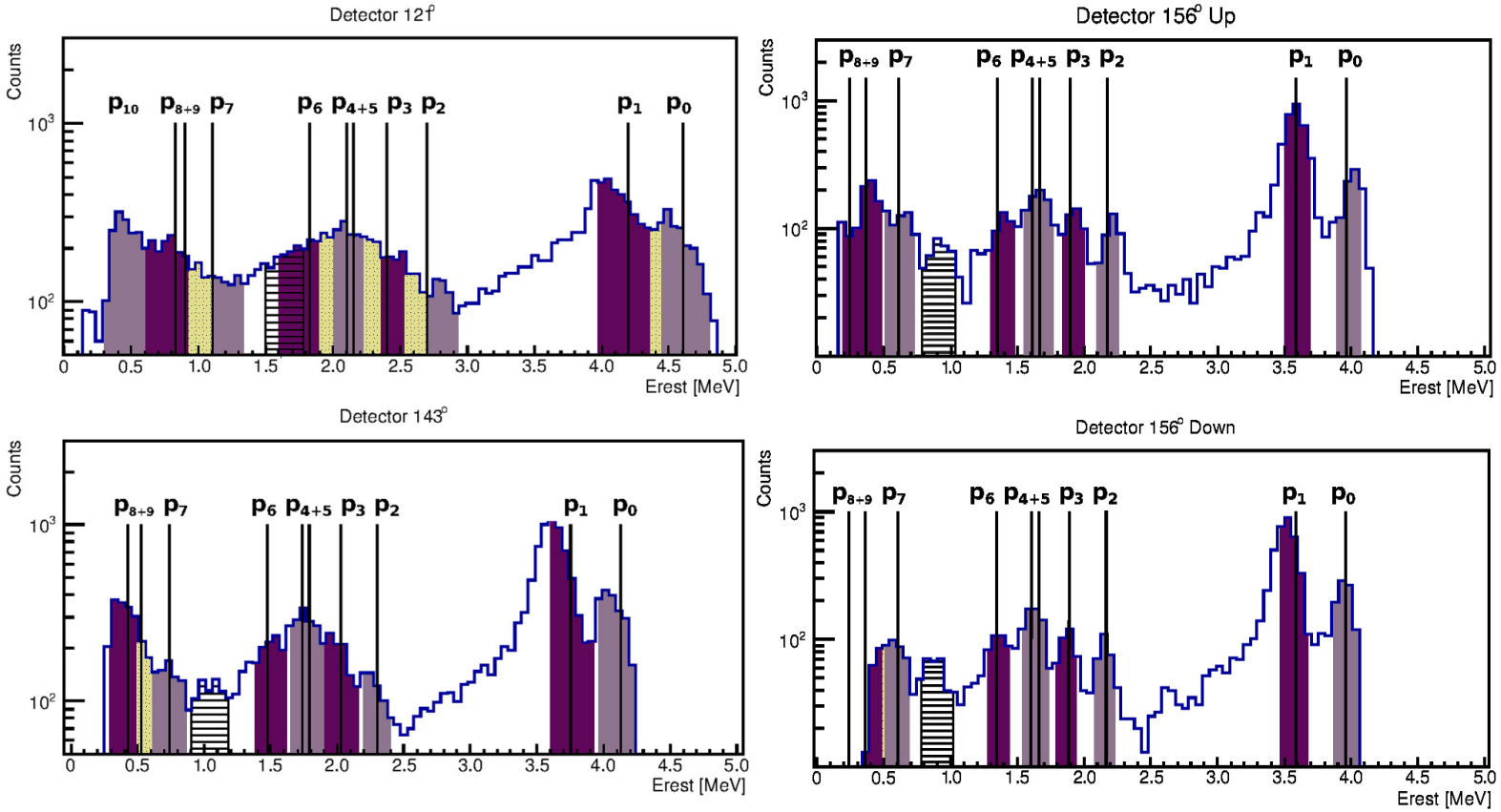

Figure 5.10: Erest spectra for the run taken with the **HOPG target with the "aquarium" (IC pressure = 50 mbar)**. The shaded bands represent the kinematic broadening of each peak but do not include the detector resolution. The clearer shaded dotted area (where present) represents the overlap in kinematic broadening of adjacent peaks. The dashed region identifies the primary protons from the ^{12}C+^{2}H reaction.

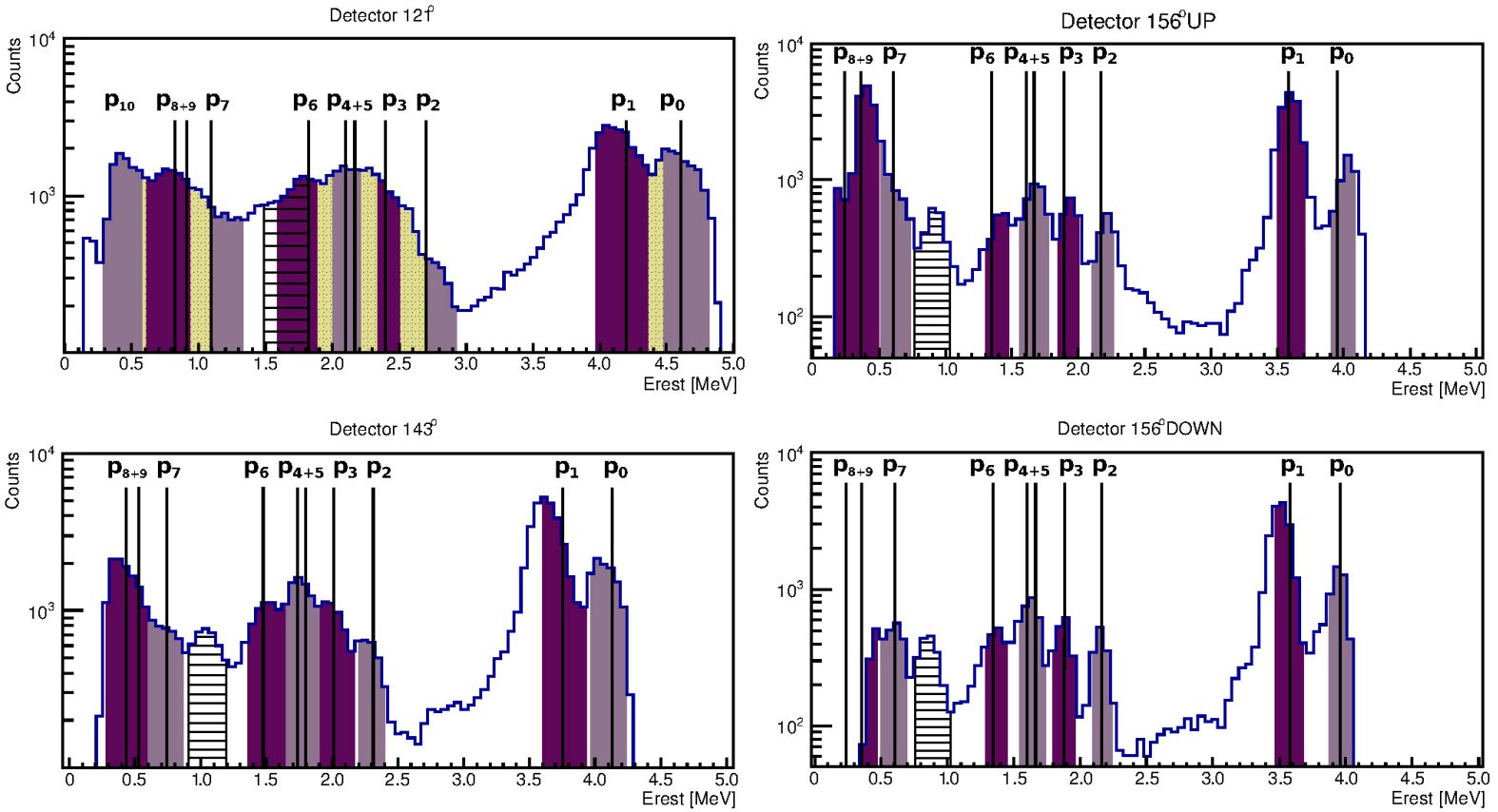

Figure 5.11: Erest spectra for the run taken with the **NG target with the "aquarium" (IC pressure = 50 mbar)**. The shaded bands represent the kinematic broadening of each peak but do not include the detector resolution. The clearer shaded dotted area (where present) represents the overlap in kinematic broadening of adjacent peaks. The dashed region identifies the primary protons from the ^{12}C+^{2}H reaction.

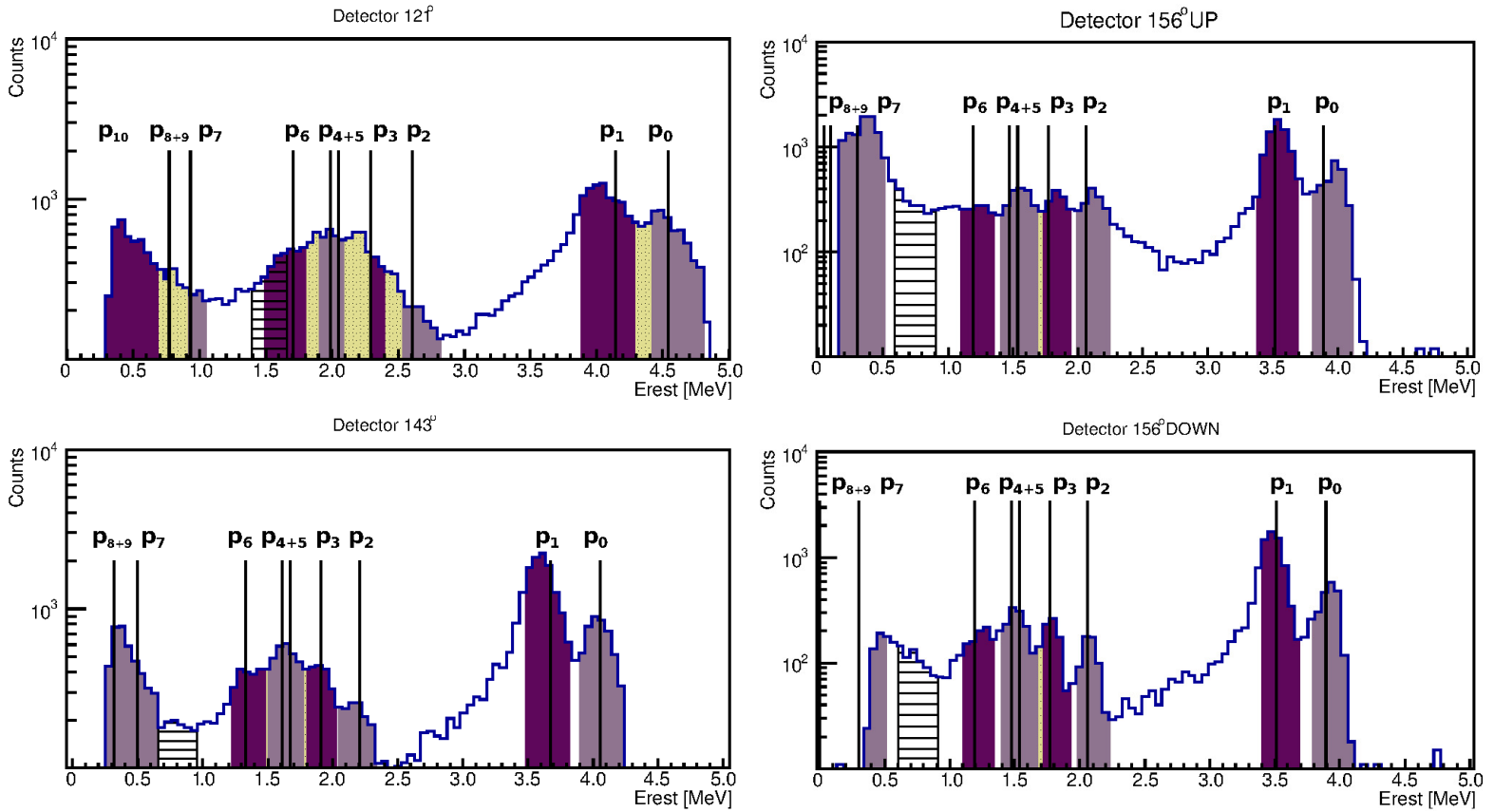

Figure 5.12: Erest spectra for the run taken with the **HOPG target without the "aquarium" (IC pressure = 70 mbar)**. The shaded bands represent the kinematic broadening of each peak but do not include the detector resolution. The clearer shaded dotted area (where present) represents the overlap in kinematic broadening of adjacent peaks. The dashed region identifies the primary protons from the ^{12}C+^{2}H reaction.

Unfortunately, the p_6 peak contribution to the 121° and 143° detectors cannot be subtracted because the $^{12}C+^{12}C$ p_6 peak heavily overlaps with other $^{12}C+^{12}C$ proton groups at all energies. On the other hand, the contribution of the p_7 peak to the primary proton group of the $^{12}C+^{2}H$ reaction can be estimated using a E = 7.6 MeV ^{12}C beam. At this energy, the p_7 peak can be separated from the $^{12}C+^{2}H$ primary protons peak (see figure 5.13), whilst maintaining a sufficient counting rate.
Using the spectra at E = 7.6 MeV, the p_7 peak can be integrated to then estimate its contribution to the $^{12}C+^{2}H$ primary protons peak for the runs at E = 8.0 MeV. To achieve this, the number of events in the p_7 peak at E= 7.6 MeV has to be "extrapolated" to the E = 8.0 MeV spectra.

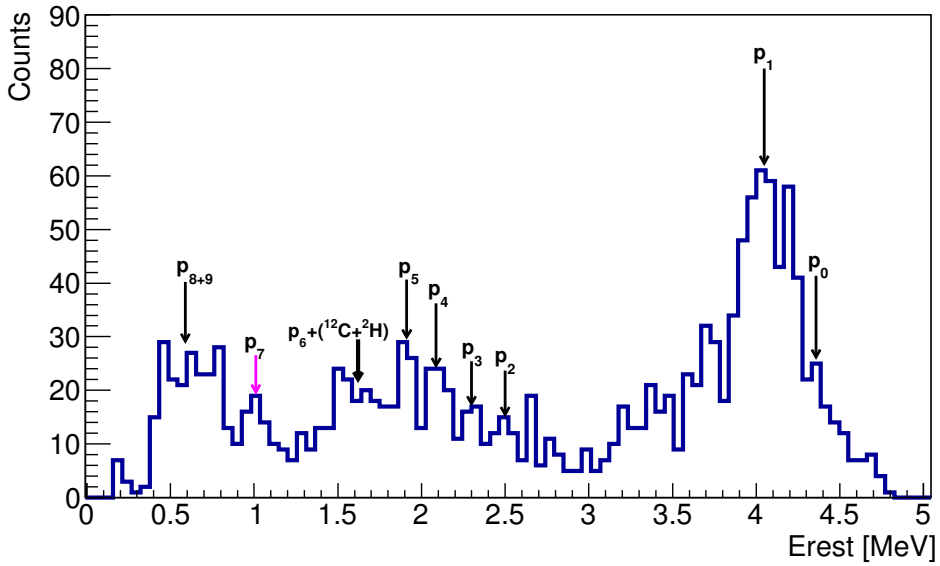

Figure 5.13: Typical GASTLY spectrum using a E= 7.6 MeV ^{12}C beam and the 156°UP detector. The IC pressure used was 35 mbar and the HOPG target.

To perform this calculation a constant energy dependence of the $^{12}C(^{12}C,p)$ reaction $\tilde{S}$-factor between E = 7.6 - 8.0 MeV was assumed on the basis of the work performed by Becker *et al.* [80]. They measured the $^{12}C+^{12}C$ reactions cross section and plot the $\tilde{S}$-factor over a wide energy region as shown in figure 5.14. It can be seen that in the region between 7.6 and 8.0 MeV, the $\tilde{S}$-factor associated to p_7 is nearly flat. However, a constant $\tilde{S}$-factor does not imply a constant cross section, thus the calculation of the p_7 peak from E = 7.6 MeV to E = 8.0 MeV can be made taking the sum of the p_0 and p_1 peaks (which are very clear in all 8.0 and 7.6 MeV spectra) and assuming

constant ratios: $\frac{p_7}{p_{0+1}}(8.0) = \frac{p_7}{p_{0+1}}(7.6)$. Knowing p_7 (in counts/C) at E = 7.6 MeV and p_{0+1} (in counts/C) at both energies, we can use the following relation:

$$p_7(8) = \frac{p_7}{p_{0+1}}(7.6\text{MeV})\ p_{0+1}(8.0\text{MeV}) \tag{5.1}$$

The p_{0+1} number of events of each run at E = 8.0 MeV should be charged-normalized in order to obtain the p_7 counting rate in counts/C. In table 5.2, all the extrapolated p_7 number of events to the E = 8.0 MeV runs are given as well as the accumulated charge Q of each run.

Table 5.2: Results of the inferred p_7 integral to the E = 8.0 MeV spectra assuming a constant energy dependence of the $^{12}C+^{12}C$ reaction $\tilde{S}$-factor and using equation 5.1. The total accumulated charge Q of each run is also provided.

Detector	**Run Name**	**Q** [C]	**Measured p_7/p_{0+1} (7.6)**	**Measured $p_{0+1}(8)$** [counts]	**Calculated $p_7(8)$** [counts/C]
121°	HOPG no aq.	$5.95\text{x}10^{-2}$	$3.80\text{x}10^{-3}$	$2.29\text{x}10^{5}$	$1.46\text{x}10^{4}$
	HOPG aq. 1	$3.06\text{x}10^{-2}$	$3.80\text{x}10^{-3}$	$2.19\text{x}10^{5}$	$2.71\text{x}10^{4}$
	HOPG aq. 2	$1.26\text{x}10^{-1}$	$3.80\text{x}10^{-3}$	$3.70\text{x}10^{6}$	$1.12\text{x}10^{5}$
	NG aq.	$1.36\text{x}10^{-1}$	$3.80\text{x}10^{-3}$	$5.69\text{x}10^{6}$	$1.59\text{x}10^{5}$
143°	HOPG no aq.	$5.95\text{x}10^{-2}$	$5.45\text{x}10^{-3}$	$7.98\text{x}10^{4}$	$7.31\text{x}10^{3}$
	HOPG aq. 1	$3.06\text{x}10^{-2}$	$5.45\text{x}10^{-3}$	$3.86\text{x}10^{4}$	$6.87\text{x}10^{3}$
	HOPG aq. 2	$1.26\text{x}10^{-1}$	$5.45\text{x}10^{-3}$	$2.52\text{x}10^{5}$	$1.09\text{x}10^{4}$
	NG aq.	$1.36\text{x}10^{-1}$	$5.45\text{x}10^{-3}$	$4.66\text{x}10^{5}$	$1.86\text{x}10^{4}$
156°UP	HOPG no aq.	$5.95\text{x}10^{-2}$	$4.03\text{x}10^{-3}$	$5.42\text{x}10^{4}$	$3.67\text{x}10^{3}$
	HOPG aq. 1	$3.06\text{x}10^{-2}$	$4.03\text{x}10^{-3}$	$4.47\text{x}10^{4}$	$5.89\text{x}10^{3}$
	HOPG aq. 2	$1.26\text{x}10^{-1}$	$4.03\text{x}10^{-3}$	$2.49\text{x}10^{5}$	$7.98\text{x}10^{3}$
	NG aq.	$1.36\text{x}10^{-1}$	$4.03\text{x}10^{-3}$	$3.56\text{x}10^{5}$	$1.06\text{x}10^{4}$
156°DOWN	HOPG no aq.	$5.95\text{x}10^{-2}$	$6.69\text{x}10^{-3}$	$6.14\text{x}10^{3}$	$6.90\text{x}10^{2}$
	HOPG aq. 1	$3.06\text{x}10^{-2}$	$6.69\text{x}10^{-3}$	$5.70\text{x}10^{3}$	$1.25\text{x}10^{3}$
	HOPG aq. 2	$1.26\text{x}10^{-1}$	$6.69\text{x}10^{-3}$	$3.78\text{x}10^{4}$	$2.01\text{x}10^{3}$
	NG aq.	$1.36\text{x}10^{-1}$	$6.69\text{x}10^{-3}$	$7.37\text{x}10^{4}$	$3.62\text{x}10^{3}$

The $p_7(8)$ contribution can now be subtracted from the $^{12}C+^{2}H$ primary protons peak integral as discussed in the following section.

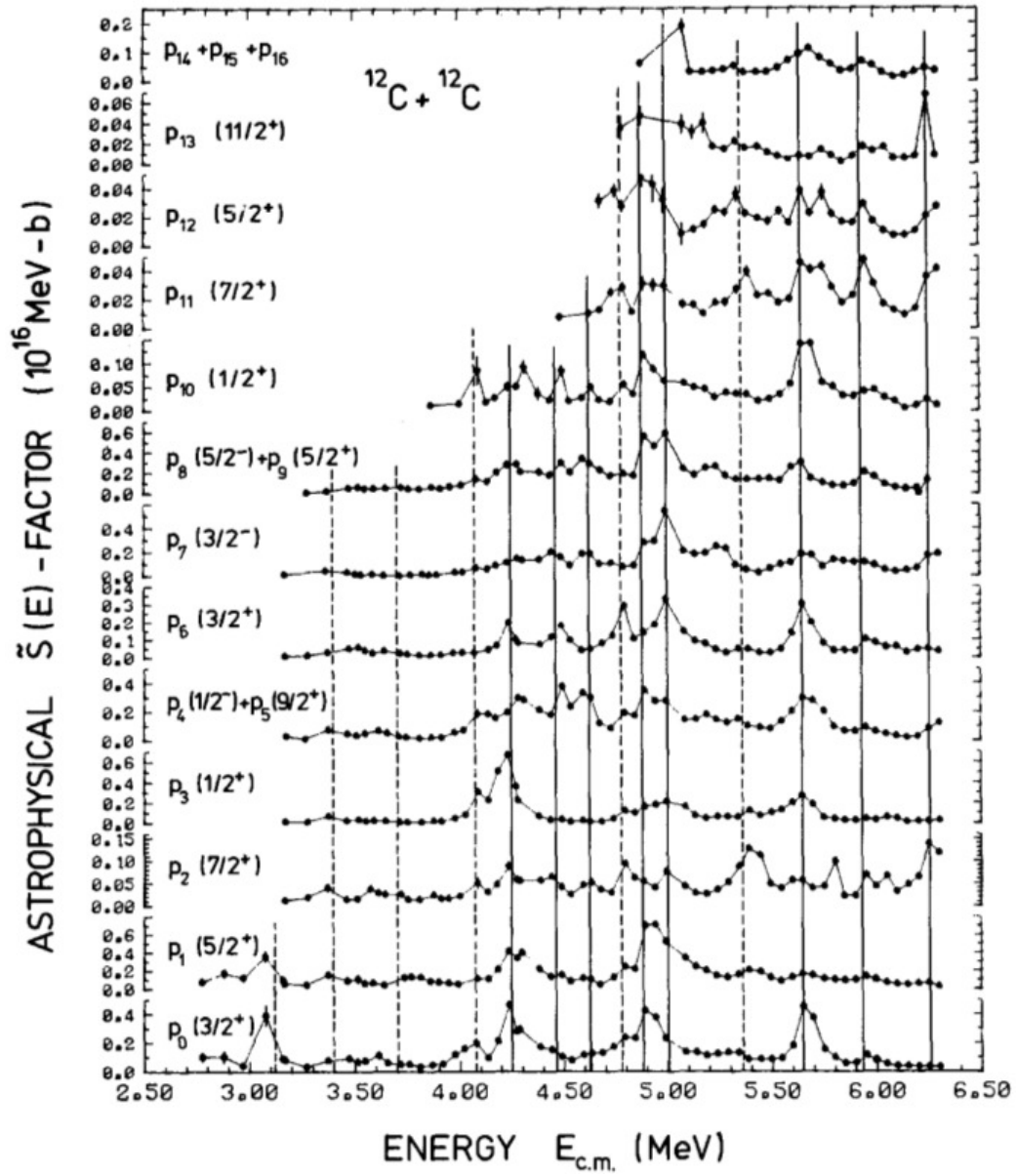

Figure 5.14: Astrophysical S̃-factor as a function of centre of mass energy for different proton groups from the ^{12}C(^{12}C, p)^{23}Na reaction [80].

5.3.4 Deuterium content changes as a function of target temperature

Having selected the data sets for the analysis, the time intervals to be used in each run and estimated the contribution of the $^{12}C(^{12}C, p_7)^{23}Na^*$ reaction, the number of events in the $^{12}C+^{2}H$ region of interest can be obtained by integrating the primary protons peak and subtracting the extrapolated $p_7(8)$ contribution.
Since each run is divided in the time intervals previously chosen, the median temperature of each interval is taken and the quantiles technique [81] is used to estimate the uncertainty in the target temperature. The charge was integrated in every interval (Q_{slice}) and used later to normalize the integral of the $^{12}C+^{2}H$ peak (p_d). The p_7 yield (counts/C) was multiplied by the total accumulated charge Q_{slice} over the time of each interval and subtracted from the counts in the $^{12}C+^{2}H$ primary protons peak. This result was normalized by Q_{slice} to obtain the deuterium primary proton counting rate (as a proxy for the targets deuterium content) [counts/C] as:

$$D = \frac{p_d - p_7\ Q_{slice}}{Q_{slice}} \tag{5.2}$$

The uncertainty on D was calculated taking into account the statistical errors of the primary protons and p_7 peaks number of events:

$$\sqrt{\delta p_d^2 + \delta p_7^2}, \tag{5.3}$$

where:

$$\delta p_d = \sqrt{\left(\frac{\sqrt{p_d}}{Q_{slice}}\right)^2 + \left(\frac{\delta Q * p_d}{Q_{slice}}\right)^2} \tag{5.4}$$

$$\delta p_7 = \sqrt{\left(\frac{\sqrt{p_7}}{Q_{slice}}\right)^2 + \left(\frac{\delta Q * p_7}{Q_{slice}}\right)^2} \tag{5.5}$$

The error in the charge δQ is given by the current integrator used in the experiment and it is less than 1%, depending on the reading settings used at the time of the experiment [82].
The deuterium content results after subtracting the calculated contribution of the $^{12}C(^{12}C,p_7)^{23}Na^*$ reaction are summarized in table D.1. In the following section, the plots of these results are shown and discussed in detail.

5.3.5 Reduction in deuterium content results

Figures 5.15 and 5.16 show the results of all four GASTLY detectors for the different cases studied: HOPG target with and without the use of the "aquarium" and natural graphite target using the "aquarium".
Considering the two detectors at 156º, one should expect the same results using one detector or the other, however, as can be seen in figure 5.16, this is not the case for one of the data sets: the HOPG target without the "aquarium" (closed circles in the figure). This difference is due to the high threshold used for the 156º DOWN detector (section 5.3.3). Such threshold cut out most of the p_7 peak, and thus its contribution to the $^{12}C+^{2}H$ region, resulting in an underestimated integral of the ^{2}H primary protons peak since the subtracted p_7 contribution takes into account the complete p_7 peak. Nonetheless, this is not a problem with the other analysed spectra since at 50 mbar, the p_7 peak can be safely accounted for. Given these circumstances, the "HOPG no aq." data set taken with the 156ºDOWN detector should not be considered. The other two data sets, however, are consistent between both 156º detectors, as expected.
All data sets taken with the 121º and 143º detectors are consistent with each other. However, the ^{2}H content measured by these detectors is higher than the one measured by the detectors at 156º. The reason for this discrepancy may be due to the contribution of the p_6 peak into the deuterium primary peak of the 121º and 143º detectors spectra (section 5.3.3).
In all sets considered, the target temperature seems to influence the deuterium contamination in the target. In addition, looking at the data from detectors 121º, 143º and 156ºUP the nitrogen "aquarium" seems to have a real influence on the deuterium contamination of the HOPG target, reducing the deuterium content of the targets to about half its original value in the 800ºC to 1100ºC region. Unfortunately, due to time constraints, the study at lower temperatures could not be performed.
Two data points with large x-error bars can be noted in figures 5.15 and 5.16. These points correspond to two time intervals where the target temperature was very unstable, causing such large uncertainties (see figure 5.9, points correspond to the first two time intervals after the excluded white region at about 1000 s).

5.3.6 Fitting procedure

In order to get a quantitative result of the reduction in deuterium contamination of the targets, power-law functions ($Ax^{B}+C$) were fitted to the data (evidently, the "HOPG aq." data set cannot be fitted, since it consists of

only two data points). Some detectors data sets were summed up to then fix the A and B parameters to perform a global fit leaving only C free. For the "HOPG no aq." case, the 156°DOWN detector data were discarded (as discussed previously); the data from the 143 and 121° detectors were summed and since the results of the detector at 156°UP are different from the others, all parameters to fit this detector were left free. For the "NG aq." data set, all data points were summed and a global fit was performed. The results of these fittings are summarized in table 5.3. The uncertainties in the deuterium counting rate results (counts/C) were on average about 5% (see table D.1). However, they were inflated by an additional ∼3% in the fitting procedure so as to make the fit $\chi^2 = 1$.
The reduction in deuterium content was computed for a target temperature range of 200°C to 1200°C. Numerical values are given in table 5.4.

Table 5.3: Fit parameters of the power-law function used to obtain the decrease in deuterium content for HOPG and NG targets. Some parameters were fixed in some cases in order to get a global fit (see text for details).

	Parameter A [counts °C/C]	**Parameter B**	**Parameter C** [counts/C]
HOPG no aq.			
121°	3.76x10^7	-5.41x10^{-2}	-2.36x10^7
143°	3.76x10^7	-5.41x10^{-2}	-2.39x10^7
156°UP	6.78x10^8	-1.05x10^0	2.49x10^5
NG aq.			
121°	5.51x10^7	-6.98x10^{-1}	4.76x10^5
143°	5.51x10^7	-6.98x10^{-1}	3.87x10^5
156°UP	5.51x10^7	-6.98x10^{-1}	-1.36x10^5
156°DOWN	5.51x10^7	-6.98x10^{-1}	-1.36x10^5

As it can be seen in table 5.4, the reduction of deuterium content in the targets (as a function of target temperature) lays between 53% and 79%, depending on the type of target and detection angle. However, the deuterium content decrease is constant (within uncertainty), regardless of the type of target used, for a given detector angle.

Table 5.4: Relative reduction in target deuterium content as a function of target temperature in the range of 200°C - 1200 °C and for different targets (HOPG and NG) with and without nitrogen "aquarium".

Detector	**Data Set**	**Deuterium reduction**
121°	HOPG no aq.	(56 ± 5) %
	NG aq.	(53 ± 2) %
143°	HOPG no aq.	(61 ± 5) %
	NG aq.	(56 ± 4) %
156°UP	HOPG no aq.	(77 ± 9) %
	NG aq.	(79 ± 5) %
156°DOWN	NG aq.	(77 ± 4) %

These results were later used in the measurements of the $^{12}C(^{12}C,p)^{23}Na$ reaction in order to keep the deuterium content of the target at its minimum: the N_2 "aquarium" was used at low beam energies where the signal/noise ratio is below 50% and the target temperature was maintained above 400°C (see chapter 6 for further details).

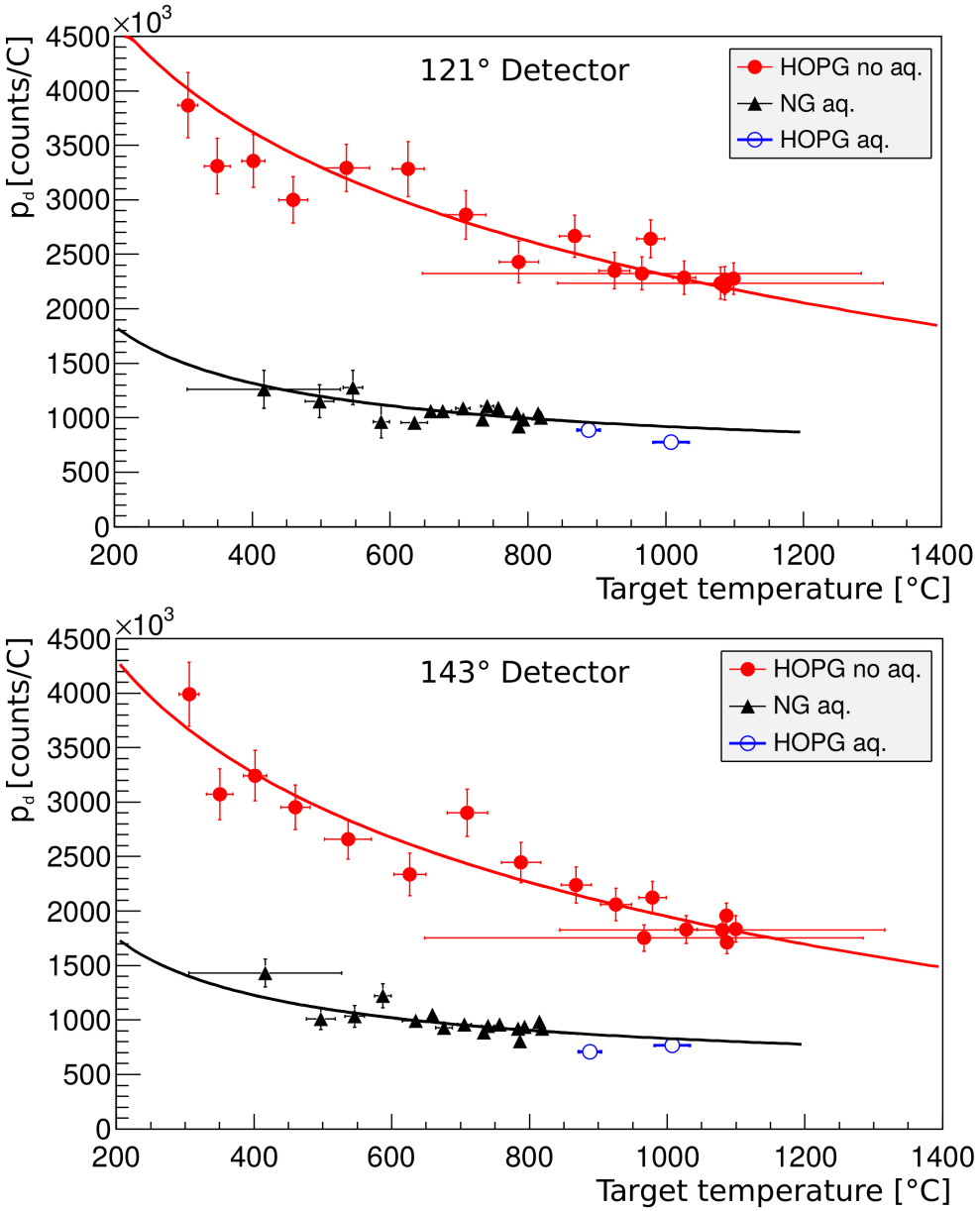

Figure 5.15: Primary proton counting rate (taken as a proxy for target deuterium content) as a function of target temperature for different targets and N_2 "aquarium" combinations, as observed with detectors 121° (top panel) and 143° (bottom panel). Lines are fits to the data using a power-law function.

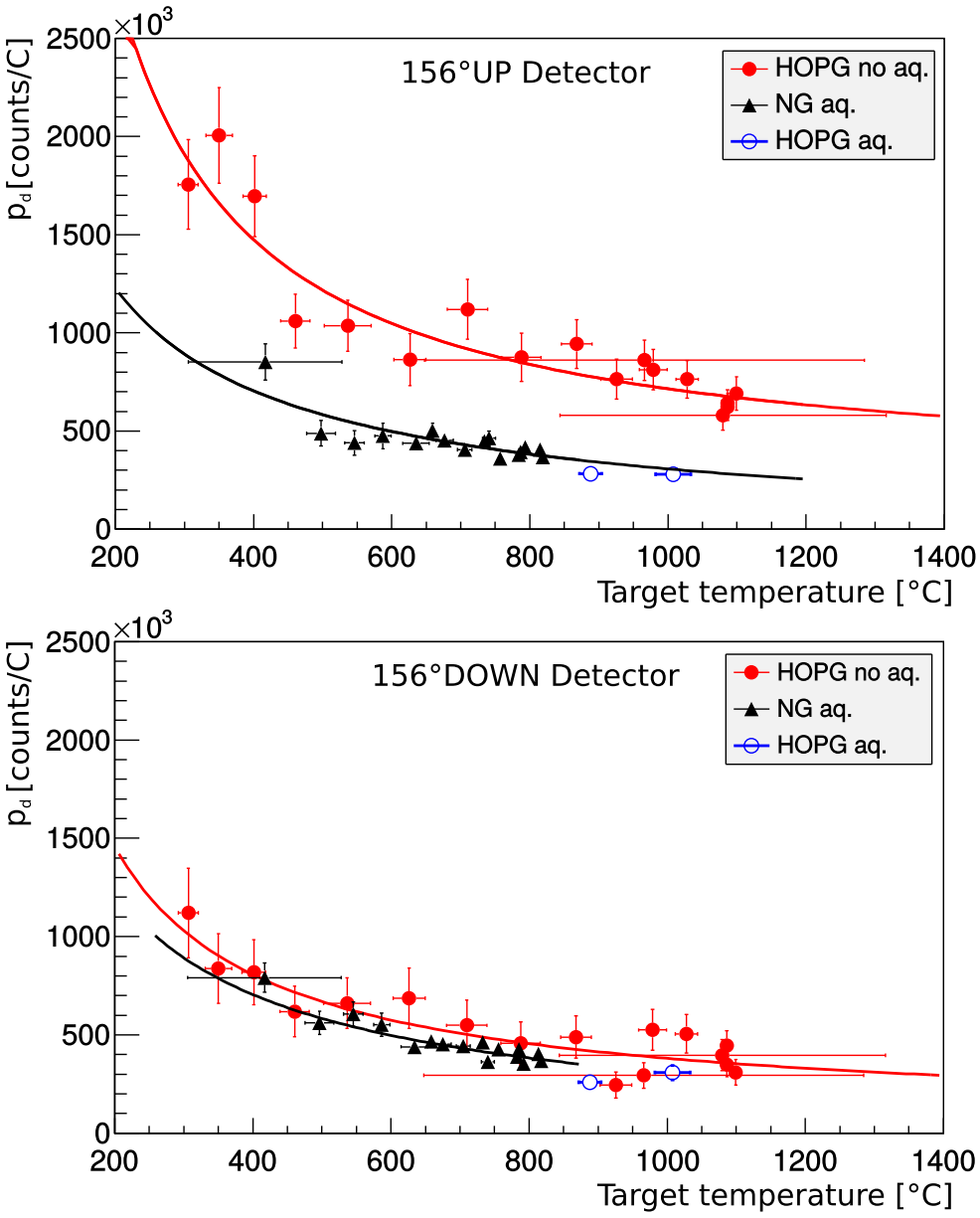

Figure 5.16: Primary proton counting rate (taken as a proxy for target deuterium content) as a function of target temperature for different targets and N_2 "aquarium" combinations, as observed with detectors 156°UP (top panel) and 156°DOWN (bottom panel). Lines are fits to the data using a power-law function.

Chapter 6

Data analysis and results of the $^{12}C(^{12}C,p)^{23}Na$ reaction measurements

As discussed previously, the aim of this work was to obtain the cross sections for each individual proton group of the $^{12}C(^{12}C,p)^{23}Na$ reaction. In order to achieve this, we used an "infinitely" thick HOPG target (1 mm) and ^{12}C beams of high intensities (of the order of tens of μA) within an energy range of E = 5.05 - 8.6 MeV in 50 keV steps. Thick target yields at all beam energies (chapter 2.2) were obtained and then differentiated at consecutive energies to obtain the "thin target yield" later converted into cross sections and S-factors. Background sources (both natural and beam induced) were properly taken into account.
This chapter details the procedures followed for background subtraction, data analysis and extraction of yields, cross sections and $\tilde{S}$-factors.

6.1 Background subtraction

In order to experimentally determine the cross section of a given nuclear reaction, several aspects have to be taken into consideration, such as the calibration of the detectors (discussed in chapter 4), a proper identification of the particle groups (appendix A) and a correct data analysis.
For the measurements of the $^{12}C+^{12}C$ reactions at CIRCE, we used the four GASTLY detectors previously described in the two position configurations mentioned in chapter 4.6 (table 4.1). In the data taking with the Old configuration, the pressure used in the ionization chambers was always maintained at 35 mbar. On the other hand, the New configuration used 35, 50 and 70 mbar of CF_4 in the ICs. All the 35 mbar data had high energies whilst the pressures of 50 and 70 mbar were used for the low energy data in order to better separate the proton locus from the electronic noise. A typical calibrated ΔE-Erest matrix taken with 35 mbar of CF_4 in the ionization chamber is shown in figure 6.1. This matrix was obtained with the 121° detector using a E = 8.6 MeV $^{12}C^{+3}$ beam impinging on the HOPG target. Two clear

loci corresponding to protons and α particles from the ^{12}C(^{12}C,p)^{23}Na and ^{12}C(^{12}C,α)^{20}Ne reactions can be seen in the figure.

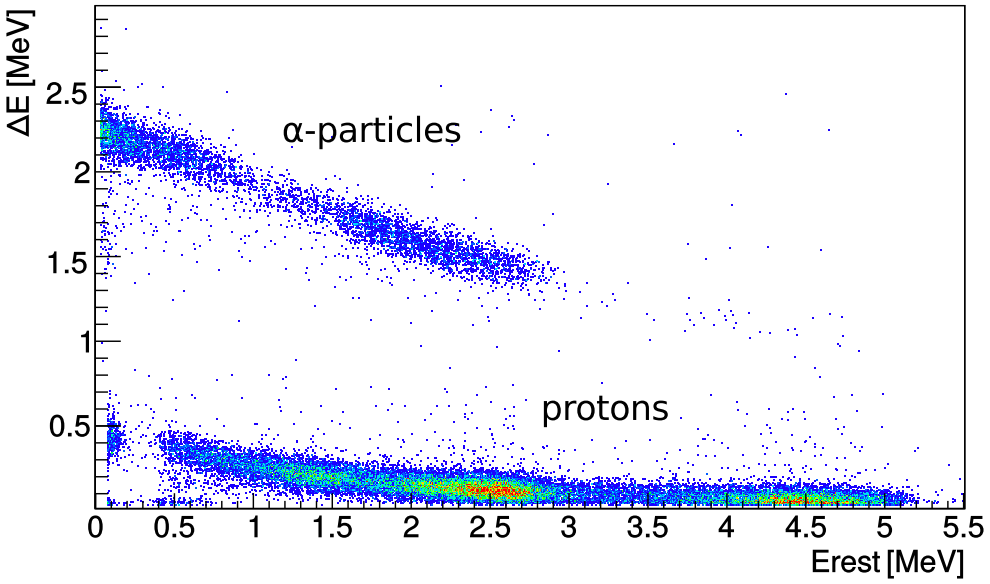

Figure 6.1: Typical calibrated ΔE-Erest matrix showing the α particles and protons loci. This matrix was obtained with a GASTLY detector placed at 121° with 35 mbar of CF_4 in the IC and using a E = 8.6 MeV $^{12}C^{+3}$ beam impinging on the HOPG target.

Given the results obtained in the target deuterium content study (section 5), at the lowest energies (E < 5.5 MeV), the nitrogen aquarium was used and the temperature of the target was maintained higher than 400 °C in order to guarantee the lowest deuterium contamination possible.

6.1.1 Natural background and electronic noise

As discussed in chapter 3, the cross sections of the ^{12}C+^{12}C reactions are very small, translating to an equally low counting rate. For this reason, having proton spectra as clean as possible is vital. The first step on the data analysis procedure must be the subtraction of natural background and electronic noise from the proton spectra. In order to achieve this, background runs of the order of days were taken in the same conditions as the ^{12}C+^{12}C measurements: one for each pressure and position configuration. These (time normalized) runs were later subtracted from the proton spectra at all beam energies studied. By doing this, we can clean the spectra from natural (cosmic) background.

Another important source of background is the electronic noise, which is mainly located in a specific area of our ΔE-Erest matrices, far from the proton locus, which gives us the opportunity of cutting it out by a proper selection of the regions of interest as shown in figure 6.2. The regions enclosed inside the continuous and dashed lines correspond to the proton locus and the protons that do not interact with the gas (ΔE = 0), respectively. These regions were used to build the proton Erest spectra. The excluded regions coincide with the α particles completely stopped in the gas (Erest = 0) and the electronic noise of the detector.

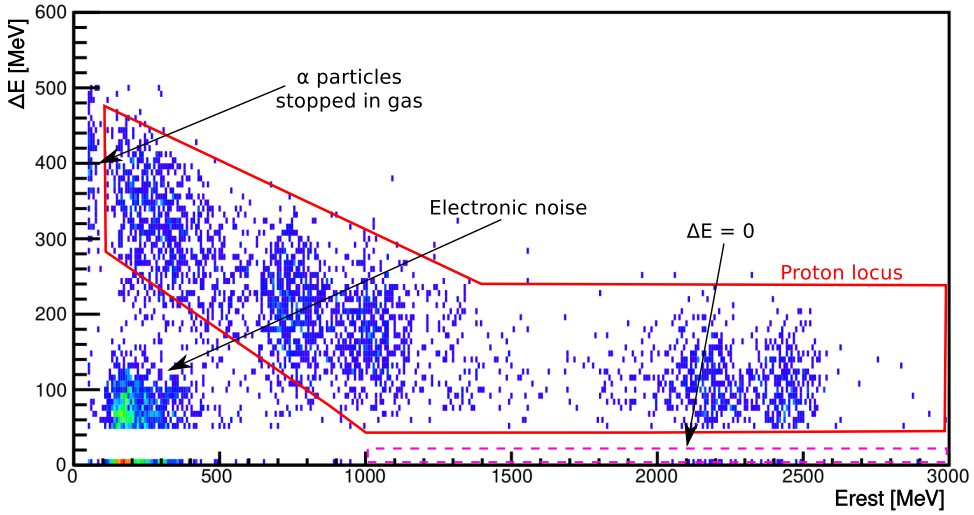

Figure 6.2: Typical $^{12}C+^{12}C$ proton matrix obtained with a detector placed at 143º with 35 mbar of CF_4 in the IC and using a E = 7.2 MeV $^{12}C^{+3}$ beam impinging on the HOPG target. The region of interest used in the analysis is enclosed in continuous and dashed lines (see text for further details).

A typical time-normalized background spectrum built after the exclusion of the regions previously mentioned is shown in figure 6.3, where a background Erest proton spectrum (dashed line) taken with the detector positioned at 156ºDOWN position (and 35 mbar of gas in the IC) shows a prominent peak at about 4.7 MeV. Systematic studies, along with energy losses and kinematic calculations, led to the conclusion that this peak was mainly due to α particles emitted by contaminants in the metal alloy used for welding the Frisch grid of the detectors. This problem was later addressed by covering the welding with a thin foil of paper. The new background obtained (in the same conditions as mentioned before) after covering the welding is also plot in figure 6.3 with a continuous line and shows no peak associated with the intrinsic radioactivity from the welding.

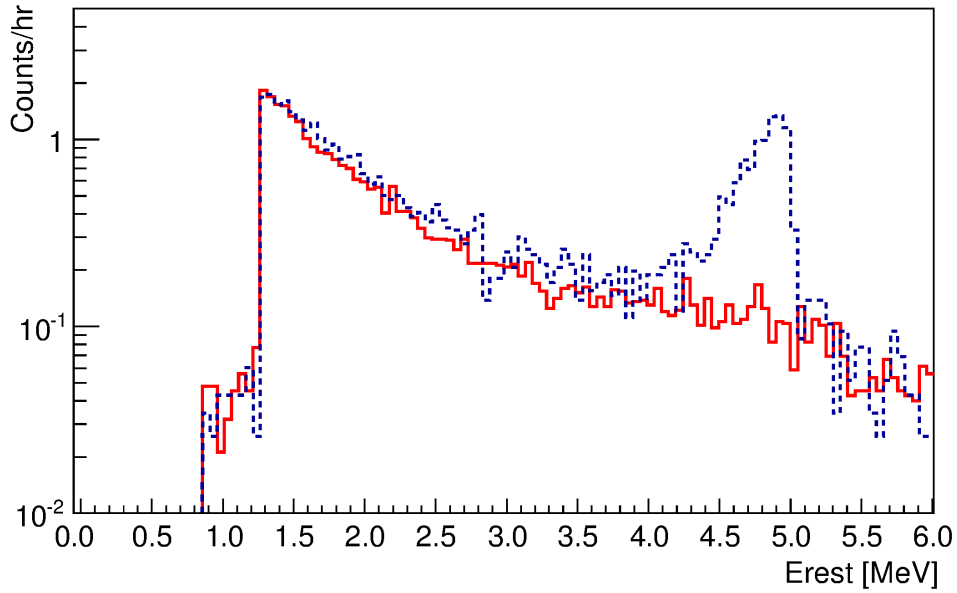

Figure 6.3: Sample time-normalized Si background spectrum obtained with the detector placed at 156°DOWN position with 35 mbar of CF_4 in the IC. The prominent peak observed (dashed line spectrum) is due to intrinsic α-decay radioactivity in the welding of the Frisch grid. The peak disappears (continuous line spectrum) when the welding is covered by a thin sheet of paper (see text for details).

Figure 6.4 shows a $^{12}C+^{12}C$ spectrum at E = 6.0 MeV taken with the 156°DOWN detector. The continuous line corresponds to the spectrum before the subtraction of the natural background while the shaded region is the background-subtracted spectrum. The dashed line corresponds to the background spectrum taken in the same conditions as the $^{12}C+^{12}C$ spectrum (the electronic noise was discarded before the subtraction).
The background subtraction becomes more critical at low energies as the counting rate of the $^{12}C+^{12}C$ reactions becomes lower. A typical signal/noise ratio plot is presented in figure 6.5 where the p_0 group (one of the most intense) of all $^{12}C+^{12}C$ runs at 35 mbar were taken. As can be seen in the figure, the background subtraction becomes critical at energies lower than E= 5.7 MeV where the signal/noise ratio falls below 50%.

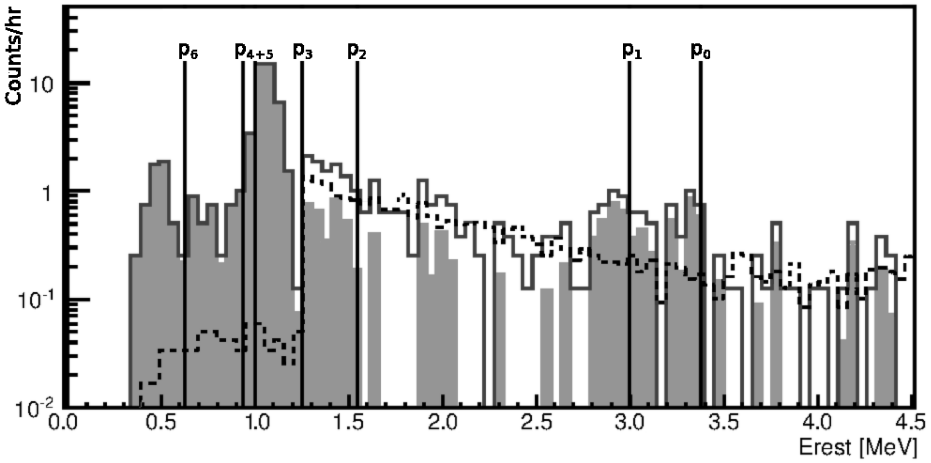

Figure 6.4: ^{12}C+^{12}C spectrum from the 156°DOWN detector at E = 6.0 MeV before (continuous line) and after (shaded area) the subtraction of the background (dashed line). The kinematically expected proton groups positions are marked with bold lines.

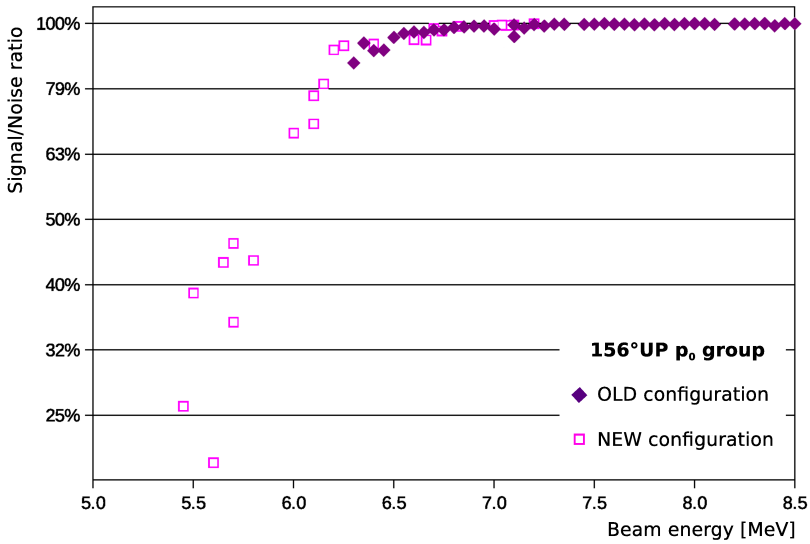

Figure 6.5: Typical signal/noise ratio plot obtained with the 156°UP detector in both configurations. The p_0 group of all ^{12}C+^{12}C runs taken using 35 mbar of gas are presented. It is clear that the background subtraction becomes critical at beam energies E < 5.7 MeV where the signal/noise ratio falls below 50%.

6.1.2 The ^{13}C contribution

In addition to the natural background and electronic noise, special attention has to be paid to any possible beam-induced background. Besides the ^{1,2}H contamination in the target (addressed in chapter 5), ^{13}C content should also be considered. Although, the nominal content of ^{13}C in the HOPG target is of only 1%, a detailed study was performed to determine its contribution to the ^{12}C+^{12}C counting rate. ^{13}C beams of energies E = 8.10, 7.80 and 7.02 MeV were produced in order to investigate the ^{13}C contribution to the ^{12}C+^{12}C reaction.
Given that the cross sections of the ^{13}C+^{12}C and ^{13}C+^{13}C reactions are very similar (figure 6.6) and the ^{13}C content of the target is of only 1%, ^{13}C+^{13}C contributions to the ^{13}C+^{12}C reaction measurements can be neglected.

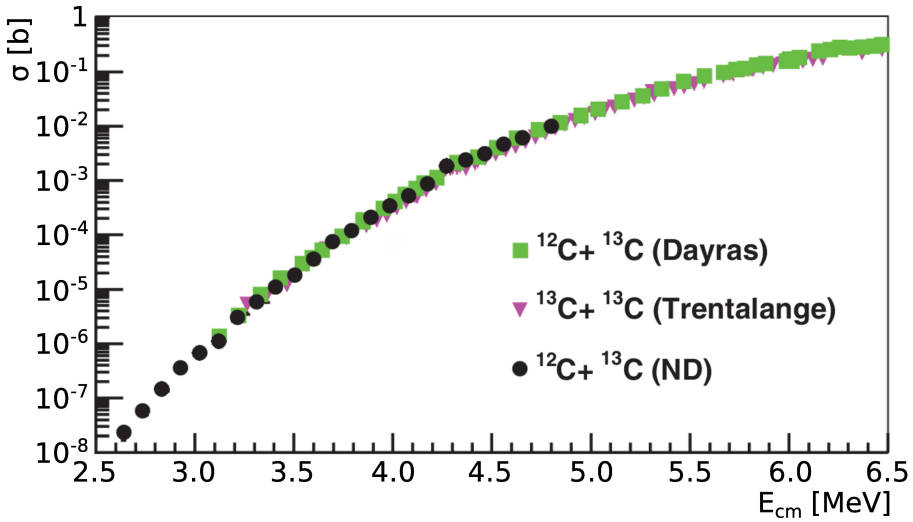

Figure 6.6: Cross sections of the ^{13}C+^{12}C and ^{13}C+^{13}C reactions measured by Dayras (squares) [83] and Trentalange (circles) [84], respectively. Additional data points for the ^{13}C+^{12}C reaction from the nuclear database are also included (triangles).

Taking the ^{12}C+^{12}C reaction cross section measured by Becker *et al.* [17], a comparison with the ^{13}C+^{12}C cross section can be performed. A plot of said reactions is shown in figure 6.7 were we can see that the greatest difference (nearly of an order of magnitude) between the ^{12}C+^{12}C cross section and other data, occurs at E_{cm} = 3.9 MeV (corresponding to our highest energy measured with the ^{13}C beam). Since for the rest of the energies, the difference between cross sections is smaller, we can focus on the ^{13}C+^{12}C contribution to the ^{12}C+^{12}C reactions at E_{cm} = 3.9 MeV.

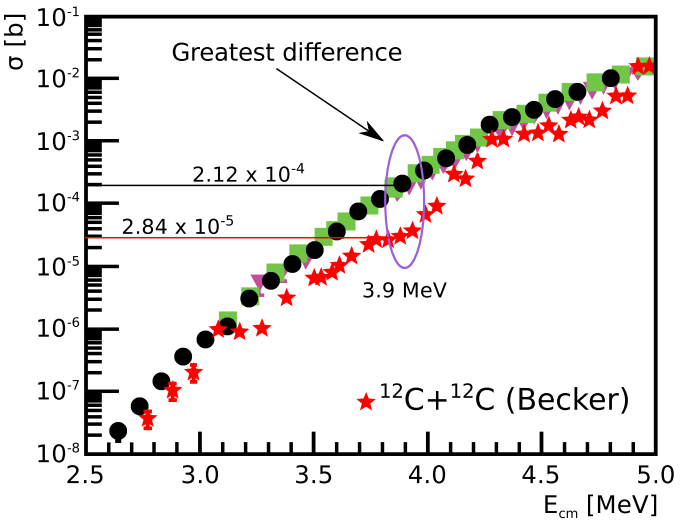

Figure 6.7: Cross sections of the ^{12}C+^{12}C reactions (star symbols) measured by Becker and the ^{12,13}C+^{13}C reactions (circles, squares and triangles). It can be seen that the largest difference between cross sections occurs at E_{cm} = 3.9 MeV.

I built a charge-normalized Erest proton spectrum for both ^{12}C and ^{13}C beams impinging on the target at E_{cm} = 3.9 MeV. Taking the ^{12}C+^{12}C spectrum and subtracting the 1% of its corresponding ^{13}C+^{12}C spectrum, we can see the contribution of the ^{13}C+^{12}C reaction to the reaction of interest (figure 6.8).

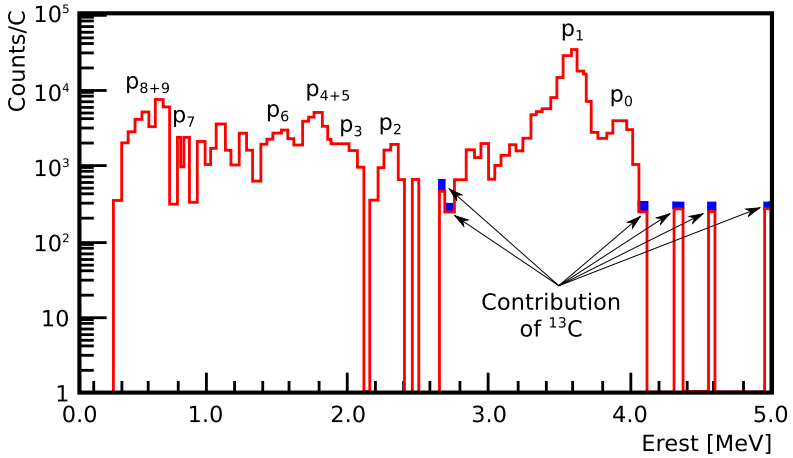

Figure 6.8: Typical ^{12}C+^{12}C Erest spectrum before (shaded area) and after (continuous line) the subtraction of its correspondent ^{13}C+^{12}C spectrum. E_{cm} = 3.9 MeV, the detector used was placed at 156°UP position and the IC had 35 mbar of pressure at all times.

Although the ^{13}C contribution is only graphically noticeable in a few energy regions, a quantitative estimate was done by taking the number of events under the $p_0 + p_1$ groups region (from properly charge-normalized spectra) and calculating the thick target yield for the ^{12}C+^{12}C spectra Y^{∞}_{12C} and ^{13}C+^{12}C spectra Y^{∞}_{13C}. The contribution from ^{13}C can then be estimated as:

$$^{13}\text{C contribution} = Y^{\infty}_{12C} - 0.01 * Y^{\infty}_{13C}, \tag{6.1}$$

where the 0.01 factor corresponds to the 1% of the ^{13}C content in the target. The results are summarized in table 6.1.

Table 6.1: Quantitative estimate of the ^{13}C contribution to the ^{12}C+^{12}C reaction measurements using the E_{cm} = 3.9 MeV data.

Detector	Y_{12C} [counts/C]	Y_{13C} [counts/C]	**^{13}C contribution**
121°	10267.8	10086.2	1.0 %
143°	14115.9	9248.6	0.7 %
156°UP	16750.4	7642.5	0.5 %
156°DOWN	15343.3	8628.1	0.6 %

In summary, the ^{13}C content of the HOPG target, contributes with less than 1% to the ^{12}C+^{12}C reaction yield at E_{cm} = 3.9 MeV. Therefore, given that the difference in (literature) cross sections is lower for the rest of the energies studied here, the ^{13}C contribution is negligible at all energies investigated.

6.2 Fitting procedure

In order to calculate the ^{12}C(^{12}C,p)^{23}Na reaction cross sections, I built the Erest spectra to obtain the number of events of each proton peak. Since the proton groups are very close to each other, a simple integration over an energy region would give a wrong reaction yield estimate. Therefore, after a correct subtraction of the background, a fitting of the different proton group peaks was performed in order to account for the contributions of each peak to the nearby ones. Given that the peaks do not have an entirely gaussian shape, it was decided to use a skewed gaussian distribution [85] and the bin likelihood method to fit the spectra using a script I wrote under ROOT [86].

The function used to fit individual peaks can be written as:

$$f(x) = A\left(\frac{\exp\left[\frac{\sigma^2+2\tau(x-\mu)}{2\tau^2}\right]\mathrm{Erfc}\left[\frac{x-\mu+\frac{\sigma^2}{\tau}}{\sigma\sqrt{2}}\right]}{2\tau}\right), \tag{6.2}$$

where A is the amplitude of the distribution, μ and σ are its centroid and standard deviation, τ corresponds to the relaxation time (shape parameter) and Erfc(x) is the complementary error function. Considering that proton peaks overlap in two groups (and the covariance between groups is zero), the fitting was done in two phases: 1) summing three skewed gaussians for p_0, p_1 and an unidentified peak (called dummy[1]) and 2) summing up four skewed gaussians for p_2, p_3, p_{4+5} (since p_4 and p_5 cannot be separated) and p_6. In the summing of these distributions, however, the parameter σ was left in common since it is proportional to the detector's resolution. A fitted spectrum using this approach is shown in figure 6.9 where the $^{12}C+^{12}C$ reaction proton groups can be clearly seen along with the previously mentioned dummy peak and the $^{12}C+^{2}H$ primary protons.

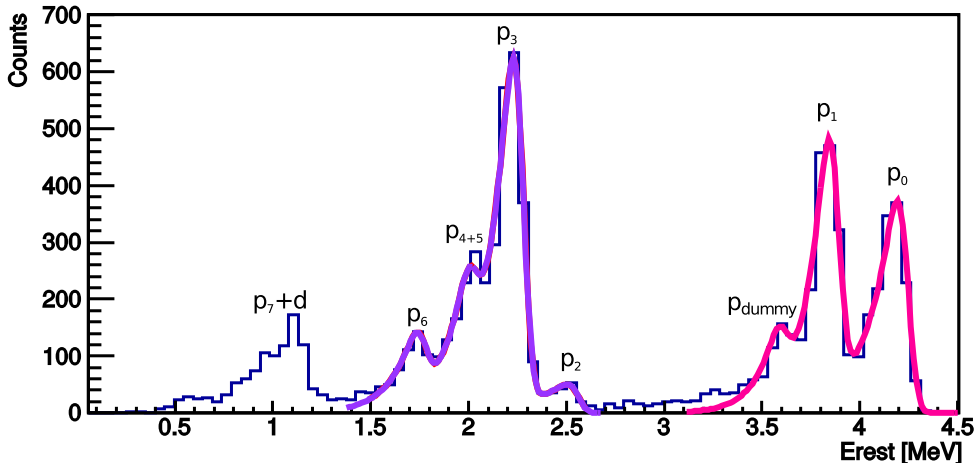

Figure 6.9: Example of a fitted spectrum using a sum of three and four skewed gaussians. This spectrum was taken with detector 156°UP and a E = 8.4 MeV ^{12}C beam. The proton groups coming from the $^{12}C+^{12}C$ reaction are labelled as $p_1 \rightarrow p_6$; p_{dummy} corresponds to an unidentified peak and d refers to the protons originated by the $^{12}C+^{2}H$ reaction.

[1]Many target and entrance window contaminants were considered and kinematic calculations were performed in an attempt to identify the "dummy" peak. However, we could not find any suitable match to the energy position of such peak.

The advantage of using this approach to fit the peaks is that the amplitude A of the fitted distribution (equation 6.2) corresponds to the area of a certain proton peak, which is already the number of events N associated to a given transition, allowing the direct calculation of the yield [85].
The uncertainty δN associated to the number of events N of each proton peak was calculated considering the statistical error of the number of events in the background spectra under the same proton peak energy region $\sqrt{\mathrm{N_{bkg}}}$, and the error δA associated to parameter A of the fitted skewed gaussian (given by ROOT):

$$\delta \mathrm{N} \;=\; \sqrt{\mathrm{N_{bkg}} \;+\; (\delta \mathrm{A})^2} \tag{6.3}$$

Using this approach, the error bars vary considerably from one data point to another due to inherent difficulties of the fitting process.
It should be noted that since the covariance matrices (given by ROOT) of the fit parameters have very small values (near to zero), the error given by the correlation between parameters was neglected.
In the case of low beam energies (E $<$ 5.5 MeV), the proton peaks could not be easily identified, thus, we had to rely on the kinematically calculated energy positions of each peak and integrate over a certain energy region in order to obtain the number of events N. The uncertainty in these cases was calculated by replacing δA with the statistical error of the number of events $\sqrt{\mathrm{N}}$. The errors were then propagated according to the cross section and $\tilde{\mathrm{S}}$-factor extraction processes (chapter 2.2). In the following sections, the yields, cross sections and $\tilde{\mathrm{S}}$-factors are given. The uncertainties presented here, correspond only to statistical errors. To get the complete cross section uncertainties, we have to consider the error in the accumulated charge ($<$1%, [82]), the error on solid angles (0.9-1.2%, table 4.6) and in the stopping power (about 8%, [11]).

6.3 Results

After fitting all proton groups at all beam energies, I proceeded to calculate the yields, cross sections and $\tilde{S}$-factors of the $^{12}C(^{12}C,p)^{23}Na$ reaction using equations 2.22 - 2.32. The results are presented in the following sections.
As discussed in chapter 5, the presence of protons produced by the ^{12}C beam impinging on the deuterium contamination of the target, is inevitable. Fortunately, in most cases, it was possible to disentangle the primary protons contribution produced by the $^{12}C+^{2}H$ reaction from proton peaks due to the $^{12}C+^{12}C$ reaction. Figure 6.10 shows spectra from four different beam energies where the deuterium peak can be seen entering the $^{12}C(^{12}C,p_6)$ region. At a beam energy of E = 8.60 MeV, the deuterium peak is positioned right over the p_7 peak. As we decrease the beam energy, the deuterium peak position stays nearly unchanged (due to heavy-light nuclei scattering mechanisms), while the $^{12}C+^{12}C$ proton groups move to lower energies. At E = 7.55 and 7.35 MeV, the contamination peak is located between p_6 and p_7. However, at a beam energy of E = 7.20 MeV, the deuterium masks completely the p_6 group. A similar behaviour can also be seen at lower beam energies, where the $^{12}C+^{2}H$ proton peak exits the p_6 group regions and enters the p_{4+5} peak, p_3 and p_2. It is important to identify at all times the deuterium contamination in order to separate these data points from the cross sections of the reaction under study.
Another artefact that can be observed in figure 6.10, is the peak separation. With a beam energy of E = 7.35 MeV (to give an example), the p_3 and p_{4+5} groups are no longer well distinguished. In these cases, when the fitting procedure was not powerful enough to separate one peak from the other, the points were discarded from the partial cross sections but used in the calculation of the "total" (the sum of all available proton groups) reaction cross sections and $\tilde{S}$-factors.

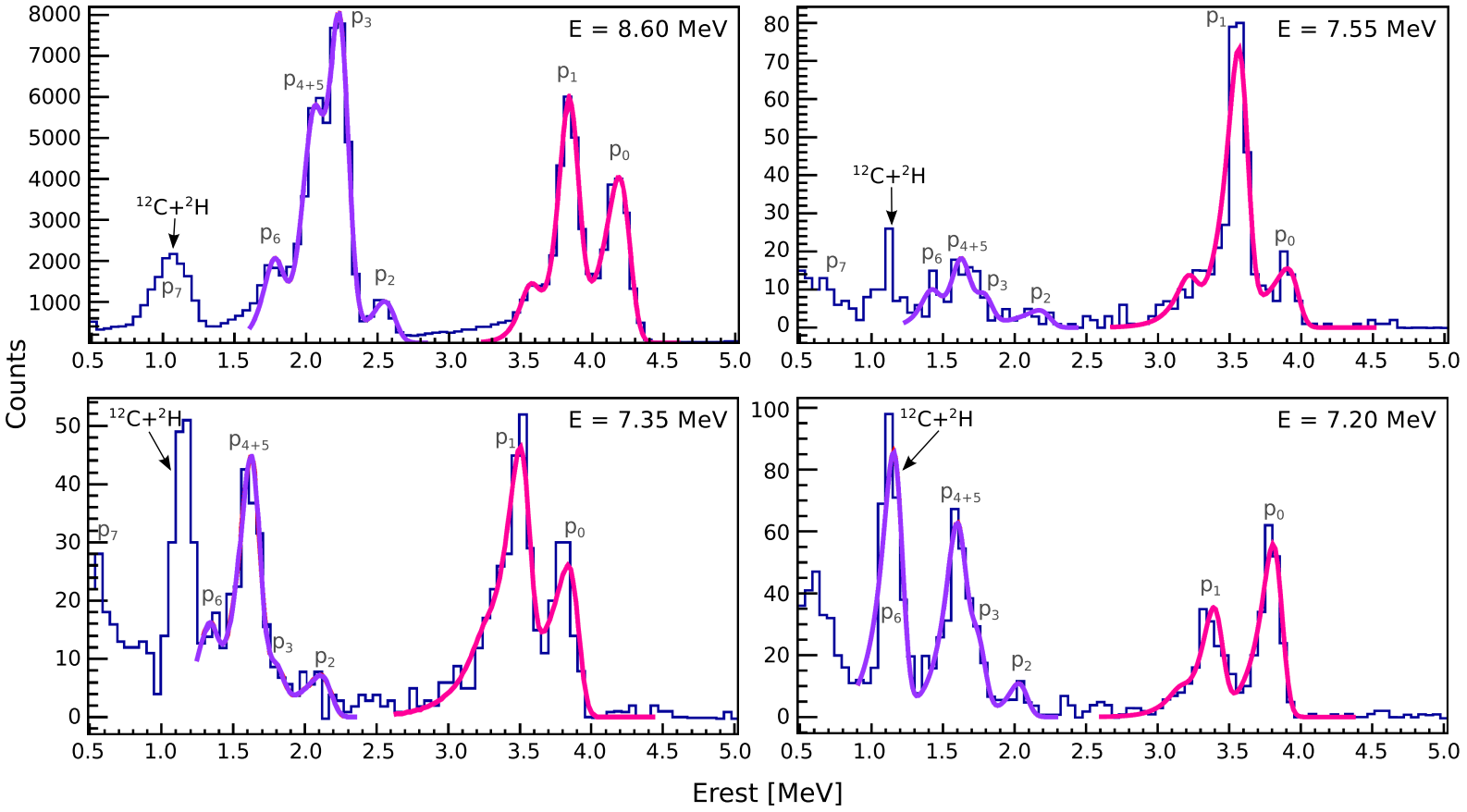

Figure 6.10: Sample fitted spectra taken with the 156°DOWN detector at four different beam energies and with 35 mbar of gas in the IC. Note how the various proton peaks from the ^{12}C(^{12}C,p)^{23}Na reaction shift towards lower energies at lower beam energy (as expected) thus progressively merging with the primary proton peak from the d(^{12}C,p)^{13}C reaction (whose location stays the same).

6.3.1 Thick target yields

With the number of events N obtained from the fitted spectra and using equation 2.22 I calculated the thick target yields for each detector and for the various experimental configurations used (different targets and gas pressure in the ICs). The thick target proton yields per steradians are presented in figures 6.11 to 6.14 where the primary protons from deuterium contamination are separated from the $^{12}C(^{12}C,p)^{23}Na$ groups and clearly indicated.
Data are divided by proton group: p_0, p_1 and p_2 are at the top of the figure while p_3, p_{4+5} and p_6 can be found at the bottom. Numerical values of these results are given in appendix D (tables D.2 to D.9).
A discrepancy in the p_0 thick target yields between Old and New configurations was observed in detector 121° and assumed to be due to a faulty amplifier cable. We thus decided to normalize the Old configuration data points to the New configuration ones by a normalization factor of 5.64. This procedure was exclusively used in the case of the p_0 group at 121°.

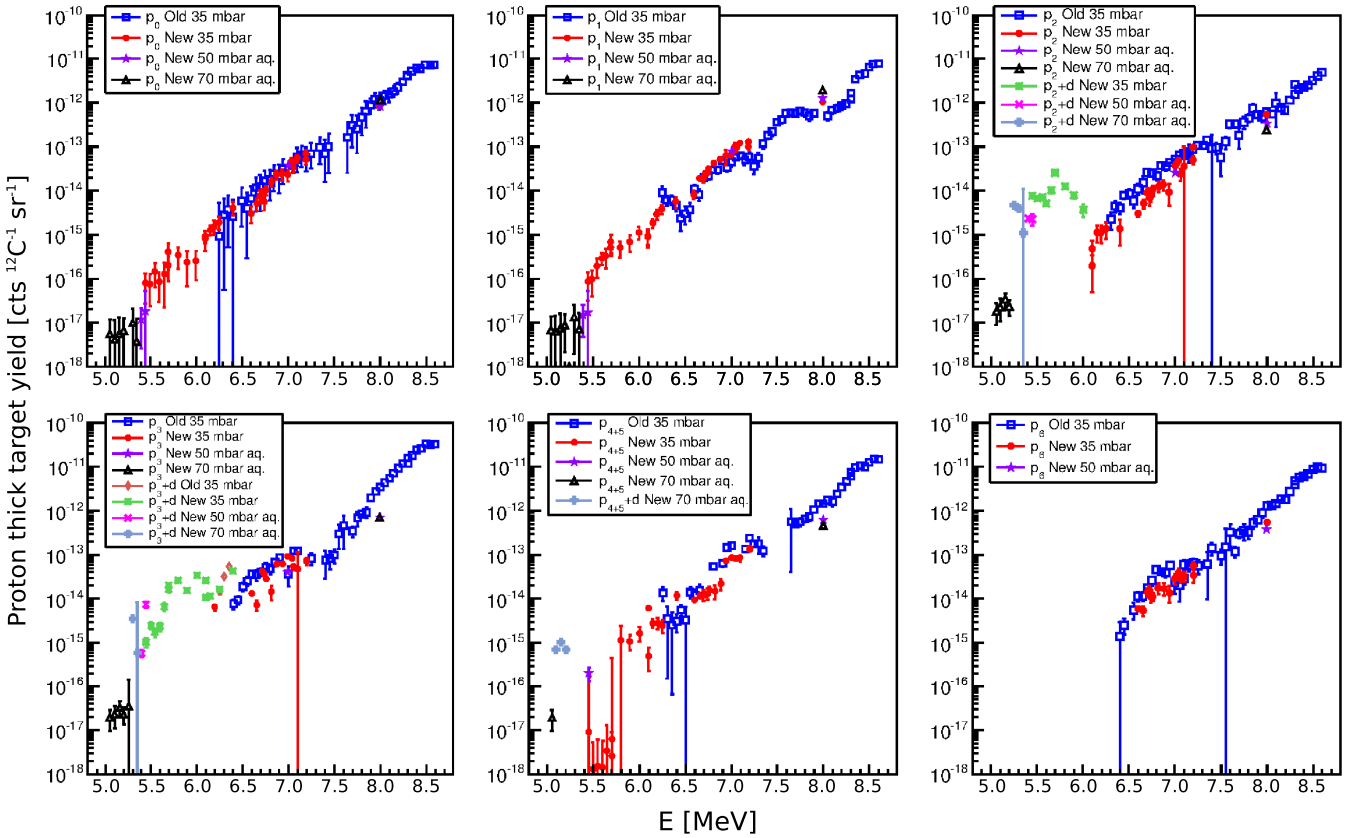

Figure 6.11: Thick target yield [counts/(^{12}C sr)] obtained with the 121° detector. Graphs show data series obtained for different configurations (Old and New) and different IC pressures. Different proton groups are shown in different plots. At some energies and proton groups, data points include contributions from primary protons coming from the ^{12}C(d,p) reaction. These are clearly indicated as "p_i+d". The p_0 group data from the Old configuration were normalized to the New configuration (see text for details). Numerical values are given in tables D.2 and D.3.

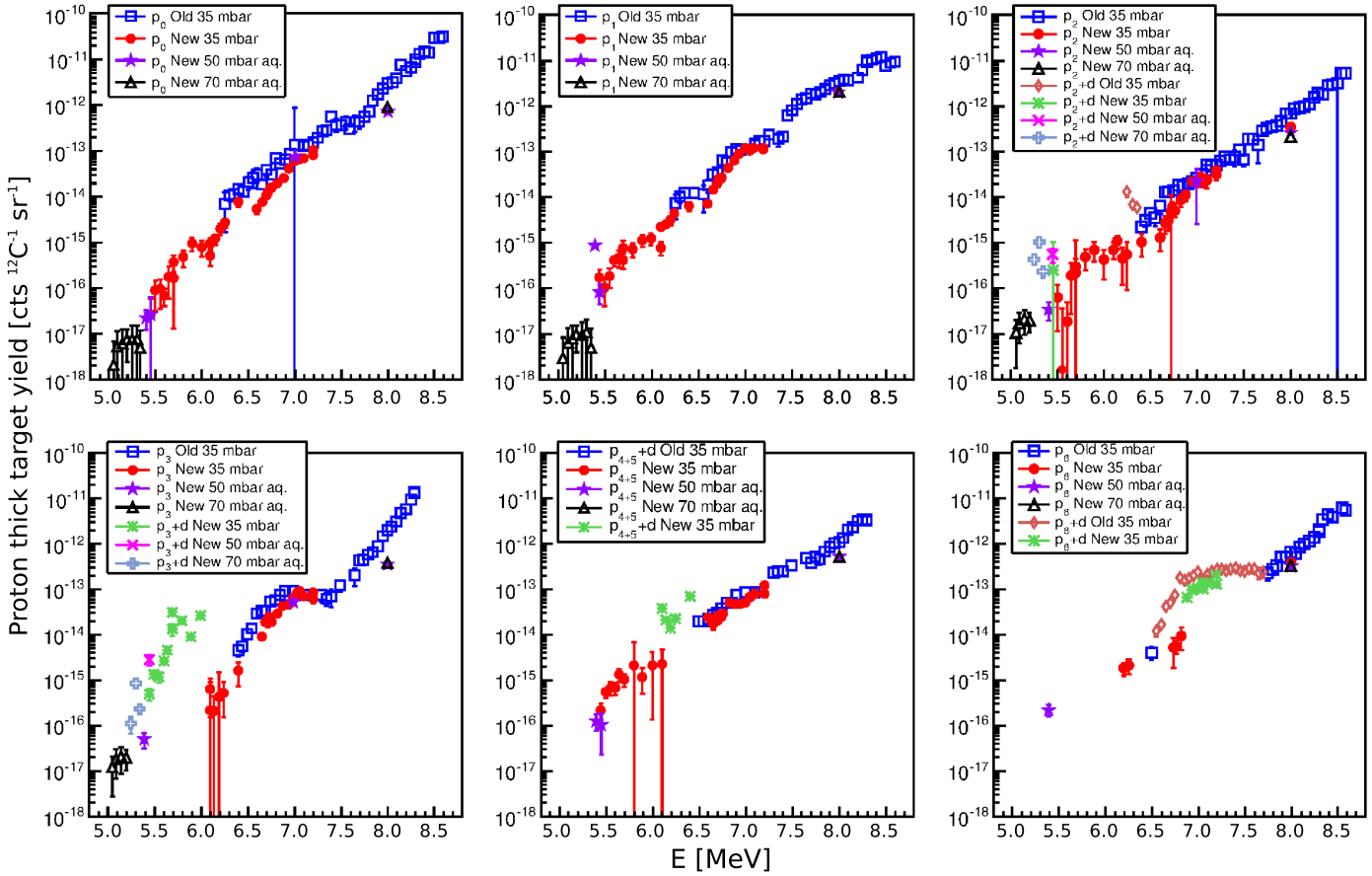

Figure 6.12: Thick target yield [counts/(^{12}C sr)] obtained with the 143° detector. Graphs show data series obtained for different configurations (Old and New) and different IC pressures. Different proton groups are shown in different plots. At some energies and proton groups, data points include contributions from primary protons coming from the ^{12}C(d,p) reaction. These are clearly indicated as "p_i+d". Numerical values are given in tables D.4 and D.5

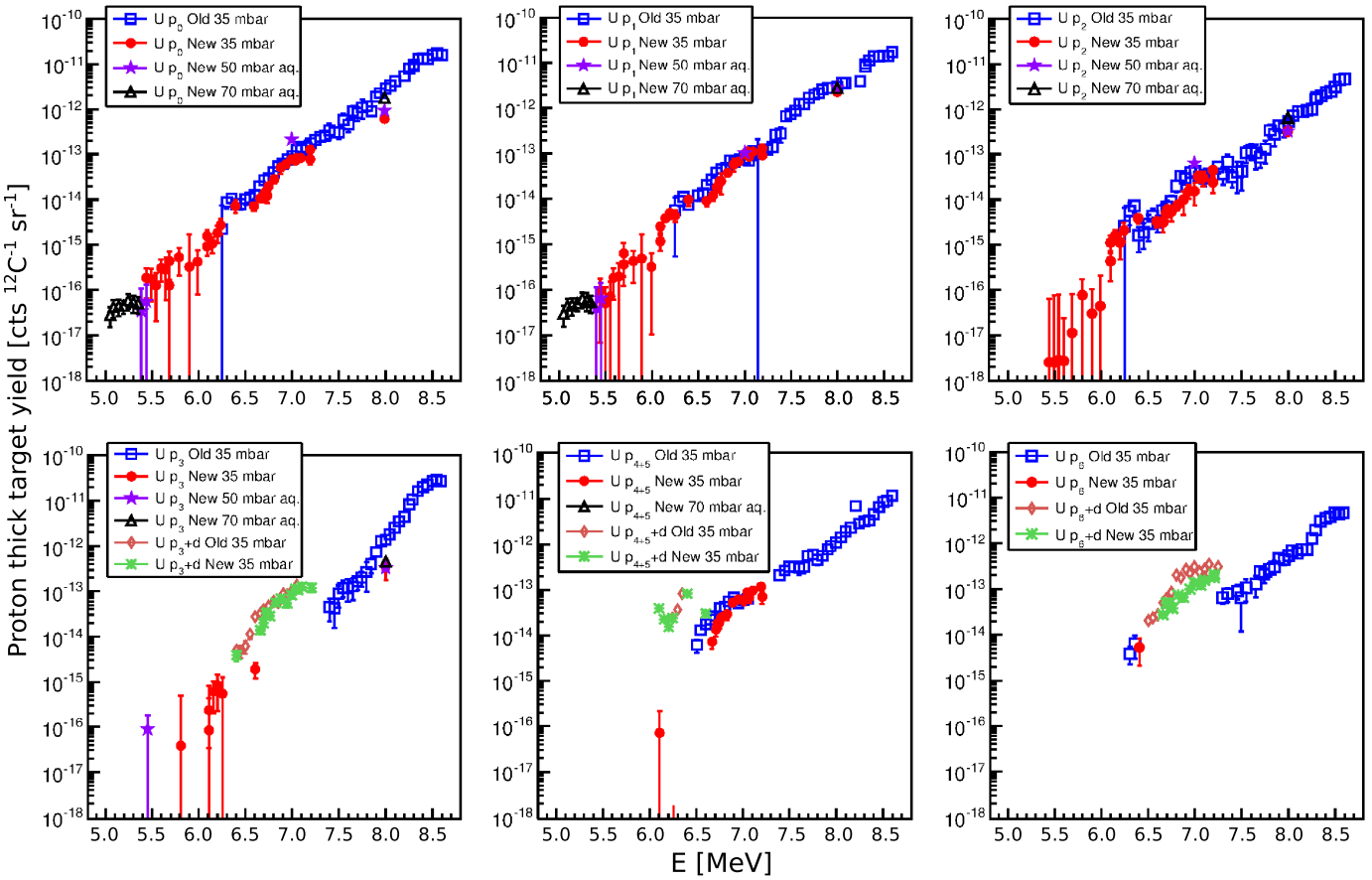

Figure 6.13: Thick target yield [counts/(^{12}C sr)] obtained with the 156°UP detector. Graphs show data series obtained for different configurations (Old and New) and different IC pressures. Different proton groups are shown in different plots. At some energies and proton groups, data points include contributions from primary protons coming from the ^{12}C(d,p) reaction. These are clearly indicated as "p$_i$+d". Numerical values are given in tables D.6 and D.7

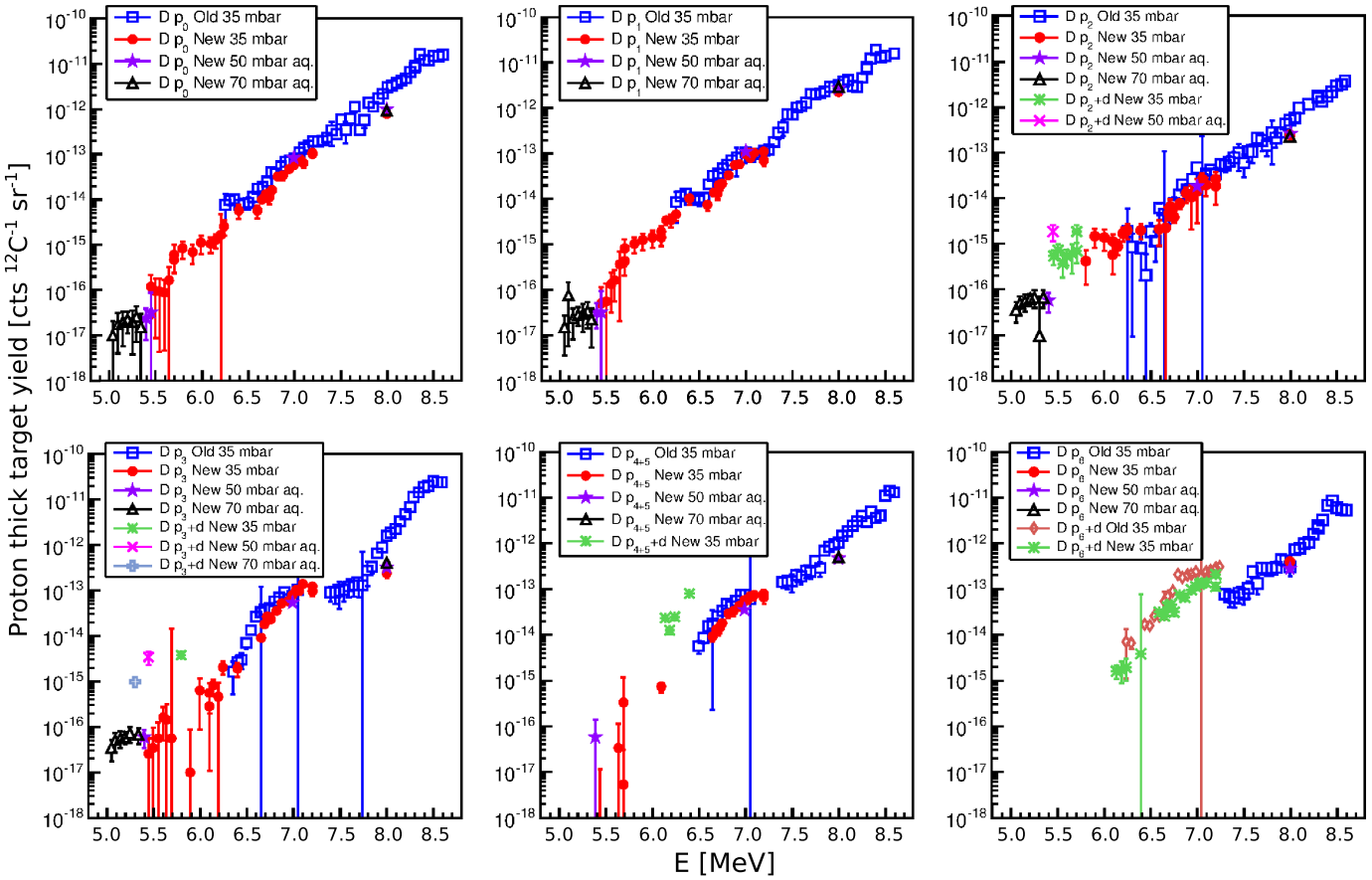

Figure 6.14: Thick target yield [counts/(^{12}C sr)] obtained with the 156°DOWN detector. Graphs show data series obtained for different configurations (Old and New) and different IC pressures. Different proton groups are shown in different plots. At some energies and proton groups, data points include contributions from primary protons coming from the ^{12}C(d,p) reaction. These are clearly indicated as "p_i+d". Numerical values are given in tables D.8 and D.9

6.3.2 Differential thin target yields

In order to obtain reaction cross sections from the thick target yield measurements, a differentiation procedure was applied to yields taken at consecutive beam energies in 50 keV steps. The resulting yield difference was then divided by the energy interval (between the two successive beam energies) and used as a measure of the thin target yield, from where cross sections can be easily inferred. Note that this differentiated thin target yield is also a differential yield (counts/steradian). The energy step was maintained as small as possible and the energy associated to each thin target yield was defined as E_{med} (equation 2.29).
As can be seen in the thick target yield results, the New configuration data are self-consistent independently of the pressure in the ionization chamber, thus results presented hereafter are simply grouped into Old (filled squares) and New configuration (filled circles). The deuterium contaminated data are still shown for completeness. Figures 6.15 to 6.18 show the obtained thin target yields per steradians.

Since the data points with large or negative uncertainties ($> 100\%$ due to a poor fitting of the peak or as a result of the differentiation process, respectively) do not provide any information, we decided to "clean" the figures and leave only the physically important data points. Such results can be found in figures 6.19 to 6.22.

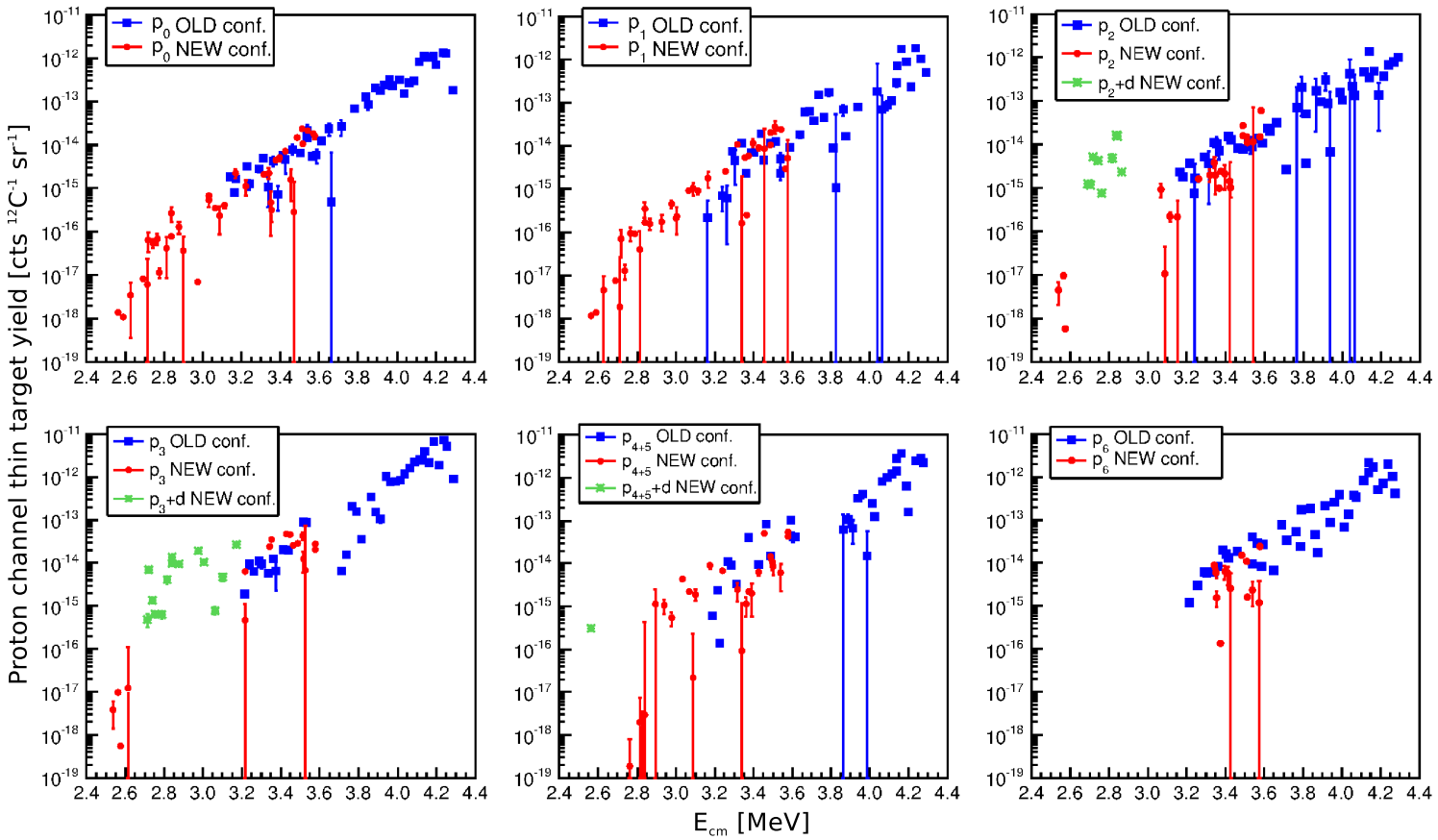

Figure 6.15: Thin target yield [counts/(^{12}C sr)] obtained with the 121° detector. Graphs show data series obtained for different configurations (Old and New). Different proton groups are shown in different plots. At some energies and proton groups, data points include contributions from primary protons coming from the ^{12}C(d,p) reaction. These are clearly indicated as "p$_i$+d".

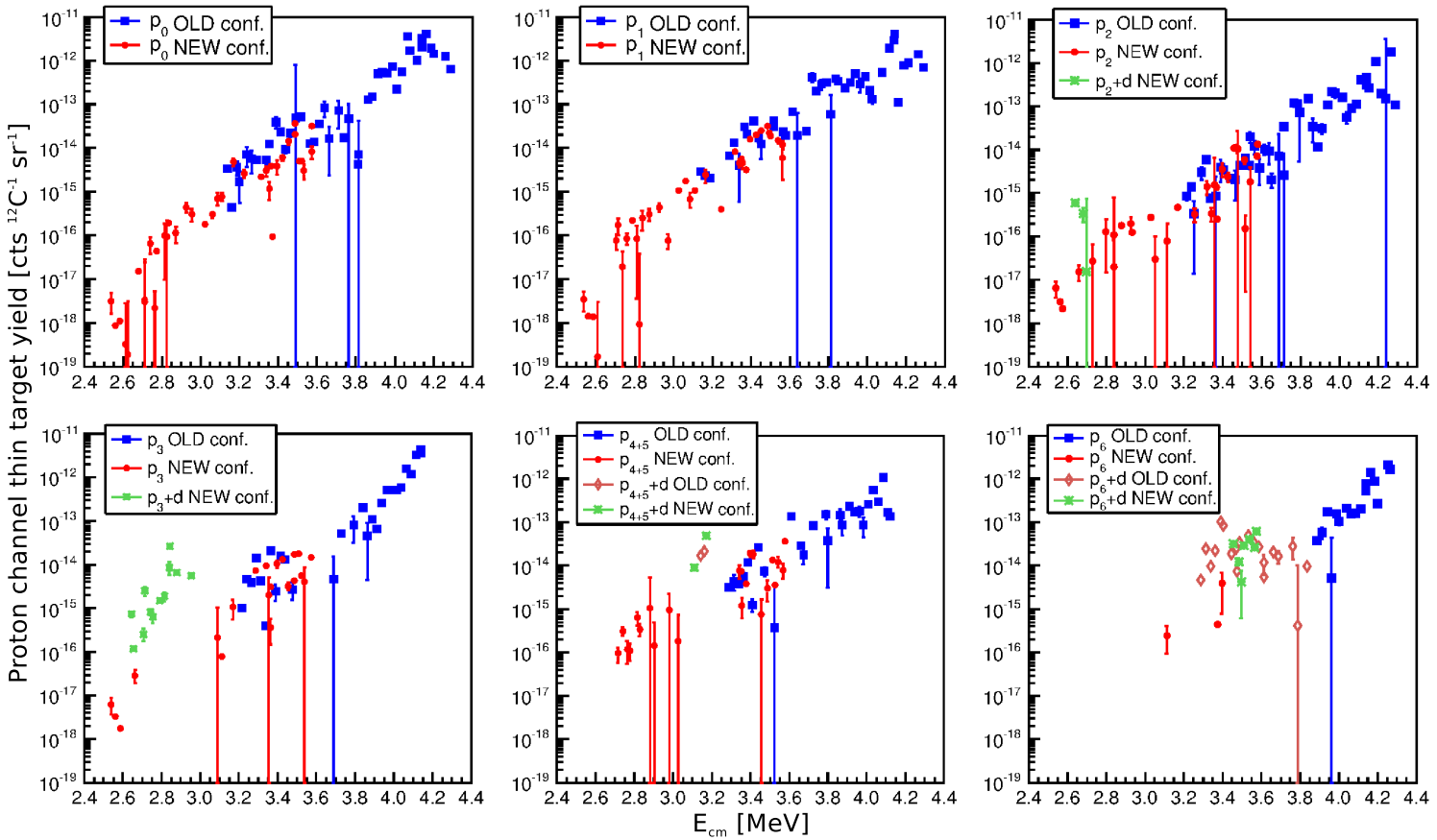

Figure 6.16: Thin target yield [counts/(^{12}C sr)] obtained with the 143° detector. Graphs show data series obtained for different configurations (Old and New). Different proton groups are shown in different plots. At some energies and proton groups, data points include contributions from primary protons coming from the ^{12}C(d,p) reaction. These are clearly indicated as "p$_i$+d".

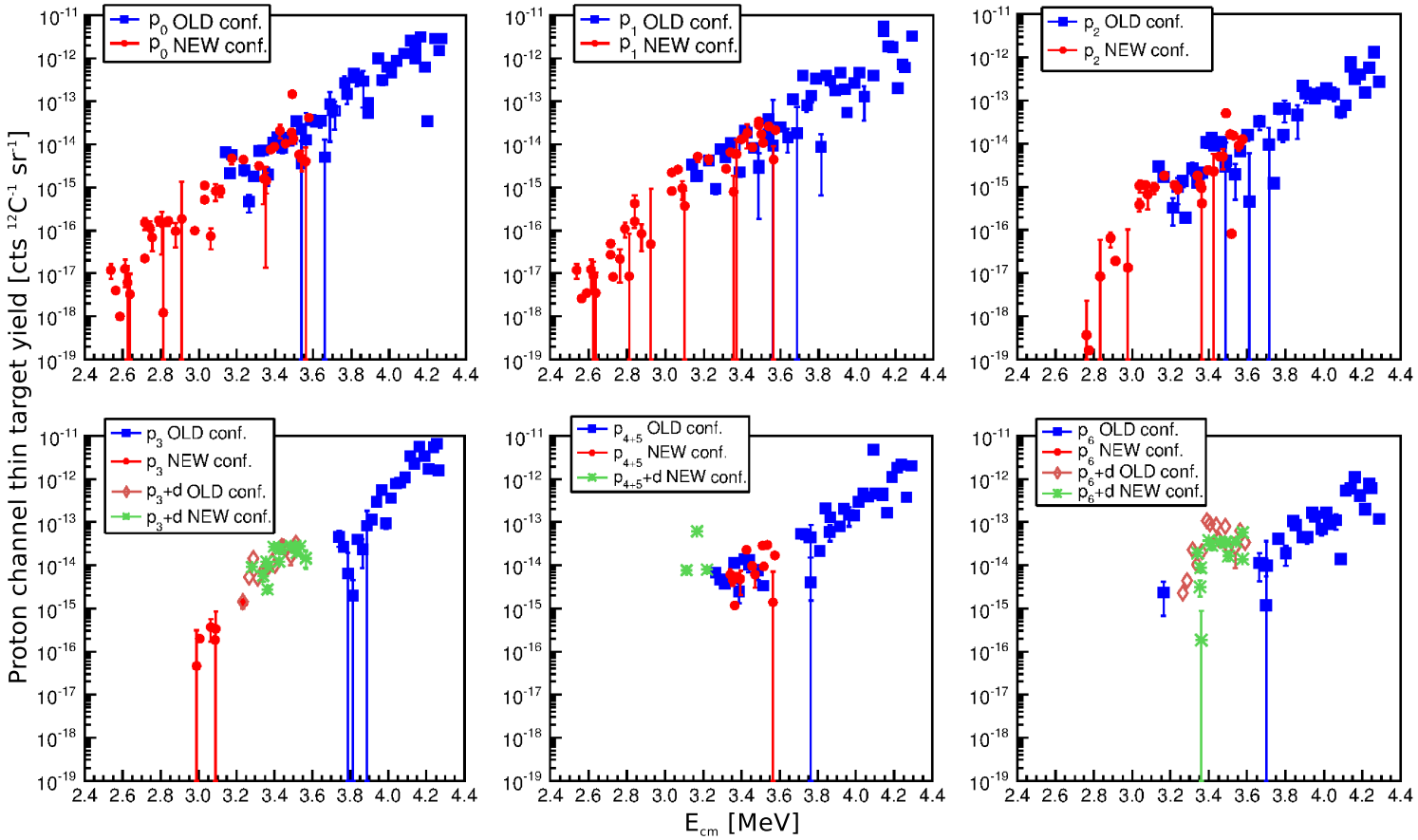

Figure 6.17: Thin target yield [counts/(^{12}C sr)] obtained with the 156°UP detector. Graphs show data series obtained for different configurations (Old and New). Different proton groups are shown in different plots. At some energies and proton groups, data points include contributions from primary protons coming from the ^{12}C(d,p) reaction. These are clearly indicated as "p$_i$+d".

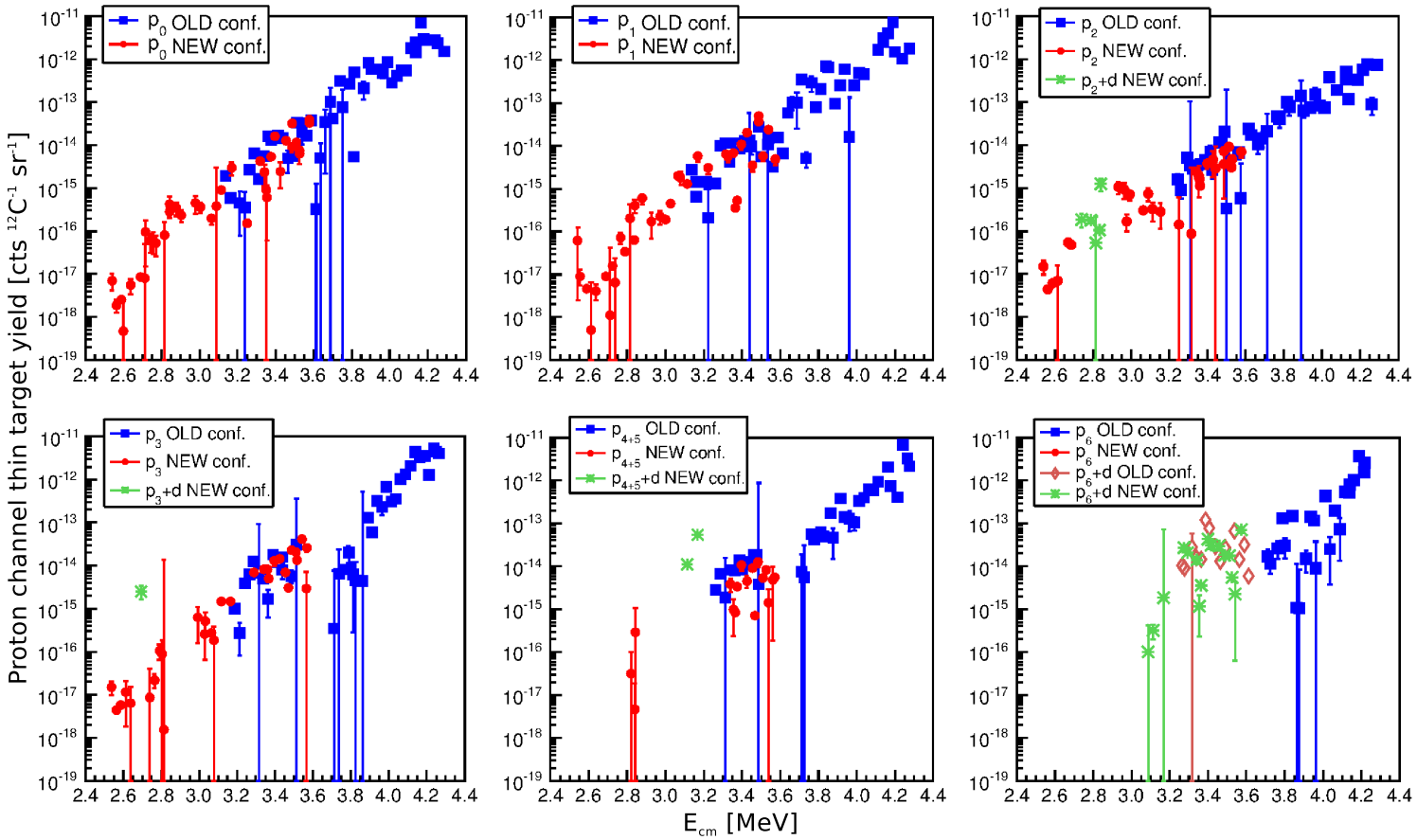

Figure 6.18: Thin target yield [counts/(^{12}C sr)] obtained with the 156°DOWN detector. Graphs show data series obtained for different configurations (Old and New). Different proton groups are shown in different plots. At some energies and proton groups, data points include contributions from primary protons coming from the ^{12}C(d,p) reaction. These are clearly indicated as "p$_i$+d".

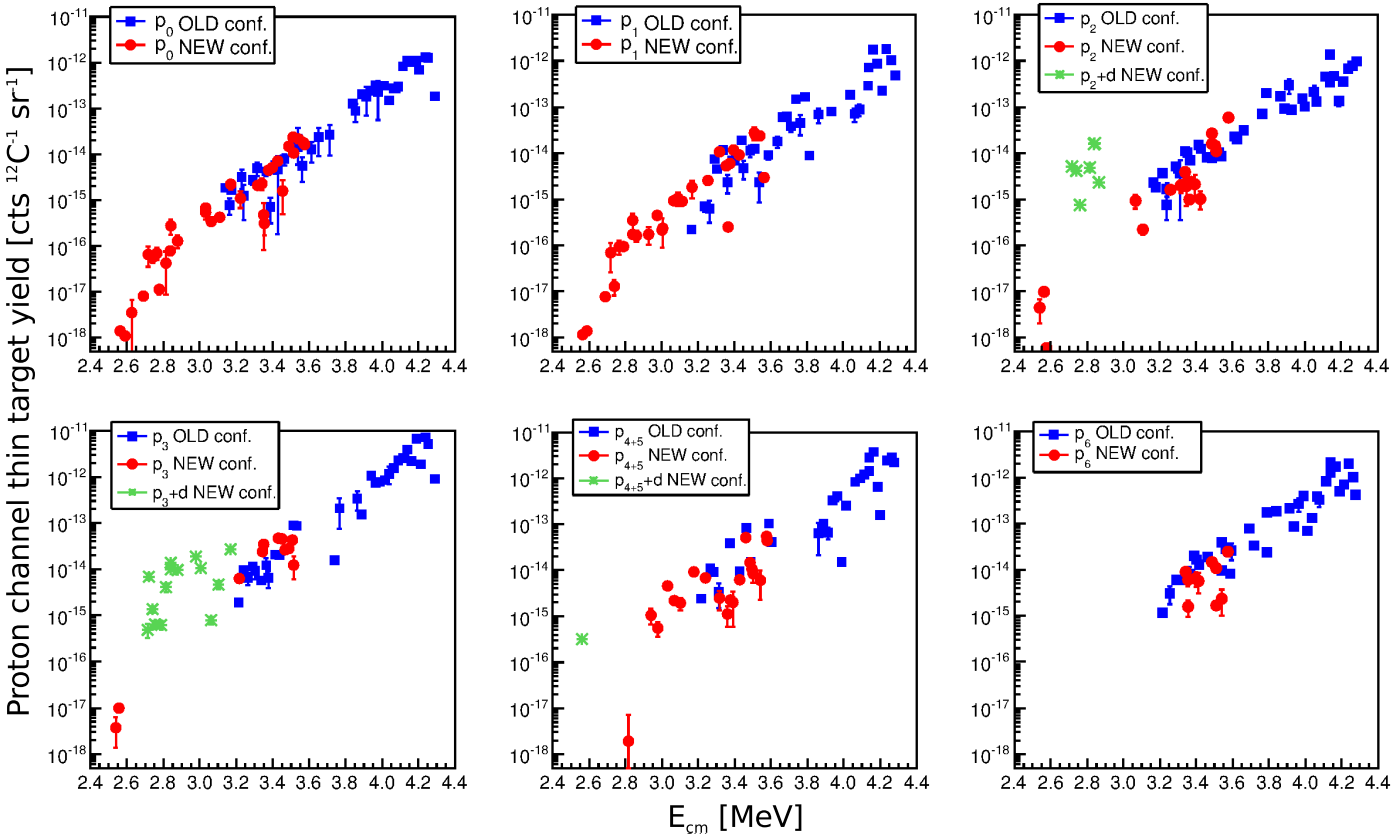

Figure 6.19: Thin target yield [counts/(^{12}C sr)] obtained with the 121° detector. Graphs show data series obtained for different configurations (Old and New). Different proton groups are shown in different plots. At some energies and proton groups, data points include contributions from primary protons coming from the ^{12}C(d,p) reaction. These are clearly indicated as "p_i+d". The data points with extremely large or negative uncertainties were removed since they do not give us any useful information.

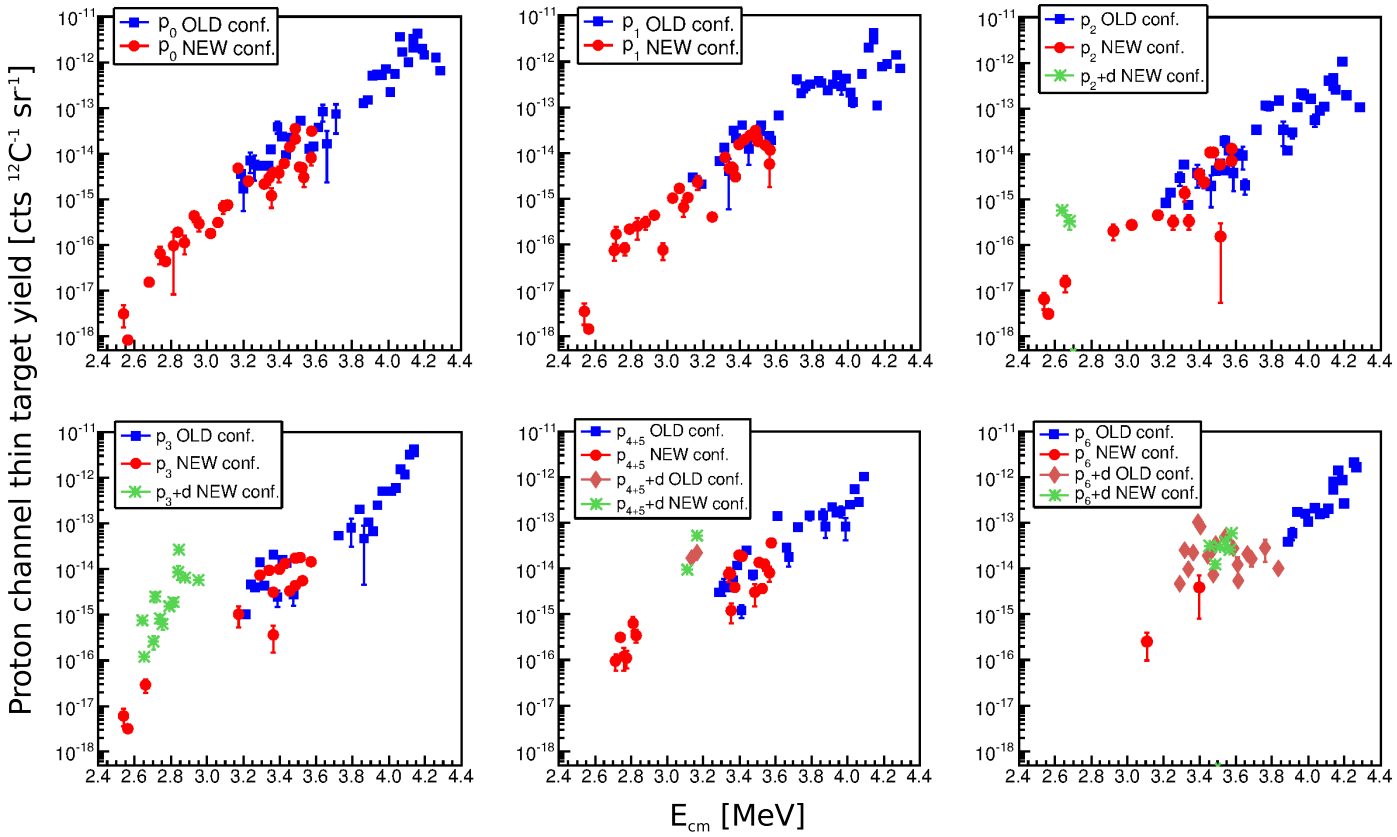

Figure 6.20: Thin target yield [counts/(^{12}C sr)] obtained with the 143° detector. Graphs show data series obtained for different configurations (Old and New). Different proton groups are shown in different plots. At some energies and proton groups, data points include contributions from primary protons coming from the ^{12}C(d,p) reaction. These are clearly indicated as "p_i+d". The data points with extremely large or negative uncertainties were removed since they do not give us any useful information.

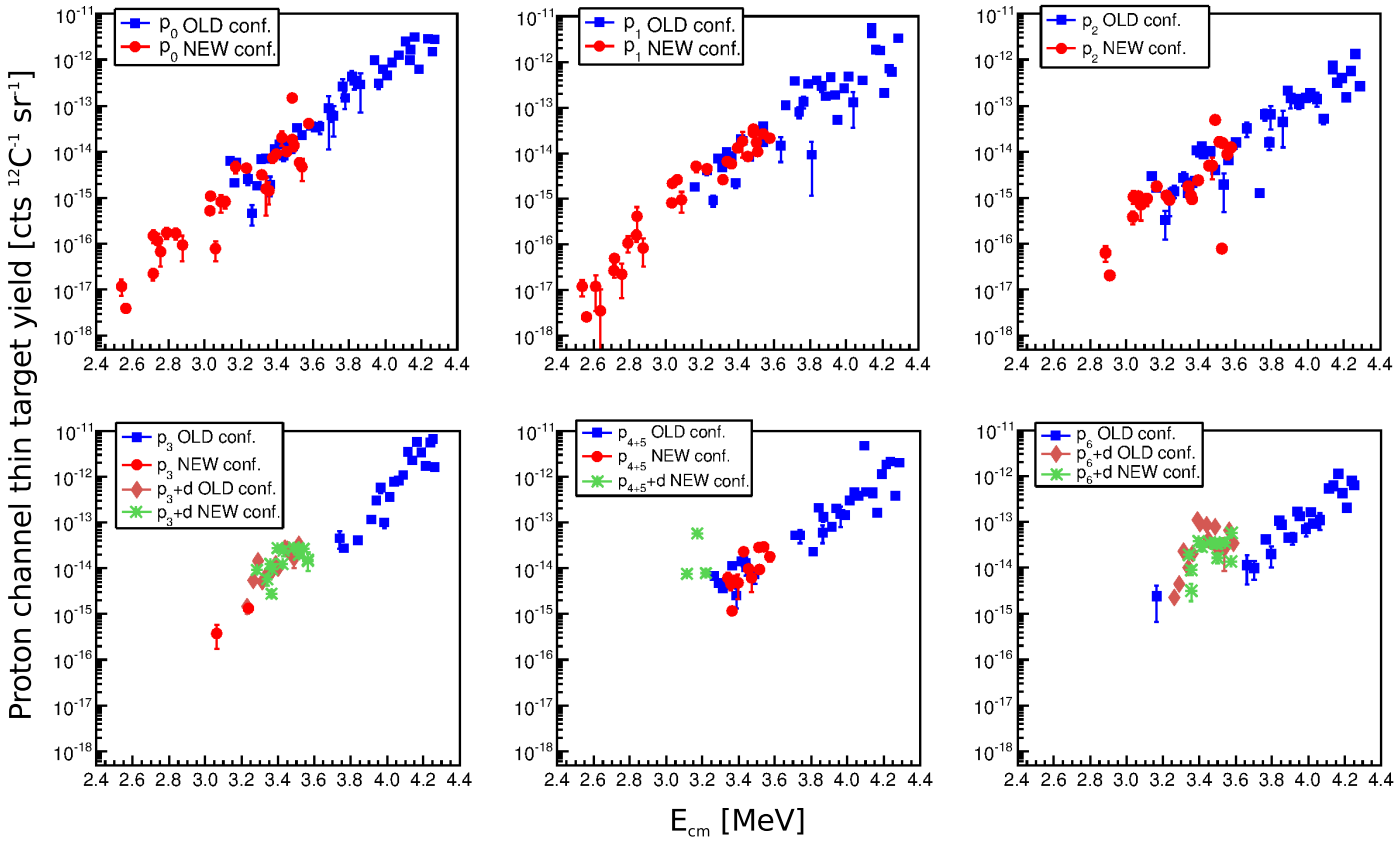

Figure 6.21: Thin target yield [counts/(^{12}C sr)] obtained with the 156°UP detector. Graphs show data series obtained for different configurations (Old and New). Different proton groups are shown in different plots. At some energies and proton groups, data points include contributions from primary protons coming from the ^{12}C(d,p) reaction. These are clearly indicated as "p_i+d". The data points with extremely large or negative uncertainties were removed since they do not give us any useful information.

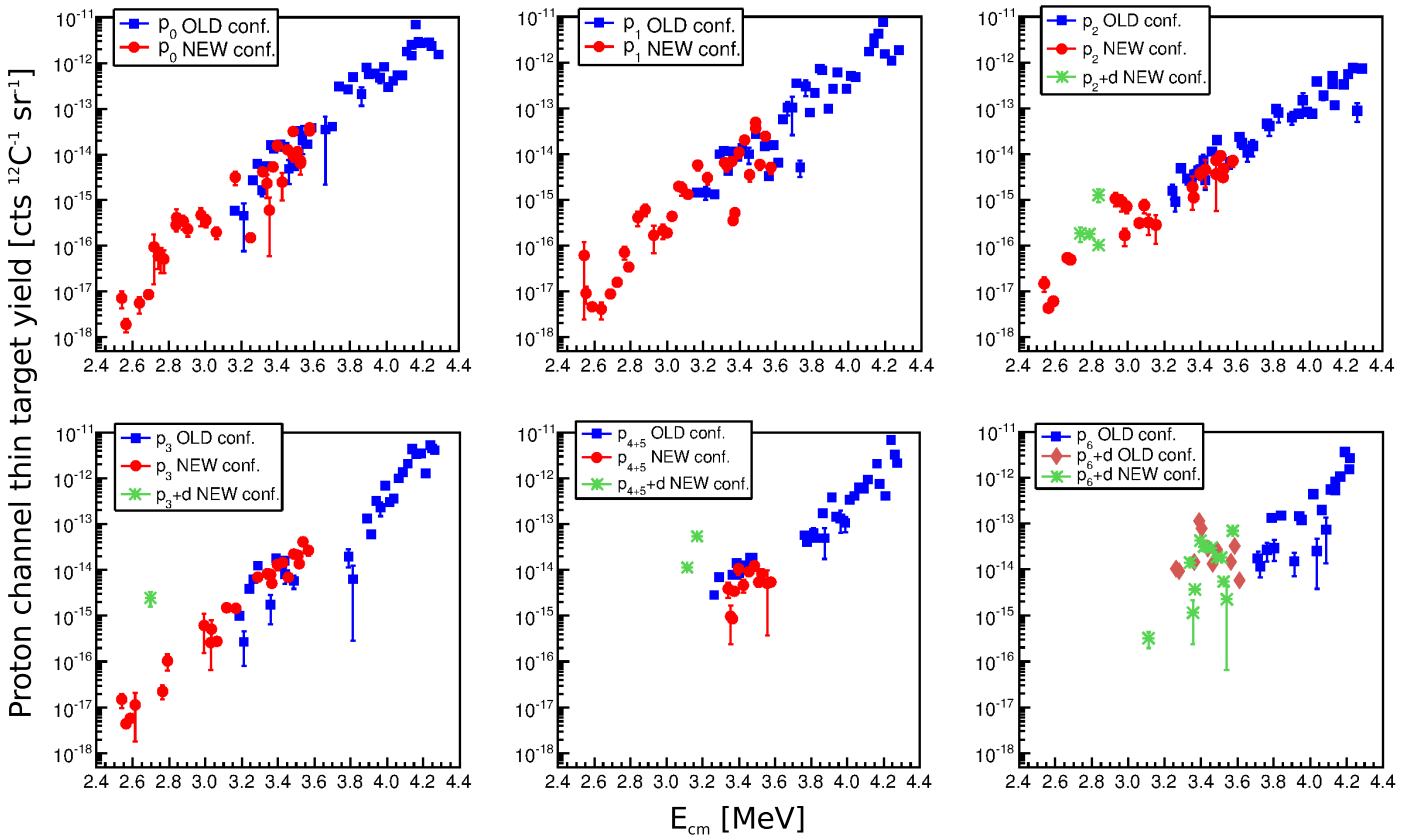

Figure 6.22: Thin target yield [counts/(^{12}C sr)] obtained with the 156°DOWN detector. Graphs show data series obtained for different configurations (Old and New). Different proton groups are shown in different plots. At some energies and proton groups, data points include contributions from primary protons coming from the ^{12}C(d,p) reaction. These are clearly indicated as "p_i+d". The data points with extremely large or negative uncertainties were removed since they do not give us any useful information.

6.3.3 Cross sections

With the thin target yields obtained so far, it is now possible to extract experimental cross sections using equation 2.27 ($\sigma(\mathrm{E}) = \frac{\epsilon\ \mathrm{Y_{diff}}}{\mathrm{W}\ \Delta}$). Since we only used three different detection angles, an angular distribution cannot be calculated, thus we present data in the form of differential cross sections (in μb/sr).

In order to get a "total" differential cross section, I summed the partial values (p_0+p_1+p_2+p_3+p_{4+5}+p_6) averaging the energies (since the effective energies for each group are different) with tolerance < 50 keV. These results can be seen in figure 6.27. The data points affected by contributions from the target deuterium contamination were excluded from the cross section calculations.

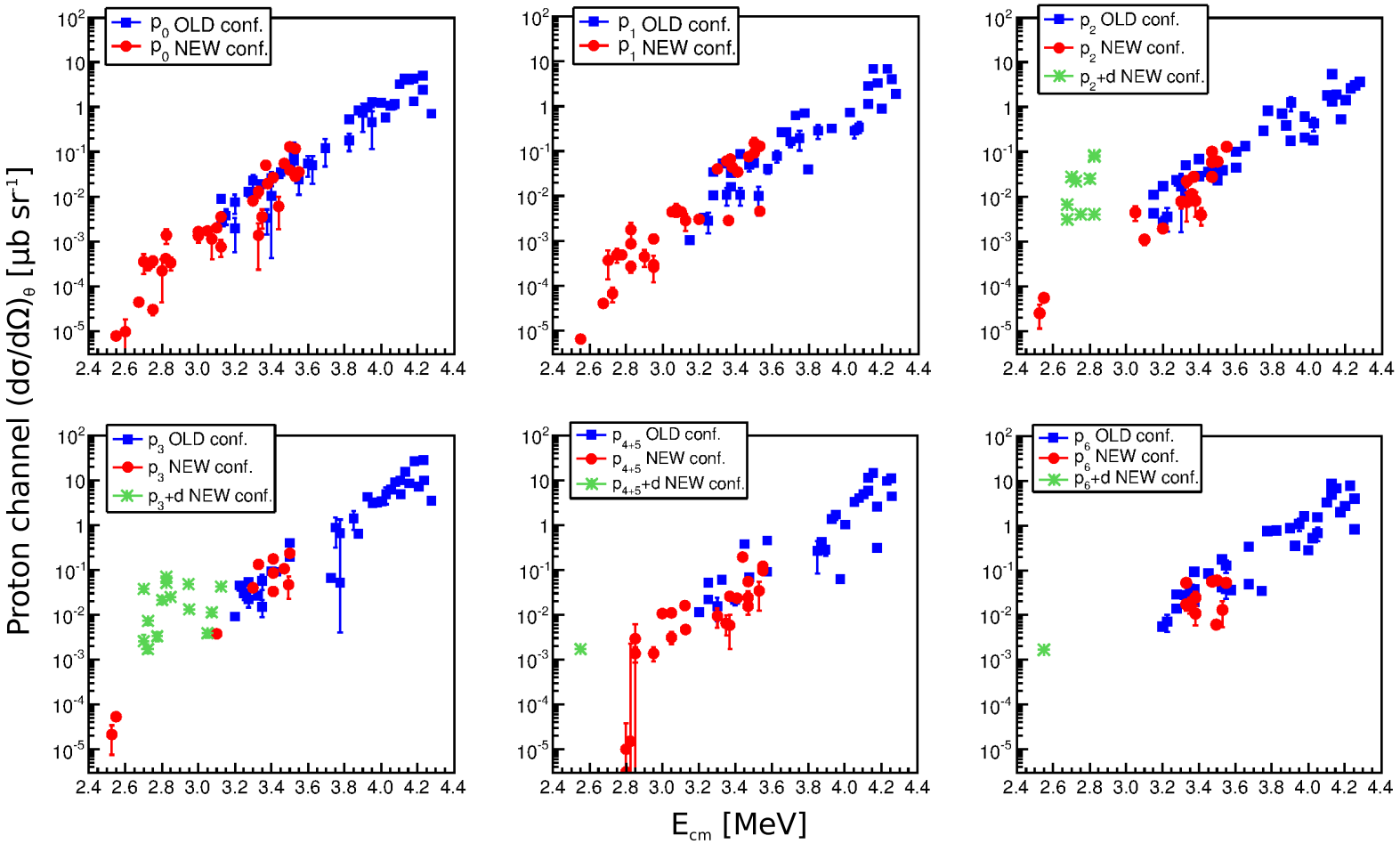

Figure 6.23: Differential cross sections [μb/sr] obtained with the 121° detector. Graphs show data series obtained for different configurations (Old and New). Different proton groups are shown in different plots.

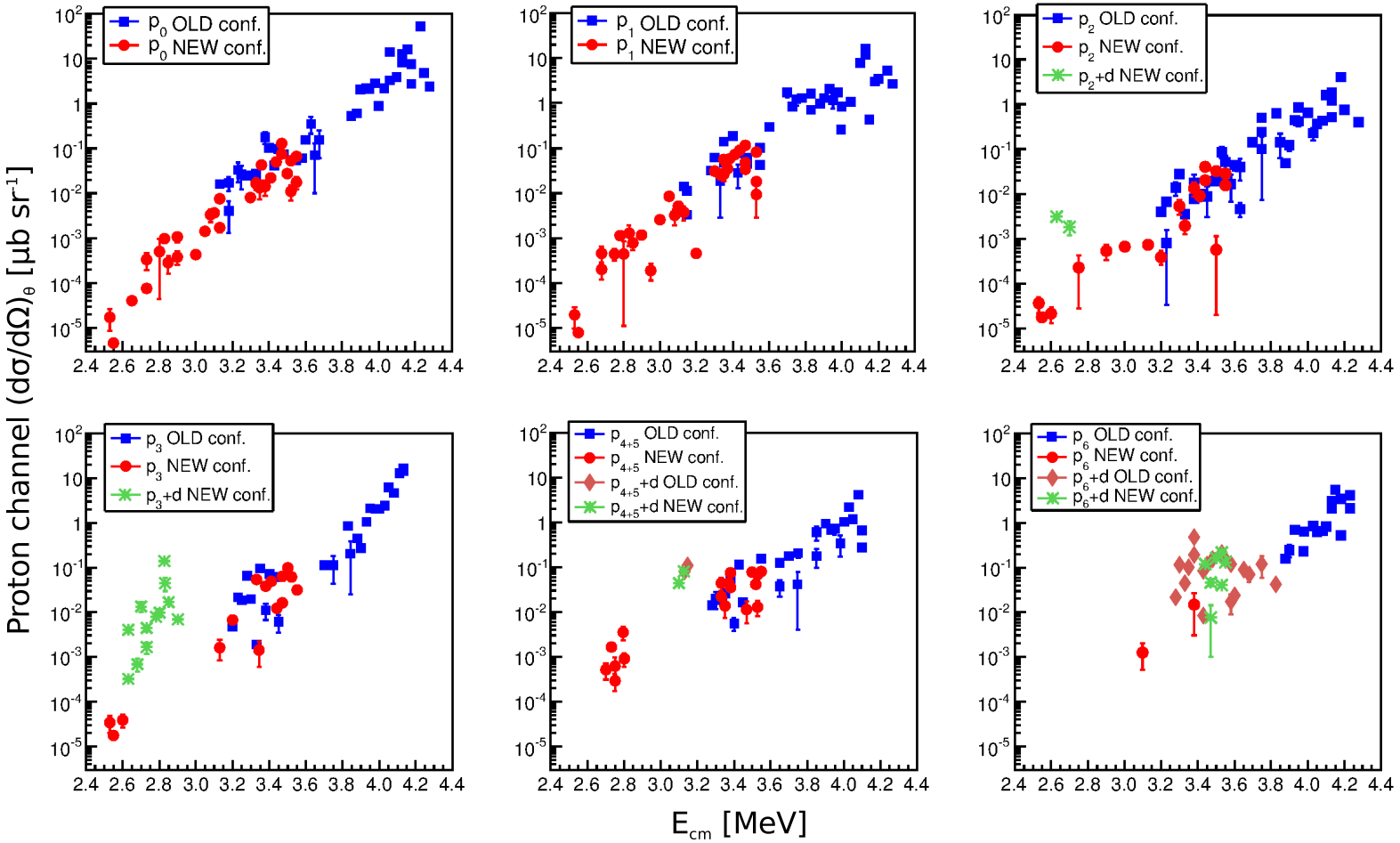

Figure 6.24: Differential cross sections [μb/sr] obtained with the 143° detector. Graphs show data series obtained for different configurations (Old and New). Different proton groups are shown in different plots..

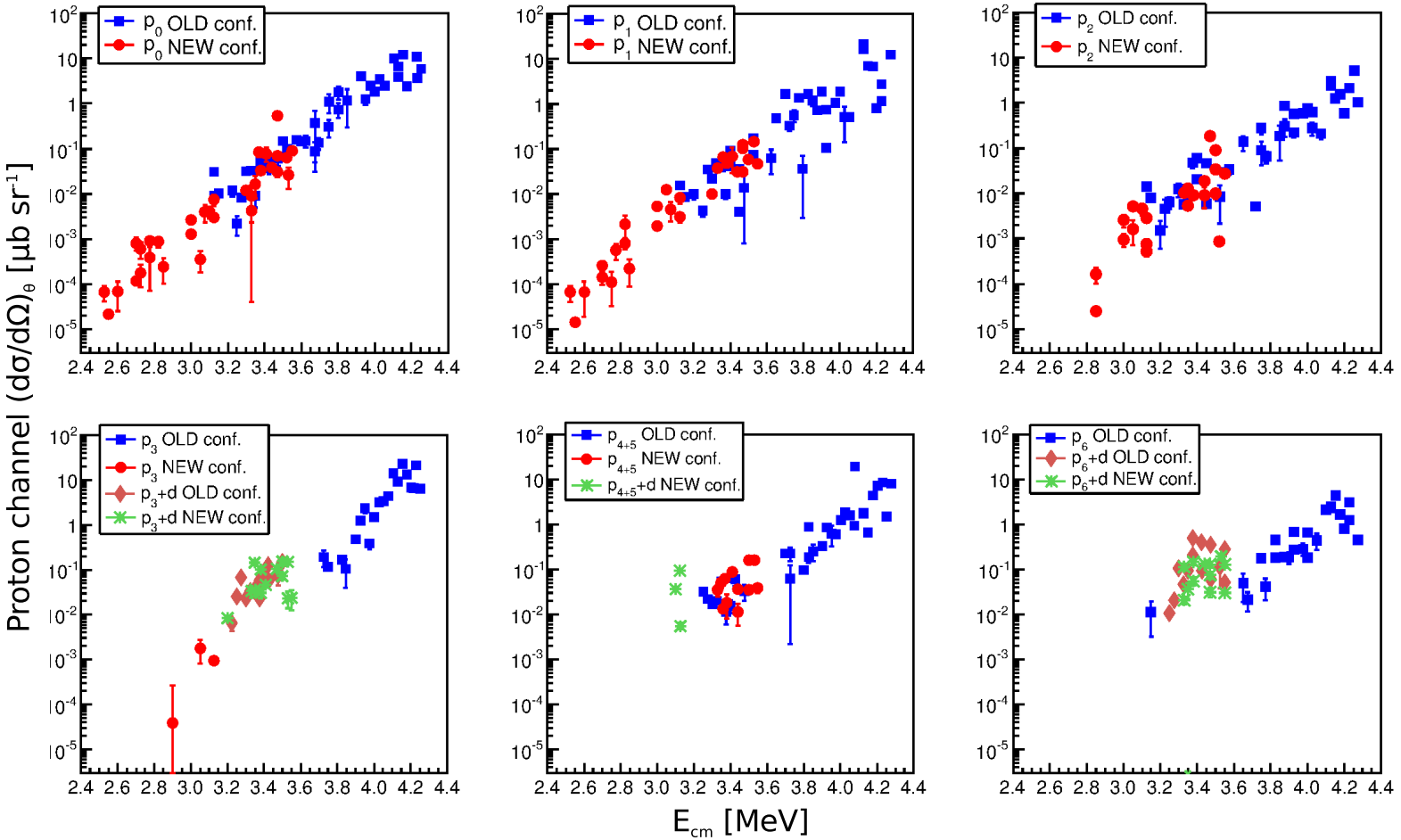

Figure 6.25: Differential cross sections [μb/sr] obtained with the 156°UP detector. Graphs show data series obtained for different configurations (Old and New). Different proton groups are shown in different plots.

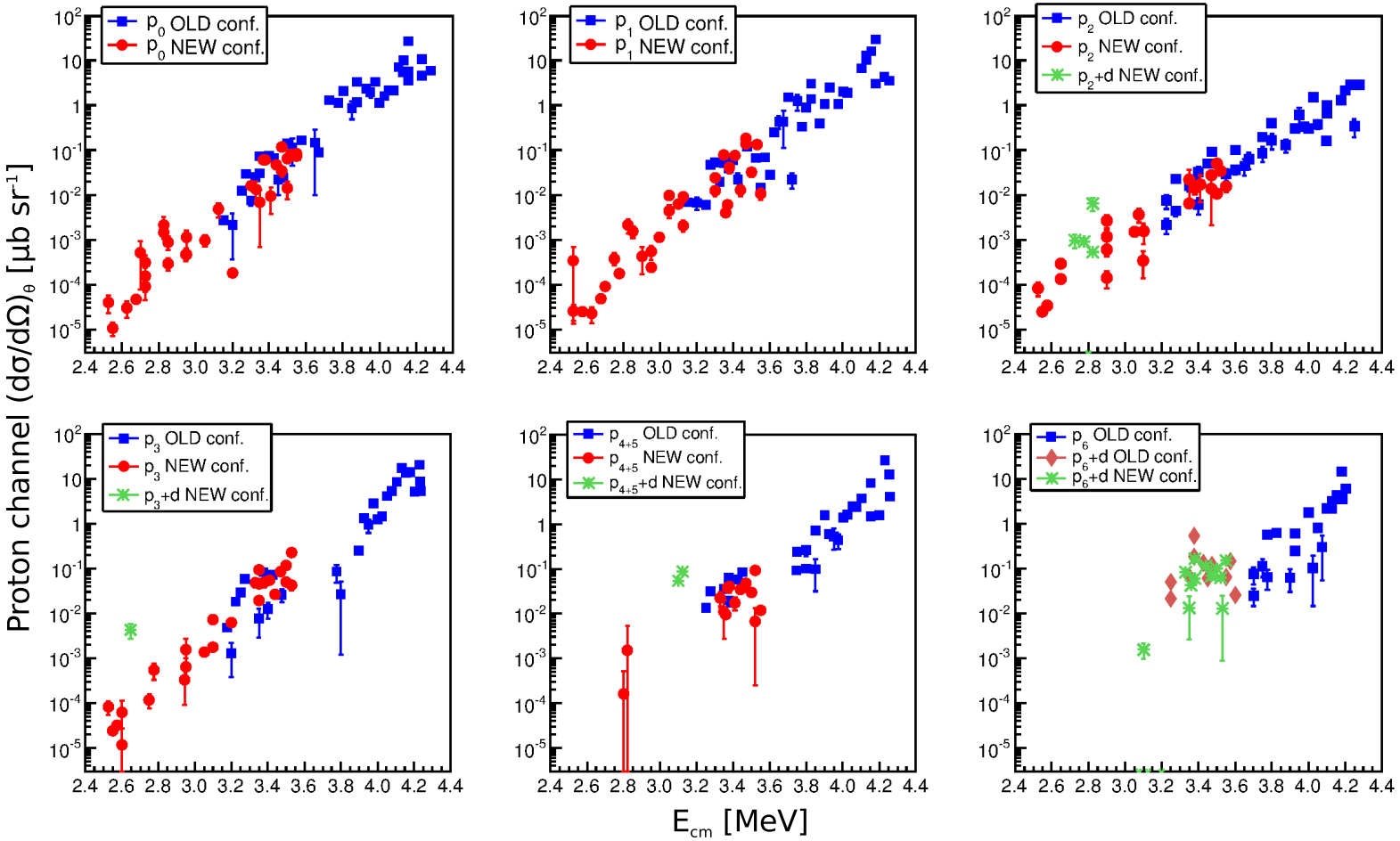

Figure 6.26: Differential cross sections [μb/sr] obtained with the 156°DOWN detector. Graphs show data series obtained for different configurations (Old and New). Different proton groups are shown in different plots.

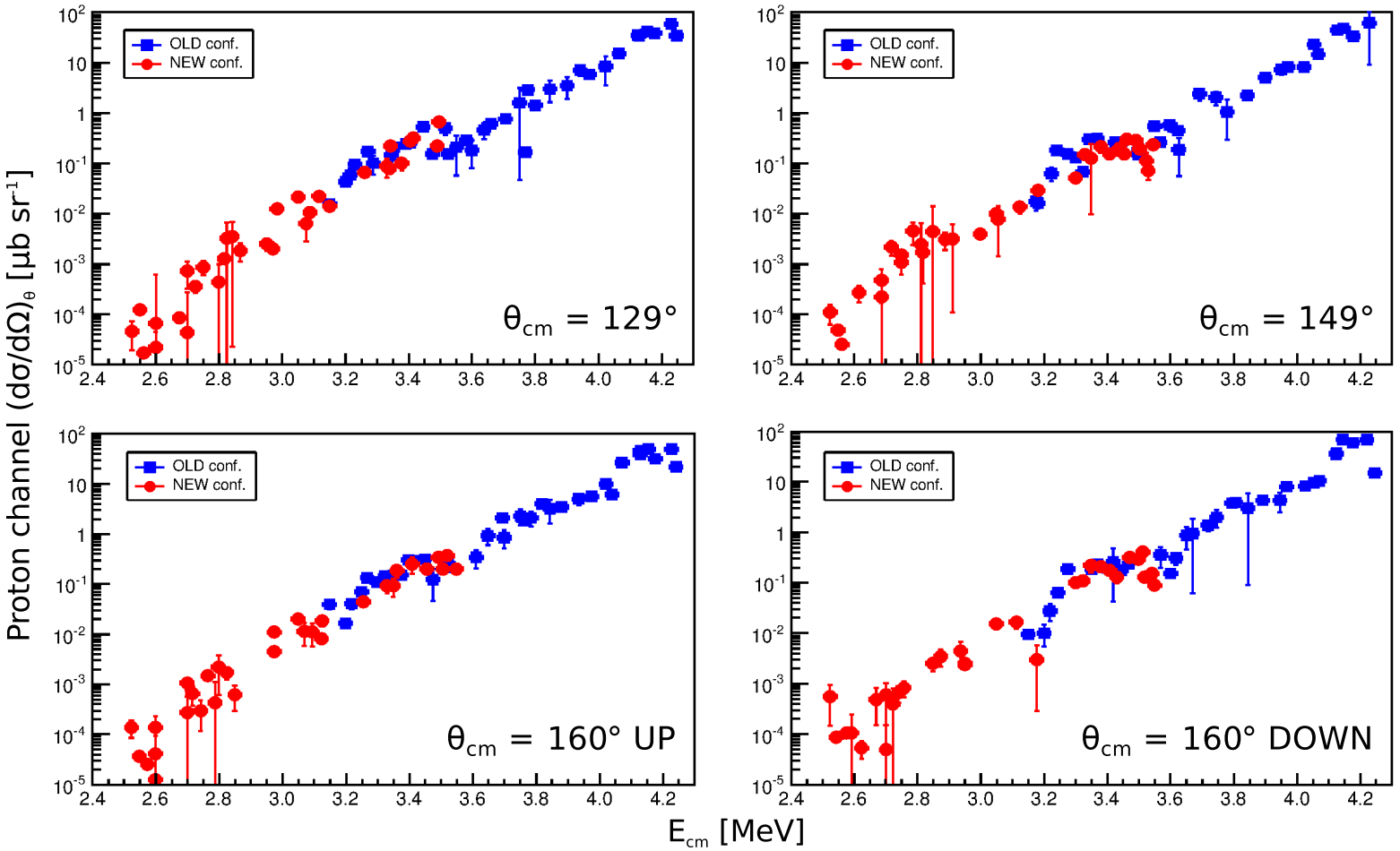

Figure 6.27: Total (summed over all proton groups) differential cross section as a function of effective centre of mass energy for the four detectors used in our measurements (the corresponding centre of mass angles are given in each plot).

As a consistency check, results obtained with both 156° (UP and DOWN) detectors are shown in figure 6.28. The consistency between data sets is generally good over the entire energy range covered, although some discrepancies remain for some individual data points.

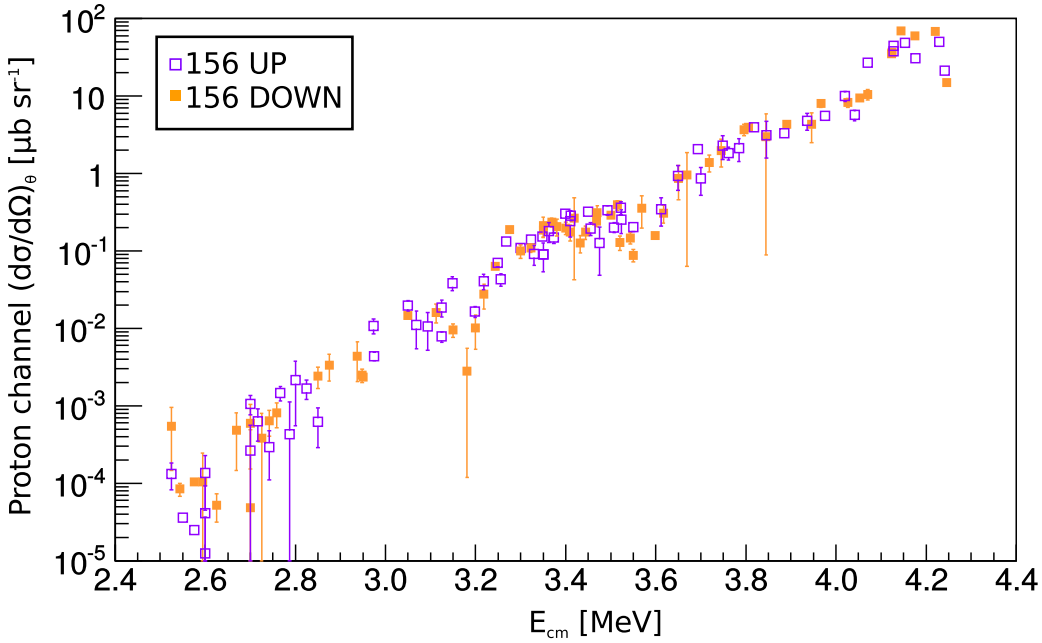

Figure 6.28: Comparison of the total differential cross sections (p_0+p_1+p_2+p_3+p_{4+5}+p_6) obtained with both detectors placed at 156°.

6.3.4 $\tilde{S}$-factors

As discussed in chapter 2.2, data from measurements involving heavy nuclei are better presented in terms of the $\tilde{S}$-factors (equations 2.32 and 2.33). For the $^{12}C+^{12}C$ reaction, the term g in the $\tilde{S}$-factor equation is taken as g = 0.46 MeV^{-1} [22]. Therefore, the modified S-factor $\tilde{S}(E)$ used for these results is given by:

$$\tilde{S}(E) = E\ \sigma(E)\ \exp\left(\frac{87.236}{\sqrt{E}[MeV]} + 0.46\ E[MeV]\right) \tag{6.4}$$

Figures 6.29 to 6.32 show these $\tilde{S}$-factors [10^{16} MeV b sr^{-1}] presented by proton group and detector configuration.

As done with the partial cross sections, the "total" $\tilde{S}$-factors (summed over all proton groups) were calculated and are shown in figures 6.33 to 6.36.

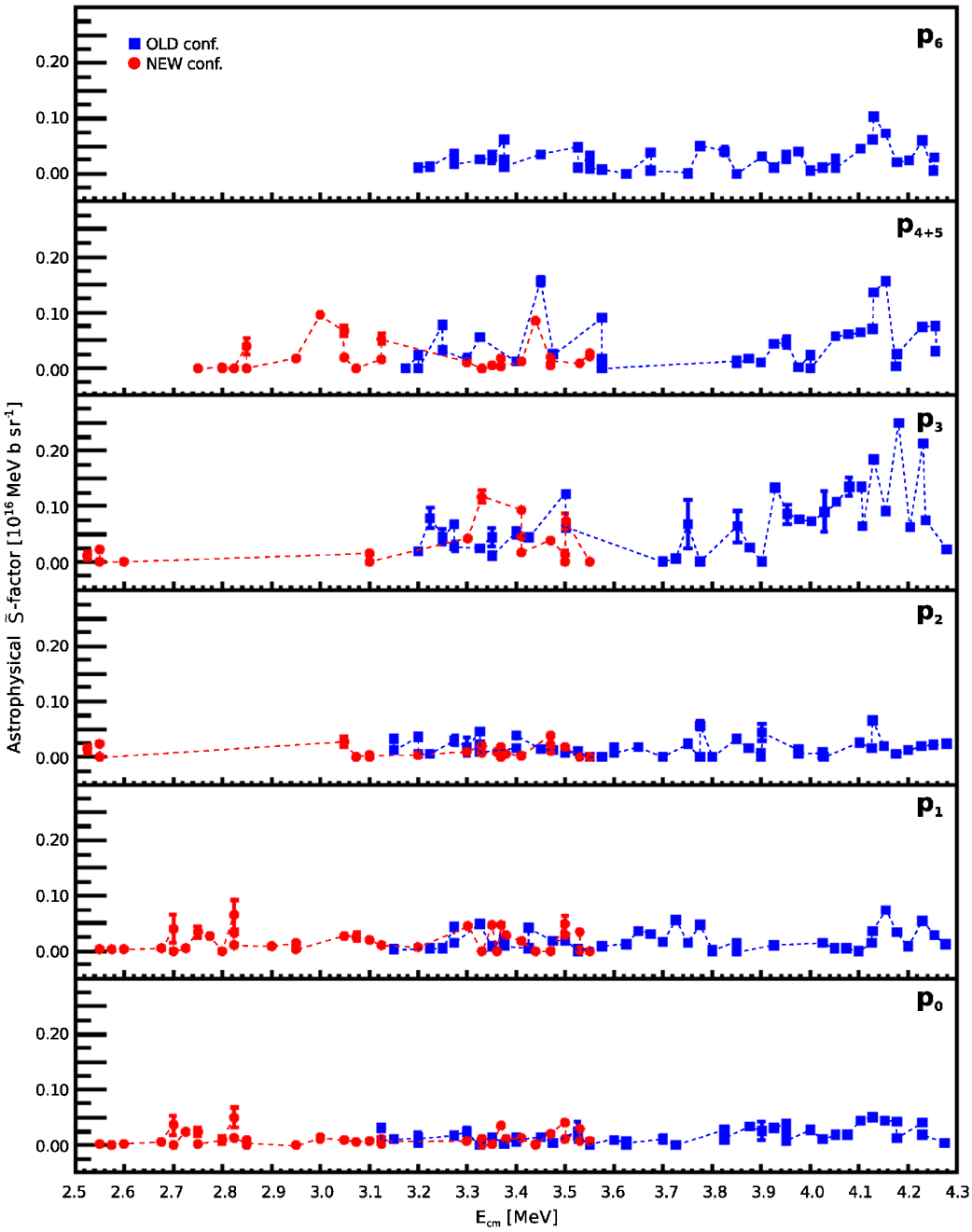

Figure 6.29: S̃-factors obtained with the 121° detector. Results are shown for different proton groups and data sets are separated into Old and New configuration. The dashed lines are only to guide the eye.

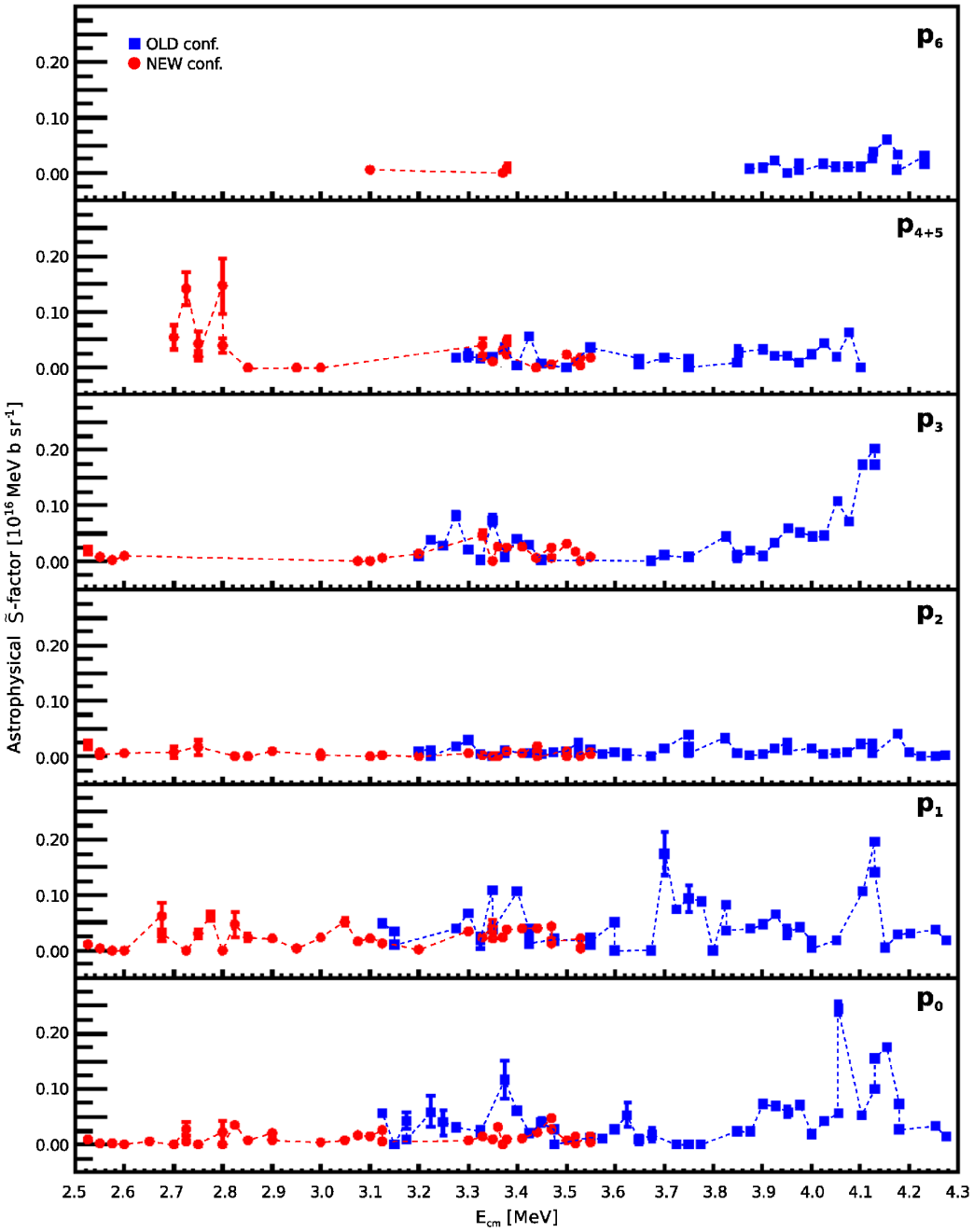

Figure 6.30: S̃-factors obtained with the 143° detector. Results are shown for different proton groups and data sets are separated into Old and New configuration. The dashed lines are only to guide the eye.

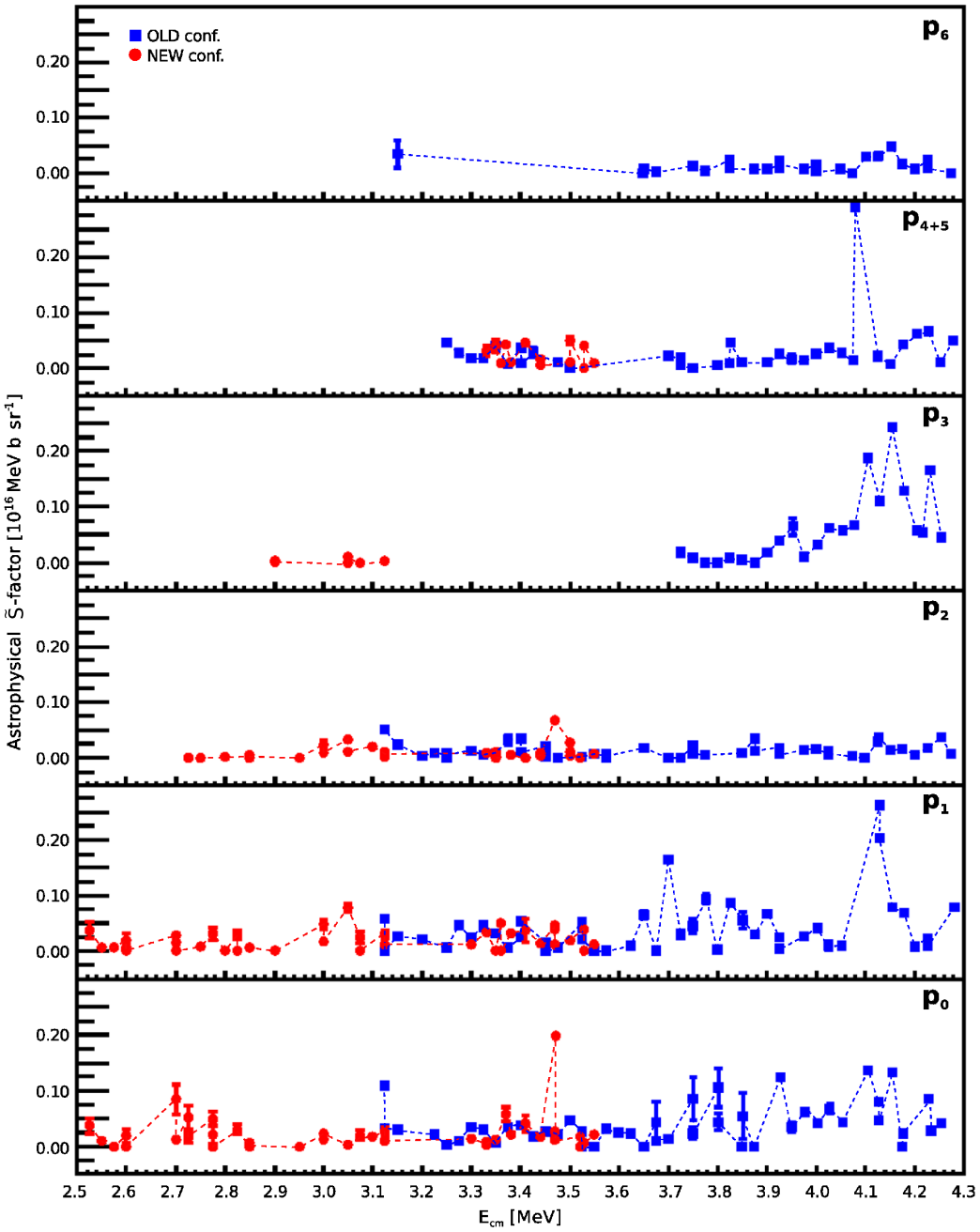

Figure 6.31: S̃-factors obtained with the 156°UP detector. Results are shown for different proton groups and data sets are separated into Old and New configuration. The dashed lines are only to guide the eye.

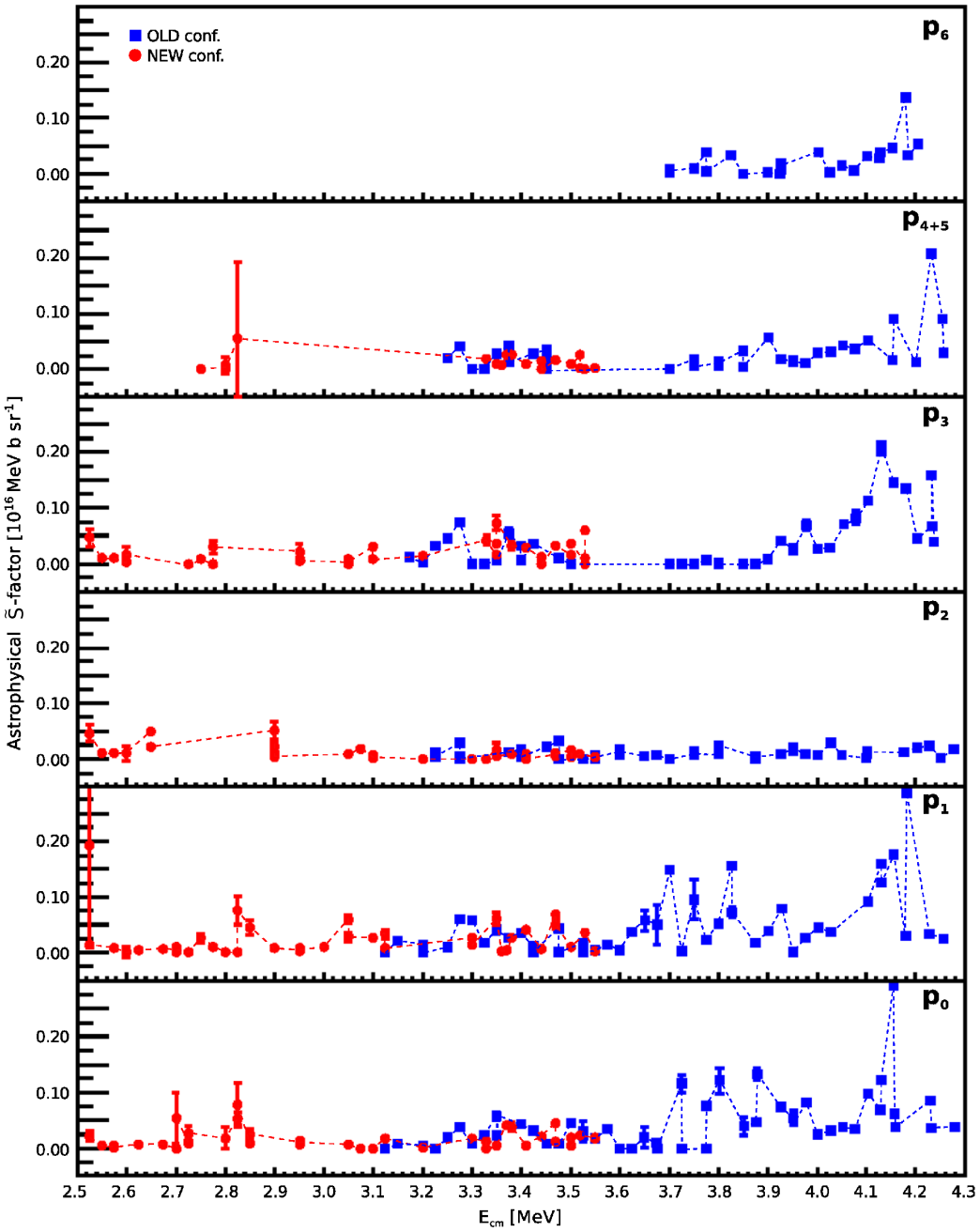

Figure 6.32: S̃-factors obtained with the 156°DOWN detector. Results are shown for different proton groups and data sets are separated into Old and New configuration. The dashed lines are only to guide the eye.

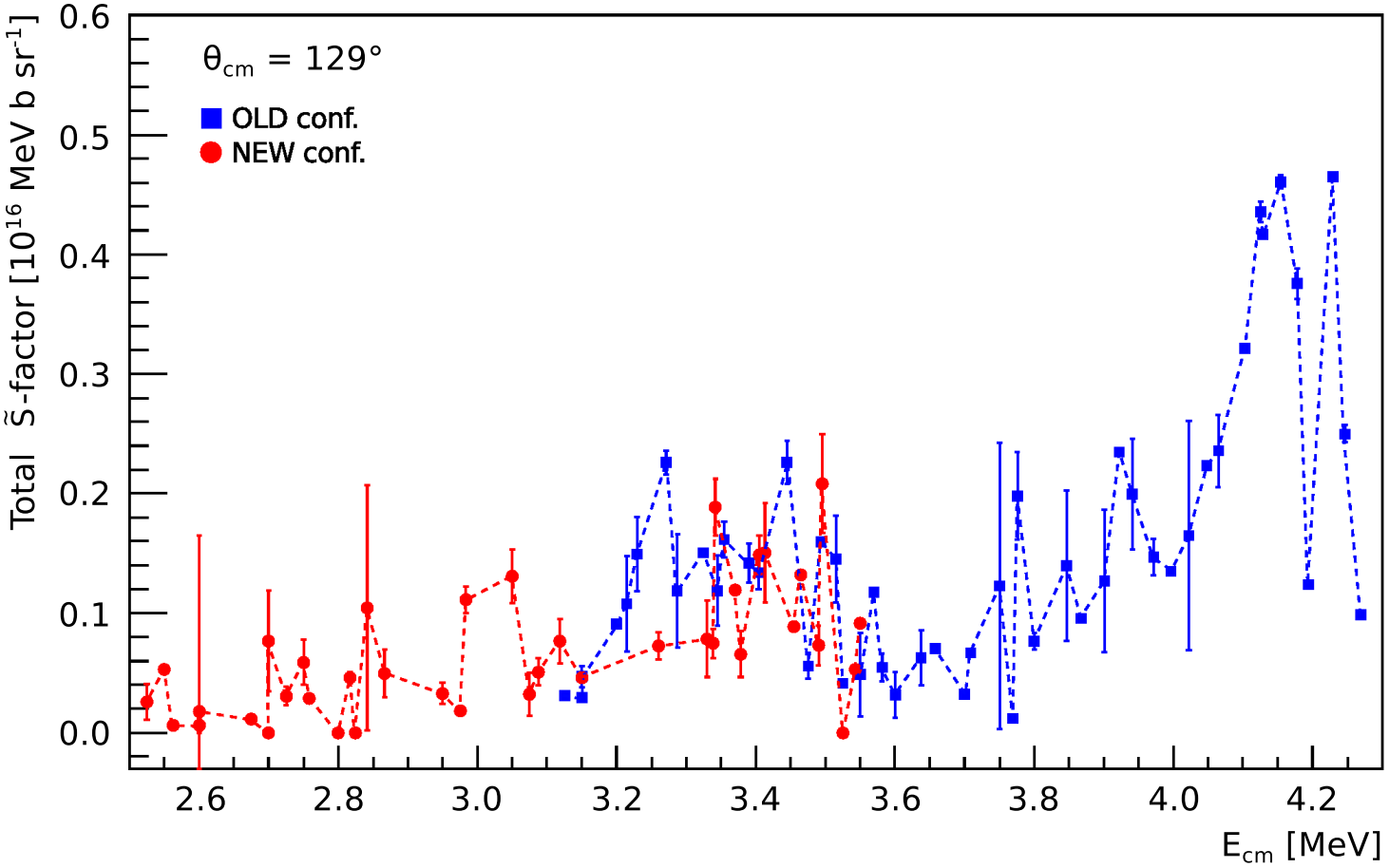

Figure 6.33: Total differential S̃-factors obtained with the $\theta_{\text{lab}} = 121^{\text{o}}$ detector. Data sets are separated into Old and New configuration. The dashed lines are only to guide the eye.

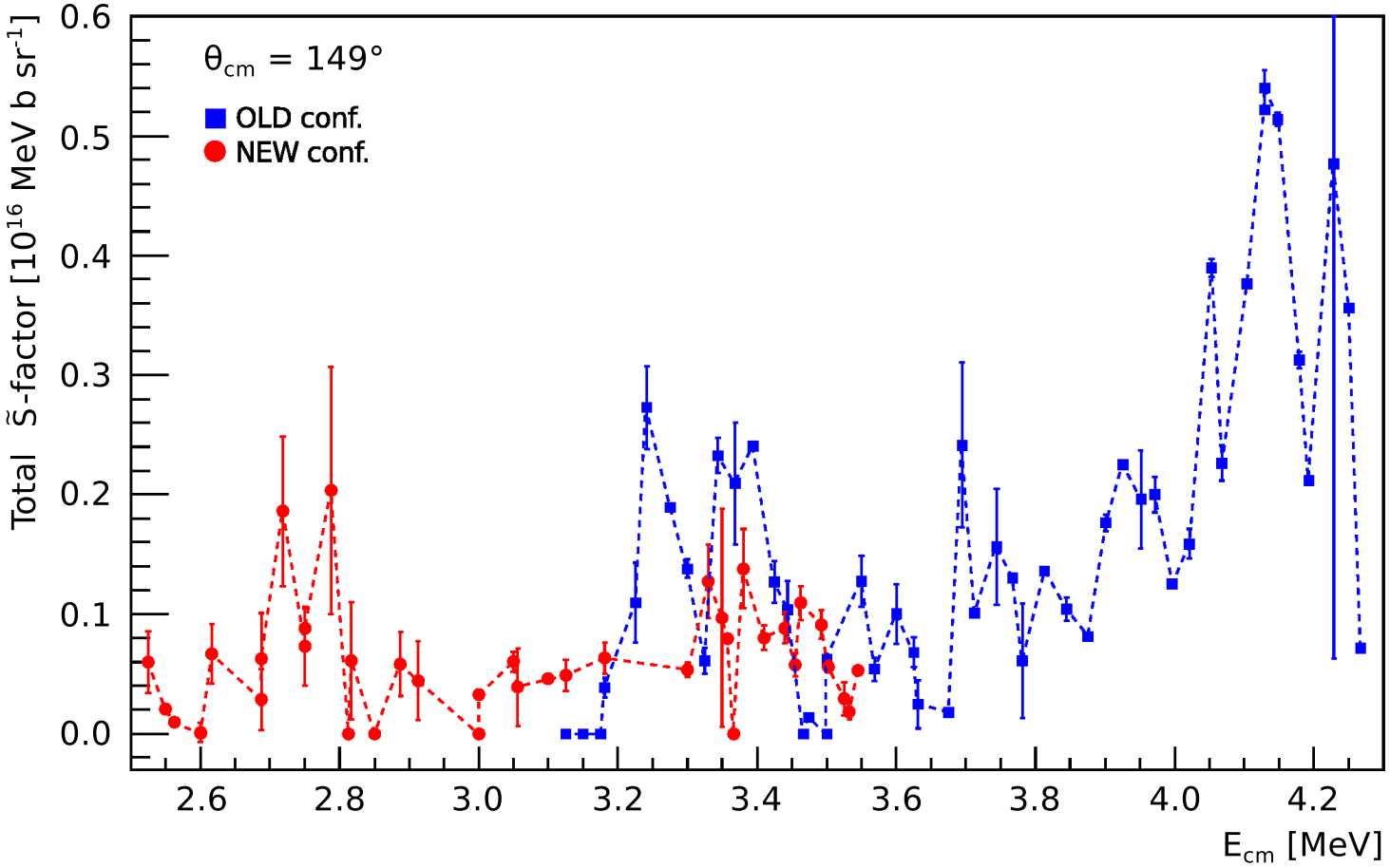

Figure 6.34: Total differential S̃-factors obtained with the $\theta_{\text{lab}} = 143^{\text{o}}$ detector. Data sets are separated into Old and New configuration. The dashed lines are only to guide the eye.

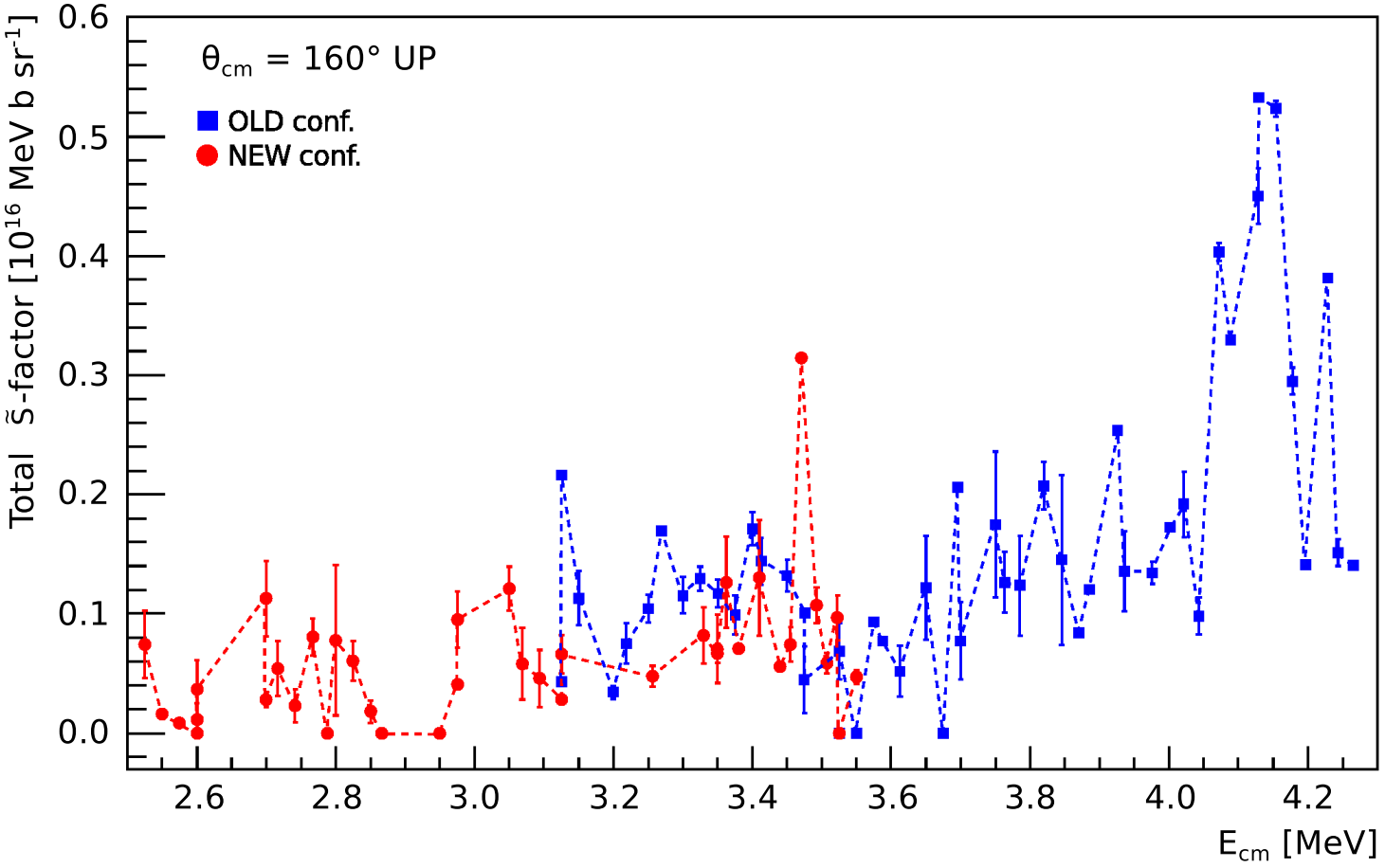

Figure 6.35: Total differential S̃-factors obtained with the $\theta_{\text{lab}} = 156°$UP detector. Data sets are separated into Old and New configuration. The dashed lines are only to guide the eye.

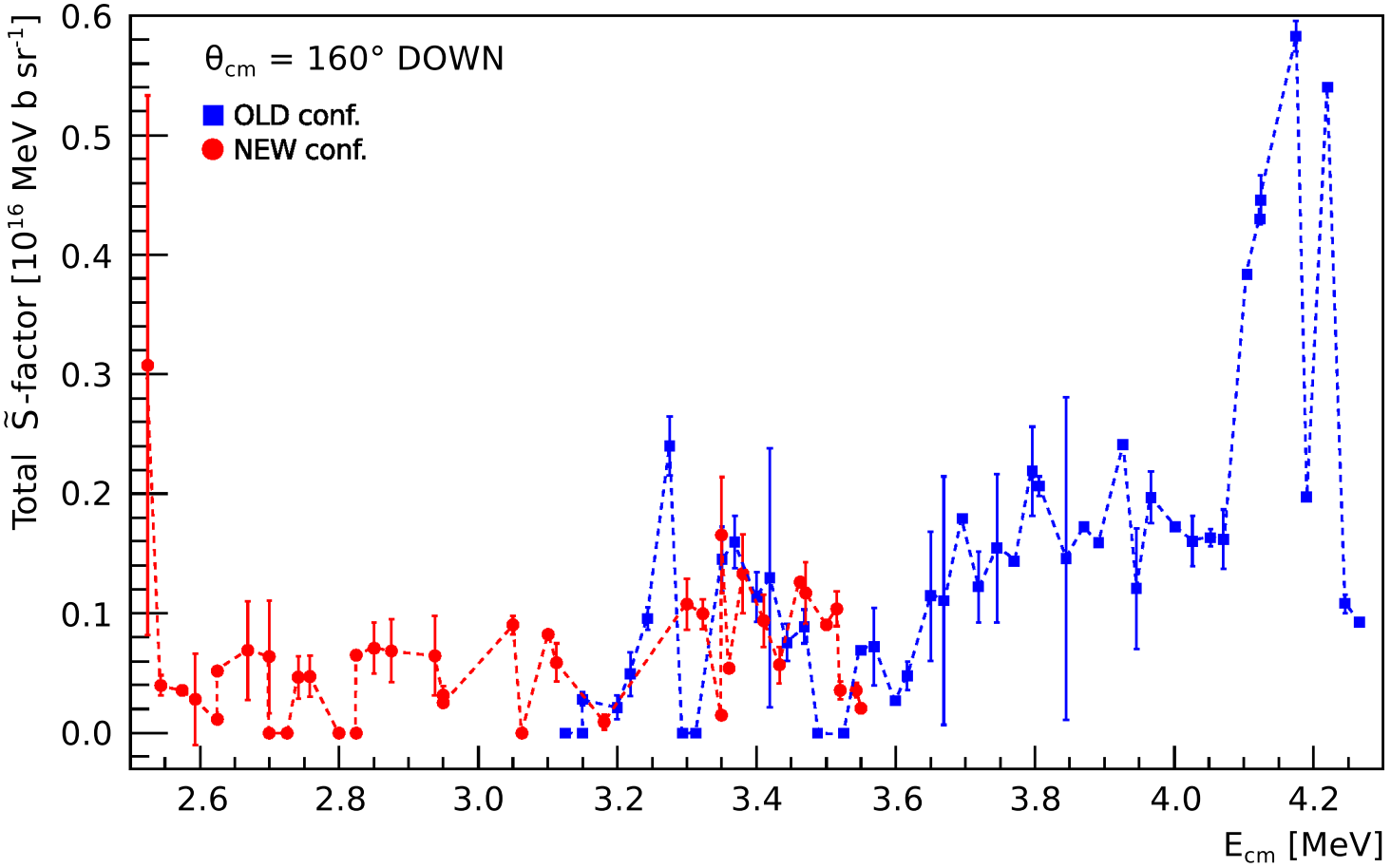

Figure 6.36: Total differential S̃-factors obtained with the $\theta_{\text{lab}} = 156°$DOWN detector. Data sets are separated into Old and New configuration. The dashed lines are only to guide the eye.

Some differences between our Old and New configurations can be seen at first glance. However, it is difficult to perform a correct comparison since the energies of each data point are different. For those data points with the same energy, the same $\tilde{S}$-factor values (within uncertainty) were obtained.

Peaks can be seen at several energies. Some of these peaks correspond to resonances reported in [17, 42–44, 49]. In figures 6.37 to 6.40, the total $\tilde{S}$-factors obtained in this work are shown along with the positions of the reported resonances in the literature. A 20 keV uncertainty in the position of the resonances was considered.

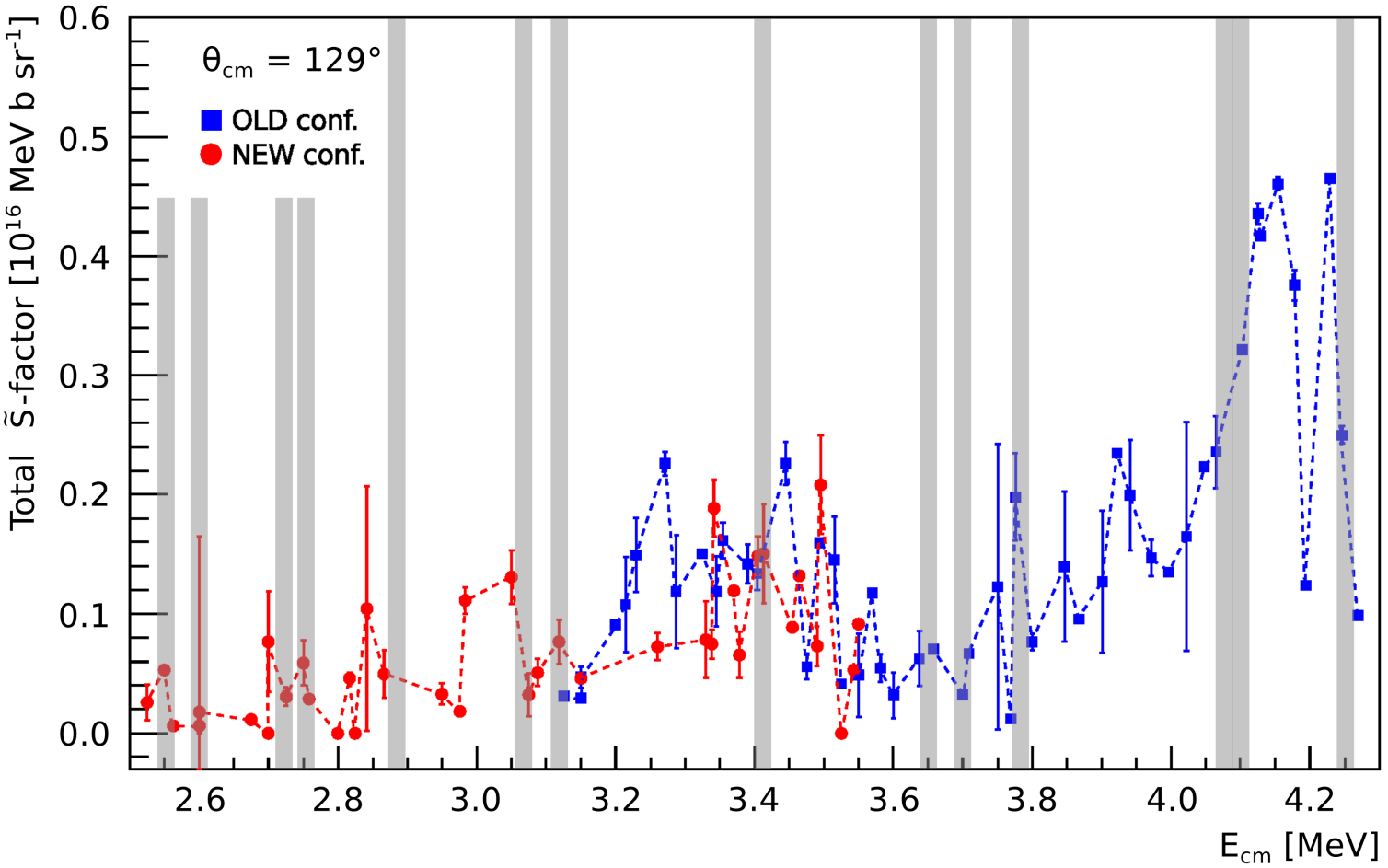

Figure 6.37: S̃-factors obtained with the 121° detector. The shaded regions correspond to the positions of the resonances reported in the works of Becker, Spillane, Zickefoose, Kettner and Aguilera.

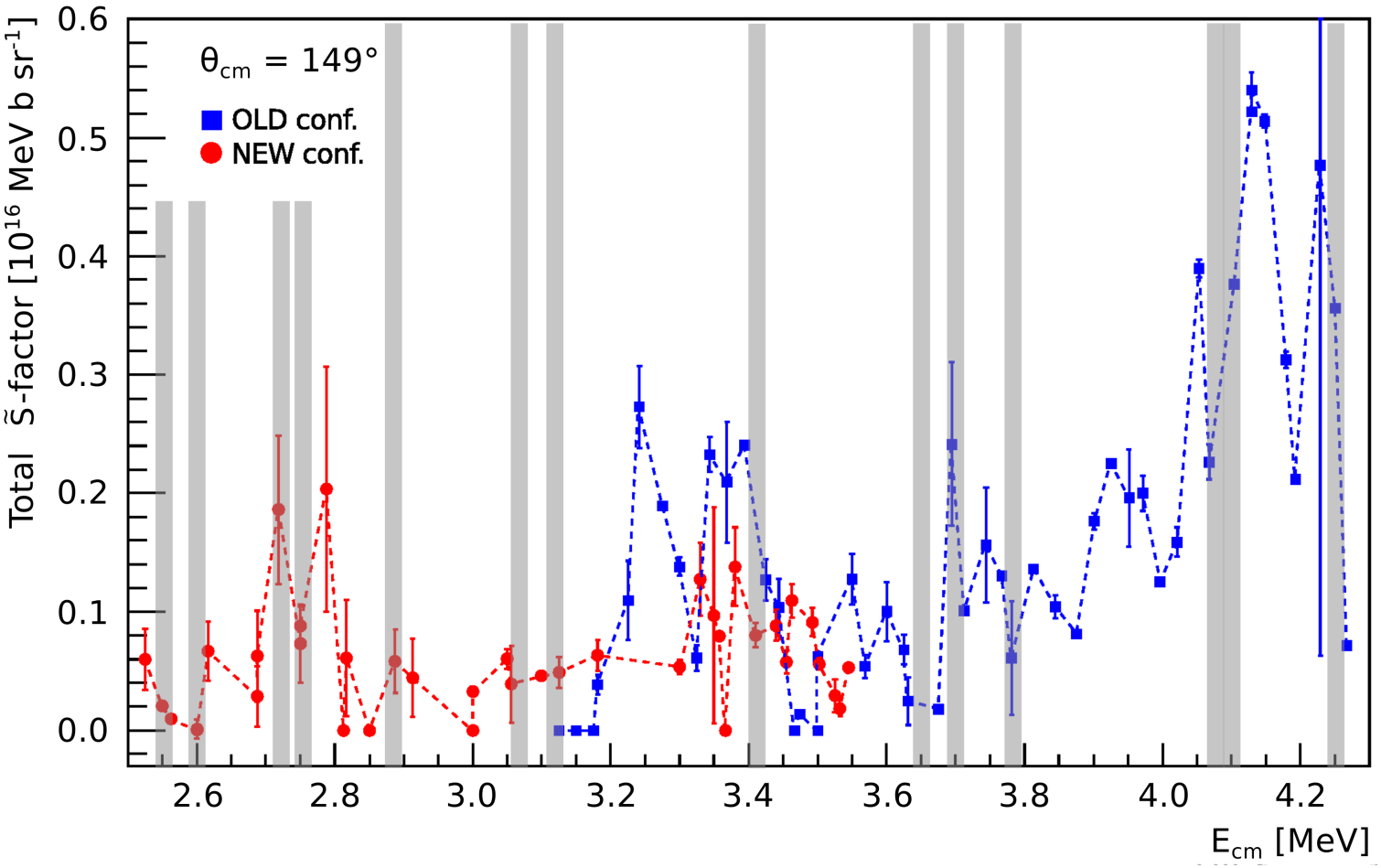

Figure 6.38: S̃-factors obtained with the 143° detector. The shaded regions correspond to the positions of the resonances reported in the works of Becker, Spillane, Zickefoose, Kettner and Aguilera.

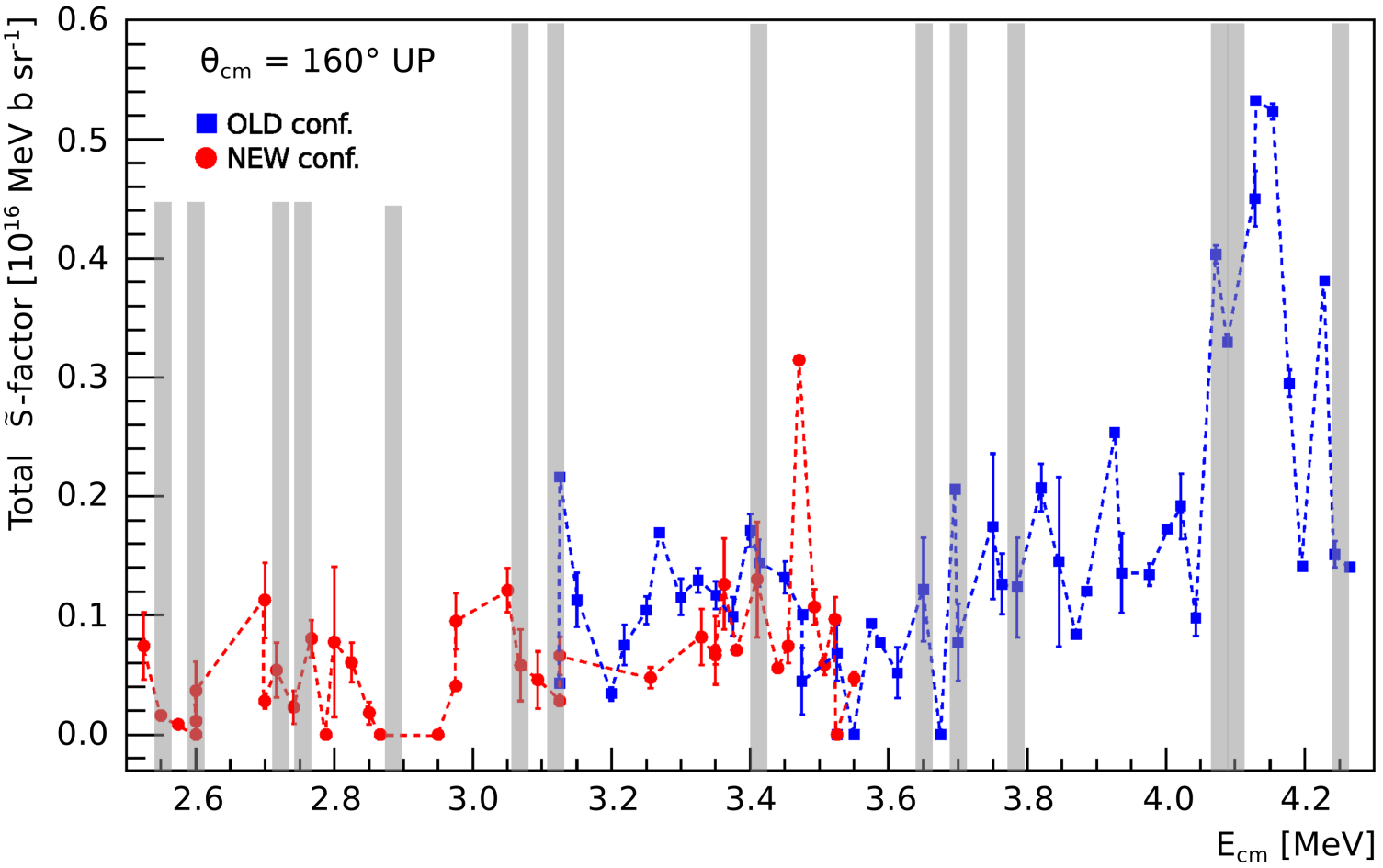

Figure 6.39: S̃-factors obtained with the 156°UP detector. The shaded regions correspond to the positions of the resonances reported in the works of Becker, Spillane, Zickefoose, Kettner and Aguilera.

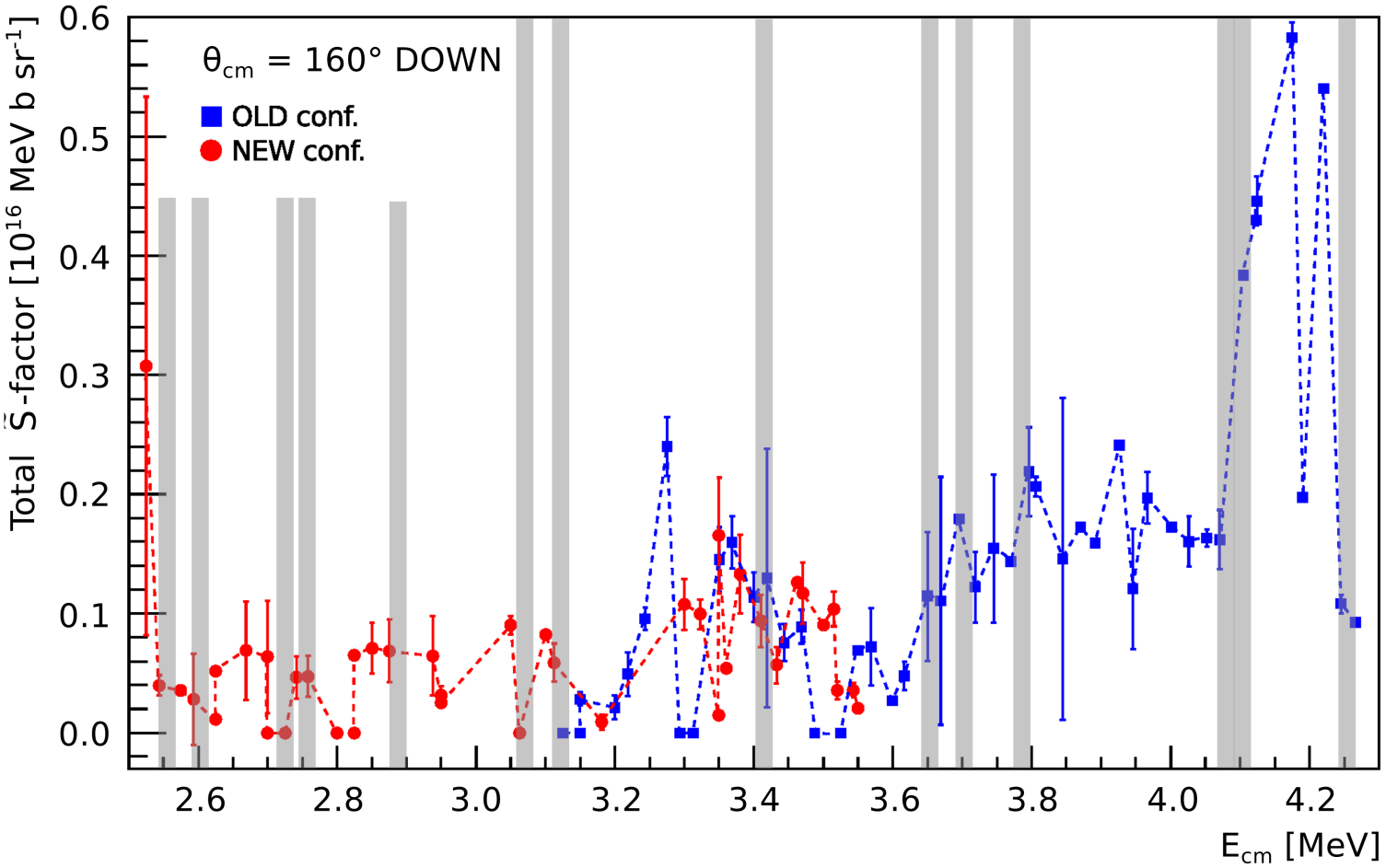

Figure 6.40: S̃-factors obtained with the 156°DOWN detector. The shaded regions correspond to the positions of the resonances reported in the works of Becker, Spillane, Zickefoose, Kettner and Aguilera.

In table 6.2, an analysis of our data at the reported resonant energies is given. When a clear peak could be seen in our data the indication "Resonance" is given. "Resonance*", "Going up" and "No peak" indicate a possible resonance, a resonance nearby and the total absence of a peak in our data, respectively. The lack of a data point at a given energy is indicated with "No data".

Table 6.2: Analysis of our data indicating if whether or not we see a resonance at the resonant centre of mass energies E_{Rcm} reported in the literature (see text for details).

E_{Rcm} [MeV]	121°	143°	156°UP	156°DOWN
4.25	Going up	Going up	No peak	No peak
4.10	Going up	Going up	No data	Going up
4.07	No data	No data	Resonance	No data
3.79	Resonance	No peak	No peak	No data
3.70	Going up	Resonance	Resonance	Resonance
3.65	Resonance	No data	Resonance	Resonance
3.41	Resonance	Going up	Resonance	Resonance
3.12	Resonance	Going up	Resonance	Going up
3.07	Going up	No data	Going up	No peak
2.88	No data	Resonance	No data	No peak
2.76	Resonance	No peak	Resonance	Resonance
2.72	No peak	Resonance	Resonance	No peak
2.60	Resonance*	Resonance*	Resonance*	Resonance*
2.56	Resonance	Going up	Going up	Going up

Nearly all the literature resonances could be confirmed with our work. However, several other peaks can be seen in our data. It should be noted that our data have the finer energy step available to date, which could suggest the presence of narrow resonances never seen before. A more in-depth analysis grounded on theoretical modelling should be performed in order to confirm these possible narrow resonances, but was beyond the scope of this work.

Chapter 7

Discussion and conclusions

In this work, the $^{12}C+^{12}C$ reactions were investigated using, for the first time, the ΔE-Erest particle identification technique to unequivocally identify protons and α particles, avoiding the need to rely on kinematic calculations to disentangle between the two. We also have been able to address the ^{2}H contamination in the carbon targets for the first time and exclude any data points that were affected by $^{12}C+^{2}H$ primary protons. The cross section data were obtained by differentiation of thick target yields at consecutive energies using, to our knowledge, the smallest available energy steps to date. We observed several resonance and resonance-like structures in our results, some of them compatible with previously reported resonances (figures 6.37 to 6.40), and some others observed for the first time. A comparison between results from two detectors at the same angle showed a general agreement, even though some discrepancies remained at a some energies.

7.1 Comparison with previous works

Given that we only measured at three different angles, an angular distribution could not be calculated. Thus, in order to compare our results with those obtained by other groups using charge particle identification, an isotropic angular distribution was assumed since all cross sections σ and modified astrophysical S-factors $\tilde{S}(E)$ available in the literature are angle integrated (following experimental angular distribution analysis). Differences between our results obtained at different angles were observed, which indicates an anisotropic angular distribution. Therefore, these comparisons should only be regarded qualitatively. Additionally, we also compared our "total" (summed over all proton groups) $\tilde{S}(E)$ with those obtained by other groups using gamma-spectroscopy. In this case, isotropic angular distributions were assumed.
Because of different type of results reported, different comparisons were made. Summaries of the results presented in previous works are given in tables 7.1 and 7.2 (for charged particle detection and gamma-spectroscopy, respectively), where "total" refers to the sum of all proton groups.

Table 7.1: Angle integrated results presented in the literature by the groups that used charged particle detection to measure the ^{12}C(^{12}C,p) reaction. Indicated are: measured energy range; detection angle used; and whether the data presented are partial or total (summed over all proton groups) cross sections or $\tilde{S}$-factors.

Group	E_{cm} [MeV]	θ_{cm} [deg]	Type of data presented
Zickerfoose *et al.* [42]	2.10-4.00	135	p_0+p_1 Y^{∞}
Mazarakis and Stevens [40]	2.45-5.00	20-80	partial and total σ
Becker *et al.* [41]	2.80-6.30	10-90	total σ and partial $\tilde{S}$(E)
Patterson *et al.* [28]	3.23-8.75	20-80	total σ

Table 7.2: Total $\tilde{S}$-factors results presented in the literature by groups that used gamma-ray detection to measure the ^{12}C(^{12}C,p) reaction. Indicated are: measured energy range and detector-target distance.

Group	E_{cm} [MeV]	Target distance [cm]
Barrón-Palos *et al.* [39]	2.25-6.00	2.0
Kettner *et al.* [43]	2.45-6.15	1.4
Spillane *et al.* [44]	2.10-4.75	2.0

7.1.1 Thick target yields

Zickerfoose *et al.* [42] measured the thick target yield of the $^{12}C(^{12}C,p_{0+1})^{23}Na$ reaction and presented they results assuming angular isotropy (W = 1). A plot showing their isotropic p_{0+1} thick target yield and our p_{0+1} data (also assuming angular isotropy) can be found in figure 7.1. A general consistency in the thick target yield trend at E< 7.20 MeV can be seen. At higher energies, Zickerfoose data points are systematically lower than ours, possibly due to an anisotropy in the angular distribution.

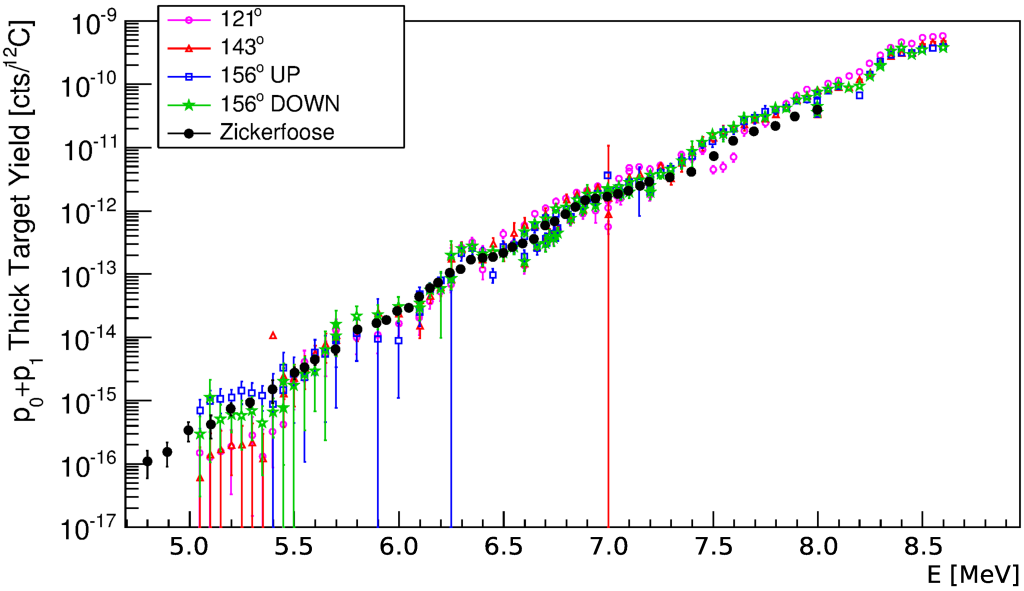

Figure 7.1: Thick target yield (after isotropy was assumed) of the p_{0+1} groups obtained by Zickerfoose [42] (filled circles) and our results (assuming angular isotropy, open symbols).

7.1.2 Partial cross sections

The angle integrated partial cross sections σ_p reported by Mazarakis and Stevens [40] were compared with our data assuming an isotropic angular distribution (figures 7.2 to 7.5). A general consistency can be appreciated at energies $E_{cm} > 2.8$ MeV. At lower energies, Mazarakis data points are considerably higher than ours possibly due to $^{1,2}H$ contamination in their targets (which we were able to reduce or discard).

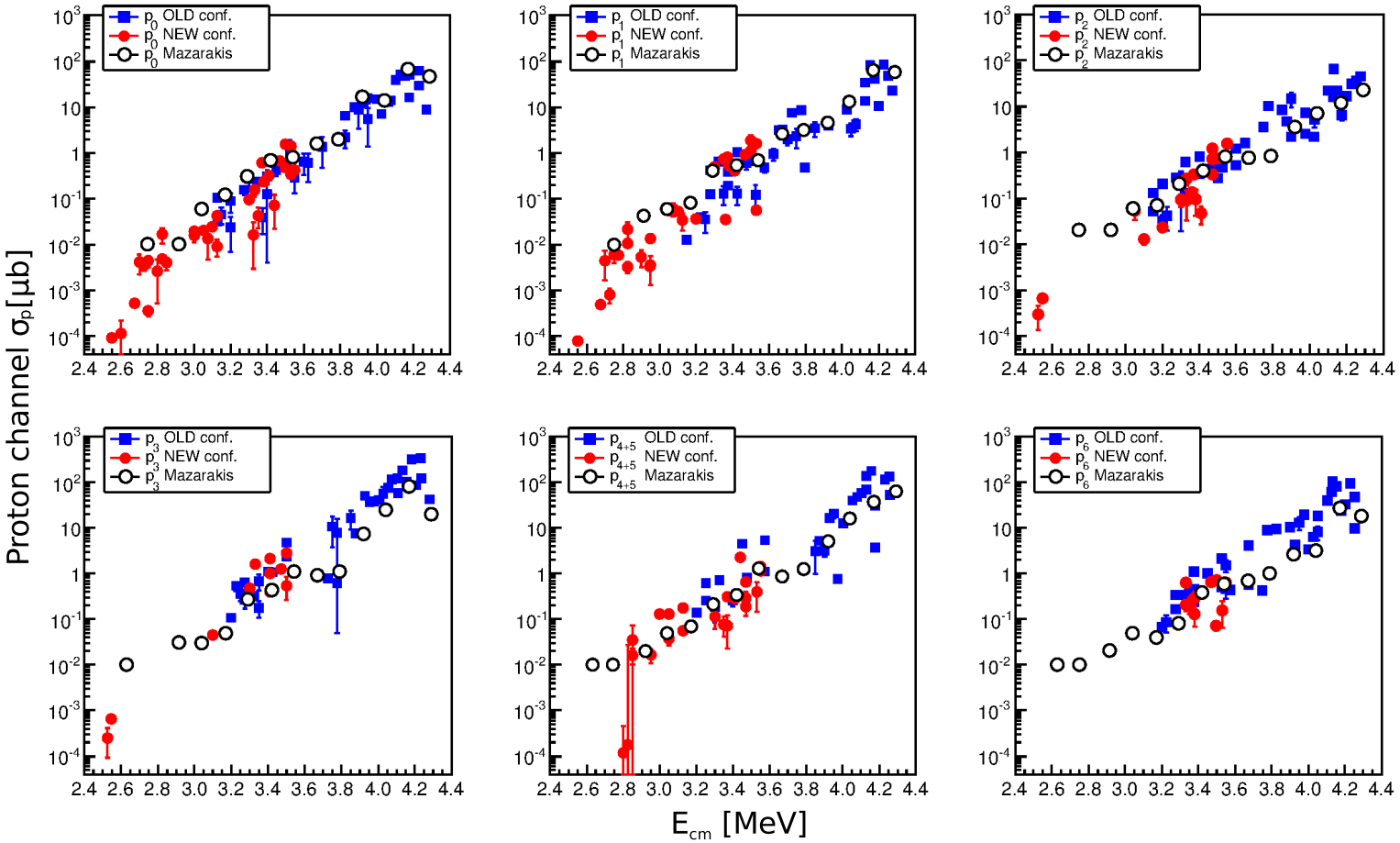

Figure 7.2: Angle integrated partial cross sections σ_p obtained by Mazarakis and Stevens. Our data from the 121° detector is also shown (assuming an isotropic angular distribution). Results are presented for different proton groups and our data sets are separated into Old and New configuration.

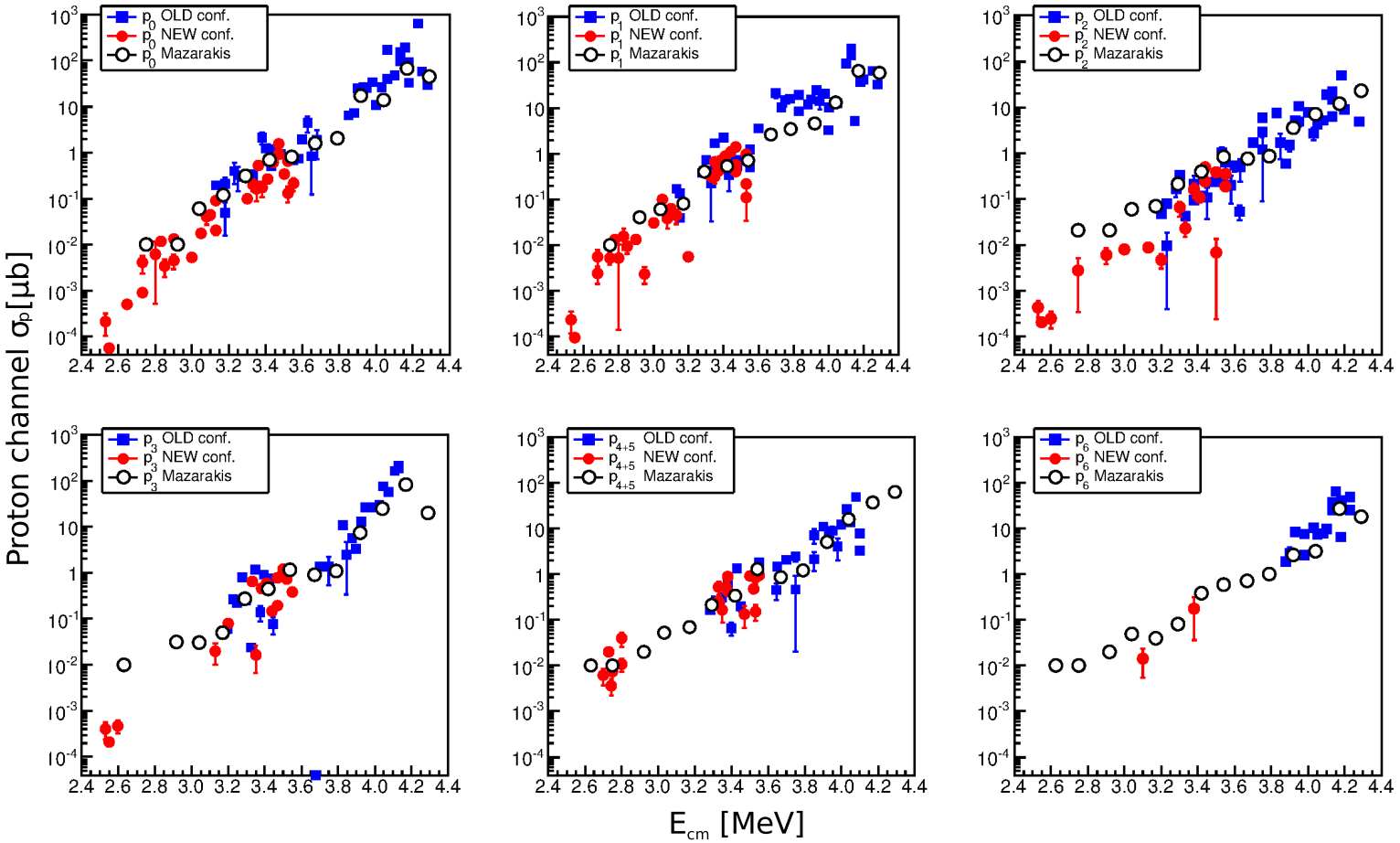

Figure 7.3: Angle integrated partial cross sections σ_p obtained by Mazarakis and Stevens. Our data from the 143° detector is also shown (assuming an isotropic angular distribution). Results are presented for different proton groups and our data sets are separated into Old and New configuration.

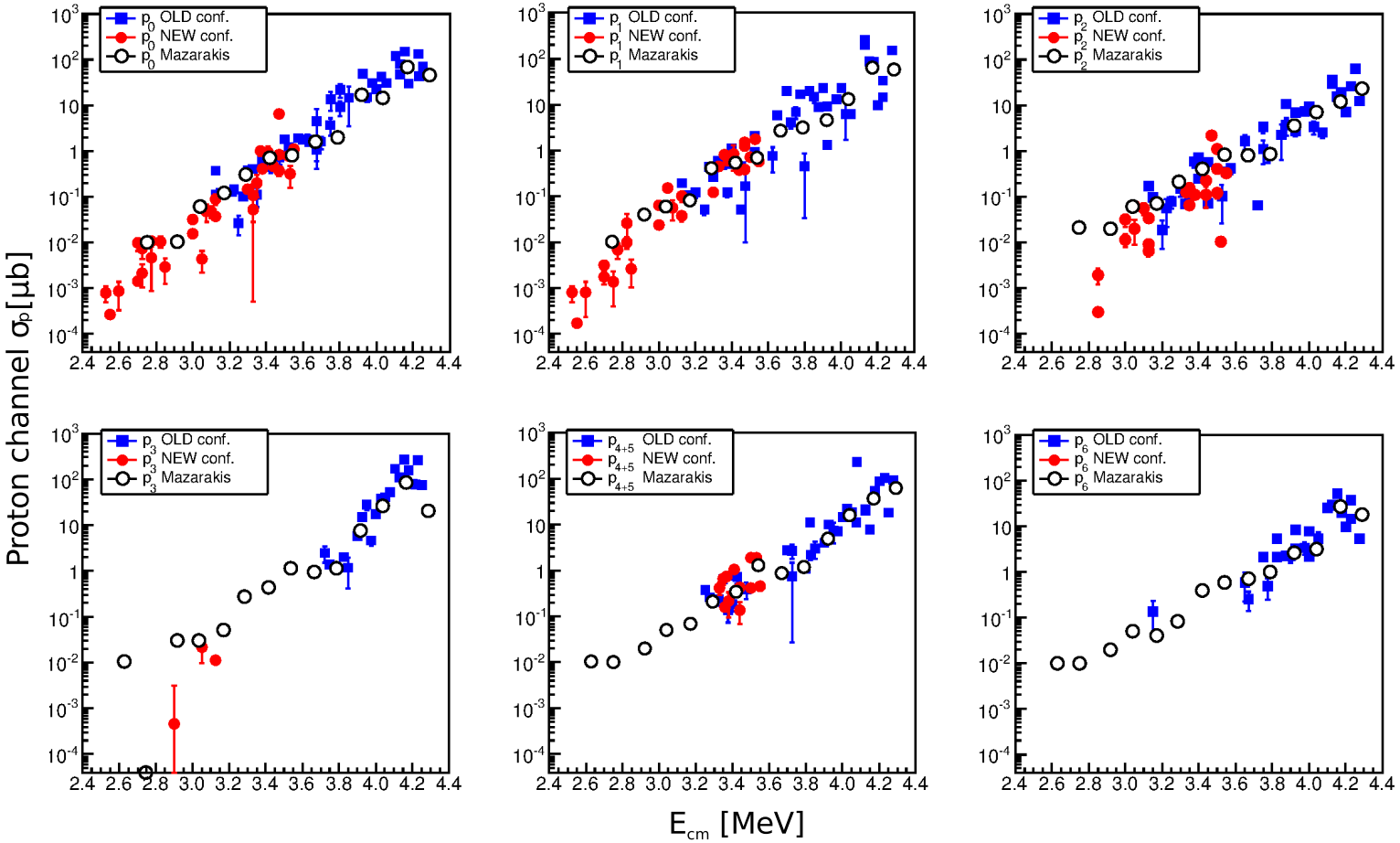

Figure 7.4: Angle integrated partial cross sections σ_p obtained by Mazarakis and Stevens. Our data from the 156°UP detector is also shown (assuming an isotropic angular distribution). Results are presented for different proton groups and our data sets are separated into Old and New configuration.

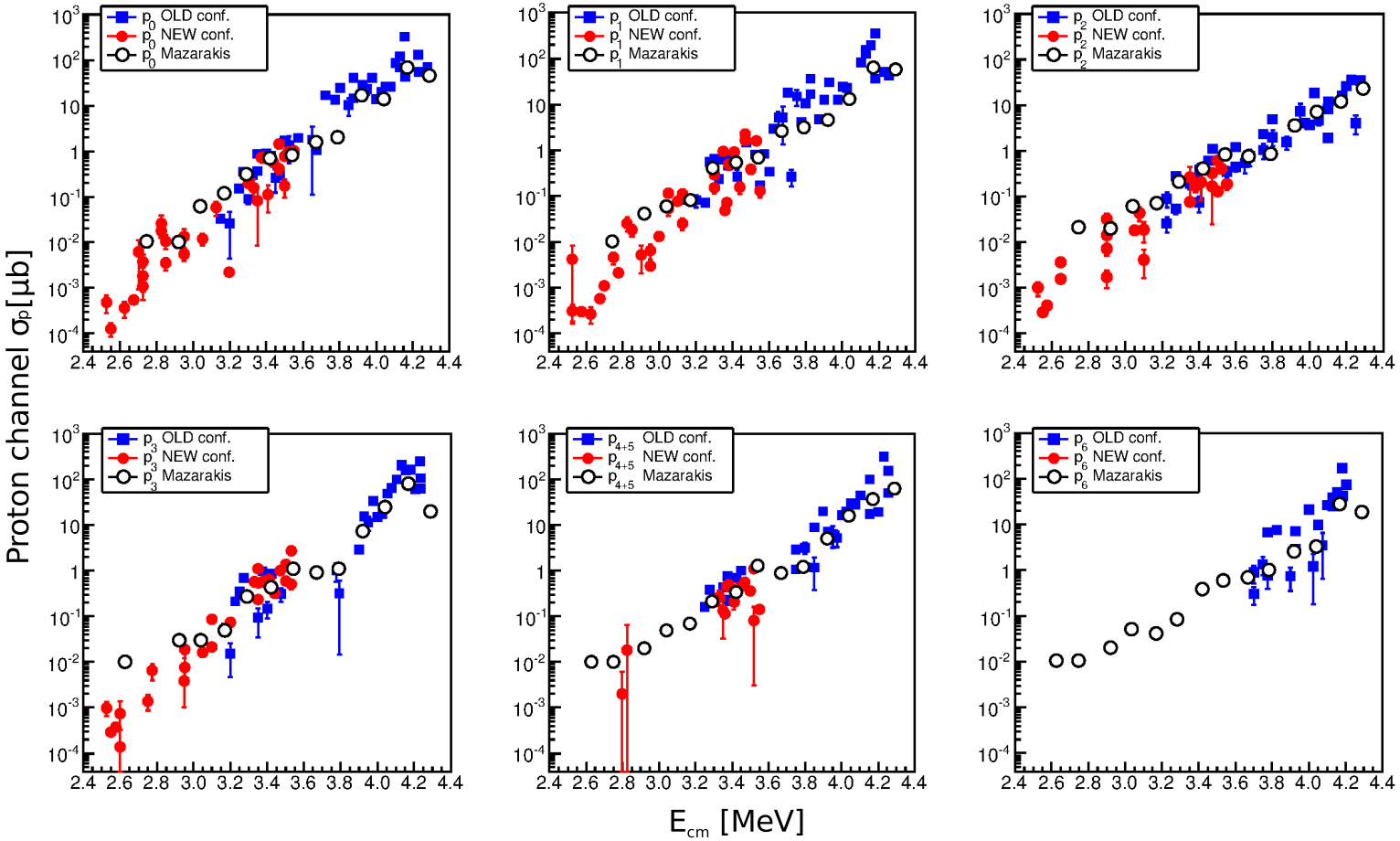

Figure 7.5: Angle integrated partial cross sections σ_p obtained by Mazarakis and Stevens. Our data from the 156°DOWN detector is also shown (assuming an isotropic angular distribution). Results are presented for different proton groups and our data sets are separated into Old and New configuration.

7.1.3 Total cross sections

From the data presented by Mazarakis and Stevens [40], which are in form of partial cross sections σ_p, I obtained the (angle integrated) total cross section by summing over all proton groups. Becker *et al.* [41] and Patterson *et al.* [28] also reported the $^{12}C+^{12}C$ reactions cross section, but in the form of total (summed over all proton groups) angle integrated cross section. In figure 7.6 a comparison between our data and those from Mazarakis, Becker and Patterson is shown. As in the case of the partial cross section results, the trend of the data reported in the literature is similar to the trend seen in our data. However, at $E_{cm} < 3.0$ MeV, Mazarakis and Stevens cross section starts to increase probably due to deuterium contamination in their targets.

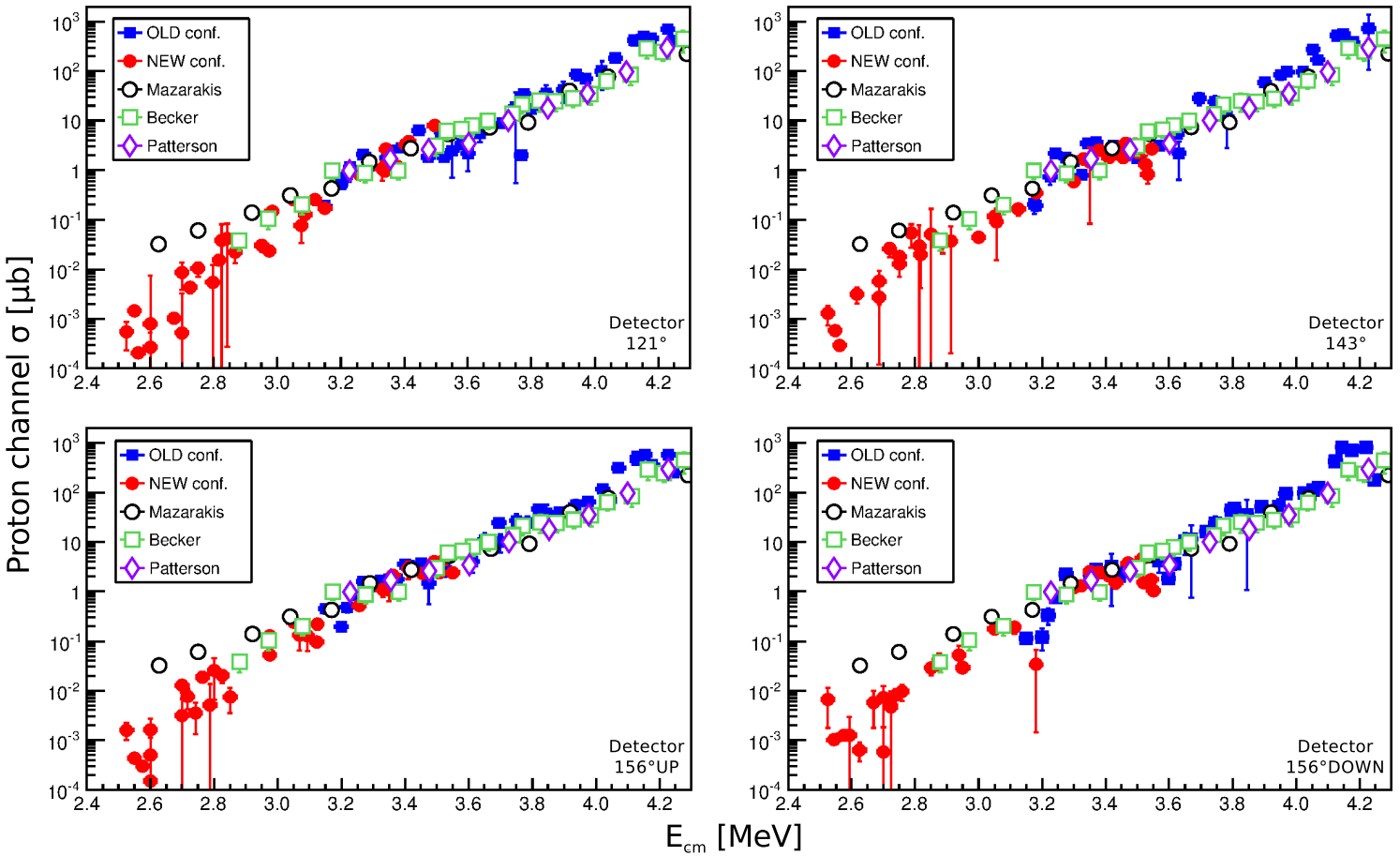

Figure 7.6: Total (summed over all proton groups) cross sections. Shown are the angle integrated data from Mazarakis and Stevens, Becker *et al.* and Patterson *et al.* as well as our data after angular isotropy was assumed. Our data is presented for different detectors and separated into Old and New configuration.

7.1.4 Partial $\tilde{S}$-factors

After extracting the reaction cross sections, we obtained the modified astrophysical $\tilde{S}$-factors. Assuming isotropy in the angular distribution, our results were compared with the angle integrated data of Mazarakis and Stevens [40] and the angle integrated results from Becker *et al.* [41], as shown in figures 7.7 to 7.10. Several differences between our data and those in the literature can be seen and possibly explained by the existence of strong anisotropies in the angular distribution.

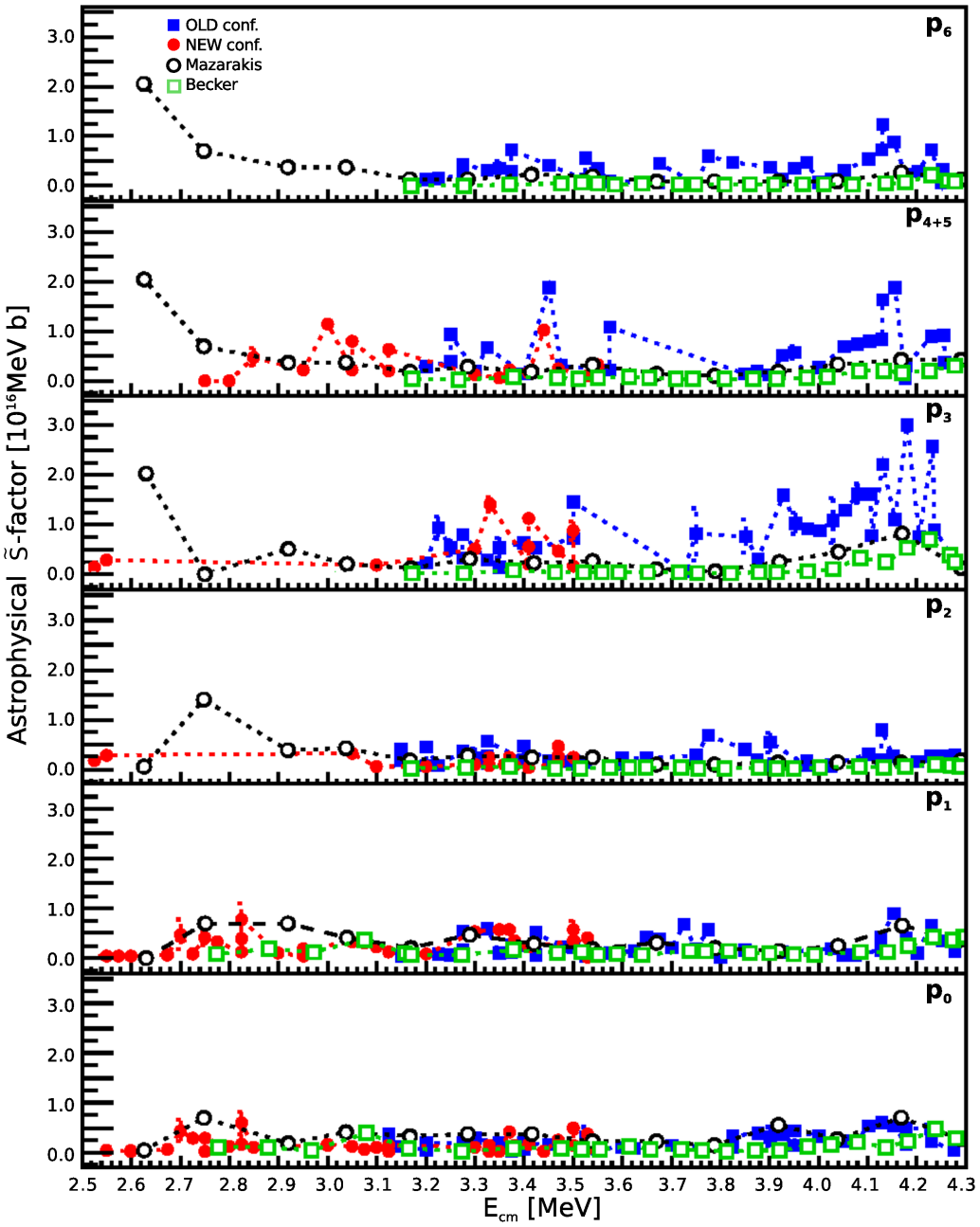

Figure 7.7: Angle integrated modified astrophysical S̃-factors obtained by Mazarakis and Becker working groups. Our data from the 121° detector is also shown (assuming an isotropic angular distribution). Results are presented for different proton groups and our data sets are separated into Old and New configuration. The dashed lines are only to guide the eye.

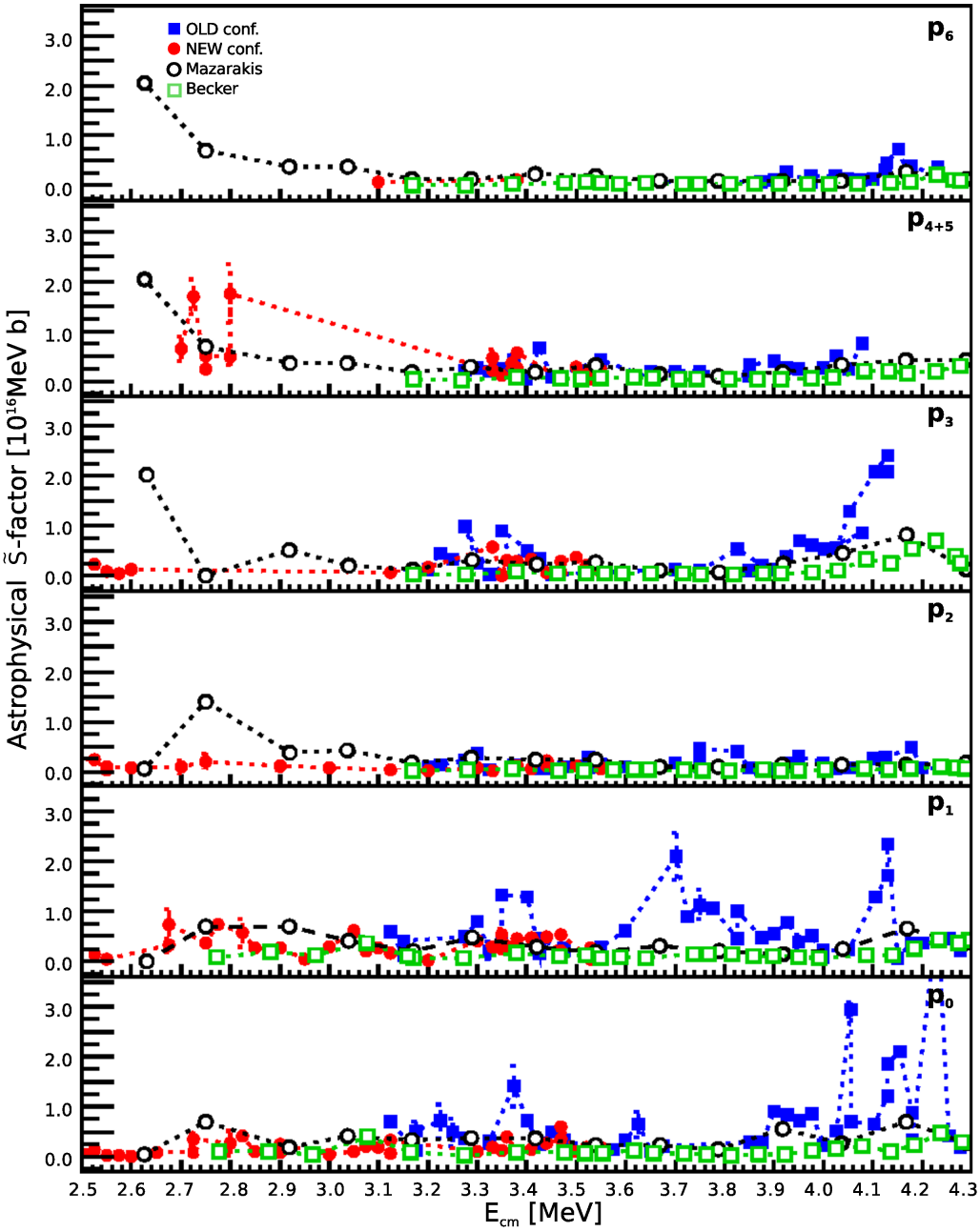

Figure 7.8: Angle integrated modified astrophysical S̃-factors obtained by Mazarakis and Becker working groups. Our data from the 143° detector is also shown (assuming an isotropic angular distribution). Results are presented for different proton groups and our data sets are separated into Old and New configuration. The dashed lines are only to guide the eye.

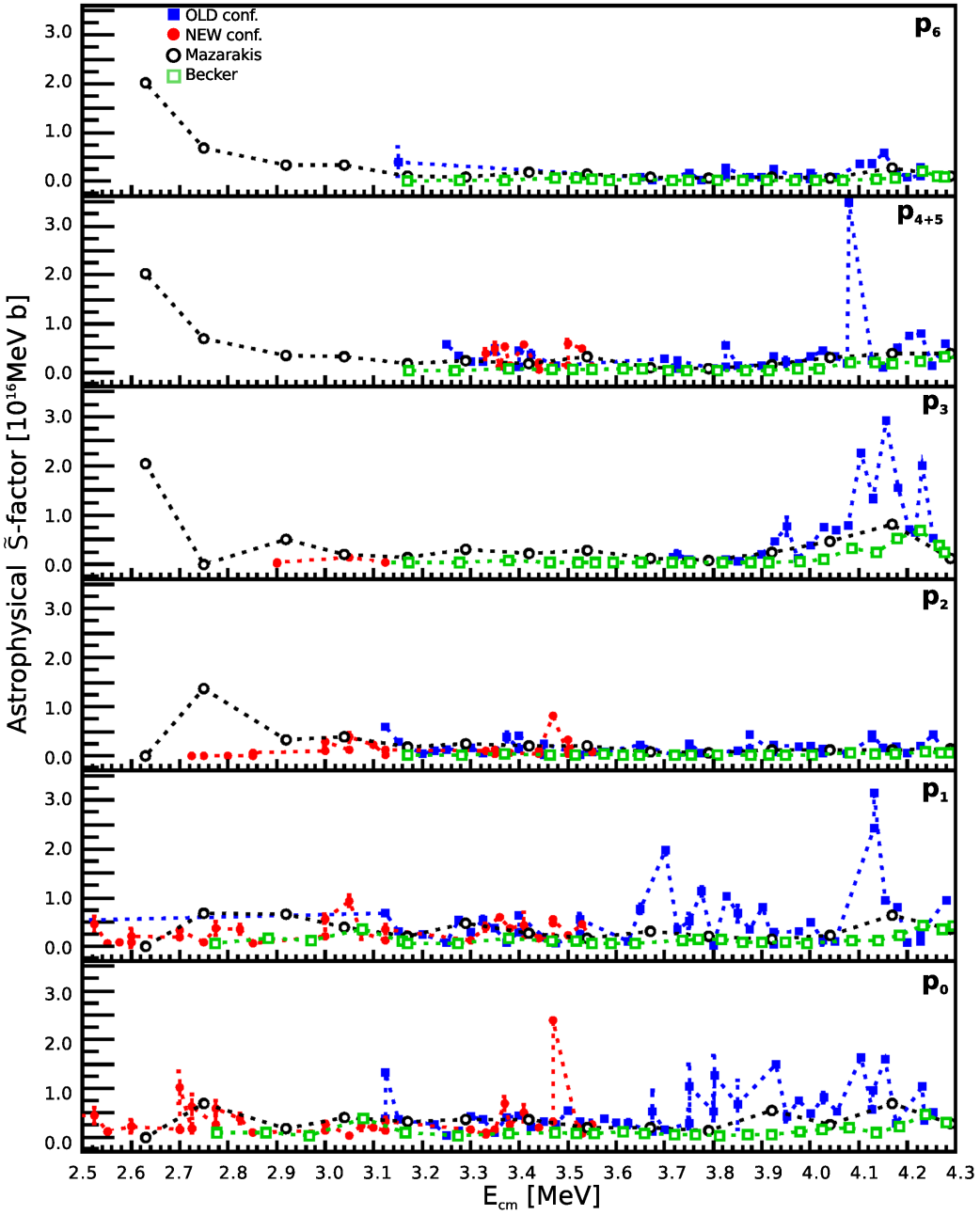

Figure 7.9: Angle integrated modified astrophysical S̃-factors obtained by Mazarakis and Becker working groups. Our data from the 156°UP detector is also shown (assuming an isotropic angular distribution). Results are presented for different proton groups and our data sets are separated into Old and New configuration. The dashed lines are only to guide the eye.

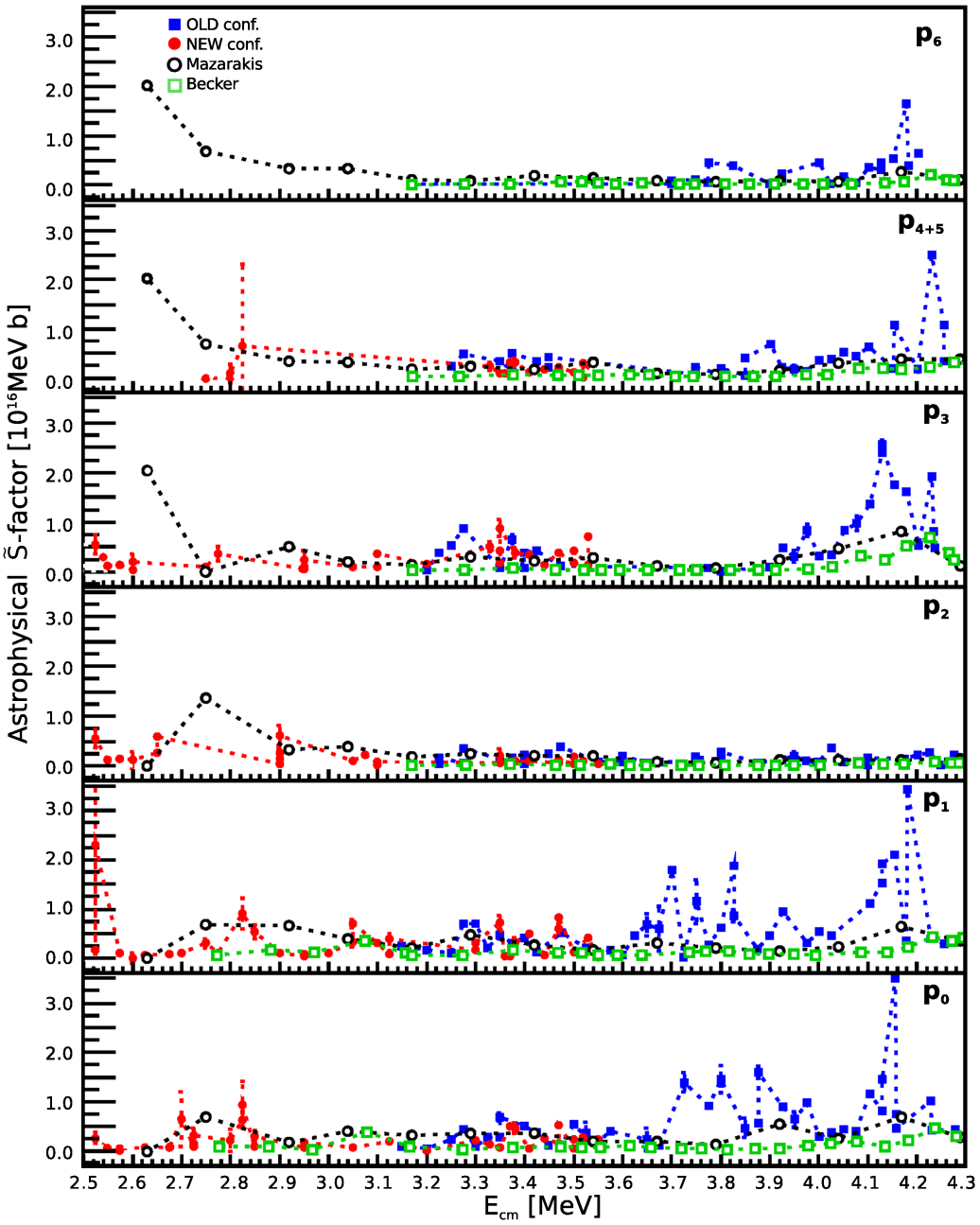

Figure 7.10: Angle integrated modified astrophysical S̃-factors obtained by Mazarakis and Becker working groups. Our data from the 156°DOWN detector is also shown (assuming an isotropic angular distribution). Results are presented for different proton groups and our data sets are separated into Old and New configuration. The dashed lines are only to guide the eye.

7.1.5 Total $\tilde{S}$-factors

As in the case of the total cross sections, the total modified astrophysical $\tilde{S}$-factors were also obtained summing over all proton groups. The angle integrated data obtained by Mazarakis and Stevens [40] and the angle integrated results reported by Becker *et al.* [41] are shown in figure 7.11, where our data (after angular isotropy was assumed) is also shown. Several discrepancies between our data and those reported in the literature can be observed. A possible explanation, as stated before, could be a strong angular dependence. Additionally, as stated in chapter 6.3.4, several other resonances can be seen in our results, suggesting the possible existence of narrow resonances.

For completeness, we made a comparison of our "total" (summed over all proton groups) modified astrophysical $\tilde{S}$-factors with three groups that measured the $^{12}C+^{12}C$ reactions using gamma-ray detection. Figure 7.12 shows the comparison of our data with those obtained by Barron-Palos *et al.* [39], Kettner *et al.* [43] and Spillane *et al.* [44]. In all cases, an isotropic angular distribution was assumed. Within uncertainty, a general consistency between our data and those of Kettner *et al.* and Spillane *et al.* can be seen at energies above $E_{cm} = 3.6$ MeV. In the $E_{cm} = 3.2$ - 3.6 MeV energy range, all data seem to agree, while at energies below $E_{cm} = 3.2$ MeV, our data is consistent only with those of Spillane *et al.*. The systematically higher data at low energies obtained by Barron-Palos *et al.* and Kettner *et al.* can be explained by means of Coulomb excitation of ^{23}Na crated in a stainless steel collimator near the target or in the Ta backing of thin targets [44]. However, Barron-Palos *et al.* consider the possibility of target contamination.

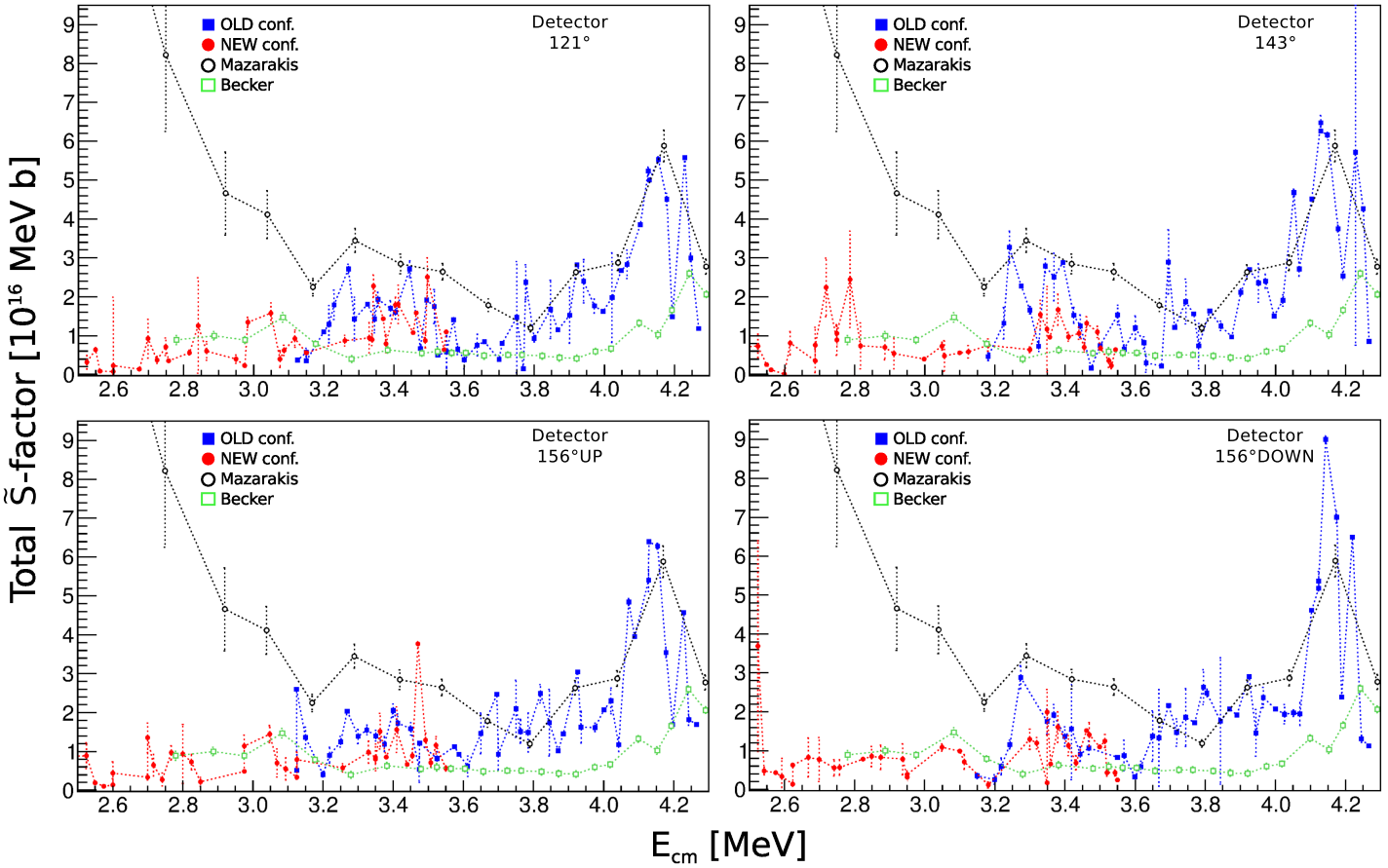

Figure 7.11: Total (summed over all proton groups) modified astrophysical S̃-factors. Shown are the angle integrated data from Mazarakis and Becker working groups and our results (assuming an isotropic angular distribution). Our data is presented for different detectors and separated into Old and New configuration. The dashed lines are only to guide the eye.

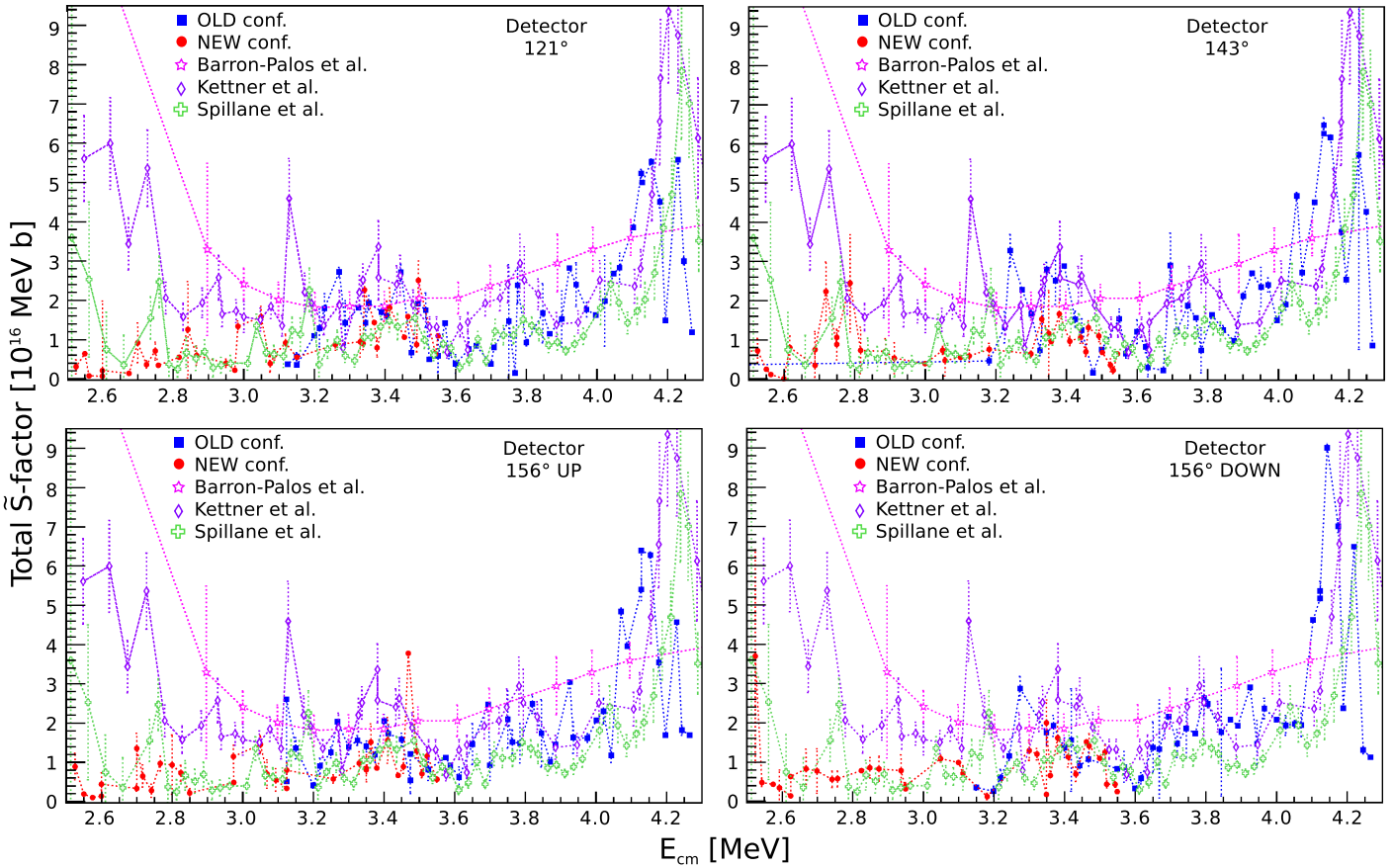

Figure 7.12: Total (summed over all proton groups) modified astrophysical $\tilde{S}$-factors. Shown are the data obtained by Barron-Palos, Kettner and Spillane working groups and our results. In all cases, an isotropic angular distribution was assumed. Our data is presented for different detectors and separated into Old and New configuration. The dashed lines are only to guide the eye.

7.2 Summary and conclusions

In this work, the measurement of the $^{12}C+^{12}C$ reactions at E_{cm} = 2.52 - 4.3 MeV was performed using the CIRCE accelerator in Caserta, Italy. However, only the proton channel results are reported in this thesis. The experimental set-up consisted in four ΔE-Erest detectors system placed at backward angles (121°, 143° and 156°) and a thick (1 mm) highly ordered pyrolytic graphite (HOPG) target. The scattering chamber was enclosed within a nitrogen atmosphere ("aquarium") in an attempt to reduce light mass elements in the residual gas that could affect the measurements of the $^{12}C+^{12}C$ reactions. Using a quadrupole mass spectrometer (QMS), a reduction of 50% of the hydrogen isotopes present in the residual gas was observed when enclosing the chamber within the "aquarium". A thermocamera was used to investigate the behaviour of the deuterium content of HOPG and natural graphite (NG) targets as a function of targets temperature. A reduction in ^{2}H contamination in the targets (regardless of type of target) in the 200°C - 1200°C temperature range was found to be 50 - 80% depending on detection angle. Additionally, the nitrogen "aquarium" seems to have a real influence on the deuterium contamination of the targets, reducing the ^{2}H content to about half its original value in the 800°C - 1000°C temperature region. When measuring the $^{12}C(^{12}C,p)$ reaction, the target temperature was monitored at all times and kept at temperatures > 400°C. In addition, we used the nitrogen "aquarium" at energies $E_{lab} < 5.50$ MeV since the signal to noise ration falls below 50%.

After a proper background analysis and subtraction, we fitted all the detectors Erest spectra with a skewed gaussian function in order to obtain the number of events N under all proton peaks (p_0 - p_6) to extract target yields, cross sections and astrophysical $\tilde{S}$-factors. The thick target yields were then differentiated at consecutive energies obtaining the thin target yield used to extract the cross section. The partial (for each proton group) differential cross sections (in μb/sr) were extracted and the "total" differential cross section (summed values of all proton groups) calculated. The $\tilde{S}$-factors were derived and presented in 10^{16}MeV barn per steradian. We could observed the resonant behaviour of the $^{12}C(^{12}C,p)$ reaction and some of the resonances reported in the literature. However, several other peaks can be seen in our data and a more in-depth analysis based on theoretical modelling should be performed in order to confirm any possible narrow resonances.

Given that our measurements were performed only at three different angles, an angular distribution could not be calculated. However, a comparison between our detection angles indicates an anisotropic angular distribution. In

order to make a qualitative comparison between our results and the data available in the literature, an isotropic angular distribution had to be assumed (since the literature data are angle integrated). The first comparison was made with our thick target yields and Zickefoose *et al.* [42] p_0+p_1 groups. A general consistency was observed at $E_{lab} < 7.20$ MeV. At higher energies, our data points are systematically higher. The partial cross sections were compared with Mazarakis and Stevens [40] results whilst the total (summed over all proton groups) cross sections were compared with Mazarakis and Stevens data, Becket *et al.* [41] results and Patterson *et al.* [28] cross sections. In all comparisons, a general consistency with our data could be observed at energies $E_{cm} > 2.8$ MeV. At lower energies, Mazarakis data points are considerably higher than ours. $\tilde{S}$ -factors were also compared with Mazarakis and Becker data and many differences could be seen. All the observed discrepancies may be explained by the existence of strong anisotropies in the angular distribution.
It should be noted that up to now, our data have the smaller energy step ever measured. Additionally, we are the first working group that have used the ΔE-Erest particle identification technique to unequivocally identify protons and alphas, avoiding the need to rely on kinematic calculations to disentangle between the two.

7.2.1 Future work

As follow up work to what we presented in this thesis, we plan to analyse the α channel of the ^{12}C+^{12}C reactions. Moreover, we are currently working on the development of four new GASTLY detectors in order to continue the measurements of both α and proton channels of the ^{12}C+^{12}C reactions at lower energies and calculate an angular distribution. The strips of the detectors would also be used, which would give us further position information of the detected particles. The extrapolation of our results to lower energies would also be attempted based on advanced theoretical models.

Appendix A

Kinematic calculations

The kinematic calculations used for peak identification in the spectra of the GASTLY detectors were performed using equation A.1 (for a given X(a,b)Y reaction) from [62].

$$E_0^{\frac{1}{2}} = \frac{(m_a m_b E_a)^{\frac{1}{2}} \cos\theta \pm \{m_a m_b E_a \cos^2\theta + (m_Y + m_b)[m_Y Q + (m_Y - m_a)E_a]\}^{\frac{1}{2}}}{m_Y + m_b} \tag{A.1}$$

where E is the kinetic energy (in the laboratory system), m the mass at rest of the given particle involved in the reaction, θ corresponds to the detection angle (with respect to the beam axis) and Q is the reaction's Q-value.

Given that we used the Erest spectra for the analysis of the $^{12}C(^{12}C,p)^{23}Na$ reaction, we have to calculate the energy that a particle deposits into the silicon detector. In order to achieve this, energy losses calculations were performed using SRIM [87]. Since the GASTLY detectors used in this experiment consist of a 2.6 μm Havar entrance window, a 116 mm ionization chamber (filled with CF_4 at various pressures[1]), a 1.6 μm Mylar foil, another 12 mm of gas and a silicon detector, we have to calculate the energy losses throughout each component of the detector before particles arrive at the SSD. To minimise uncertainties, the energy loss calculations were performed by a numerical integration of finer thicknesses of each detector element.

[1]The density of the CF_4 at each pressure was calculated assuming a density at atmospheric pressure of 3.66x10^{-3} g/cm^3 [88].

Appendix B

Detectors calibration for α particles

As discussed in chapter 4, the calibration of our detectors was performed using protons. However, another detector calibration was performed using an α source given that it is needed for the future analysis of the α channel. Incidentally, we used the silicon detectors α calibration for the foil measurements discussed in appendix C.

B.1 Silicon detectors calibration

A calibrated α source containing ^{241}Am (5.486 MeV) and ^{239}Pu (5.157 MeV) was placed in front of the silicon detectors (with an empty IC and after removing the foils). Erest spectra were produced and a Gaussian function was used to fit the peak corresponding to each α peak of the source (see figure B.1). The centroid if the fit (in channels) was then associated to the energy of the α peak. The following calibration functions were obtained:

- 156°UP: f(x) [MeV] = 0.001696 x[ch] - 0.049340
- 156°DOWN: f(x) [MeV] = 0.001589 x[ch] - 0.092696
- 143°: f(x) [MeV] = 0.001582 x[ch] - 0.114909
- 121°: f(x) [MeV] = 0.001537 x[ch] - 0.102388

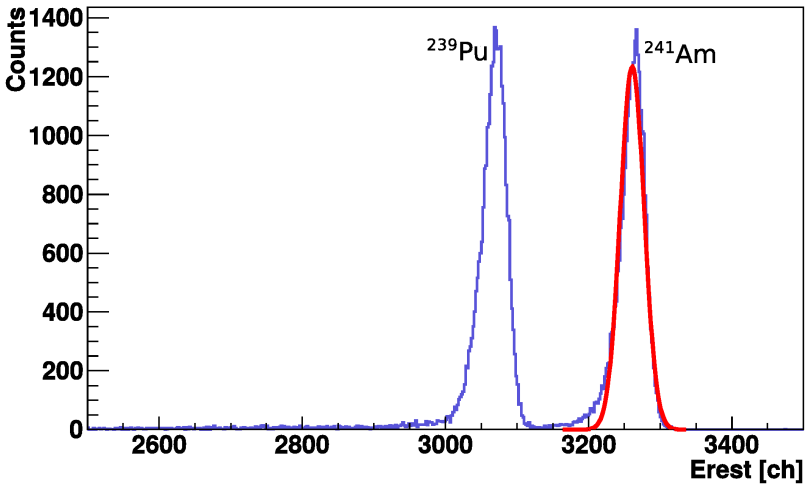

Figure B.1: Typical Erest spectrum obtained with the α source placed in front of detector 156°UP. A Gaussian function fitting the ^{241}Am peak can be seen.

B.2 Ionization chambers calibration

A calibration was performed using the same calibrated α source mentioned in the SSD calibration. Considering that the α source has only two peaks, and in order to obtain a precise calibration, the ionization chambers were filled with gas at different pressures: 35, 50 and 70 mbar (figure B.2). The energy losses in foils and gas at each pressure were calculated and associated to the centroid (in channels) of a Gaussian function fitted to each peak of the α source (see figures B.3 and B.4). The following calibration functions were obtained:

- 156°UP: f(x) [MeV] = 0.001086 x[ch] + 0.214875
- 156°DOWN: f(x) [MeV] = 0.001005 x[ch] + 0.187389
- 143°: f(x) [MeV] = 0.001027 x[ch] + 0.340268
- 121°: f(x) [MeV] = 0.001083 x[ch] + 0.306982

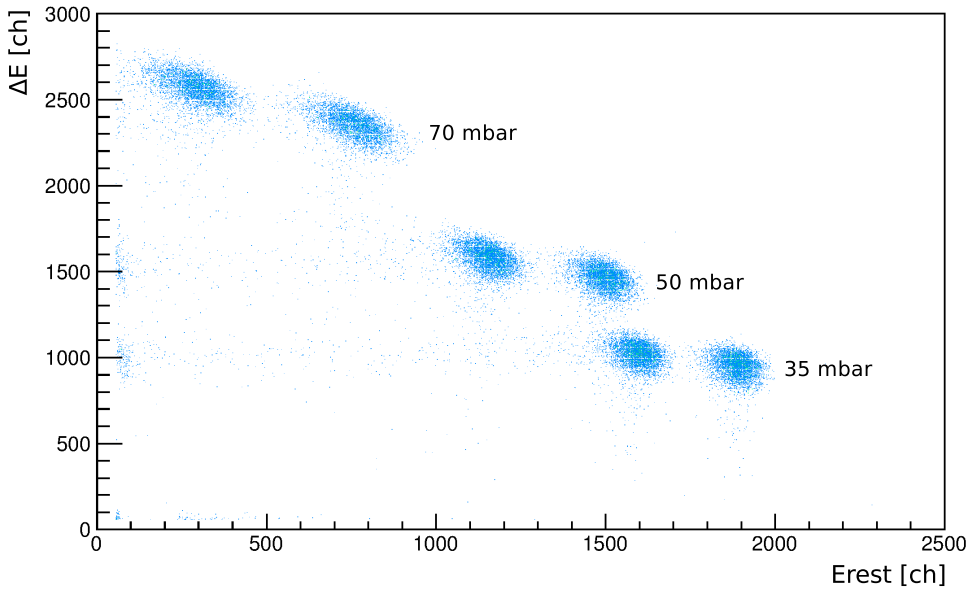

Figure B.2: ΔE-Erest matrix of the calibrated α source at different IC pressures.

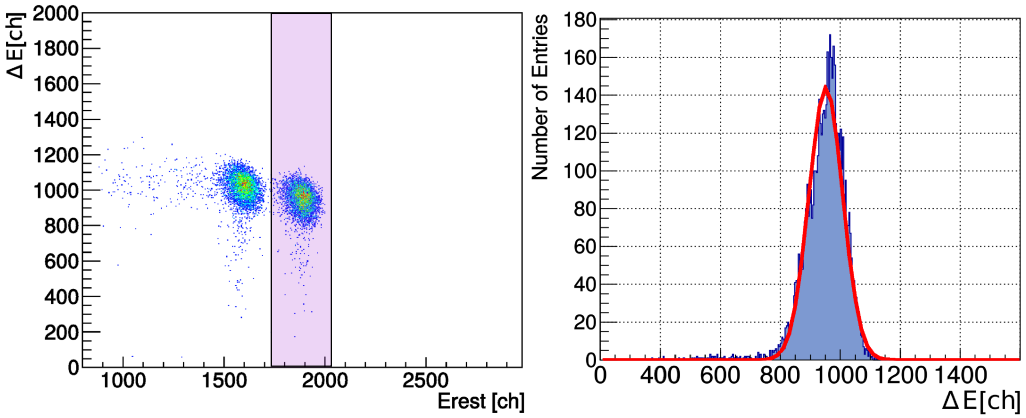

Figure B.3: Typical α source ΔE-Erest matrix used for alpha calibration of the GASTLY detectors (left) and ΔE projection of the marked area in the matrix (^{241}Am peak; right). A Gaussian function (bold line) was fitted to the projection. This data was taken using the 156°UP detector and 35 mbar in the IC.

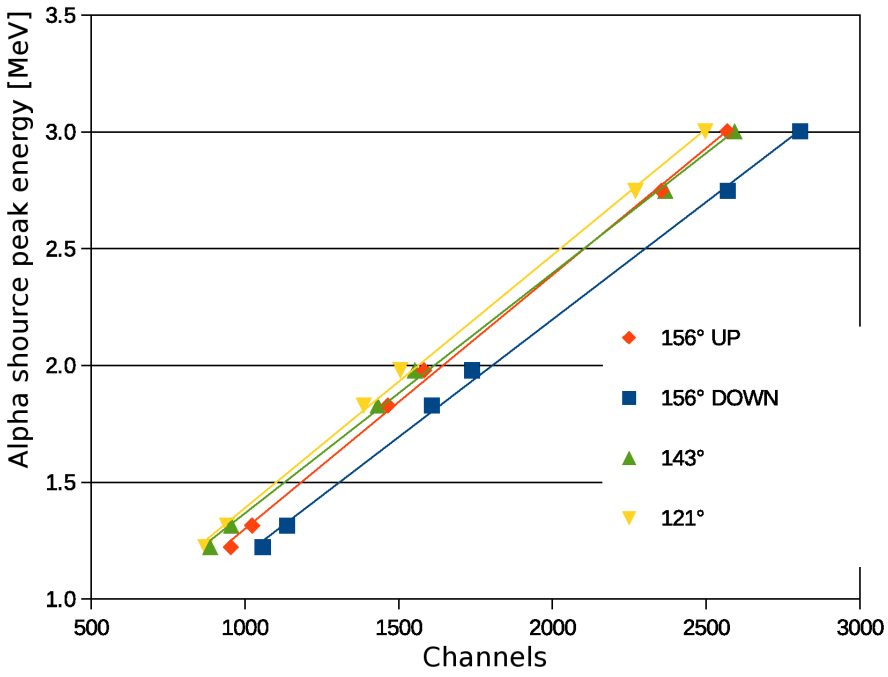

Figure B.4: Calibration functions of the ionization chambers using a calibrated α source and three different pressures of CF_4 (35, 50 and 70 mbar).

B.3 Ionization chamber efficiency measurements

The measurement of the silicon detectors efficiency was discussed in chapter 4.7. For completeness, we present here the results of the measured efficiency of the ionization chambers.
Using $\eta = \frac{N_d}{A_\alpha R_t}$, where A_α is the α source activity at the moment of the measurement and given that $\eta = \Omega/4\pi$, the efficiency and solid angle of the ionization chambers (filled with 100 mbar of CF_4 to completely stop the α particles) was measured. The results are presented in table B.1.

Table B.1: Values for the IC efficiency measurements. The second and third columns correspond to the calculation of the alpha source activity at the moment the measurements were performed, the next two columns are the runtime and number of events of each run. The resultant efficiency and the derived solid angle are shown in the last two columns. The uncertainties in the solid angle were calculated propagating the statistical error of N_d.

Detector	**t [days]**	$\mathbf{A_\alpha}$ **[Bq]**	$\mathbf{R_t}$ **[s]**	$\mathbf{N_d}$	η_{IC}	Ω **[msr]**
121°	2084	4075.831	434	14848	0.0084	**105** ± 0.9
143°	2081	4075.832	424	14725	0.0085	**107** ± 0.9
156°UP	2086	4075.830	815	12357	0.0037	**47** ± 0.4
156°DOWN	2087	4075.830	745	11969	0.0039	**49** ± 0.5

Appendix C

Foils thickness measurements

An important component in the kinematic calculations of the particles detected is the accurate knowledge of the foils thickness. A foil thickness can be determined by measuring the energy loss of particles through them. Therefore, a measurement of the particles energies with and without the foil, combined with a knowledge of stopping powers for a given combination of particle and material can be used to determine the thickness of foils. In this experiment both α-particles and proton beams were used to measure the thickness of the Havar entrance windows and Mylar foils used in the detectors.
Using the same calibrated α source described previously, proton beams of E = 1, 2, 3 and 4 MeV impinging in a gold foil and the energy loss tables provided by SRIM [87], the energy deposited in the silicon detectors with the foils in place was recorded and compared with the energy deposited in the detectors after removing all foils. The results obtained with both α source and proton beams are summarized in tables C.1 and C.2, respectively.

Table C.1: Results of the foils thicknesses measurements using an α source. The energies measured with and without foils in front of the detectors are given in columns three and two, respectively. The last column is the calculated (using SRIM) thickness of the foil.

Foil (isotope)	**E no foil [MeV]**	**E after foil [MeV]**	**SRIM [μm]**
Havar (Am)	5.49	4.60	2.5
	5.49	4.56	2.6
Havar (Pu)	5.16	4.23	2.5
	5.16	4.19	2.6
Mylar (Am)	5.49	5.31	1.6
Mylar (Pu)	5.16	4.97	1.6
Havar+Mylar(Am)	5.49	4.35	2.6+1.6
Havar+Mylar(Pu)	5.16	3.97	2.6+1.6

Table C.2: Results of the foils thicknesses measurements using E = 1, 2, 3 and 4 MeV proton beams impinging in a gold foil. The energies measured with and without foils in front of the detectors are given in columns three and two, respectively. The last column is the calculated (using SRIM) thickness of the foil.

Foil (E_{beam} [MeV])	**E no foil [MeV]**	**E after foil [MeV]**	**SRIM [μm]**
Havar (1)	0.98	0.70	2.4
Havar (2)	1.97	1.79	2.5
Havar (3)	2.94	2.81	2.5
Havar (4)	3.92	3.80	2.6
Havar (1)	0.98	0.72	2.2
Havar (2)	1.97	1.79	2.4
Havar (3)	2.94	2.80	2.6
Havar (4)	3.92	3.78	2.6
Mylar (1)	0.99	0.93	1.6
Mylar (2)	1.97	1.93	1.7
Mylar (3)	2.95	2.92	1.8
Mylar (4)	3.94	3.89	1.8
Mylar (1)	0.99	0.93	1.6
Mylar (2)	1.97	1.92	1.8
Mylar (3)	2.95	3.01	1.5
Mylar (4)	3.94	3.87	1.8

The results obtained using the α source and the proton beams impinging into a gold foil are self consistent within 0.2 μm uncertainty. Thus, the thickness of our foils are: (2.6 $\pm$ 0.2) μm for the Havar window, and (1.6 $\pm$ 0.2) μm for the Mylar foil.

Appendix D

Numerical Results Tables

In this appendix, tables containing the net counting rates of the primary protons (D.1) from the $^{12}C+^{2}H$ reaction discussed in chapter 5 and the numerical values of the $^{12}C+^{12}C$ thick target yields (D.2 - D.9) are given. Uncertainties (statistical) are shown in % and quoted in parenthesis.

Table D.1: Target temperatures and net counting rates (counts/C) in the primary proton peaks after subtraction of the p_7 contribution (see text for details, chapter 5). Uncertainties are presented between parenthesis [%].

Target temp. [°C]	**121°** [counts/C]	**143°** [counts/C]	**156°UP** [counts/C]	**156°DOWN** [counts/C]
		HOPG target without N_2 "aquarium"		
1087 (1)	2.18x10^6 (1)	1.70x10^6 (1)	6.20x10^5 (2)	3.48x10^5 (2)
1086 (1)	2.24x10^6 (1)	1.95x10^6 (1)	6.37x10^5 (2)	4.44x10^5 (2)
1099 (1)	2.26x10^6 (2)	1.83x10^6 (2)	6.87x10^5 (3)	3.08x10^5 (4)
1080 (22)	2.22x10^6 (2)	1.82x10^6 (2)	5.76x10^5 (4)	3.96x10^5 (3)
966 (33)	2.30x10^6 (2)	1.74x10^6 (2)	8.57x10^5 (3)	2.93x10^5 (4)
1028 (2)	2.26x10^6 (2)	1.82x10^6 (2)	7.60x10^5 (4)	5.05x10^5 (3)
979 (2)	2.62x10^6 (2)	2.12x10^6 (2)	8.09x10^5 (4)	5.24x10^5 (3)
926 (2)	2.33x10^6 (3)	2.05x10^6 (2)	7.60x10^5 (4)	2.44x10^5 (6)
868 (3)	2.65x10^6 (3)	2.23x10^6 (3)	9.39x10^5 (4)	4.88x10^5 (4)
788 (4)	2.41x10^6 (4)	2.44x10^6 (3)	8.71x10^5 (5)	4.56x10^5 (5)
710 (4)	2.84x10^6 (3)	2.90x10^6 (3)	1.12x10^6 (5)	5.48x10^5 (5)
626 (4)	3.26x10^6 (3)	2.33x10^6 (3)	8.60x10^5 (6)	6.85x10^5 (5)
536 (6)	3.28x10^6 (2)	2.65x10^6 (2)	1.03x10^6 (3)	6.60x10^5 (3)
460 (5)	2.97x10^6 (3)	2.95x10^6 (2)	1.06x10^6 (4)	6.18x10^5 (4)
402 (4)	3.34x10^6 (3)	3.24x10^6 (2)	1.69x10^6 (3)	8.15x10^5 (4)
350 (5)	3.29x10^6 (3)	3.07x10^6 (3)	2.00x10^6 (3)	8.37x10^5 (4)
307 (5)	3.85x10^6 (3)	3.98x10^6 (3)	1.75x10^6 (4)	1.12x10^6 (4)
		NG target with N_2 "aquarium"		
418 (27)	1.10x10^6 (18)	1.4x10^6 (5)	8.4x10^5 (6)	7.8x10^5 (5)
498 (4)	9.94x10^5 (17)	9.8x10^5 (6)	4.8x10^5 (10)	5.5x10^5 (5)
546 (3)	1.12x10^6 (15)	1.0x10^6 (6)	4.3x10^5 (11)	6.0x10^5 (5)
587 (2)	8.05x10^5 (22)	1.2x10^6 (5)	4.6x10^5 (10)	5.4x10^5 (6)
635 (3)	7.99x10^5 (6)	9.7x10^5 (2)	4.3x10^5 (3)	4.3x10^5 (2)
659 (1)	9.04x10^5 (5)	1.0x10^6 (2)	4.9x10^5 (3)	4.6x10^5 (2)
677 (2)	9.04x10^5 (5)	9.0x10^5 (2)	4.4x10^5 (3)	4.5x10^5 (2)
706 (1)	9.29x10^5 (5)	9.4x10^5 (2)	3.9x10^5 (3)	4.4x10^5 (2)
735 (1)	8.26x10^5 (5)	8.6x10^5 (2)	4.4x10^5 (3)	4.5x10^5 (2)
741 (1)	9.48x10^5 (5)	9.2x10^5 (2)	4.5x10^5 (3)	3.5x10^5 (3)
757 (1)	9.34x10^5 (5)	9.4x10^5 (2)	3.5x10^5 (4)	4.2x10^5 (2)
786 (1)	7.64x10^5 (6)	7.8x10^5 (2)	3.8x10^5 (3)	4.2x10^5 (2)
784 (1)	8.81x10^5 (5)	9.0x10^5 (2)	3.7x10^5 (4)	3.8x10^5 (2)
793 (1)	8.28x10^5 (5)	9.2x10^5 (2)	4.1x10^5 (3)	3.4x10^5 (3)
815 (1)	8.82x10^5 (5)	9.6x10^5 (2)	4.0x10^5 (3)	4.0x10^5 (2)
819 (1)	8.46x10^5 (5)	9.0x10^5 (2)	3.6x10^5 (4)	3.6x10^5 (3)
		HOPG target with N_2 "aquarium"		
1008 (3)	7.6x10^5 (6)	7.5x10^5 (4)	2.8x10^5 (8)	3.0x10^5 (5)
889 (2)	7.8x10^5 (8)	7.0x10^5 (5)	2.7x10^5 (7)	2.5x10^5 (6)

Table D.2: Thick target yields [cts $^{12}C^{-1}$ sr^{-1}] for the different proton groups of the $^{12}C(^{12}C,p)^{23}Na$ reaction at $\theta_{lab} = 121^o$ (Old configuration). Uncertainties are given in % in parenthesis (those larger than 100% are marked with a + sign). Beam energies are in MeV.

$\mathbf{E}_{lab}$	$\mathbf{p}_0$	$\mathbf{p}_1$	$\mathbf{p}_2$	$\mathbf{p}_3$	$\mathbf{p}_{4+5}$	$\mathbf{p}_6$
121^o Old CONFIGURATION						
8.60	7.46E-12 (1)	8.19E-12 (1)	5.11E-12 (1)	3.39E-11 (1)	1.53E-11 (1)	9.68E-12 (1)
8.55	7.27E-12 (4)	7.68E-12 (2)	4.10E-12 (2)	3.29E-11 (1)	1.60E-11 (1)	1.03E-11 (2)
8.50	7.32E-12 (3)	6.60E-12 (1)	3.28E-12 (2)	3.50E-11 (1)	1.30E-11 (1)	9.24E-12 (1)
8.45	5.93E-12 (3)	4.72E-12 (2)	2.58E-12 (2)	2.76E-11 (1)	1.04E-11 (1)	7.16E-12 (1)
8.40	6.35E-12 (5)	4.48E-12 (3)	2.20E-12 (5)	2.56E-11 (1)	1.09E-11 (2)	6.43E-12 (3)
8.35	5.21E-12 (5)	3.57E-12 (3)	2.06E-12 (4)	1.87E-11 (1)	1.03E-11 (2)	5.89E-12 (2)
8.30	4.14E-12 (5)	1.75E-12 (4)	1.56E-12 (4)	1.64E-11 (1)	6.41E-12 (2)	4.10E-12 (3)
8.30	4.19E-12 (8)	1.30E-12 (7)	2.63E-12 (5)	1.23E-11 (2)	7.88E-12 (3)	5.02E-12 (4)
8.25	3.07E-12 (7)	9.96E-13 (6)	1.20E-12 (5)	1.24E-11 (2)	4.89E-12 (3)	2.77E-12 (4)
8.20	2.22E-12 (19)	8.81E-13 (20)	7.14E-13 (16)	9.75E-12 (6)	3.62E-12 (10)	1.91E-12 (16)
8.15	1.91E-12 (19)	7.90E-13 (19)	8.03E-13 (20)	7.42E-12 (4)	2.57E-12 (12)	1.95E-12 (13)
8.10	1.62E-12 (23)	7.17E-13 (18)	1.01E-12 (72)	5.78E-12 (12)	1.70E-12 (22)	1.55E-12 (12)
8.05	1.47E-12 (24)	5.25E-13 (20)	5.77E-13 (15)	4.56E-12 (5)	1.83E-12 (12)	1.42E-12 (13)
8.00	1.15E-12 (37)	-	6.28E-13 (21)	3.69E-12 (7)	1.57E-12 (14)	1.34E-12 (18)
7.95	1.24E-12 (26)	-	4.69E-13 (23)	2.87E-12 (10)	1.55E-12 (14)	9.30E-13 (22)
7.90	9.11E-13 (27)	6.08E-13 (13)	5.53E-13 (12)	2.07E-12 (6)	1.12E-12 (11)	6.54E-13 (18)
7.85	6.59E-13 (50)	5.26E-13 (22)	7.78E-13 (26)	9.83E-13 (27)	7.71E-13 (20)	5.64E-13 (26)
7.80	4.72E-13 (46)	6.25E-13 (18)	4.62E-13 (19)	8.72E-13 (15)	7.03E-13 (19)	3.40E-13 (32)
7.75	2.62E-13 (69)	6.81E-13 (17)	3.63E-13 (32)	7.11E-13 (36)	5.94E-13 (23)	3.70E-13 (40)
7.70	3.06E-13 (50)	6.08E-13 (15)	1.85E-13 (52)	3.59E-13 (27)	5.28E-13 (18)	3.22E-13 (23)
7.65	1.72E-13 (84)	6.16E-13 (16)	3.46E-13 (16)	-	6.02E-13 (93)	1.26E-13 (27)
7.60	-	6.07E-13 (16)	3.42E-13 (21)	4.85E-13 (70)	-	3.40E-13 (52)
7.55	-	4.31E-13 (17)	1.32E-13 (32)	3.21E-13 (55)	-	1.57E-13 (+)
7.50	-	3.83E-13 (14)	5.86E-14 (64)	1.03E-13 (34)	-	1.01E-13 (38)
7.45	1.01E-13 (73)	2.28E-13 (19)	9.64E-14 (31)	8.68E-14 (45)	-	-
7.40	7.27E-14 (76)	1.88E-13 (17)	9.36E-14 (+)	7.99E-14 (62)	-	1.48E-13 (32)
7.35	9.66E-14 (53)	1.22E-13 (21)	1.43E-13 (17)	-	1.31E-13 (26)	6.56E-14 (84)
7.30	-	5.70E-14 (33)	1.10E-13 (16)	-	1.87E-13 (40)	-
7.25	7.22E-14 (50)	3.81E-14 (35)	1.13E-13 (15)	8.68E-14 (29)	1.88E-13 (14)	5.86E-14 (34)
7.20	5.91E-14 (51)	6.24E-14 (23)	8.88E-14 (16)	-	2.51E-13 (11)	6.95E-14 (22)
7.15	6.61E-14 (42)	5.28E-14 (24)	7.75E-14 (44)	-	1.44E-13 (16)	6.08E-14 (29)
7.10	6.04E-14 (40)	6.60E-14 (18)	6.34E-14 (16)	1.30E-13 (18)	-	6.23E-14 (27)
7.10	5.30E-14 (20)	6.32E-14 (10)	7.32E-14 (7)	-	-	3.08E-14 (28)
7.05	3.81E-14 (22)	6.08E-14 (7)	6.41E-14 (6)	1.31E-13 (11)	-	2.09E-14 (56)
7.00	-	4.76E-14 (23)	5.25E-14 (16)	3.86E-14 (49)	1.70E-13 (11)	2.51E-14 (45)
6.95	3.13E-14 (49)	3.57E-14 (21)	4.42E-14 (17)	-	1.54E-13 (11)	6.06E-14 (17)
6.90	2.31E-14 (57)	5.07E-14 (16)	3.58E-14 (20)	9.17E-14 (13)	6.77E-14 (19)	4.09E-14 (20)
6.85	2.43E-14 (44)	3.07E-14 (18)	3.83E-14 (14)	7.08E-14 (20)	-	4.45E-14 (17)
6.80	1.83E-14 (47)	3.07E-14 (16)	2.26E-14 (21)	4.95E-14 (22)	5.78E-14 (17)	4.83E-14 (18)
6.75	1.76E-14 (46)	2.33E-14 (19)	2.59E-14 (15)	5.57E-14 (24)	-	2.72E-14 (26)
6.70	1.32E-14 (55)	2.09E-14 (16)	2.67E-14 (16)	4.27E-14 (19)	-	1.86E-14 (19)
6.65	1.21E-14 (50)	8.62E-15 (29)	1.52E-14 (44)	3.66E-14 (27)	1.66E-14 (34)	1.23E-14 (24)
6.60	6.90E-15 (63)	1.17E-14 (19)	1.13E-14 (28)	3.87E-14 (12)	1.31E-14 (28)	1.23E-14 (26)
6.55	4.00E-15 (92)	3.84E-15 (44)	5.97E-15 (30)	2.67E-14 (24)	1.50E-14 (28)	5.92E-15 (41)
6.50	6.01E-15 (71)	3.19E-15 (42)	8.84E-15 (22)	2.00E-14 (22)	3.42E-15 (+)	-
6.45	-	2.45E-15 (48)	8.06E-15 (19)	1.01E-14 (20)	5.80E-15 (27)	2.70E-15 (40)
6.40	2.69E-15 (+)	4.81E-15 (24)	4.20E-15 (29)	8.04E-15 (24)	3.28E-15 (44)	1.46E-15 (+)
6.35	3.70E-15 (85)	6.64E-15 (26)	4.72E-15 (28)	-	2.65E-15 (97)	-
6.30	2.87E-15 (98)	6.40E-15 (27)	2.31E-15 (44)	-	3.68E-15 (96)	-
6.25	9.59E-16 (+)	9.56E-15 (39)	-	-	1.42E-14 (34)	-

Table D.3: Thick target yields [cts $^{12}C^{-1}$ sr^{-1}] for the different proton groups of the $^{12}C(^{12}C,p)^{23}Na$ reaction at $\theta_{lab} = 121^{o}$ (New configuration). Uncertainties are given in % in parenthesis (those larger than 100% are marked with a + sign). Beam energies are in MeV.

$\mathbf{E}_{lab}$	$\mathbf{p}_0$	$\mathbf{p}_1$	$\mathbf{p}_2$	$\mathbf{p}_3$	$\mathbf{p}_{4+5}$	$\mathbf{p}_6$
121^{o} New CONFIGURATION						
7.20	7.38E-14 (14)	1.30E-13 (19)	9.92E-14 (14)	7.10E-14 (17)	1.47E-13 (12)	5.92E-14 (21)
7.20	5.36E-14 (17)	1.02E-13 (17)	5.23E-14 (21)	7.80E-14 (19)	1.36E-13 (14)	3.54E-14 (32)
7.10	5.69E-14 (13)	1.24E-13 (13)	3.69E-14 (+)	4.94E-14 (+)	9.05E-14 (18)	3.42E-14 (25)
7.06	3.47E-14 (18)	9.93E-14 (18)	2.51E-14 (31)	5.52E-14 (19)	8.42E-14 (15)	3.17E-14 (23)
7.04	4.81E-14 (14)	1.03E-13 (22)	4.96E-14 (19)	8.67E-14 (15)	8.68E-14 (15)	4.13E-14 (23)
7.00	2.35E-14 (21)	7.34E-14 (18)	3.81E-14 (20)	9.20E-14 (13)	9.05E-14 (13)	3.00E-14 (27)
7.00	4.05E-14 (6)	8.38E-14 (6)	2.64E-14 (11)	4.23E-14 (9)	-	-
6.94	2.49E-14 (19)	6.25E-14 (40)	9.73E-15 (53)	6.24E-14 (14)	7.54E-14 (12)	1.45E-14 (42)
6.88	2.32E-14 (16)	5.36E-14 (14)	1.41E-14 (28)	6.39E-14 (12)	2.22E-14 (30)	1.79E-14 (31)
6.82	1.58E-14 (17)	4.40E-14 (14)	1.30E-14 (27)	1.49E-14 (36)	1.56E-14 (35)	1.86E-14 (27)
6.76	1.05E-14 (16)	3.19E-14 (12)	1.08E-14 (21)	2.97E-14 (14)	1.59E-14 (21)	1.19E-14 (23)
6.74	5.83E-15 (26)	2.56E-14 (16)	8.26E-15 (30)	3.86E-14 (13)	1.35E-14 (29)	1.17E-14 (27)
6.72	8.04E-15 (24)	2.54E-14 (17)	7.22E-15 (34)	4.37E-14 (13)	-	1.65E-14 (24)
6.70	7.71E-15 (23)	1.98E-14 (21)	9.22E-15 (25)	-	1.23E-14 (27)	1.49E-14 (22)
6.66	5.34E-15 (21)	1.96E-14 (12)	5.18E-15 (23)	7.32E-15 (26)	1.22E-14 (18)	5.44E-15 (27)
6.60	3.16E-15 (30)	8.50E-15 (22)	3.09E-15 (17)	1.34E-14 (9)	9.68E-15 (11)	6.19E-15 (12)
6.40	4.33E-15 (24)	5.81E-15 (29)	1.39E-15 (60)	-	1.22E-14 (22)	-
6.25	2.00E-15 (24)	3.93E-15 (23)	1.39E-15 (42)	-	2.52E-15 (35)	-
6.20	1.57E-15 (26)	2.97E-15 (26)	1.16E-15 (45)	6.83E-15 (18)	2.85E-15 (29)	-
6.15	1.32E-15 (19)	1.88E-15 (22)	1.15E-15 (43)	-	2.83E-15 (21)	-
6.10	9.63E-16 (22)	9.16E-16 (33)	2.03E-16 (76)	-	5.08E-16 (57)	-
6.10	8.20E-16 (35)	9.39E-16 (47)	4.90E-16 (55)	-	6.26E-15 (14)	-
6.00	2.61E-16 (46)	1.16E-15 (32)	-	-	1.70E-15 (37)	-
5.90	2.53E-16 (51)	6.93E-16 (41)	-	-	1.12E-15 (38)	-
5.80	3.50E-16 (37)	5.09E-16 (41)	-	-	1.20E-15 (+)	-
5.70	2.15E-16 (40)	5.21E-16 (34)	-	-	2.69E-18 (+)	-
5.70	4.14E-16 (44)	7.12E-16 (44)	-	-	6.50E-18 (+)	-
5.65	1.33E-16 (58)	3.42E-16 (47)	-	-	3.46E-18 (+)	-
5.60	8.88E-17 (47)	3.00E-16 (31)	-	-	1.44E-18 (+)	-
5.55	1.50E-16 (40)	2.02E-16 (47)	-	-	1.55E-18 (+)	-
5.50	7.68E-17 (50)	1.02E-16 (61)	-	-	1.35E-18 (+)	-
5.45	8.10E-17 (48)	8.90E-17 (64)	-	-	9.10E-18 (+)	-
5.45	1.90E-17 (+)	1.75E-17 (+)	-	-	2.07E-16 (38)	-
5.40	1.25E-17 (55)	1.55E-17 (69)	-	-	-	-
5.35	3.96E-18 (+)	7.44E-18 (+)	-	-	-	-
5.30	1.06E-17 (73)	1.40E-17 (88)	-	-	-	-
5.25	-	-	-	3.67E-17 (+)	-	-
5.20	6.93E-18 (65)	9.22E-18 (77)	2.44E-17 (40)	2.40E-17 (41)	-	-
5.15	5.79E-18 (98)	7.75E-18 (+)	3.40E-17 (40)	3.36E-17 (40)	-	-
5.10	4.34E-18 (+)	6.52E-18 (+)	2.38E-17 (53)	2.34E-17 (54)	-	-
5.05	5.81E-18 (81)	7.13E-18 (+)	1.92E-17 (53)	1.94E-17 (52)	1.96E-17 (52)	-

Table D.4: Thick target yields [cts $^{12}C^{-1}$ sr^{-1}] for the different proton groups of the $^{12}C(^{12}C,p)^{23}Na$ reaction at $\theta_{lab} = 143^o$ (Old configuration). Uncertainties are given in % in parenthesis (those larger than 100% are marked with a + sign). Beam energies are in MeV.

$\mathbf{E}_{lab}$	$\mathbf{p}_0$	$\mathbf{p}_1$	$\mathbf{p}_2$	$\mathbf{p}_3$	$\mathbf{p}_{4+5}$	$\mathbf{p}_6$
143° Old CONFIGURATION						
8.60	3.13E-11 (1)	1.01E-11 (1)	5.30E-12 (1)	-	-	5.67E-12 (1)
8.55	3.06E-11 (1)	9.36E-12 (2)	5.18E-12 (2)	-	-	6.15E-12 (2)
8.50	2.93E-11 (1)	7.91E-12 (1)	3.29E-12 (99)	-	-	-
8.45	1.48E-11 (1)	1.27E-11 (1)	3.13E-12 (2)	-	-	3.95E-12 (2)
8.40	1.53E-11 (1)	1.17E-11 (2)	2.93E-12 (4)	-	-	4.58E-12 (3)
8.35	1.33E-11 (1)	1.09E-11 (1)	1.83E-12 (4)	-	-	3.67E-12 (3)
8.30	8.96E-12 (2)	1.08E-11 (1)	2.04E-12 (3)	1.32E-11 (1)	3.35E-12 (3)	2.22E-12 (3)
8.30	1.02E-11 (2)	9.62E-12 (2)	1.89E-12 (5)	1.38E-11 (2)	3.51E-12 (4)	1.96E-12 (5)
8.25	6.77E-12 (2)	6.51E-12 (2)	1.56E-12 (4)	9.39E-12 (2)	3.54E-12 (3)	1.40E-12 (4)
8.20	5.72E-12 (6)	4.45E-12 (7)	1.14E-12 (11)	6.01E-12 (5)	3.36E-12 (8)	1.19E-12 (13)
8.15	7.72E-12 (5)	-	1.02E-12 (11)	4.79E-12 (5)	2.29E-12 (9)	1.02E-12 (13)
8.10	3.95E-12 (5)	3.90E-12 (6)	9.30E-13 (12)	3.15E-12 (10)	1.98E-12 (11)	8.54E-13 (17)
8.05	3.37E-12 (4)	3.98E-12 (4)	8.71E-13 (11)	2.53E-12 (11)	1.41E-12 (12)	6.33E-13 (21)
8.00	3.14E-12 (6)	3.76E-12 (6)	7.04E-13 (15)	1.99E-12 (11)	1.15E-12 (17)	6.86E-13 (19)
7.95	2.39E-12 (7)	3.32E-12 (7)	7.17E-13 (14)	1.46E-12 (11)	1.06E-12 (14)	5.21E-13 (21)
7.90	1.84E-12 (5)	3.02E-12 (4)	4.92E-13 (12)	9.21E-13 (11)	8.71E-13 (12)	5.16E-13 (14)
7.85	1.27E-12 (9)	2.49E-12 (7)	3.81E-13 (20)	6.54E-13 (17)	6.96E-13 (17)	3.36E-13 (27)
7.80	7.36E-13 (12)	2.16E-12 (8)	3.49E-13 (20)	5.84E-13 (21)	4.60E-13 (26)	2.74E-13 (27)
7.75	5.81E-13 (18)	1.91E-12 (9)	3.37E-13 (22)	4.71E-13 (26)	5.23E-13 (25)	2.34E-13 (35)
7.70	4.46E-13 (30)	1.96E-12 (10)	3.02E-13 (18)	4.22E-13 (19)	3.72E-13 (21)	-
7.65	4.49E-13 (40)	1.56E-12 (15)	1.45E-13 (62)	2.08E-13 (42)	4.87E-13 (16)	-
7.60	3.12E-13 (16)	1.50E-12 (8)	1.89E-13 (24)	-	-	-
7.55	4.42E-13 (32)	1.17E-12 (16)	1.93E-13 (20)	-	-	-
7.50	3.93E-13 (22)	8.63E-13 (12)	7.02E-14 (28)	1.25E-13 (28)	3.34E-13 (13)	-
7.45	3.75E-13 (32)	6.55E-13 (21)	1.10E-13 (22)	-	-	-
7.40	5.56E-13 (15)	2.24E-13 (17)	7.49E-14 (41)	7.01E-14 (45)	2.49E-13 (13)	-
7.35	2.99E-13 (24)	1.99E-13 (33)	6.75E-14 (21)	6.52E-14 (31)	2.61E-13 (12)	-
7.30	2.82E-13 (20)	-	7.52E-14 (24)	7.73E-14 (32)	2.31E-13 (11)	-
7.25	1.95E-13 (11)	2.50E-13 (10)	6.54E-14 (20)	-	-	-
7.20	1.57E-13 (10)	1.79E-13 (10)	5.46E-14 (19)	-	-	-
7.15	1.42E-13 (10)	1.83E-13 (10)	5.06E-14 (16)	-	-	-
7.10	1.29E-13 (11)	1.59E-13 (11)	5.41E-14 (17)	7.82E-14 (17)	8.54E-14 (16)	-
7.10	1.43E-13 (5)	1.48E-13 (5)	3.81E-14 (11)	-	-	-
7.05	-	-	3.36E-14 (10)	-	-	-
7.00	1.39E-13 (99)	-	2.70E-14 (19)	9.20E-14 (11)	8.51E-14 (12)	-
6.95	8.83E-14 (12)	1.16E-13 (13)	2.24E-14 (23)	-	-	-
6.90	6.53E-14 (10)	1.21E-13 (9)	2.03E-14 (19)	8.91E-14 (10)	7.73E-14 (11)	-
6.85	5.55E-14 (9)	1.03E-13 (7)	1.80E-14 (21)	7.51E-14 (11)	5.10E-14 (13)	-
6.80	7.17E-14 (21)	5.94E-14 (20)	1.85E-14 (32)	5.85E-14 (12)	4.97E-14 (12)	-
6.75	3.11E-14 (11)	6.95E-14 (11)	1.44E-14 (26)	5.60E-14 (11)	3.76E-14 (13)	-
6.70	3.81E-14 (29)	3.74E-14 (24)	1.35E-14 (15)	3.42E-14 (10)	3.17E-14 (11)	-
6.65	1.83E-14 (20)	3.32E-14 (17)	1.27E-14 (17)	3.37E-14 (11)	2.77E-14 (18)	-
6.60	3.24E-14 (31)	1.93E-14 (31)	6.59E-15 (34)	2.92E-14 (12)	2.32E-14 (13)	-
6.55	2.68E-14 (38)	1.22E-14 (60)	3.49E-15 (35)	1.46E-14 (16)	2.00E-14 (17)	-
6.50	2.08E-14 (33)	-	4.62E-15 (24)	1.05E-14 (18)	2.04E-14 (11)	4.08E-15 (32)
6.45	1.33E-14 (25)	1.30E-14 (20)	3.14E-15 (28)	5.64E-15 (27)	-	-
6.40	1.53E-14 (23)	-	2.26E-15 (31)	4.58E-15 (30)	-	-
6.35	1.15E-14 (19)	1.33E-14 (17)	-	-	-	-
6.30	1.10E-14 (25)	1.09E-14 (28)	-	-	-	-
6.25	7.47E-15 (77)	7.81E-15 (55)	-	-	-	-

Table D.5: Thick target yields [cts $^{12}C^{-1}$ sr^{-1}] for the different proton groups of the $^{12}C(^{12}C,p)^{23}Na$ reaction at $\theta_{lab} = 143^o$ (New configuration). Uncertainties are given in % in parenthesis (those larger than 100% are marked with a + sign). Beam energies are in MeV.

$\mathbf{E}_{lab}$	$\mathbf{p}_0$	$\mathbf{p}_1$	$\mathbf{p}_2$	$\mathbf{p}_3$	$\mathbf{p}_{4+5}$	$\mathbf{p}_6$
143^o New CONFIGURATION						
7.20	1.03E-13 (13)	1.21E-13 (13)	3.83E-14 (22)	8.47E-14 (17)	1.21E-13 (14)	-
7.20	7.94E-14 (18)	1.15E-13 (15)	3.19E-14 (29)	6.42E-14 (22)	7.87E-14 (20)	-
7.10	7.09E-14 (16)	1.25E-13 (12)	2.46E-14 (33)	6.96E-14 (22)	8.33E-14 (19)	-
7.06	7.29E-14 (14)	1.09E-13 (12)	2.26E-14 (26)	9.03E-14 (15)	7.02E-14 (17)	-
7.04	6.78E-14 (15)	1.13E-13 (12)	2.86E-14 (23)	8.44E-14 (15)	6.64E-14 (18)	-
7.00	6.25E-14 (15)	1.23E-13 (11)	2.25E-14 (25)	6.55E-14 (16)	5.21E-14 (19)	-
7.00	7.77E-14 (6)	-	2.20E-14 (94)	5.19E-14 (8)	-	-
6.94	4.07E-14 (19)	9.03E-14 (12)	2.27E-14 (22)	4.74E-14 (16)	4.89E-14 (17)	-
6.88	2.64E-14 (20)	6.50E-14 (12)	1.13E-14 (29)	4.40E-14 (16)	4.81E-14 (16)	-
6.82	2.01E-14 (20)	4.48E-14 (13)	8.78E-15 (31)	3.02E-14 (19)	4.93E-14 (15)	9.92E-15 (52)
6.76	1.61E-14 (16)	2.85E-14 (12)	5.07E-15 (29)	1.96E-14 (18)	2.89E-14 (13)	5.81E-15 (33)
6.74	1.60E-14 (20)	2.53E-14 (18)	6.23E-15 (31)	2.46E-14 (16)	2.48E-14 (18)	5.34E-15 (66)
6.72	1.20E-14 (23)	2.56E-14 (17)	4.81E-15 (+)	2.13E-14 (31)	2.62E-14 (30)	-
6.70	1.08E-14 (21)	2.05E-14 (15)	3.19E-15 (42)	1.92E-14 (17)	2.49E-14 (29)	-
6.66	7.70E-15 (18)	1.57E-14 (13)	2.84E-15 (42)	9.31E-15 (20)	1.69E-14 (27)	-
6.60	5.46E-15 (24)	7.24E-15 (22)	1.38E-15 (50)	-	2.49E-14 (24)	-
6.40	7.81E-15 (23)	6.83E-15 (26)	1.03E-15 (54)	1.61E-15 (58)	-	-
6.25	2.81E-15 (27)	4.41E-15 (22)	5.60E-16 (87)	5.27E-16 (75)	-	2.17E-15 (35)
6.20	2.02E-15 (29)	3.29E-15 (24)	4.78E-16 (76)	4.42E-16 (+)	-	1.91E-15 (31)
6.15	1.30E-15 (28)	2.59E-15 (20)	1.09E-15 (32)	2.17E-16 (+)	-	-
6.10	5.27E-16 (42)	7.92E-16 (33)	-	6.38E-16 (79)	2.39E-15 (+)	-
6.10	9.85E-16 (31)	2.37E-15 (21)	7.32E-16 (41)	2.27E-16 (+)	-	-
6.00	7.98E-16 (39)	1.28E-15 (30)	4.47E-16 (65)	-	2.19E-15 (96)	-
5.90	9.43E-16 (34)	1.20E-15 (30)	7.10E-16 (47)	-	1.19E-15 (59)	-
5.80	4.90E-16 (41)	7.35E-16 (35)	5.00E-16 (51)	-	2.16E-15 (+)	-
5.70	3.73E-16 (41)	4.17E-16 (39)	3.14E-16 (+)	-	1.04E-15 (31)	-
5.70	1.67E-16 (96)	7.70E-16 (44)	2.23E-16 (+)	-	-	-
5.65	1.74E-16 (71)	5.05E-16 (41)	2.02E-16 (88)	-	1.34E-15 (33)	-
5.60	7.19E-17 (41)	4.16E-16 (29)	1.97E-17 (+)	-	6.72E-16 (31)	-
5.55	9.62E-17 (67)	1.91E-16 (48)	1.55E-18 (+)	-	6.80E-16 (33)	-
5.50	9.39E-17 (65)	1.04E-16 (63)	6.48E-17 (86)	-	5.55E-16 (29)	-
5.45	2.67E-17 (+)	1.84E-16 (46)	-	-	2.26E-16 (40)	-
5.45	2.71E-17 (+)	8.39E-17 (48)	-	-	1.09E-16 (78)	-
5.40	2.36E-17 (46)	8.85E-16 (4)	3.63E-17 (44)	5.03E-17 (39)	1.25E-16 (42)	2.28E-16 (28)
5.35	5.18E-18 (+)	5.32E-18 (+)	-	-	-	-
5.30	7.63E-18 (+)	1.13E-17 (92)	-	-	-	-
5.25	7.77E-18 (+)	9.90E-18 (93)	-	-	-	-
5.20	7.43E-18 (72)	9.73E-18 (63)	2.03E-17 (48)	2.02E-17 (48)	-	-
5.15	6.29E-18 (+)	8.32E-18 (93)	2.12E-17 (59)	2.17E-17 (58)	-	-
5.10	5.41E-18 (+)	6.81E-18 (+)	1.80E-17 (68)	1.83E-17 (67)	-	-
5.05	2.12E-18 (+)	3.15E-18 (+)	1.12E-17 (86)	1.20E-17 (81)	-	-

Table D.6: Thick target yields [cts $^{12}C^{-1}$ sr^{-1}] for the different proton groups of the $^{12}C(^{12}C,p)^{23}Na$ reaction at $\theta_{lab} = 156^{o}$UP (Old configuration). Uncertainties are given in % in parenthesis (those larger than 100% are marked with a + sign). Beam energies are in MeV.

$\mathbf{E}_{lab}$	$\mathbf{p}_0$	$\mathbf{p}_1$	$\mathbf{p}_2$	$\mathbf{p}_3$	$\mathbf{p}_{4+5}$	$\mathbf{p}_6$
156°UP Old CONFIGURATION						
8.60	1.63E-11 (1)	1.78E-11 (1)	4.85E-12 (1)	2.73E-11 (1)	1.13E-11 (1)	4.54E-12 (1)
8.55	1.79E-11 (2)	1.44E-11 (2)	4.57E-12 (3)	2.96E-11 (1)	9.21E-12 (3)	4.42E-12 (4)
8.50	1.63E-11 (1)	1.45E-11 (1)	3.19E-12 (3)	2.79E-11 (1)	8.81E-12 (2)	4.58E-12 (2)
8.45	1.34E-11 (1)	1.38E-11 (1)	2.60E-12 (4)	2.21E-11 (1)	6.52E-12 (2)	3.76E-12 (3)
8.40	1.40E-11 (2)	1.36E-11 (2)	2.44E-12 (5)	2.03E-11 (2)	4.57E-12 (4)	3.55E-12 (4)
8.35	1.33E-11 (2)	1.17E-11 (2)	2.02E-12 (5)	1.68E-11 (2)	3.40E-12 (4)	3.10E-12 (4)
8.30	1.01E-11 (2)	9.79E-12 (2)	1.69E-12 (5)	1.08E-11 (2)	3.23E-12 (4)	1.94E-12 (5)
8.30	9.35E-12 (3)	8.48E-12 (4)	1.83E-12 (8)	1.07E-11 (3)	3.26E-12 (6)	1.98E-12 (7)
8.25	8.31E-12 (3)	4.03E-12 (4)	1.04E-12 (8)	8.33E-12 (3)	2.78E-12 (5)	1.32E-12 (7)
8.20	5.65E-12 (8)	-	9.60E-13 (18)	4.66E-12 (8)	7.33E-12 (5)	7.54E-13 (21)
8.15	-	-	9.05E-13 (17)	3.51E-12 (10)	2.30E-12 (12)	7.39E-13 (25)
8.10	4.32E-12 (8)	3.62E-12 (10)	9.20E-13 (15)	2.63E-12 (10)	1.89E-12 (11)	6.23E-13 (22)
8.05	3.41E-12 (7)	3.48E-12 (7)	7.58E-13 (15)	1.80E-12 (10)	1.40E-12 (11)	7.00E-13 (15)
8.00	2.93E-12 (10)	2.99E-12 (10)	5.59E-13 (23)	1.42E-12 (18)	1.08E-12 (18)	5.29E-13 (27)
7.95	2.28E-12 (11)	2.71E-12 (10)	4.05E-13 (40)	1.32E-12 (17)	9.30E-13 (18)	4.56E-13 (27)
7.90	1.96E-12 (9)	2.85E-12 (6)	4.39E-13 (18)	7.23E-13 (12)	7.71E-13 (12)	4.91E-13 (15)
7.85	9.44E-13 (19)	2.66E-12 (11)	2.92E-13 (47)	4.03E-13 (36)	5.57E-13 (23)	3.15E-13 (33)
7.80	1.21E-12 (23)	2.18E-12 (11)	3.57E-13 (31)	2.81E-13 (65)	4.73E-13 (26)	2.68E-13 (34)
7.75	1.15E-12 (45)	1.99E-12 (14)	1.36E-13 (53)	1.96E-13 (39)	6.15E-13 (19)	2.20E-13 (38)
7.70	8.48E-13 (34)	1.68E-12 (12)	8.87E-14 (43)	1.70E-13 (35)	5.52E-13 (17)	2.44E-13 (30)
7.65	9.26E-13 (32)	1.27E-12 (15)	1.11E-13 (57)	1.28E-13 (52)	3.33E-13 (28)	1.31E-13 (51)
7.60	4.77E-13 (32)	1.26E-12 (14)	1.29E-13 (39)	1.26E-13 (51)	3.10E-13 (30)	-
7.55	6.02E-13 (36)	9.07E-13 (16)	1.12E-13 (40)	1.19E-13 (42)	3.24E-13 (24)	1.10E-13 (51)
7.50	3.24E-13 (28)	7.67E-13 (14)	4.38E-14 (62)	9.05E-14 (53)	3.19E-13 (21)	6.73E-14 (84)
7.45	3.25E-13 (22)	6.83E-13 (12)	4.26E-14 (66)	4.26E-14 (66)	2.64E-13 (19)	8.84E-14 (36)
7.40	3.52E-13 (37)	2.77E-13 (38)	3.29E-14 (41)	4.62E-14 (52)	2.08E-13 (23)	-
7.35	2.61E-13 (20)	2.59E-13 (19)	7.22E-14 (39)	-	-	7.81E-14 (35)
7.30	2.55E-13 (17)	1.41E-13 (24)	3.85E-14 (43)	-	-	6.61E-14 (30)
7.25	2.19E-13 (15)	1.26E-13 (21)	5.46E-14 (28)	-	-	-
7.20	1.85E-13 (15)	-	-	-	-	-
7.15	1.46E-13 (43)	9.91E-14 (+)	3.81E-14 (28)	-	-	-
7.10	1.33E-13 (14)	1.12E-13 (15)	3.11E-14 (32)	-	-	-
7.10	1.53E-13 (8)	8.93E-14 (11)	3.64E-14 (15)	-	-	-
7.05	1.29E-13 (8)	7.14E-14 (10)	3.44E-14 (11)	-	6.33E-14 (11)	-
7.00	9.43E-14 (17)	8.04E-14 (19)	4.42E-14 (39)	-	5.97E-14 (23)	-
6.95	8.05E-14 (15)	7.71E-14 (15)	4.12E-14 (22)	-	5.20E-14 (20)	-
6.90	6.58E-14 (16)	6.85E-14 (15)	3.02E-14 (24)	-	6.99E-14 (17)	-
6.85	5.72E-14 (14)	7.02E-14 (12)	3.45E-14 (19)	-	5.60E-14 (14)	-
6.80	4.20E-14 (15)	4.88E-14 (14)	2.07E-14 (27)	-	4.13E-14 (17)	-
6.75	3.03E-14 (17)	4.65E-14 (13)	9.62E-15 (30)	-	3.86E-14 (15)	-
6.70	2.82E-14 (15)	3.74E-14 (16)	7.38E-15 (31)	-	2.65E-14 (16)	-
6.65	2.06E-14 (19)	2.63E-14 (16)	6.06E-15 (36)	-	2.20E-14 (18)	-
6.60	1.34E-14 (23)	2.12E-14 (16)	3.24E-15 (39)	-	1.82E-14 (18)	-
6.55	1.15E-14 (27)	1.31E-14 (23)	4.50E-15 (49)	-	1.32E-14 (21)	-
6.50	1.10E-14 (26)	1.21E-14 (23)	3.04E-15 (58)	-	6.11E-15 (33)	-
6.45	8.33E-15 (25)	-	2.01E-15 (57)	-	-	-
6.40	8.34E-15 (24)	7.67E-15 (22)	1.67E-15 (56)	-	-	-
6.35	1.13E-14 (24)	1.11E-14 (22)	7.60E-15 (30)	-	-	6.40E-15 (54)
6.30	9.09E-15 (26)	9.22E-15 (23)	5.85E-15 (51)	-	-	3.91E-15 (43)
6.25	2.35E-15 (+)	5.74E-15 (91)	2.75E-15 (+)	-	-	-

Table D.7: Thick target yields [cts $^{12}C^{-1}$ sr^{-1}] for the different proton groups of the $^{12}C(^{12}C,p)^{23}Na$ reaction at $\theta_{lab} = 156^{o}$UP (New configuration). Uncertainties are given in % in parenthesis (those larger than 100% are marked with a + sign). Beam energies are in MeV.

$\mathbf{E}_{lab}$	$\mathbf{p}_0$	$\mathbf{p}_1$	$\mathbf{p}_2$	$\mathbf{p}_3$	$\mathbf{p}_{4+5}$	$\mathbf{p}_6$
156°UP New CONFIGURATION						
7.20	1.30E-13 (17)	1.35E-13 (17)	4.44E-14 (29)	-	1.19E-13 (21)	-
7.20	7.99E-14 (24)	8.97E-14 (23)	2.49E-14 (43)	-	7.28E-14 (30)	-
7.10	8.67E-14 (20)	1.13E-13 (18)	3.14E-14 (37)	-	1.01E-13 (20)	-
7.06	8.17E-14 (19)	8.51E-14 (19)	3.27E-14 (30)	-	7.14E-14 (22)	-
7.04	7.57E-14 (20)	1.08E-13 (17)	3.26E-14 (30)	-	9.12E-14 (20)	-
7.00	8.09E-14 (18)	9.68E-14 (17)	1.55E-14 (54)	-	6.14E-14 (23)	-
7.00	2.13E-13 (5)	1.02E-13 (8)	6.71E-14 (5)	-	-	-
6.94	6.14E-14 (19)	6.73E-14 (19)	1.55E-14 (35)	-	6.52E-14 (20)	-
6.88	5.07E-14 (28)	5.85E-14 (32)	1.03E-14 (56)	-	5.50E-14 (19)	-
6.82	2.91E-14 (23)	3.93E-14 (20)	7.92E-15 (28)	-	3.06E-14 (25)	-
6.76	1.99E-14 (27)	2.57E-14 (49)	5.40E-15 (39)	-	2.56E-14 (19)	-
6.74	1.23E-14 (31)	2.57E-14 (23)	5.95E-15 (27)	-	1.99E-14 (27)	-
6.72	1.38E-14 (30)	1.96E-14 (28)	6.15E-15 (28)	-	1.87E-14 (28)	-
6.70	1.23E-14 (28)	1.87E-14 (23)	4.98E-15 (31)	-	1.39E-14 (29)	-
6.66	1.07E-14 (21)	1.19E-14 (24)	3.10E-15 (39)	-	7.48E-15 (28)	-
6.60	7.42E-15 (25)	9.07E-15 (27)	3.32E-15 (27)	1.98E-15 (37)	-	-
6.40	7.65E-15 (32)	9.77E-15 (28)	4.01E-15 (27)	-	-	5.46E-15 (60)
6.25	2.77E-15 (38)	4.31E-15 (30)	2.15E-15 (46)	5.71E-16 (+)	-	-
6.20	1.90E-15 (42)	4.91E-15 (26)	1.16E-15 (60)	8.26E-16 (76)	-	-
6.15	1.05E-15 (41)	3.91E-15 (20)	1.58E-15 (34)	6.31E-16 (67)	-	-
6.10	9.71E-16 (41)	1.17E-15 (42)	4.51E-16 (66)	2.47E-16 (86)	7.55E-17 (+)	-
6.10	1.56E-15 (35)	2.59E-15 (28)	1.15E-15 (44)	8.82E-17 (+)	-	-
6.00	4.30E-16 (83)	3.29E-16 (99)	4.57E-17 (+)	-	-	-
5.90	3.27E-16 (+)	4.99E-16 (+)	3.17E-17 (+)	-	-	-
5.80	5.60E-16 (61)	4.50E-16 (68)	7.83E-17 (+)	4.01E-17 (+)	-	-
5.70	4.61E-16 (62)	3.61E-16 (70)	-	-	-	-
5.70	1.31E-16 (+)	6.30E-16 (73)	1.15E-17 (+)	-	-	-
5.65	2.85E-16 (84)	1.95E-16 (+)	-	-	-	-
5.60	3.11E-16 (52)	1.86E-16 (68)	2.79E-18 (+)	-	-	-
5.55	1.30E-16 (87)	7.15E-17 (+)	3.01E-18 (+)	-	-	-
5.50	1.80E-16 (69)	4.90E-17 (+)	2.62E-18 (+)	-	-	-
5.45	1.93E-16 (65)	9.18E-17 (97)	2.54E-18 (+)	-	-	-
5.45	5.92E-17 (+)	6.86E-17 (+)	-	8.76E-17 (+)	-	-
5.40	3.56E-17 (+)	4.02E-17 (+)	-	-	-	-
5.35	5.00E-17 (43)	5.41E-17 (43)	-	-	-	-
5.30	5.30E-17 (45)	5.97E-17 (44)	-	-	-	-
5.25	5.98E-17 (39)	6.32E-17 (40)	-	-	-	-
5.20	4.65E-17 (31)	5.04E-17 (32)	-	-	-	-
5.15	4.55E-17 (42)	4.66E-17 (43)	-	-	-	-
5.10	4.13E-17 (46)	4.39E-17 (46)	-	-	-	-
5.05	2.89E-17 (49)	3.14E-17 (49)	-	-	-	-

Table D.8: Thick target yields [cts $^{12}C^{-1}$ sr^{-1}] for the different proton groups of the $^{12}C(^{12}C,p)^{23}Na$ reaction at θ_{lab} = 156°DOWN (Old configuration). Uncertainties are given in % in parenthesis (those larger than 100% are marked with a + sign). Beam energies are in MeV.

$\mathbf{E}_{lab}$	$\mathbf{p}_0$	$\mathbf{p}_1$	$\mathbf{p}_2$	$\mathbf{p}_3$	$\mathbf{p}_{4+5}$	$\mathbf{p}_6$
156°DOWN Old CONFIGURATION						
8.60	1.64E-11 (1)	1.67E-11 (1)	3.91E-12 (1)	2.43E-11 (1)	1.36E-11 (1)	5.57E-12 (1)
8.55	1.49E-11 (2)	-	3.14E-12 (4)	2.48E-11 (1)	1.48E-11 (2)	5.70E-12 (3)
8.50	1.53E-11 (1)	1.47E-11 (1)	3.05E-12 (3)	2.55E-11 (1)	1.14E-11 (2)	6.16E-12 (2)
8.45	1.24E-11 (1)	1.36E-11 (1)	2.26E-12 (3)	2.00E-11 (1)	4.18E-12 (3)	8.78E-12 (2)
8.40	1.26E-11 (2)	1.99E-11 (2)	1.68E-12 (6)	1.87E-11 (2)	3.75E-12 (4)	7.16E-12 (3)
8.35	1.68E-11 (2)	1.20E-11 (2)	1.33E-12 (6)	1.50E-11 (2)	5.16E-12 (3)	3.35E-12 (4)
8.30	9.54E-12 (2)	7.64E-12 (3)	1.57E-12 (6)	1.14E-11 (2)	2.96E-12 (4)	2.24E-12 (5)
8.30	8.38E-12 (4)	8.38E-12 (4)	1.74E-12 (8)	1.17E-11 (3)	3.07E-12 (6)	2.51E-12 (6)
8.25	6.90E-12 (3)	4.88E-12 (4)	-	6.99E-12 (3)	4.16E-12 (4)	1.67E-12 (6)
8.20	5.01E-12 (7)	3.09E-12 (14)	1.21E-12 (16)	4.79E-12 (10)	3.16E-12 (11)	1.09E-12 (19)
8.15	4.44E-12 (7)	3.18E-12 (14)	-	3.39E-12 (8)	2.54E-12 (9)	1.01E-12 (14)
8.10	3.88E-12 (7)	4.42E-12 (7)	1.01E-12 (14)	2.33E-12 (10)	1.89E-12 (11)	8.06E-13 (16)
8.05	3.45E-12 (6)	3.92E-12 (6)	6.11E-13 (16)	1.96E-12 (9)	1.46E-12 (10)	7.79E-13 (14)
8.00	3.16E-12 (9)	3.40E-12 (9)	5.32E-13 (23)	1.63E-12 (16)	1.11E-12 (17)	3.22E-13 (40)
7.95	2.29E-12 (11)	3.12E-12 (9)	4.46E-13 (27)	9.07E-13 (18)	9.95E-13 (15)	4.37E-13 (23)
7.90	1.80E-12 (7)	3.11E-12 (5)	2.91E-13 (17)	6.68E-13 (12)	8.59E-13 (10)	4.65E-13 (14)
7.85	1.19E-12 (16)	2.47E-12 (10)	2.13E-13 (38)	3.35E-13 (29)	7.08E-13 (18)	3.13E-13 (31)
7.80	1.42E-12 (17)	2.19E-12 (11)	2.92E-13 (81)	2.73E-13 (58)	2.98E-13 (36)	2.97E-13 (30)
7.75	5.85E-13 (31)	2.09E-12 (13)	1.47E-13 (41)	1.36E-13 (+)	4.33E-13 (25)	2.97E-13 (31)
7.70	3.69E-13 (23)	2.15E-12 (9)	1.86E-13 (43)	1.32E-13 (49)	2.49E-13 (29)	2.96E-13 (28)
7.65	1.16E-12 (24)	1.38E-12 (12)	2.05E-13 (33)	1.33E-13 (47)	2.63E-13 (31)	1.39E-13 (42)
7.60	6.44E-13 (27)	1.16E-12 (14)	1.04E-13 (47)	1.27E-13 (44)	1.97E-13 (32)	2.46E-13 (27)
7.55	3.64E-13 (49)	1.08E-12 (19)	1.10E-13 (39)	1.06E-13 (44)	2.14E-13 (30)	1.07E-13 (40)
7.50	6.13E-13 (15)	7.73E-13 (11)	6.14E-14 (53)	9.73E-14 (61)	1.54E-13 (43)	7.95E-14 (39)
7.45	2.86E-13 (17)	7.68E-13 (11)	1.00E-13 (61)	9.06E-14 (45)	1.56E-13 (33)	8.55E-14 (39)
7.40	3.50E-13 (53)	4.00E-13 (37)	7.88E-14 (34)	9.02E-14 (37)	1.48E-13 (26)	6.73E-14 (39)
7.35	2.43E-13 (28)	2.94E-13 (23)	6.34E-14 (33)	-	-	7.05E-14 (40)
7.30	2.07E-13 (16)	1.88E-13 (18)	5.26E-14 (31)	-	-	8.03E-14 (14)
7.25	2.02E-13 (14)	1.27E-13 (18)	5.91E-14 (28)	-	-	-
7.20	2.01E-13 (13)	1.21E-13 (18)	3.47E-14 (35)	-	-	-
7.15	1.62E-13 (13)	1.04E-13 (18)	4.10E-14 (27)	-	-	-
7.10	1.44E-13 (16)	1.01E-13 (21)	3.41E-14 (26)	-	-	-
7.10	1.38E-13 (6)	1.05E-13 (8)	3.39E-14 (14)	-	-	-
7.05	1.17E-13 (6)	8.93E-14 (8)	2.74E-14 (+)	1.06E-13 (+)	6.15E-14 (+)	-
7.00	8.31E-14 (15)	1.12E-13 (13)	4.82E-14 (23)	7.44E-14 (19)	7.71E-14 (17)	-
6.95	7.74E-14 (14)	8.35E-14 (16)	2.71E-14 (25)	6.83E-14 (17)	7.71E-14 (16)	-
6.90	7.23E-14 (12)	8.75E-14 (63)	1.52E-14 (33)	8.96E-14 (14)	5.75E-14 (17)	-
6.85	5.70E-14 (13)	7.31E-14 (13)	1.98E-14 (33)	7.28E-14 (14)	4.40E-14 (18)	-
6.80	3.97E-14 (14)	5.92E-14 (12)	1.24E-14 (31)	5.99E-14 (14)	4.96E-14 (15)	-
6.75	4.27E-14 (14)	5.03E-14 (13)	7.87E-15 (32)	4.09E-14 (14)	3.50E-14 (16)	-
6.70	2.59E-14 (14)	3.84E-14 (12)	4.16E-15 (37)	3.92E-14 (12)	2.66E-14 (15)	-
6.65	2.01E-14 (17)	3.40E-14 (13)	4.68E-15 (+)	3.38E-14 (+)	1.80E-14 (99)	-
6.60	1.84E-14 (16)	2.18E-14 (18)	6.36E-15 (28)	2.67E-14 (14)	1.60E-14 (19)	-
6.55	1.17E-14 (23)	1.13E-14 (24)	1.15E-15 (68)	1.36E-14 (18)	8.86E-15 (25)	-
6.50	8.92E-15 (30)	9.89E-15 (26)	1.87E-15 (54)	7.02E-15 (27)	5.87E-15 (31)	-
6.45	8.55E-15 (25)	1.12E-14 (20)	2.04E-16 (+)	2.99E-15 (40)	-	-
6.40	8.08E-15 (22)	9.68E-15 (18)	8.18E-16 (81)	2.70E-15 (37)	-	-
6.35	1.08E-14 (24)	1.34E-14 (20)	-	1.66E-15 (69)	-	-
6.30	1.02E-14 (24)	1.19E-14 (20)	8.75E-16 (+)	-	-	-
6.25	8.20E-15 (71)	9.00E-15 (65)	1.89E-15 (+)	-	-	-

Table D.9: Thick target yields [cts $^{12}C^{-1}$ sr^{-1}] for the different proton groups of the $^{12}C(^{12}C,p)^{23}Na$ reaction at θ_{lab} = 156°DOWN (New configuration). Uncertainties are given in % in parenthesis (those larger than 100% are marked with a + sign). Beam energies are in MeV.

$\mathbf{E}_{lab}$	$\mathbf{p}_0$	$\mathbf{p}_1$	$\mathbf{p}_2$	$\mathbf{p}_3$	$\mathbf{p}_{4+5}$	$\mathbf{p}_6$
156°DOWN New CONFIGURATION						
7.20	1.06E-13 (19)	1.12E-13 (19)	1.87E-14 (63)	1.25E-13 (19)	7.93E-14 (23)	-
7.20	1.00E-13 (21)	6.96E-14 (26)	2.70E-14 (41)	1.00E-13 (22)	6.85E-14 (28)	-
7.10	6.55E-14 (24)	1.07E-13 (19)	1.97E-14 (47)	1.41E-13 (16)	7.36E-14 (24)	-
7.06	7.86E-14 (19)	8.16E-14 (19)	2.73E-14 (32)	9.73E-14 (18)	7.21E-14 (22)	-
7.04	7.09E-14 (20)	1.02E-13 (18)	2.41E-14 (34)	1.05E-13 (17)	6.33E-14 (23)	-
7.00	5.88E-14 (22)	9.63E-14 (18)	1.47E-14 (83)	8.31E-14 (19)	5.77E-14 (23)	-
7.00	8.27E-14 (8)	1.10E-13 (7)	1.85E-14 (17)	5.53E-14 (10)	3.55E-14 (11)	-
6.94	4.92E-14 (21)	5.81E-14 (19)	1.09E-14 (83)	5.95E-14 (19)	4.45E-14 (22)	-
6.88	3.60E-14 (24)	5.45E-14 (19)	1.26E-14 (39)	5.22E-14 (19)	3.48E-14 (24)	-
6.82	3.34E-14 (21)	3.31E-14 (22)	7.92E-15 (27)	3.70E-14 (20)	2.99E-14 (23)	-
6.76	1.69E-14 (21)	2.17E-14 (20)	3.96E-15 (26)	2.32E-14 (17)	1.86E-14 (20)	-
6.74	1.13E-14 (32)	2.11E-14 (23)	5.95E-15 (28)	2.61E-14 (20)	1.51E-14 (29)	-
6.72	1.34E-14 (29)	2.08E-14 (24)	6.78E-15 (43)	2.65E-14 (21)	1.42E-14 (31)	-
6.70	1.28E-14 (26)	1.36E-14 (27)	4.78E-15 (32)	1.79E-14 (22)	1.32E-14 (27)	-
6.66	1.04E-14 (20)	1.45E-14 (18)	2.25E-15 (+)	9.22E-15 (22)	9.16E-15 (23)	-
6.60	5.94E-15 (32)	7.88E-15 (28)	2.16E-15 (59)	-	-	-
6.40	5.78E-15 (36)	1.08E-14 (27)	2.01E-15 (39)	2.01E-15 (35)	-	-
6.25	2.64E-15 (38)	4.72E-15 (28)	2.04E-15 (37)	2.04E-15 (34)	-	-
6.20	1.71E-15 (+)	3.35E-15 (34)	1.71E-15 (35)	4.76E-16 (+)	-	-
6.15	1.31E-15 (35)	3.53E-15 (22)	9.30E-16 (37)	8.41E-16 (35)	-	-
6.10	1.10E-15 (37)	1.45E-15 (37)	6.08E-16 (64)	5.53E-16 (69)	7.55E-16 (25)	-
6.10	1.09E-15 (39)	1.94E-15 (30)	1.17E-15 (45)	2.81E-16 (+)	-	-
6.00	1.18E-15 (44)	1.48E-15 (41)	1.40E-15 (50)	6.62E-16 (86)	-	-
5.90	7.10E-16 (45)	1.25E-15 (42)	1.53E-15 (44)	1.01E-17 (+)	-	-
5.80	8.31E-16 (44)	1.08E-15 (39)	4.33E-16 (73)	-	-	-
5.70	4.70E-16 (52)	4.44E-16 (54)	-	-	5.21E-18 (+)	-
5.70	6.09E-16 (65)	8.04E-16 (63)	-	5.85E-17 (+)	3.42E-16 (+)	-
5.65	1.70E-16 (+)	3.77E-16 (95)	-	1.49E-16 (+)	3.32E-17 (+)	-
5.60	8.70E-17 (+)	1.68E-16 (66)	-	1.66E-16 (70)	2.79E-19 (+)	-
5.55	9.33E-17 (+)	1.32E-16 (81)	-	5.68E-17 (+)	3.01E-19 (+)	-
5.50	9.47E-17 (94)	5.72E-17 (+)	-	3.39E-17 (+)	2.62E-19 (+)	-
5.45	1.25E-16 (81)	5.05E-17 (+)	-	2.49E-17 (+)	1.41E-18 (+)	-
5.45	3.29E-17 (+)	3.37E-17 (+)	-	-	-	-
5.40	2.45E-17 (68)	3.26E-17 (58)	6.06E-17 (45)	6.01E-17 (45)	5.93E-17 (+)	-
5.35	1.55E-17 (+)	2.32E-17 (76)	6.64E-17 (42)	6.87E-17 (41)	-	-
5.30	2.60E-17 (74)	3.43E-17 (62)	9.92E-18 (+)	-	-	-
5.25	2.02E-17 (84)	3.00E-17 (65)	6.99E-17 (41)	7.39E-17 (39)	-	-
5.20	2.23E-17 (53)	2.94E-17 (45)	6.25E-17 (30)	6.20E-17 (31)	-	-
5.15	1.97E-17 (75)	2.46E-17 (65)	5.60E-17 (42)	5.60E-17 (42)	-	-
5.10	1.77E-17 (80)	8.00E-17 (93)	5.14E-17 (46)	5.14E-17 (46)	-	-
5.05	1.03E-17 (+)	1.51E-17 (81)	3.59E-17 (51)	3.58E-17 (51)	-	-

Bibliography

[1] C. Angulo. *Lecture Notes in Physics*, 764 (2009) 253–282.

[2] F. Hoyle. *Monthly notes of royal Astrophysics society*, 106 (1946).

[3] F. Hoyle. *Astrophysical journal supplement*, 1 (1954).

[4] A. Aprahamian et al. *Progress in Particle and Nuclear Physics*, 54 (2005) 535–613.

[5] H. Reeves. *Stellar Evolution and Nucleosynthesis*. Gordon and Breach, Science Publishers Inc., 1968.

[6] C. Rolfs and W. Rodney. *Cauldrons in the Cosmos*. The University of Chicago Press, 1988.

[7] S. G. Ryan and A. J. Norton. *Stellar Evolution and Nucleosynthesis*. Cambridge University Press, 2010.

[8] A. C. Phillips. *The Physics of Stars*. Wiley, 1994.

[9] D. Clayton. *Principles of Stellar Evolution and Nucleosynthesis*. The University of Chicago Press, 1983.

[10] C. Hayashi. *Publications of the Astronomical Society of Japan*, 13 (1961) 450–452.

[11] C. Iliadis. *Nuclear Physics of Stars*. Wiley-VCH, 2007.

[12] H. Bethe. *Physical Review C*, 55 (1939) 103.

[13] C.F. Weizsacker. *Zeitschrift für Physik*, 39 (1938) 633.

[14] D. Rapagnani et al. 407 (2017) 217–221.

[15] L. Gasques et al. *Physical Review C*, 72 (2005) 025806.

[16] C.A. Barnes et al. volume 6. Plenum, New York, 1985.

[17] S. A. Becker and I. Iben. *The Astrophysical Journal*, 237 (1980) 111–129.

[18] O. Straniero et al. *Journal of Physics (NPA6)*, 665 (2016) 012008.

[19] K. Schawinski et al. *Science*, 321 (2008) 223–226.

[20] E. Salpeter. *Physical review*, 88 (1952).

[21] M. Wiescher. *Annual Review of Astronomy and Astrophysics*, 50 (2012) 165–210.

[22] D. G. Yakovlev et al. *Astro-ph - arXiv*, 1 (2010) 1010.2430.

[23] R. A. Wolf. *Physical Review*, 137 (1965) B1634.

[24] D. C. Black. *Geochimica et Cosmochimica Acta*, 36, 1972.

[25] H. Frauenfelder and E.M. Henley. *Subatomic Physics*. Prentice-Hall, 1974.

[26] T. Spillane. *Study of the fusion reaction* ^{12}C $+^{12}$ C *towards the Gamow energy*. PhD thesis, University of Conneticut, 2008.

[27] C. R. Brune and D. B. Sayre. *Nuclear Instruments and Methods in Physics Research A*, 698 (2013) 49–59.

[28] J.R. Patterson et al. *Astrophysics journal*, 157 (1969).

[29] S.E. Woosley et al. *Astropysical Journal*, 607 (2004).

[30] I. Baraffe et al. *Astropysical Journal*, 615 (2004).

[31] F. Strieder and C. Rolfs. *Progress in Particle and Nuclear Physics*, 59 (2007) 562–578.

[32] M. Pignatari et al. *The Astrophysical Journal*, 762 (2013) 31.

[33] M. Limongi. *VI European Summer School on Experimental Nuclear Astrophysics*, (2011).

[34] B. Bucher et al. *EPJ Web of Conferences*, 93 (2015) 03009.

[35] M.E. Bennett et al. *Monthly Notices of the Royal Astronomical Society*, 420 (2012) 3047–3070.

[36] R.L. Cooper et al. *Astrophysical Journal*, 702 (2009).

[37] A. Cumming and L. Bildsten. *Astrophysical Journal Letters*, 559 (2001).

[38] X. Tang et al. *Nuclear Physics and Power*, 14 (2013) 3.

[39] L. Barrón-Palos et al. *Nuclear Physics A*, 779 (2006) 318–332.

[40] M.G. Mazarakis and W.E. Stephens. *Phys. Rev. C*, 7 (1973) 1280–1287.

[41] H.W. Becker et al. *Zeitschrift für Physik A, Atoms and Nuclei*, 312 (1981) 305–312.

[42] J. Zickefoose. ^{12}C+^{12}C *Fusion: Measurement and Advances Toward the Gamow Energy.* PhD thesis, University of Conneticut, 12 2010.

[43] K.U. Kettner et al. *Zeitschrift für Physik A, Atoms and Nuclei*, 75 (1980) 65–75.

[44] T. Spillane et al. *Physical Review Letters*, 98 (2007) 122–501.

[45] P. Rosales and E.F. Aguilera. *Revista Mexicana de Física S4*, 49 (2003) 88–91.

[46] M.D. High and B. Ĉujec. *Nuclear Physics A*, 282 (1977) 181–188.

[47] L. Barrón-Palos et al. *Revista Mexicana de Física S2*, 50 (2004) 18–23.

[48] L. Barrón-Palos et al. *European Physics Journal A*, 25 (2005) 645–646.

[49] E. Aguilera et al. *Physical Review C*, 73 (2006) 064601.

[50] C.L. Jiang et al. *Nuclear Instruments and Methods in Physics Research Section A*, 682 (2012) 12–15.

[51] D. Santiago-Gonzalez et al. *European Physics Journal, Web of conferences*, 117 (2016) 09011.

[52] E. Bravo et al. *Astronomy and Astrophysics*, 535 (2011) A114.

[53] B.R. Fulton. *Contemporary Physics*, 40 (1999).

[54] M. Freer and A.C. Merchant. *Journal of Physics G: Nuclear and Particle Physics*, 23 (1997) 261.

[55] D.A. Bromley et al. *Physical Review Letters*, 4 (1960).

[56] L.J. Satkowiak et al. *Physical Review C*, 26 (1982) 5.

[57] C. L. Jiang et al. *Physical Review Letters*, 110 (2013) 072701.

[58] C.L. Jiang et al. *Physical Review C*, 75 (2007) 015803.

[59] X.D. Tang et al. *Nuclear Physics in Astrophysics V*, 337 (2012) 012016.

[60] F. Terrasi et al. *Nuclear Instruments and Methods in Physics Research B*, 259 (2007) 14–17.

[61] Y. Saitoh et al. *Review of Scientific Instruments*, 71 (2000) 2.

[62] K.S. Krane. *Introductory Nuclear Physics*. Wiley, 1955.

[63] Michigan State University. Cosy nfinty. B149 Biomedical and Physical Sciences Building. http://cosyinfinity.org/.

[64] Flir Systems. Flir sc325. http://www.flir.com/thg.

[65] Pfeiffer Vaccum. *Operating Manual AMS current integrator*. Asslar, Deutschland.

[66] M. Romoli, L. Morales-Gallegos, et al. Development of a two-stage detection array for low energy light charged-particles in nuclear astrophysics applications. *European Physical Journal*, (in preparation), (2017).

[67] J. F. Devaux, G. Lê, and B. Pees. Application of eco-profile methodology to polyamide 11. Arkema, France. http://omnexus.com/tc/pa11-pa12/index.aspx.

[68] Canberra Industries Inc. Pips silicon detectors catalogue, http://www.canberra.com/products/detectors/pips-detectors-single-multiple.asp.

[69] M. Romoli et al. *European Physical Journal A*.

[70] M. Romoli et al. *IEEE Transactions on Nuclear Science*, 52 (2005) 5.

[71] A. Ordine et al. *IEEE Transactions on Nuclear Science*, 45 (1998) 3.

[72] W. Catford. Catkin, kinematic calculation spreadsheet. University of Surrey, 2004. http://personal.ph.surrey.ac.uk/ phs1wc/kinematics/.

[73] M.E. Bennett et al. *Proceedings of Science*.

[74] Michio Inagaki. *New Carbons, Control of Structure and Functions*. Elsevier, 2000.

[75] N.N. Adrianova et al. *Nuclear Instruments and Methods in Physics Research B*, 273 (2012) 56–60.

[76] A.M. Borisov et al. *Nuclear Instruments and Methods in Physics Research B*, 256 (2007) 363–367.

[77] C.P. Herrero and R. Ramirez. *IOP Publishing*, (2010) (submitted).

[78] Y. Ferro et al. *Journal of Chemical Physics*, 116 (2002) 18.

[79] G. Debras and G. Deconnick. *Journal of Radioanalytical and Nuclear Chemistry*, 38 (1977).

[80] H.W. Becker et al. *Zeitschrift für Physik A, Atoms and Nuclei*, 465 (1995) 453–465.

[81] P.R. Bevington and D.K. Robinson. *Data Reduction and Error Analysis for the Physical Sciences*. McGraw-Hill, 2003.

[82] National Electrostatics Corp. *Instruction Manual No. 2HT068600 for AMS current integrator*. Middleton, WI, USA, 7 2004.

[83] R. A. Dayras et al. *Nuclear Physics A*, 265 (1976) 153–188.

[84] S. Trentalange et al. *Nuclear Physics A*, 483 (1988) 406–428.

[85] C. G. Bruno. *Underground measurements of hydrogen-burning reactions on* $^{17,18}O$ *at energies of astrophysical interest*. PhD thesis, The University of Edinburgh, 2017.

[86] CERN. https://root.cern.ch/.

[87] J. Ziegler et al. *Nuclear Instruments and Methods in Physics Research Section B: Beam Interactions with Materials and Atoms*, 268 (2010).

[88] O. B. Tarasov and D. Bazin. *Nuclear Instruments and Methods in Physics Research B*, 204 (2003) 174–178.